University of Alberta

Micromechanical Resonators

by

Holly Dawn Rourke ©

A thesis submitted to the Faculty of Graduate Studies and Research in partial fulfillment of the

requirements for the degree of *Master of Science*

Department of *Electrical and Computer Engineering*

Edmonton, Alberta

Fall 2005

Canada

University of Alberta

Library Release Form

Name of Author: *Holly Dawn Rourke*

Title of Thesis: *Micromechanical Resonators*

Degree: *Master of Science*

Year this Degree Granted: *2005*

Permission is hereby granted to the University of Alberta Library to reproduce single copies of this thesis and to lend or sell such copies for private, scholarly or scientific research purposes only.

The author reserves all other publication and other rights in association with the copyright in the thesis, and except as herein before provided, neither the thesis nor any substantial portion thereof may be printed or otherwise reproduced in any material form whatsoever without the author's prior written permission.

_____

Signature

Abstract

This thesis presents preliminary work in the development and application of a commercial MEMS process to the field of Radio Frequency MicroElectroMechanical Systems (RF MEMS). Specifically, a micromechanical resonator is discussed. An electrostatically actuated cantilever beam with a resonant frequency in the low kHz range is designed, fabricated, and tested. In this work, a generalized, MEMS prototyping process, Micragem, developed by Micralyne Inc., is used, and, in collaboration with Micralyne, this microfabrication process is further developed. Optical and electrical characterization methods were developed to sense the displacement (and ultimately the resonant frequency) of the device.

Acknowledgements

It is with great pleasure that I recognize those who helped, supported, facilitated, and educated me during my master studies.

First, I would like to acknowledge Micralyne Inc. because this research would have never been completed nor have been successful without this company. Thank you for supporting my research through the industrial NSERC and allowing me to fabricate my devices in Micralyne's microfabrication facility. The level of quality and yield I was able to achieve by fabricating at Micralyne was far above what a graduate student expects. At this time, I would like to also acknowledge the staff at Micralyne because they were extremely supportive, by lending an ear or helping me along with intelligent conversations and input. My gratitude is extended towards Patrick Wright, Yan Loke, Glen Fitzpatrick, Collin Twanow, Tiensheng Zhou, Bruce Alton, Chris Lumb and Bob Lyons.

Thank you, NSERC, for the financial support for my research. Your continued support for research is much appreciated. Many thanks to Dr. Christopher Backhouse for being my supervisor. You have moulded me into an independent thinker and, by creating a free environment, my skills in project leadership and direction were able to blossom.

Next, I would like to recognize the technicians in the Electrical and Computer Engineering department at the University were instrumental in helping me understand and improve my testing methods. I learned most from the technicians and I thank you very much for answering my numerous electrical/electronics questions. I would like to recognize Ben Bathgate, Alan Lim, Don Mullin, and Steve Drake for this.

In addition, I would like to thank Dean Spicer because he was instrumental getting me started with the interferometer set-up. A lot of time and effort was saved because he was able to allot me access to much of the equipment that I needed. Most importantly, I appreciate that Dean is willing to share his knowledge, ideas, and skills. Brian Moore was a pleasure to work with and I am proud that he was eager to combine his ideas with my devices. I would also like to recognize Yuebin Ning and Graham McKinnon who took an interest in my research and were there to offer guidance, suggestion, equipment, and test devices at times when I needed those most. Huge thanks to the Nanofab and its staff for use of the characterization tools and to Ken Westra who offered excellent advice in troubleshooting testing methods.

I would like to recognize my parents for their support during this endeavour and their continual willingness to lend an ear or encouragement. Also, thank you, mom, for being a grammatical wizard.

The people who helped me during this degree are near and dear to my heart. I appreciate the interactions and relationships I developed with the people during graduate studies and hope that I will be able to repay each and every one of you, as I am indebted.

Table of Contents

List of Tables

List of Figures

List of Abbreviations

CNTs:	Carbon Nanotubes
d_{BS}:	Beam-to-Substrate Separation
ECE:	Electrical and Computer Engineering
FEA:	Finite Element Analysis
f_R:	Resonant Frequency
HeNe:	Helium Neon Laser Source
HF:	High Frequency (3-30 MHz)
GRIN:	Gradient Index lens
IC:	Integrated Circuit
ICPRIE:	Inductively-Coupled Reactive Ion Etcher
IF:	Intermediate Frequency Stage of a Heterodyne Receiver
KOH:	Potassium Hydroxide
MEMS:	MicroElectroMechanical Systems
Micragem:	Micralyne Generalized MEMS
Q:	Q-factor or Quality factor
PZT:	Lead Zirconate Titanate
ROC:	Radius of Curvature
RFICs:	Radio Frequency Integrated Circuits
RF MEMS:	Radio Frequency MicroElectroMechanical Systems
SAW:	Surface Acoustic Wave
SCS:	Single Crystal Silicon
SEM:	Scanning Electron Microscope
Si:	Silicon
SiO_2:	Silicon Dioxide
SOI:	Silicon-On-Insulator Wafer
TED:	Thermoelastic Energy Dissipation
TGG:	Terbium Gallium Garnet
UHV:	Ultra High Vacuum ($<10^{-9}$ Torr)
VHF:	Very High Frequency (30-300 MHz)
V_P:	Applied Polarization Voltage or Bias Voltage
V_{th}:	Threshold Voltage

Chapter 1 – Introduction

This research was conducted in collaboration with Micralyne Inc. to further develop their multi-user process, Micragem, while exploring the feasibility of Radio Frequency MicroElectroMechanical Systems (RF MEMS). Specifically, the area of micromechanical resonators is explored.

Electrostatically-actuated, microfabricated single-crystalline cantilever beams are fabricated, characterized, and their behaviour analyzed with the intention of either scaling the design to meet wireless communications requirements or to adapt their function for use in a biological mass sensor. The cantilevers were designed to be excited at their fundamental resonance in the low kHz region with a typical length, width, and thickness of 200μm, 25μm, and 2μm, respectively. In effect, the function of a micromechanical resonating device is to receive an electrical signal, to convert it to a mechanical signal, to process it in the mechanical domain, and then to reconvert it to an electrical signal further processing by electronics.

MEMS resonators, such as the micromechanical resonator in this work, are potential candidates to replace current off-chip, frequency selective mechanical components, such as crystal, ceramic and SAW devices in wireless communication systems [1]. Many of these non-semiconductor devices are made of crystals such as quartz and lithium niobate, which are not compatible materials with IC processing. This means that these devices have to be connected to Radio Frequency Integrated Circuits (RFICs) at the board level [2].

Because of MEMS compatibility with semiconductor processing, these hold the potential to be fully integrated devices, reducing production costs and, more importantly, size. Micromechanical resonating structures offer other advantages as well. They can exhibit

excellent quality factors (Q) largely because their operation is mechanical. Quality factors greater than 10,000 are increasingly reported and, extraordinarily, a Q of 200,000 [3] has been recently reported. This is far better than integrated circuits, which are typically able to provide Qs under 75 [4]. For example, the integrated coils for semiconductor-based inductors, which are often used in conjunction with capacitors for filter applications, are able to provide Qs of 10 at 300MHz. Off-chip inductors such as air coils and printed circuit board (PCB) coils can provide Q's of 60 and better at 300MHz. [4]

The project presented in this work is complete for the simplest of examples - the cantilever beam - for use as a micromechanical resonator. It is presented in its entirety including design, modeling, fabrication, testing, and characterization.

The background research is presented in Chapter 2. Because RF MEMS form such an extensive area of research, the background has been limited to micromechanical resonators. Included in the background are the methods of actuation and measurement, sources of loss in the resonator, and applications with state-of-the-art examples.

In Chapter 3, the design is outlined, including expected values for the resonator with respect to the threshold voltage, resonator frequency, induced current and quality factor. Limiting the threshold voltage is considered to be of the utmost importance in the design of a MEMS switch but is not necessarily true for the design of the MEMS resonator. In the case of an electrostatically actuated resonator, the threshold voltage acts as an estimation of the maximum DC voltage that can be applied to the beam before it closes and is unable to resonate. The resonance frequency is the fundamental frequency at which the cantilever resonates and the quality factor is the ratio of the energy stored in the system to the energy dissipated per cycle. It is desired that the movement of the cantilever be detected by monitoring the change in capacitance between the beam and the bottom electrode as the cantilever moves. This change in capacitance can induce a current at the bottom electrode under the cantilever beam, which, when extracted to the bonding pads, must be sufficiently large for detection. The integrated method for

detection is crucial in order to make on-chip electrical testing feasible. This calculation, as well as the entire analytical design, is presented in this chapter. The importance of the chapter is that it provides the basis for comparison throughout the work's entirety.

The fabrication, utilizing Micralyne's Micragem process, is explained in Chapter 4. The multi-user fabrication process was tested and improved during the course of this work. Two iterations of the cantilevers are fabricated, with the improvements added in the second run resulting in a more stable, reliable process for Micragem. Following these refinements, Micralyne, through the Canadian Microelectronics Corporation (CMC), offered the microfabrication service as a prototyping process across Canada. Academic researchers will further test the diversity and flexibility of the process. While further stabilization of the process is in progress, Micragem is becoming a reliable method for prototyping MEMS systems for both academic and industrial endeavours.

Upon fabrication, the testing and characterization of the devices are outlined and results presented. Preliminary testing, such as static testing and an unsuccessful attempt to sense the dynamic movement of the cantilever beam electrically, is presented in Chapter 5. (Static testing includes monitoring how much the cantilever is displaced with an applied, DC voltage potential.) The electrical testing method is briefly presented and a full explanation of why the capacitive gap (the gap between the cantilever beam and the bottom electrode) is too large for this method of testing to be feasible using the current design.

An alternative testing approach for characterizing the dynamic motion of the cantilever beam is presented in Chapters 6 and 7, with results presented in Chapter 8. The method of interferometry is utilized to sense the motion of the cantilever beam. A bench-top interferometer is assembled and presented in Chapter 6. The test set-up is then characterized to ensure that it is suitable for the measurement of submicron movement of the cantilever beam in the kHz range, as is explained in Chapter 7. The experimental results for an electrostatically actuated, cantilever based, micromechanical resonator are finally presented in Chapter 8. The results include two responses – driven and transient

responses. From the results, the resonant frequency, the quality factor, and the transient responses (including damping factors) are found and compared to the expected values of Chapter 3.

Finally, improvements to both the design and test method are presented in Chapter 9. A novel tuning fork design that has no support losses is presented and preliminarily modeled. A fibre interferometer is developed with Brian Moore, a doctoral candidate in electrical engineering, who has been developing non-contact characterization methods. In collaboration with him, we developed and applied his design to the testing of resonating cantilever beams. These results are presented and potential commercial uses for the method are described. Finally, applications are discussed in this chapter with respect to their requirement for a high quality factor for on-chip sensing.

This work is an exploration of the application of Micragem to micromechanical resonators. A relatively large cantilever beam that resonates at low frequency is explored and its behaviour analyzed with the intention of scaling down the design for use as harmonic radar tags for biological applications. (Scaling down refers to maintaining the relative dimensions of a device but reducing them by a factor to achieve higher frequencies.) The candidate fabricated the micromechanical resonators at Micralyne's microfabrication facility using their prototyping process, Micragem. The collaborative effort enabled further development of the process. Upon fabrication of the kHz-range devices, it was found that detection of the displacement of the beam via electrical methods was not possible with the set-up used (although initial calculations deemed it plausible). This was disappointing because on-chip detection is critical to the development of integrated, self-contained units. Since neither quality factor nor resonant frequency could be characterized with electrical methods, optical methods based on interferometry were used to characterize the dynamic motion of the beams. Although air damping was expected to dominate the energy losses and limit the quality factor, it was a surprise that the effects were so heavily dependent upon the width of the beam. Future directions include a design with negligible support losses and encapsulations in vacuum to increase the performance of the device.

~4~

Chapter 2 - Background Research

1 Introduction

The development of micromechanical resonating structures is a challenging and active area of research because they have been proven to function with higher quality factors than their electronic counterparts. However, their small geometries and (optimally) vacuum environments make the manufacturing and packaging of them arduous. The following chapter attempts to summarize micromechanical resonators. First, the motivations for this area of research are explored through their application as mass sensors or frequency selective components. Secondly, various methods of actuation and measurement are outlined, and possible types of energy losses, which limit the device's quality factor, are explained. Finally, state-of-the-art examples reported in the literature are summarized.

2 Importance of Quality Factor

The quality factor, Q, of a resonator is extremely important for many applications such as those described below. The quality factor indirectly tells how long an oscillation will go on after a momentary excitation or defines the 'sharpness' of the resonance. The Q factor of a resonant system is a measure of the energy stored versus the energy dissipated in the system. It is defined by $Q = 2\pi \cdot \frac{E}{\Delta E}$, where E is the energy of oscillation and ΔE is the energy loss over one cycle of motion because of dissipation (i.e. work against friction). Other definitions include: (1) the centre frequency, f_o, divided by the bandwidth, Δf, $Q = f_o/\Delta f$, where the bandwidth is defined as the 3dB change in level on either side of the centre frequency, $\Delta f = f_2 - f_1$ and (2) $Q = \frac{\sqrt{mk}}{b}$, where m is the mass, k is the spring constant, and b is the mechanical resistance (or damping factor). As damping is introduced into a resonant system, the Q factor diminishes.

Micromechanical resonators have the potential of offering extremely high Q factors, which offer higher sensitivities in both the fields of mass sensing and wireless communications. Figure 2-1 illustrates the sharpness of resonance curves with varying Q factors. The y-axis is the ratio of the oscillatory amplitude, x, to the maximum oscillatory amplitude, x_{MAX}, of the resonant device, and the x-axis is a ratio of the angular frequency, ω, to the natural resonant frequency, ω_o, of the device. For signal processing devices, high Q directly translates into low insertion loss [5].
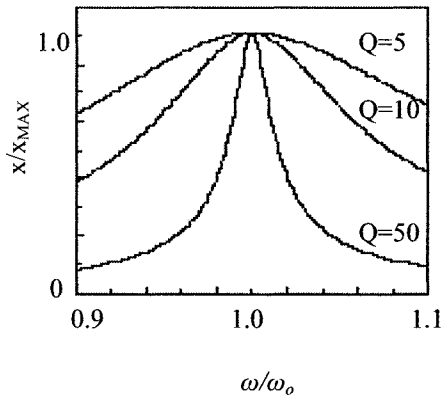
Figure 2-1: Sharpness of resonance curves with varying quality factors

3 Applications

Mechanical resonators are a far-reaching technology, suitable for a wide variety of applications. Two application areas of particular interest are mass sensors and frequency-selective components in wireless communications. As sensors, micromechanical devices can be used for the measurement of pressure, acceleration, strain, temperature, vibration, rotation, proximity, acoustic emission, and many other phenomena. Micromechanical resonators used for mass sensing are explored here as a viable application. Secondly, micromechanical resonators are applicable to the area of wireless communications. In communication systems, there is a large number of off-chip, bulky, frequency-selective components that need to be assembled at the board level. The possibility of eliminating the cost-heavy assembly and reducing board sizes has fuelled the demand for integrated micromechanical resonant devices. In a smaller, niche area of wireless communications, harmonic radar tags are used for the tracking of such items. The application of the micromechanical resonators to harmonic radar tracking is novel in its approach and is explored, as well.

3.1 Mass Sensing

Micromechanical cantilevers are natural candidates for mass sensing applications because of their miniscule active masses (effective masses) and their capability of achieving high quality factors. The difference between the effective mass and the real cantilever mass is that only a fraction of the cantilever is involved in its motion. The largest deflection takes place near the free end with a decay to zero at the clamped end. For cantilever beams, multiplying the total mass by the integral of a normalized function describing the mode shape yields a measure of the active mass [6]. The effective mass for a uniform cantilever of rectangular cross section is [7]:

$$m_e = \frac{33}{140} m \qquad \text{Equation 2-1}$$

Advantages of microfabricated mass sensors include the small size and required sample volume, mass production possibilities, increased reproducibility of device performance and possibility of integration with electronics and optics.

Microfabricated cantilevers are used in two fundamentally different ways for sensing applications [8]:

1. Static method – Detection of the static bending caused by mass loading onto a flexible cantilever on which a chemically active layer is coated [9-15]. Although this method is not entirely related to the work of micromechanical resonators, it is included because the device could potentially be used in this regard.

2. Dynamic method – This method requires the use of the cantilever as a micromechanical resonator. A shift in resonance due to mass loading is detected [3, 7, 10, 16-19].

Detection with these devices is evident because either (1) stress or (2) frequency is proportional to the mass loading. Addition of a mass will cause the (1) stress or the (2) frequency to change; thus, by monitoring these parameters, the mass loading can be deduced. These devices are highly sensitive with reports of mass sensitivities ranging from a few picograms [11-15, 17, 18, 20, 21], to as low as 10^{-18}g [3]!

~7~

3.1.1 Static Deflection

The static deflection of a cantilever beam can be monitored in order to detect a wide variety of adsorbents. If a chemically active layer is coated on the surface of a cantilever, the deflection before and after the layer has been exposed to the test environment is recorded. Because the cantilever is a bimorph structure with one layer changing stress characteristics with adsorption (the active layer), deflection of the cantilever occurs. For example, alcohol vapour can be measured with a photoresist-coated cantilever because the photoresist contracts when it is exposed to alcohol vapour [10]. A great advantage of this method is that it can be used in liquid media [14, 19] where incorporation with microfluidics is of great interest.

The sensitivity of a static device is increased by using long and soft (i.e. small spring constant) cantilevers in order to achieve large deflections [8]. However, quantitative evaluation is difficult because the stress induced by the adsorption is often unpredictable [3]. Also, because a change in temperature also causes a deflection, added error is included in the measurement. It has been suggested that to reduce background noise such as thermal drift and turbulence around the probe, a reference cantilever is crucial [13]. The reference cantilever would not be subjected to the mass loading but would be subjected to the environment, so drifts due to other variables can be subtracted from the mass measurement.

The most commonly used method for detecting the cantilever deflection is optics-based. By shining a laser beam onto the cantilever and monitoring the reflection (e.g. in AFM), the detection of cantilever deflections in the sub-angstrom regime has been reported [19]. However, integrated readouts are advantageous because they are more compact, require less adjustment and alignment, and facilitate work in liquids. Built-in piezoresistive readouts [19] sensitive to stress changes [10] are reported examples of integrated detection for cantilever-based sensor applications.

~8~

3.1.2 Dynamic Sensing

For a micromechanical resonator, the natural frequency of the system is equal to the square root of the spring constant divided by the mass, $\omega_o = \sqrt{k/m}$ (discussed in detail in Chapter 8). If the spring constant and effective mass of the cantilever beam are known, then any additional mass on the cantilever beam causes a frequency shift, which can be used to deduce the amount of mass loading. Resonant mass sensors are already employed in many diverse fields of science and technology. Among the most sensitive realizations are those based on the acoustic modes of crystals, thin films, and micron-sized cantilevers [22].

This application of micro-sized cantilever beams was first proposed by Cleveland *et al.* when they were investigating the spring constant of micromechanical cantilever beams used in scanning force microscopy (SFM) [7]. They determined that by measuring the beam's resonant frequencies before and after adding small end masses, the spring constant could be calculated by measuring the change in resonant frequency. During this exercise of characterizing the spring constant, the application of mass sensing was born with an estimated mass resolution of 0.5ng.

Resonator sensors are continually being scaled down and miniaturized. Smaller and thinner resonators cause increased resonant frequencies and smaller spring constants, which reportedly increase sensitivity [3]. From the example described above, measurements were made on 200μm long, 36 μm-wide V-shaped Si_3Ni_4 cantilevers, fundamentally resonating at 22.4kHz, and a 9.4kHz shift in frequency for a 44ng end mass was reported [7]. More recently, ultra thin (170nm) single-crystalline silicon cantilevers have achieved a mass resolution below 10^{-18}g from the noise level of ~0.001Hz in ultrahigh vacuum [3]. These mass sensors were used to find the hydrogen storage capacity of a small number of carbon nanotubes (CNTs).

Another very interesting application of mass sensing using microcantilever resonators is their recent use to detect DNA strands with a specific sequence [23]. Highly sensitive and selective DNA detection has attracted extensive attention for its importance in

~9~

genetic diagnostics. The core idea is to measure the mass change of a microfabricated cantilever induced by DNA hybridization through the shift of the resonance frequency of the cantilever [23].

There are two properties central to establishing the sensitivity of resonant mass sensors: (a) the effective vibratory mass of the resonator (Equation 2-1) and (b) the short- and long-term resonance frequency stability of the device [22]. The effective vibratory mass is determined by the geometry and configuration of the resonant structure and by the properties of the materials composing it. As was discussed at the beginning of this chapter, the square root of the mass of the device is directly proportional to the quality factor, so a high Q increases sensitivity. As for the stability of the resonator, external effects such as the medium it is in will affect the stability. For example, in air, environmental effects such as inconsistent humidity levels can affect its stability - one of the main reasons why most highly sensitive resonators are actuated in vacuum. One such example saw resonant frequencies slightly increasing until reaching stable values 2-3 hours after being put into UHV. It was explained in the report as adsorbed contaminations such as water molecules being desorbed in the UHV, which results in stabilizing the resonant frequency [3].

Given the recent realization of nanomechanical devices operating at microwave frequencies [24], prospects for weighing individual, electrically neutral molecules with single-Dalton[*] sensitivity are now feasible. [22]

3.2 Switchable Filters

The off-chip components used as bandpass filters of the radio frequency (RF) and intermediate frequency (IF) stages of heterodyning transceivers must interface with integrated electronics at the board level. This means that they are not integrated upon fabrication of the circuit but are manufactured separately and then introduced. This drives up the cost of assembly. In addition, the discrete components (such as crystal filters and surface acoustic wave (SAW) devices) used in RF and IF stages are a

---

[*] The SI defines 1 Dalton (Da) as 1/12 the mass of the C^{12} atom. $1 Da = 1.66 \times 10^{-27}$ kg.

magnitude or so larger than is possible with micromechanical resonators. The potential of miniaturized communication devices offers far-reaching opportunities, thus driving research in developing comparable, miniaturized filters.

IC-compatible microelectromechanical IF filters using integrated resonators with Q's in the thousands to achieve filter Q's in the hundreds have been demonstrated using a polysilicon surface micromachining technology. These filters are composed of two clamped-clamped beam (attached at both ends) micromechanical resonators coupled by a soft flexural-mode mechanical spring [25]. The centre frequency of a given filter is determined by the resonance frequency of the constituent resonators, while the coupling-spring dimensions and its location between the resonators determine the bandwidth.

Instead of conforming to the conventional architecture of filter technology, improving by direct replacement of off-chip high-Q passive components, a bottom-up approach is a possibility. A bottom-up approach means that instead of replacing components within the existing infrastructure of circuit design, the infrastructure is redesigned to best utilize new components. A switched-filter front-end is proposed by Nguyen in lieu of the tuneable filter used today [26]. The scheme proposed employs a bank of switches and filters. There is a pair of switches and a high-Q fixed filter for each desired input channel. The circuit reduces phase noise in the RF section and reduces dynamic-range requirements in the IF amplifier and mixer, enabling better performance with cheaper components [27].

Problems do exist, however, with the implementation of these resonators for wireless communications. The structures exhibit a far better response in vacuum because air molecules cause energy loss and, hence, reduced Q of the device. Developing vacuum packaging for long-term operation is a difficult task, which may be the largest stumbling block for their widespread replacement of current off-chip components. Traditional vacuum wafer bonding methods include anodic, glass frit, eutectic, solder, reactive and fusion bonding. Glass frit sealing has been coupled with silicon, Pyrex, CMOS integrated MEMS, capacitive and piezoresistive devices [28]. Conventional anodic

~11~

bonding produces cavity pressures in the 100-400 Torr range [29] and solder bonding around 1-2 Torr [30].

Long-term stability and reliability of bonded wafer packaging techniques is difficult because (1) there can be small gas leakages along the bonding interface, (2) gases can be generated during the bonding process and (3) outgassing inside the cavity all will lead to a significant pressure increase inside the sealed cavity. Even if a bond technique is optimized, there is still the presence of gasses in the sealed cavity, which limits the vacuum of the package. For example, oxygen gas is generated during the anodic bonding process originating from the mobile oxygen ions inside the bonding glass [31]; and glass frit and solder can outgas water or carbon dioxide [32]. Other gases commonly present in a sealed cavity are H_2, N_2, and CO. Getters are such material that can chemically absorb active gases, such as those mentioned. For example, the presence of Ti in a sealed cavity has been reported to yield vacuum packages from 1-2 x 10^{-3} Torr without vacuum degradation at 1000h [33]. More complicated getter pumps such as a non-evaporable getter material (NEG) or NanoGetters are effective methods for reducing the total amount of gases trapped inside the cavity. One approach to the NEG uses a Ni/Cr ribbon covered with a mixture of porous Ti and Zr-V-Fe alloy that is cut to size and placed in the cavity before it is sealed [29]. Another approach for the NEG is to use a powder mixture of Zr, V and Fe to pattern the capping substrate before bonding [34]. The NEG does not adsorb gasses when exposed to air prior to usage because oxides and carbides cover its surface. However, these oxides and carbides are diffused into the bulk and an active metallic surface is formed at around 400°C [29]. A pressure as low as 1 x 10^{-5} Torr was reported using an internal NEG [29]. Alternatively, the NanoGetter can be comprised of a multi-layer, reactive metal stack of Group IVA-VIA transition metals commonly used to getter gases [32, 35]. The Nanogetters can be used to achieve vacuum level under 8.5 x 10^{-4} Torr over a period of 8 months [32].

In addition to packaging difficulties, the capacitive gap spacing used to sense the resonating movement must be made very small at the frequency ranges required of cellular phone networks, creating a challenge for fabrication of the devices. For example,

~12~

extension of the frequency range of capacitive MEMS resonators into the low GHz range requires process technologies that can yield 10-100 nanometre capacitive gap spacing between the high quality factor (Q) resonating structure and the drive and sense electrodes [1]. Smaller capacitive gaps are required in order to increase the capacitive coupling between the beam and the sensing electrode and will be explored further in Chapter 5.

3.3 Harmonic Radar Tags

The last potential application area presented for micromechanical resonators is harmonic radar tags for use in biological tracking. Harmonic radar provides the ability to track very small animals and insects. Tags for biological tracking must have an insignificant weight so as not to affect the animal or insect's natural movements. For example, the maximum tag weight is 3 mg for the Colorado potato beetle before it affects its flight pattern [36].

Conventional radar receives at the frequency of transmission while the harmonic radar receiver is tuned to a harmonic of the transmitter. In other words, the device is tuned to be excited by f_o but will re-emit a harmonic. This eliminates the conventional radar scatter from surrounding objects and allows one to detect the tag that is emitting the harmonic signal. Harmonic radar is described in [37, 38].

The tag used to attach to the insect or animal is a transceiver. Its action is to capture the incident signal, to convert it to the maximum power possible in the second harmonic, and to radiate the signal back to the receiver. The capturing and transmitting stages are achieved with a single dipole antenna while a Schottky diode in parallel with an inductive loop forms the frequency conversion stage for most currently used tags [39, 40]. One such tag, manufactured by Alberta Microelectronics Centre weighs 17.6mg [39] and a similar design is reported as being manufactured at the USDARS Areawide Pest Management Research Unit (College Station, TX) with a weight of 11.6mg. The tags have been recently reported for tracking the movement of individual Anaplophora glabripennis adults (beetles) in China [41]. The researchers' only complaint with the tags

~13~

is that they were often rendered undetectable after several days in the field; thus, reliability is an issue in the case of long-term studies.

The micromechanical resonators described in this work could perform the frequency conversion stage and, potentially replace the Schottky diode in parallel with the inductive loop. Because the electrostatically actuated cantilever beam is well-known to have non-linear current-voltage characteristics when operated beyond small displacement assumptions [42], it will naturally produce harmonics of an applied sinusoidal signal [43]. To our knowledge, the application of the micromechanical resonator in this regard is thought to be novel.

4 Methods of Actuation

The various methods of actuating of cantilever beams are diverse and are based on physical principles. Piezoelectric actuation is a very popular method; however, as microfabrication methods have advanced, electrostatic actuation has become a more commonly used method. Thermal and magnetic methods are also used, where thermal movement is very attractive to biological applications because of its ability to work within fluids such as microfluidic channels, but is known to be a much slower method than either piezoelectric or electrostatic actuation. These actuation methods are explained in the following sub-sections.

4.1 Piezoelectric

Piezoelectric material demonstrates the electromechanical property called the piezoelectric effect. The piezoelectric effect occurs when a permanently polarized material is capable of acquiring an electric charge when subjected to mechanical stress. Conversely, when a piezoelectric object undergoes an electrical charge, observed mechanical distortions take place in what is known as Electrostriction. A simple schematic of this movement is shown in Figure 2-2. Illustrated in (a) is a piezoelectric material, such as polysilicon or lead zirconate titanate (PZT), without any applied voltage or nearby electric field. In (b), a voltage potential is applied across the thickness of the

~14~

sample, resulting in a reduced thickness, while the length and width are slightly increased.
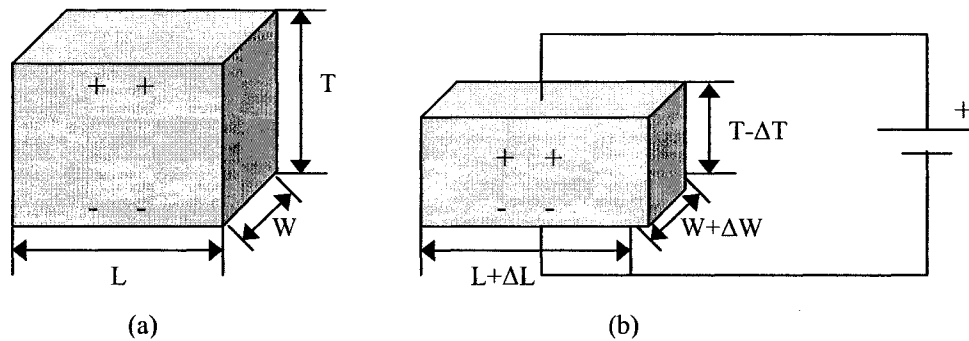
Figure 2-2: Schematic of motion of piezoelectric material
(a) Inactivated (no voltage applied) (b) Activated (voltage applied across thickness)

In other words, piezoelectric materials are used to communicate motion by applying an electric field in a direction that produces the desired sense of strain, which leads to a deformation of the material. For example, using polysilicon beams and designing electrodes where the resulting field creates the motion desired can achieve cantilever actuation. Reported in the literature is a piezoelectric microelectromechanical switch actuated with a lead zirconate titanate (PZT) thin film [44]. Also found in the literature is a silicon nitride microcantilever resonator with the PZT thin film that is used as both the microactuator and the microsensor [45]. Piezoelectrics are also known for their excellent operating bandwidth and can generate large forces in a compact size, but traditionally they have very small displacements [46]. Typical free strains induced in the elements are on the order of 0.1% to 0.2% [47].

4.2 Electrostatic

Electrostatic actuation is based on the electromagnetic force between charged particles. There are positive and/or negative charges set by applied voltages between specific structural members. Coulomb forces are then created between these two oppositely charged structural members; and, if the structural members are not restrained, motion is produced. The attractive force between two oppositely charged plates is generated by the electric field, E, as shown in Figure 2-3 below. Devices utilizing electrostatic actuation

are easily fabricated, actuate quickly, and integrate easily with CMOS technology. However, electrostatic actuation is feasible only within nonconductive media.
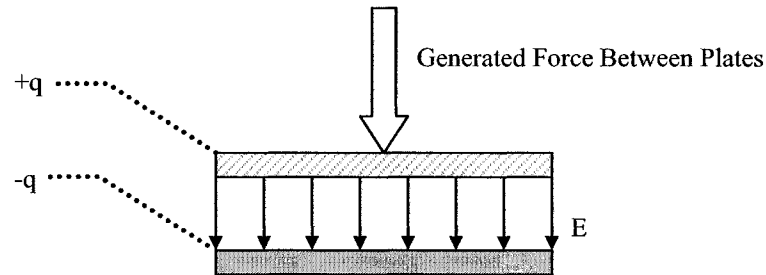
Figure 2-3: Attractive nature of the electrostatic force between two charged plates

4.3 Thermal

Thermal actuation uses thermal expansion and contraction to induce motion. A current that is forced through an element usually produces an increase in temperature due to the electrical resistance of the element. Using the heat produced from the passing current to accentuate or control motion of structural members is achieved using two main methods: (1) asymmetrical designs that take advantage of temperature differences due to differences in dimensions [48] or (2) differences in thermal expansion coefficients of the layer materials (bimorph effect) [17, 18]. A structure composed of asymmetrical parallel arms connected at the top and separately fixed at the bottom will create motion when current flows. The difference in size creates a difference in electrical resistance which, in turn, causes the smaller arm to heat up more (higher current density) than the larger arm to which it is attached. This difference in temperature in the overall structure causes motion because the expansion of a material is proportional to its change in temperature. Schematics illustrating how using either (a) physical dimensional change or (b) different materials (with differing thermal expansions) can create motion are given in Figure 2-4.

~16~

No Current   Current   No Heat   Heat
      (a)   (b)
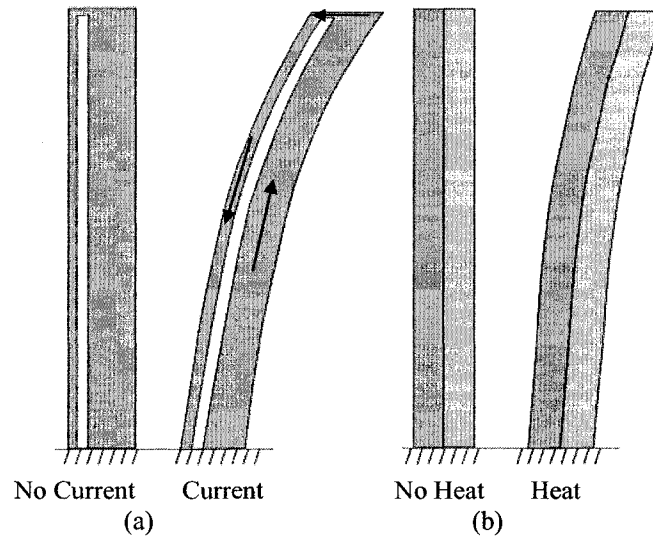
Figure 2-4: Illustration of thermal motion
(a) Current passing through two differing sized members will cause temperature differences (due to differing resistances) that cause motion (b) Heating a bimaterial member will cause motion because of the difference in thermal expansion coefficients

4.4 Magnetic

Magnetically-induced or current-induced fields create forces which can be used to produce motion. A beam placed in a uniform magnetic field with an electrical signal passing through a lead attached on the beam generates a Lorentz force. The Lorentz force is the force acting on a moving particle with charge q and velocity v in a magnetic field B: $\vec{F} = q\vec{v} \times \vec{B}$. The direction of the Lorentz force is perpendicular to those of the magnetic field and the velocity. In this case of the resonator, this force causes the beam to vibrate transversely. Cleland and Roukes fabricated, tested, and reported a micromechanical resonator actuated in this manner [49, 50].

5 Measurement Techniques

Many techniques for detecting the resonant motion of the cantilever have been reported in the literature including piezoelectric and piezoresistive, optical techniques, and capacitive sensing. Piezoelectric, piezoresistive, and capacitive sensing offer on-chip detection, which is of great interest for miniaturizing entire systems or for integration with electronics. Conversely, optical techniques such as reflectance, interferometry, Doppler vibrometry, and stroboscopes are external to the device and are usually large in

~17~

comparison. These methods of measurement are further discussed in the subsections below.

5.1 Piezoelectric and Piezoresistive Methods

As was described in the previous section, a voltage applied across a piezoelectric material causes deformation of the material (refer to Figure 2-2). Conversely, for deformation of a piezoelectric material, a voltage is created. By monitoring the induced voltage, the degree of movement can be deduced. A similar technique is applied with the use of piezoresistive materials except the resistance of the material changes upon deformation. Reports of cantilever deflection or resonance frequency changes detected by embedding piezoresistors in the cantilever base are found in the literature [10, 17-19].

5.2 Optical Techniques

Optical measurement methods are non-contacting, non-destructive, and externally operated systems. The methods described here are Doppler vibrometer, stroboscopes, and interferometry.

5.2.1 Doppler Vibrometry

Laser doppler vibrometry is a technique possible for use in characterization of both the quality factor and resonant frequency of a micromechanical resonator. The main advantage to this technique is that it is easily integrated with ultrahigh vacuum technology for testing of resonators in the absence of a medium [3, 51, 52], the importance of which is discussed below in Section 5.

Any traveling wave (including light waves) undergoes a frequency shift when reflected from a moving target. With suitable detection systems, one can measure the frequency difference between the transmitted laser signal and the one reflected from the target material (the cantilever beam, in this case). Near resonance and depending on the value of Q, for a small increase in frequency, there can be a very large change in amplitude of the resonating element. A cantilever's change in amplitude at and near resonance

~18~

including its relation to Q is further detailed in Chapter 8. For this situation, the speed at which the cantilever moves at resonance versus near resonance is dramatically increased, which is then detected and analyzed.

5.2.2 Stroboscopes

Various forms of stroboscopes work well in defining the resonance frequency of a device. Stroboscopes are able to "slow down" repetitive motions because they only permit viewing at specific times. For example, if we are only allowed to see an object each time it makes one complete rotation, the object will always appear to be in the same place, and hence stationary.

An ingenious approach to measuring the resonance with strobing is done by Mihailovich and MacDonald using the scanning electron microscope (SEM) [53]. The measured resonance curves were obtained from SEM micrographs of the microresonator. In their SEM method, a portion of the vibrating microresonator is viewed at high magnification. By adjusting the scan rate of the probe electron beam (which acts like the strobe described above), the image of the vibrating resonator shows a clear periodic pattern. The amplitude of this pattern gives the vibration amplitude of the resonator. The resonant frequency is then found by measuring the vibration amplitude for various actuation frequencies. At resonance, the vibration amplitude far exceeds those of surrounding frequencies.

5.2.3 Interferometry

Optical interference techniques are often used to detect and measure the motion of micromachined beams. The method is very sensitive because changes in interference are observed from changes in optical path length. A basic arrangement of the interferometer is the Michelson interferometer (shown in Figure 6-1). A monochromatic, coherent light beam is split by a half-silvered mirror or cube beam splitter. The two beams are then incident on mirrors which reflect them back on the beam splitter where they are

recombined. On recombination, there is constructive or destructive interference depending on whether the difference in path length is an integral or integral + ½ number of wavelengths. Displacement measurements are achieved by replacing one of the mirrors with the moving device. As the cantilever beam moves in the path of one of the light beams, the difference in path lengths between the two light beams alters, changing the interference upon recombination. The change in interference can be monitored with a photodetector. This method is used to characterize the resonating cantilevers of this work, and is further explained in Chapters 6, 7, and 8.

Reports in the literature of interference techniques are very widespread. Michelson interferometers [54, 55] and Fabry-Perot interferometers [56] are shown to measure submicron displacement. Other examples measuring the motion of MEMS structures using interferometric optical techniques are reported [57-59].

5.3 Capacitive Sensing

Although optical methods are non-contacting and non-destructive, for practical use of the micromechanical resonator, an electronic readout is of great interest because MEMS can be incorporated with on-chip circuitry to achieve better performance, more reasonable package sizes, and lower fabrication costs. As the beam moves, it acts as a time varying capacitor and there is a corresponding time-varying induced current on the bottom electrode as illustrated in Figure 2-5. More detailed wiring is discussed in Chapter 5. In the figure there are two electrodes separated by a gap under the cantilever beam. One of the electrodes is used to create an electrostatic force to create motion, dx/dt, and a current is induced in the other because its capacitance changes with the motion of the cantilever, dC/dx, due to the changing gap size. On-chip circuitry could be used to detect this induced current. However, the small movement (typically, submicron) induces small currents.
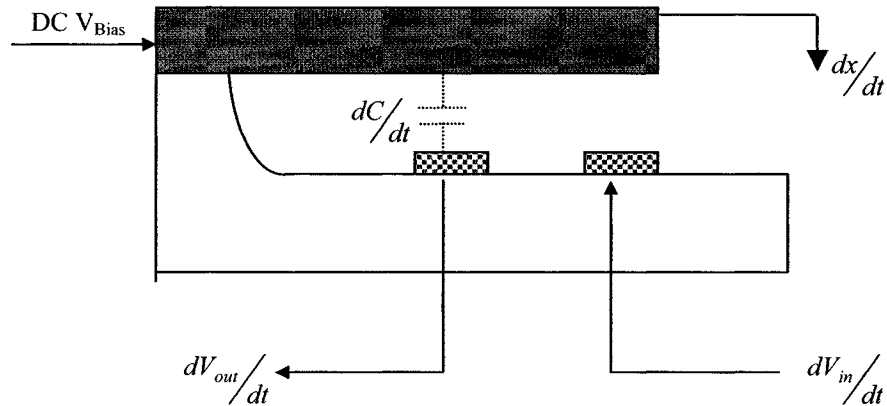
Figure 2-5: On-chip deflection monitoring through capacitive sensing

For such devices, however, as dimensions are scaled down to allow higher frequencies, the capacitive transducer gaps (separation between the resonating structure and the sensing electrode) must also be scaled accordingly so that the electromechanical coupling can keep up with rising resonator stiffness-to-mass ratio. Electromechanical coupling is a measure of the efficiency of conversion of mechanical motion to an electric signal, and vice versa. In the case of the micromechanical resonator, it is the efficiency of the beam's motion to produce an induced current due to its change in capacitance. Difficulties in reducing the capacitive gaps are outlined in the literature and it is recommended that as a consequence for VHF and above frequencies, capacitive transducer gaps of less than 1000Å are required [60]. This is further described in Chapter 5.

6 Sources of Energy Loss in Micromechanical Resonators

Except in a superconductor or superfluids, real oscillators always have some form of damping. In an electric circuit there is resistance and in a mechanical oscillator, such as the micromechanical resonator in this work, there is friction. The energy loss of vibrating MEMS devices remains one of the barriers for their practical applications as resonators for sensors and RF telecommunication systems, or as gyroscopes for navigation systems. These devices require Q-factors on the order of thousands at resonance peaks for accurate frequency selectivity and low power consumption [61, 62].

~21~

The frequency range of micromechanical resonators can extend well into the gigahertz range. For a clamped-clamped beam resonator made of silicon, the dimensions required for 1GHz operation are length $\approx 4\mu$m, width = 2μm, thickness = 2μm [25]. However, there are many factors that prevent this from being realistically achievable. For example, energy losses such as from air damping, fixed end supports, and from surface interactions of the device all lead to the degradation of the quality factor. In addition, frequency dependent losses such as air damping become increasingly evident with increased frequency because the damping force constant is proportional to the velocity of the device, $\vec{F}_{Damping} = -b\vec{v}$, (see Equation 8-1). This is the case for viscous damping, which is assumed in this work and is typical when modelling similar MEMS devices [63-65]. Viscous models are adequate for air in a device that has a minimum feature size on the order of microns or larger and is operated at either atmospheric pressure or a pressure that is slightly below atmospheric pressure [66]. With this in mind, even if a device is scaled down so that it resonates at 1 GHz, the low quality factor may inhibit resonant motion to such a degree that the increase in amplitude of the device at resonance is not detectable.

Dimensions of resonators are being reduced to increase the frequency at which they resonate. However, as the dimensions become small, effects that are negligible in macro-scale devices become prominent. The effects of air damping caused by fluid-structure interaction [63, 67], vibration transmission to adjacent device components or at support points [68, 69], thermodynamic damping that results in heat generation in the material [70], adsorbing/desorbing molecules, outgassing, fluctuations in temperature and random vibrations are all possible sources of energy loss that affect the Q-factor of resonating micro- and nanostructures. The following sub-sections further detail each of these loss mechanisms.

For the work presented here, the micromechanical resonators are of the micron-scale and the most dominant loss is air damping, as will be shown analytically in Chapter 3 and verified experimentally in Chapter 8. Beyond air damping (for micromechanical resonators operating in vacuum) the sources of energy loss consist mainly of support loss,

thermoelastic loss, and surface loss [52, 71]. However, it should be noted that at submicron dimensions especially, the frequency noise due to temperature fluctuations and adsorption/desorption is likely to limit the applications of ultra-small resonators [72]. Although these are of less concern given the scope of this work, scaling down a design is often a consideration; therefore, these are included for the sake of completeness. The devices in this work are of micron scale; however, it is the intention that they form the basis for future, scaled-down devices, operating at higher frequencies with exceptional Q factors.

6.1 Thermoelastic Energy Dissipation (TED)

Thermoelastic Energy Dissipation (TED) [73, 74] is a result of irreversible heat flow across temperature gradients produced by inhomogeneous compression and expansion of the oscillating beam [75]. In the case of a cantilever beam, this heat flow occurs across the thickness during vibration and is considered an important mechanism of damping for vacuum operated micromechanical resonators. When the beam is deflected, one side of the beam is under compression while the other is under tension, causing the stress-induced temperature gradient in the beam with the compressive side warm and the tensile side cool [52]. Energy is then lost as it moves across the temperature gradient by way of conduction through the material. The rate of energy dissipation due to this heat flow is dependent upon the cantilever geometry of the device, material, and working temperature [52, 76].

Thermoelastic dissipation has been studied by a number of researchers. It has been reported that the thermoelastic loss is negligible for cantilevers with thickness H<500nm and length L>10μm. However, the same report claims that TED becomes significant for beams tested in vacuum with a beam thickness of H>500nm and length of L>10μm [52]. Thermoelastic dissipation is typically not a factor for submicron-thick cantilevers, but is shown to be significant for silicon nitride cantilevers as thin as 2.3μm [76] and can be a dominant source of energy loss in single-crystal silicon cantilevers as thin as 10μm [77].

~23~

6.2 Air Damping

Air damping is due to the reactionary forces of the individual air molecules through which the beam travels. This force is in the opposing direction to the beam's movement so air damping limits the maximum amplitude of the device. Air damping decreases as the number of air molecules with which the beam comes in contact is reduced or as the beam's surface-to-volume ratio. For a given micromechanical resonator, to analyze how the damping of a cantilever varies with the pressure level, the pressure range from high vacuum to atmosphere is divided into three regions [78]:

1. Intrinsic damping region: in this region, the air damping is negligible because there is a very small number of molecules that can possibly contact the beam
2. Free-Molecular region: the damping is caused by independent collision of non-interacting air molecules with the moving surface of the vibrating beam
3. Viscous region: air acts as a viscous fluid and creates a highly damping/resistive medium.

The regime in which a flow exists can be characterized by the Knudsen number, K_n [79]. As shown below in Equation 2-1, K_n is equal to the mean free path, λ, that a gas particle will travel before it undergoes a collision divided by the characteristic length of the flow, d.

$$K_n = \frac{\lambda}{d}$$

Equation 2-2

In flows with very low Knudsen numbers, typically $K_n < 0.01$, collision processes will dominate and the flow will remain in local thermodynamic equilibrium, which is also known as the continuum regime. In this regime, also called the viscous region, the beam's resistance to motion is due to viscosity of the air. On the other side of the scale, where $K_n > 10$, is the free-molecular regime. As was described above, the beam's resistance to motion is due to inertia of air molecules hit by the impeding device. In this region, the fluid can deviate drastically from local thermodynamic equilibrium so the validity of the continuum model breaks down. In between these two regions is a

~24~

transitional region where the flow characteristics are in transition between continuum flow and free-molecular flow.
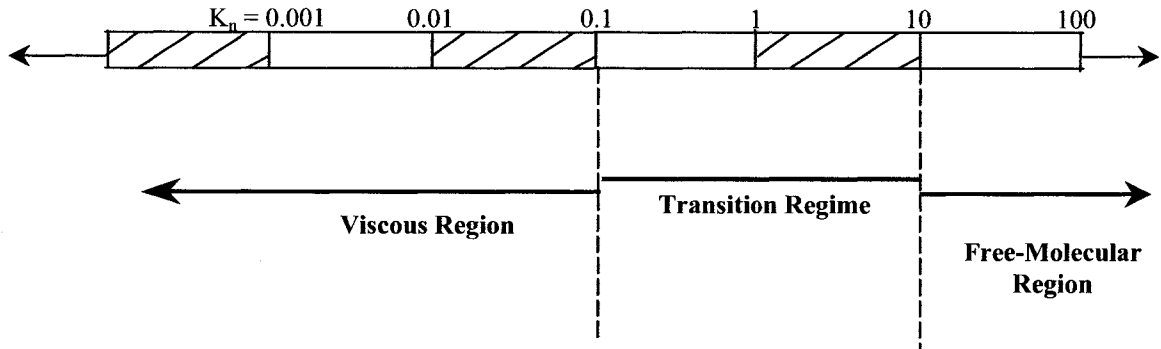
Figure 2-6: Flow regimes characterized by Knudsen number

For typical micromechanical resonators, it is found that the greatest loss mechanism while operating in open air (viscous region) is air damping. It is in the viscous region that typical micromechanical resonators perform with lowest Q factors because there is the greatest number of air molecules colliding with the beam. For example, in an experiment conducted by Zook *et al.* [80], the measured quality factor of an oscillating microbeam decreases with increasing pressure in the range of 10^{-2} Torr to 10^4 Torr, indicating that viscous air damping is the dominant loss mechanism within this pressure range.

As expected, it has been reported that the lower the pressure, the better the quality factor. For example, the frequency response for a 3.7μm-wide, 40μm-long beam resonator with 350nm capacitive gaps was measured in vacuum and air [81]. The quality factor was found to be 1800 in vacuum whereas it was only 300 in air. It is reported that the Q of vacuum-operated microresonators can approach 10^5, a value about one thousand times larger than the same device operated in air [78]. The pressure at which the surrounding air becomes significant is not an area of agreement in reports. Commonly reported are micromechanical resonators that are placed in a vacuum chamber capable of being pumped to pressures below 1 mTorr [53, 78], which is low enough that dissipation due to surrounding gases is insignificant.

~25~

It can, therefore, be concluded that the excellent performance of vacuum microresonators stems, in large part, from the high mechanical Q-factors achievable in the near-absence of a medium.

Attempting to model the effects of air damping is currently a very active, important area of research. Models using continuum models [63] or models that operate in the free-molecule regime [66] are reported - the importance of the latter being for beams operated at low pressure or nanoscale beams operating at atmosphere because under these circumstances, the continuum model breaks down. A common feature of air in these examples is that gas rarefaction effects are so significant that the interaction between each molecule and the moving structures must be accounted for individually in order to obtain an accurate prediction of the fluid effects on oscillating devices [66], so the air cannot be modelled as a continuum. In addition, with nanoscale beams, the surface becomes increasingly influential to the behaviour of the material, where a continuum model assumes that the bulk of the material dominates the material's properties.

6.3 Support Loss

In the design of high-Q resonators, it is beneficial for the vibrating volume of the resonators to be attached to the stationary support structure at nodal locations. Otherwise, mechanical energy is transmitted from the vibrating structure to the substrate through the supports [25, 61, 62, 72]. These losses are known in the literature as support losses, anchor losses, or clamping losses and the reduction/elimination of them is very desirable for applications where a high quality factor is required.

Support losses for a beam actuated in the normal direction to the substrate can be explained by simple beam theory. During flexural vibration, a cantilever beam exerts both a vibrating shear force and moment on its fixed end as shown by the free body diagram in Figure 2-7. In (a), a schematic of a cantilever beam is shown from the side. "A" represents where the cantilever is anchored to the substrate and "F" represents the

force applied to the beam tip to create motion. By summing the moments about "A", the reactionary shear force, V, and moment, M, at the support are illustrated.

(a)   (b)
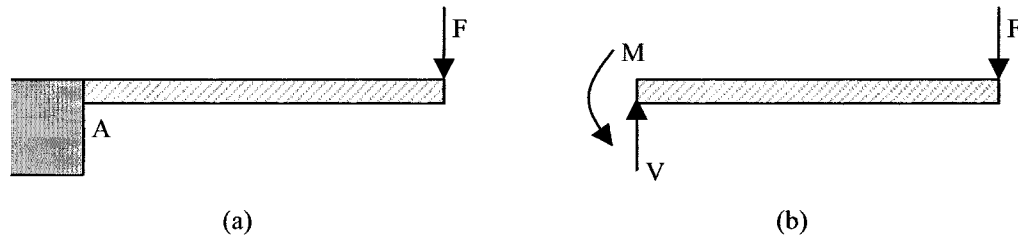
Figure 2-7: Free body diagram of a cantilever beam

In other words, the resonator vibrations create forces which act as external forces to the substrate, which then excite elastic waves propagating into the support causing the support structure to absorb some of the vibration energy of the beam resonator [62, 71]. It has been reported that when the transverse elastic wavelength of the propagating wave is much larger than the thickness of the beam, the coupling between the resonant modes of a beam resonator and the elastic wave modes in its support is very weak [69]. The elastic wavelength is the ratio of the propagation velocity of the wave in the substrate to the frequency of the excitation source (same as the resonant frequency of the cantilever) [71]. In other words, the elastic wave in the support is not then expected to have an effect on the resonant modes of the beam [71]. However, it has been reported that the resonant frequency of the beam decreases up to 5% due to substrate flexibilities interacting with beam at the anchors [69]. Possibly, the substrate flexibilities cause a less rigid support; therefore, the fixed boundary condition often assumed is not valid.

Wong *et al.* [82] report that the support losses in their designs increase with increasing centre frequency of the resonator. They deduce that this ultimately limits the achievable high Q-factors for high frequency (HF) to very high frequency (VHF) applications. Qualitatively, it is predicted that support loss increases a hundredfold for every tenfold increase in resonator centre frequency in the case of beam resonators that are supported at both ends [62]. The cantilever beam reported in this work is supported at one end only, so the effect is expected to follow the same trend as is reported for a doubly-

~27~

supported device, but to a lesser degree because there is only one leakage path for support loss. Regardless, the trend creates further challenge for increasing the resonant frequency of these devices while still retaining an extraordinarily high quality factor.

In addition to the centre frequency affecting the degree to which support losses affect the quality factor, the size of the resonating structure is also a factor. The shorter the beams, the higher the support loss [52]. For the beam resonators, the support loss is proportional to the third power of the length to width ratio $(l/w)^3$ [76]; and if the length to width ratio is less than 100 ($l/w<100$), the quality factors are reported as being limited by the support losses [52]. As well as the experimental observations just presented, an analytical model [71] and computational model [83] have been derived for estimating the support loss.

Because of the limits which support losses put on the quality factor, focus has been put on novel designs to minimize or alleviate the problem. It has been proposed that one possible approach could be to use submicron dimensions at the support cross section to avoid the Q-limiting support losses [6, 69]. This approach was done to reduce the stiffness of the device (i.e. reduce the spring constant) in order to obtain less coupling between the beam and the substrate at the anchor. Unfortunately, smaller size often coincides with smaller power handling [61] and increases susceptibility to environmental effects [72], such as contamination or thermal fluctuations. Another method, and an area of research, has been on design improvements that can alleviate the support loss, e.g., using the free-free beam designs [60, 84, 85]. These designs use nodal locations - locations where there is no movement at resonance - to connect the resonating medium to the substrate.

6.4 Surface Loss

On the macro scale, the surface interaction with the environment does not typically cause significant damping of a resonant device. However, as devices are scaled to micron sizes, the surface to volume ratio increases to a point where surface interaction can no longer be ignored. A cube (with side length, l, has a volume $V = l^3$ and a surface area $S = 6 \cdot l^2$) is used to illustrate why surface effects become significant on smaller scales [86].

~28~

The surface-to-volume ratio for this cube is S/V = $6 \cdot l^{1}$. Now, a length reduction by a factor of 10 creates a volume reduction by a factor of 10^{3}, whereas the surface area is only reduced by a factor of 10^{2}. Therefore, the S/V ratio is increased by 10, as well. As downscaling continues, the surface of the object becomes an increasingly dominant entity, as shown qualitatively. For a silicon beam 100nm-long, 10nm-wide and 10nm-thick, it contains only about 5 x 10^{5} atoms with some 3 x 10^{4} of these atoms residing at the surface. In other words, more than 10% of the constituents are surface or near-surface atoms [87].

The quality factor is found to decrease with decreasing cantilever thickness, indicating surface loss mechanisms [76]. Reaching a similar interpretation, Yang *et al.* report that surface modification affects the Q factors of the thinner structures more than those of the thicker ones [88]. These authors found that when the thicknesses of cantilevers increase to 500nm, the Q values of the cantilevers increase to approximately three times that of the corresponding ones for 170nm thick cantilevers.

There are techniques for surface preparation that reduce effects of surface loss. It has been reported that annealing at 900-1000°C in UHV to remove any native oxide or surface absorbents enhances the Q values considerably [88] - up to one order of magnitude (up to 2.5x10^{6}) for cantilevers of 30-90μm in length and 170nm thick [52]. It is reported that the effect is due to surface modification, not thermal effects, and varying tests confirm this [51, 88].

7   State-of-the-Art Examples

Many different fabrication methods have been utilized to make cantilever beams because they are such simple structures. Of the cantilever beams, Ono *et al.*'s <100>-oriented silicon cantilevers with a thickness of 170nm, width of 6μm, and length of 48-50 μm were found to produce the most impressive results with respect to quality factor [3]. These cantilevers were introduced into an UHV chamber and flash annealed at about 1000°C by flowing a current into the silicon base supporting the cantilevers at a base pressure of 2x10^{-8} Pa. After this treatment, the measured Q factor in UHV was increased

up to about 200,000. After about 1 week leaving the cantilever in UHV, the Q factor decreased to about 50,000.

However, the more complicated, state-of-the-art resonators use novel fabrication or design techniques to create their devices. As mentioned previously, minimizing the capacitive gaps is essential for integrating the device with on-chip circuitry. A fabrication process has been demonstrated that combines polysilicon surface micromachining, metal electroplating, and a side-wall sacrificial-spacer technique, to achieve high-aspect-ratio, sub-micron, lateral capacitive gaps between a micromechanical structure and its metal electrodes, without the need for advanced lithographic and etching technology [60]. Among the devices demonstrated using this process are lateral free-free beam micromechanical resonators (Q is 10,470 at 10.47 MHz)[85], contour mode disk resonators (Q is 9400 at 156 MHz)[60], and temperature-compensated micromechanical resonators (Q is 10,317 at 13.5 MHz, with a –200ppm frequency variation over a full 80°C range) [60].

The aforementioned fabrication technique gave very impressive results but used polysilicon as the material for the resonating structure. Single crystal silicon (SCS) is a more attractive structural material than polysilicon for microresonators due to its inherently high mechanical quality factor and independence from various process parameters [89]. For example, a 510μm long, 5.5μm wide, 20μm thick single-crystalline silicon clamped-clamped beam resonator was operated in its third resonance mode at 1MHz and demonstrated a Q of 11,000 under vacuum [89]. The process utilized the single crystal silicon for the resonator with sub-micron gap spacing (700nm reported) and patterned polysilicon for the driving and sensing pads. The first three modes of resonance for both a clamped-free (cantilever beam) and a clamped-clamped beam are shown below in Figure 2-8.
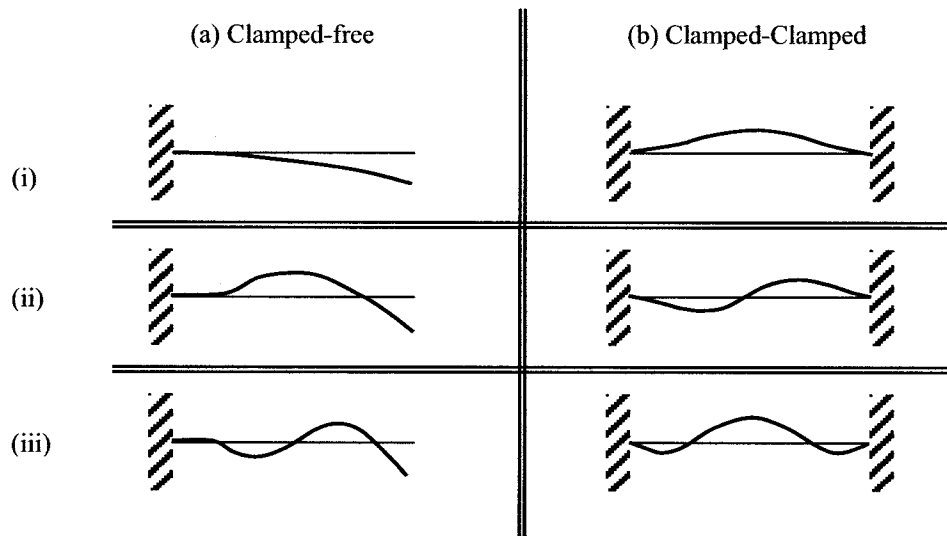
Figure 2-8: Mode Shapes of Beam Vibrations
(a) Clamped-free beam (cantilever beam) (b) Clamped-clamped beam
(i) Fundamental mode, (ii) 2nd mode, (iii) third mode

Not only have novel fabrication techniques been utilized to improve performance of the devices, but ingenious designs have also been developed. A lateral free-free beam resonator was designed to suppress energy losses to the substrate through the supports at its resonance frequency [60]. The design attaches the resonant beam at its nodal locations by four flexural supports. The support beams were designed so they would resonate in the second mode at the fundamental frequency of the suspended beam. This means that the beam attachment locations correspond to nodal points for both the support beams (nodal locations at the ends of the beams) and the primary resonating beam. This creates a high (ideally infinite) impedance location through which very little energy is transferred, hence, through which very little energy is dissipated [2]. The contour-disk resonator described above for a novel fabrication technique also takes advantage of attachment at a nodal location. At resonance, expansion and contraction of the disk along its radius are produced, commencing from the nodal location where it is connected to the substrate [90].

A collection of reported micromechanical resonators is included in Appendix A for reference to examples of reported results with respect to resonant frequency and quality factor.

~31~

8 Conclusion

This chapter has introduced the field of microresonators, outlined its importance through explanations of various applications including wireless communication, mass sensing for biological applications, and harmonic radar tags, and has shown state-of-the-art examples of novel devices. An explanation is made of methods of actuation, detection, and possible sources of loss that degrade the quality factor of the device. In upcoming chapters, the groundwork for research and introduction to the device including the analytical design are presented, as well as the chosen method of fabrication. Finally, the characterization and testing are presented and compared to both the analytical design and to reports in the literature.

Chapter 3 – Design

1 Introduction

This chapter introduces the design of a capacitively driven micromechanical resonator. The analytical design in this chapter is presented as the prelude to the experimental results in following chapters. The micromechanical resonator is first introduced by a general description of the design, following an explanation of the expected displacement characteristics with respect to applied voltage potential. Next, the device is shown as a forced, damped harmonic oscillator and the differential equation representing this is described. The analytical design is then presented including the threshold voltage, resonant frequency, induced current, extracted signal, and quality factor. Finally, presented is the multi-physics finite element analysis (using ANSYS simulations) that was used to aid in the design.

2 Theoretical Movement

The micromechanical resonators of this work are capacitively driven, also termed electrostatically actuated. Electrostatic actuation means that, because the cantilever beam is basically a parallel plate capacitor with one plate unfixed, movement of the beam will occur when there is any difference in voltage between the two plates (the fixed plate being the bottom electrode and the unfixed plate being the beam, in this case). This movement will occur independent of polarity. Static bending of the beam occurs when this voltage difference is present and not varying with time. However, if the bottom electrode is grounded and an AC signal is applied to the beam, deflection of the beam is related to the voltage potential between the electrodes, and varies with the frequency of the driving voltage. It should be noted that because the beam is attracted to the bottom electrode regardless of polarity, the beam's displacement should occur at twice the frequency of the driving voltage. At a given frequency, the beam is closest to the bottom electrode at both the maximum positive applied voltage and at the maximum negative

~33~

applied voltage. Movement is shown graphically in Figure 3-1 and schematically in Figure 3-2. As depicted in Figure 3-1, if the beam is driven with an AC 1 V_{p-p} peak to peak signal (shown by the solid line; voltage units are arbitrary) and the bottom electrode is at ground, the response of the beam will be a rectified sinusoid (illustrated by a dotted line).

Expected Beam Response

Time
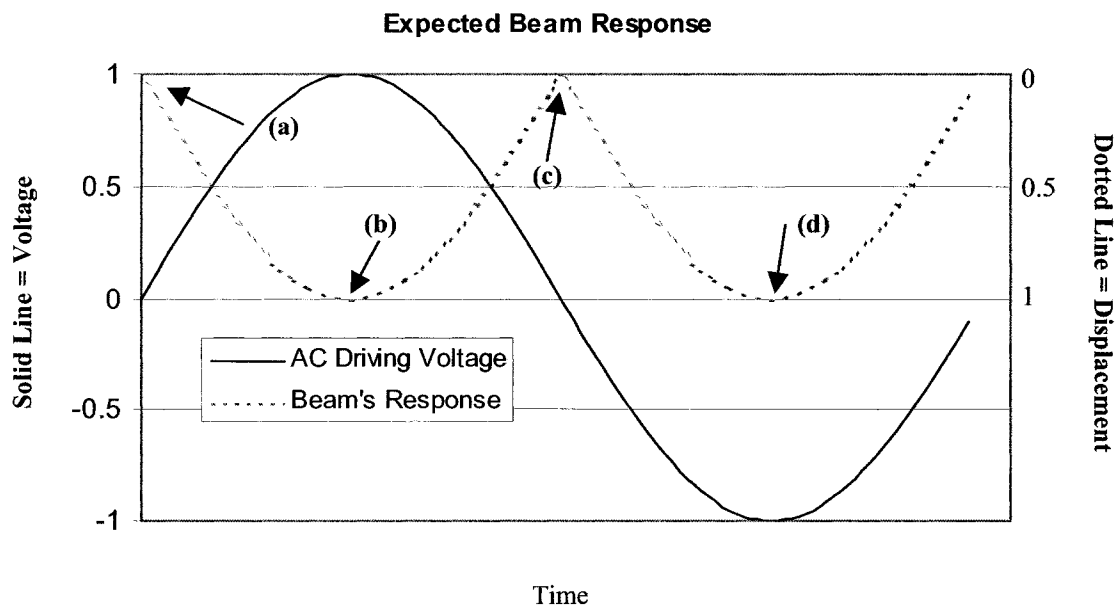
Figure 3-1: Expected beam response with respect to AC driving voltage Beam's displacement is two periods for each period of driving voltage. (a), (c) - Zero voltage potential causes no displacement (b), (d) - Maximum voltage potential causes maximum displacement of the beam

Now, to further visualize the movement, the letters placed on the graph of Figure 3-1 above mark the beam's response corresponding to Figure 3-2 below. It is shown that the beam is not displaced when there is no voltage potential (or no applied voltage as in this case) which occurs at (a) and (c) and deflects whether there is a positive or negative potential across the gap, maximum occurring at (b) and (d). In the following section, the device is described in terms of a forced, damped, harmonic oscillator.

~34~

Side View

(a) 0V — Sensing Pad

(b) +1V

(c) 0V

(d) -1V
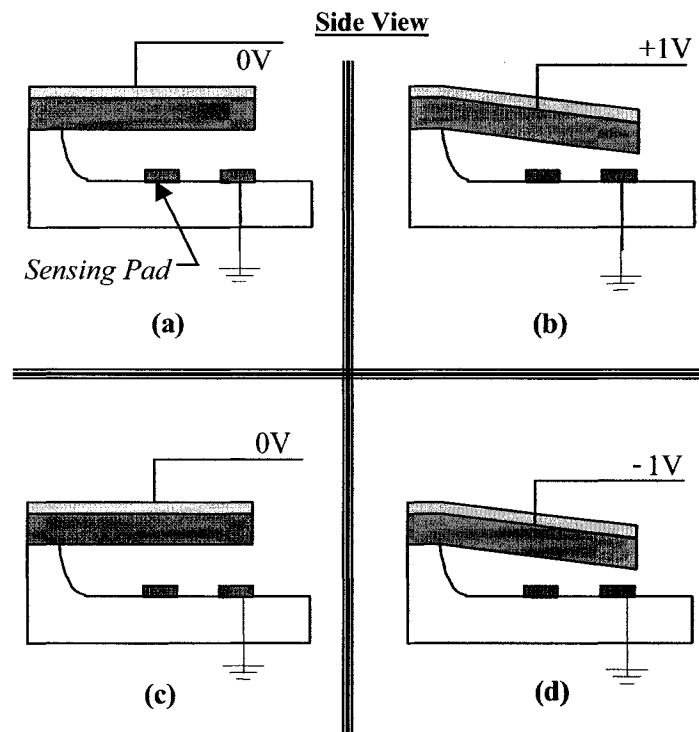
Figure 3-2: Graphical representation of response of beam to AC driving voltage

3 First Principles - Forced, Damped, Harmonic Oscillator

Damped oscillatory motion occurs widely in nature and everyday life. Examples include the swinging of a pendulum, the bouncing of a car's front-end suspension (particularly visible if the `shocks' are worn out), or the vibration of a string plucked on one's guitar. The micromechanical resonator is a damped, mechanical oscillator that can be modelled as an inertial mass attached to a spring that supplies a restoring force and whose movement is damped by a force in the direction opposite to its motion.

The resonating cantilever beam system in this work can be represented as a forced, damped, harmonic oscillator shown in Figure 3-3 below. In (a), the side view of a forced-motion cantilever beam is shown resonating (resonance illustrated by the shaded beams). The cantilever is a forced motion oscillator because a sinusoidal electrostatic force is applied between the beam and the bottom electrodes causing its movement. In (b), the micromechanical resonator is shown as a mass-spring oscillator with a dashpot damper to simulate the result of the opposing force caused by the energy losses such as

~35~

contact friction between the beam and its surroundings or support losses. (See Section 6 - "Sources of Energy Loss in Micromechanical Resonators" in Chapter 2 for more detail). Viscous damping is assumed in this work which implies a linear relationship between the damping constant, b, and velocity, dx/dt. The spring represents the internal restoring force of the beam's material and the beam element is driven by an external harmonic force $F=F_o cos(\omega t)$. The equation of motion, $F=m_e a$, of the mass element is [91, 92]:

$$F_o \cos(\omega \cdot t) - b \frac{dx}{dt} - kx = m_e \frac{d^2 x}{dt^2}$$

Equation 3-1

or,

$$m_e \frac{d^2 x}{dt^2} + b \frac{dx}{dt} + kx = F_o \cos(\omega \cdot t)$$

Equation 3-2

Where:

F_o = initial amplitude of the driving force [N]
ω = angular frequency of the driving force [Hz]
m_e = effective mass of the beam element [kg] (Equation 2-1)
b = damping force constant [kg/s]
k = spring constant (of mass-less spring) [N/m]
x = vertical displacement of the beam tip [m]

(a)   (b)
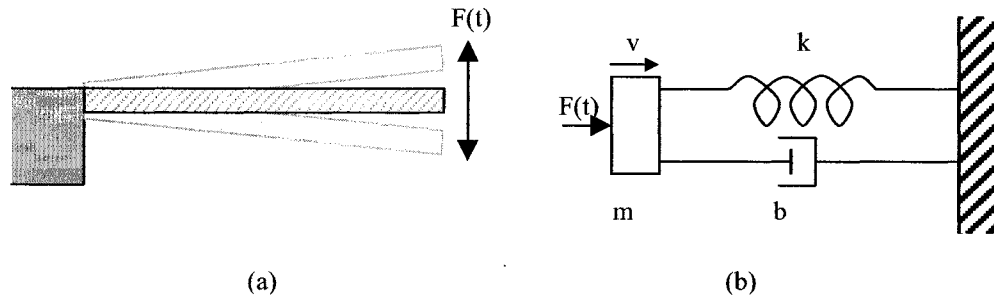
Figure 3-3: Resonant beam represented as forced, damped harmonic oscillator
Schematic of (a) Resonating Cantilever Beam (b) Forced, Damped Harmonic Oscillator

The displacement is harmonic with the same frequency as the driving force so the displacement of the tip of the beam is of the form:

$$x = x_o \cos(\omega t - \alpha)$$

Equation 3-3

~36~

If the driving force is the same frequency as a resonant frequency of the beam, the amplitude will be greatly increased as was described in Chapter 2. The amplification factor is also the quality factor.

The ordinary differential equation (ODE) presented (Equation 3-2) is fundamental to the movement of a micromechanical resonator and will be expanded on further in Chapter 8 for experimental analysis. Because an electrostatically actuated, capacitively sensed micromechanical resonator is both a mechanical and electrical device, the electrical analogy of the ODE represented in Figure 3-3 is also included. It is important to note that both the mechanical and electrical ODEs are equivalent. Conversion to the electrical analogy of the forced, damped harmonic oscillator (represented as a LCR circuit), as well as other terms, is included in Appendix B. Most important to note when converting the mechanical resonant system to the LCR resonant system are:

- the inverse of the spring constant, k, is analogous to capacitance
- the effective mass, m_e, is analogous to inductance
- the damping coefficient, b, is analogous to electrical resistance.

Upon this introduction to the ODE that represents the device, the analytical design of a micromechanical resonator operating in the low kHz range is presented in the following section.

4 Beam Calculations

Expressions for the threshold voltage, V_{th}, (the voltage potential between the beam and the lower electrode that causes spontaneous closing of the beam-to-substrate gap), the fundamental resonant frequency, f_R, induced current, and the extracted signal calculation are presented with results for a cantilever-based micromechanical resonator. A side view schematic of the metal-coated cantilever beam is shown below in Figure 3-4. The important dimensions outlined in the figure are the beam height (h_B), length (l_B), width (b_B), separation of the electrodes (d), gap between beam and the electrodes (d_{BS}), position of the electrodes, metal thickness (h_M) and the deflection of the beam is distance x.

~37~

NOTE:
Width of beam, b_B, is into the page.

<u>Legend</u>

Metal 1 – Ti/Pt/Au

Pyrex

Silicon

Metal 2 = Cr/Au
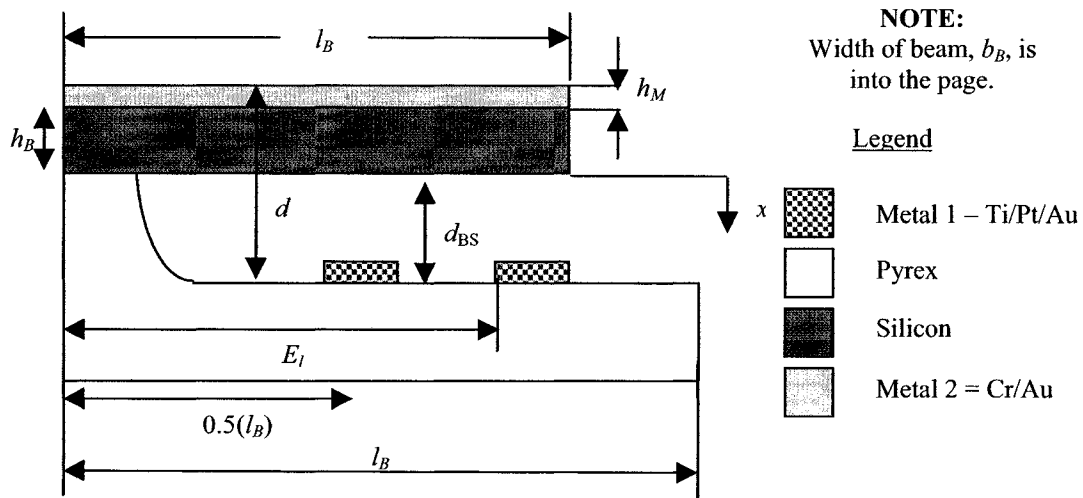
Where:

b_B = Beam width

d_{BS} = Beam-to-substrate distance

d = Electrode separation

l_B = Beam length

h_B = Beam height

h_M = Top electrode thickness

x = Beam Deflection

E_l = Distance to actuation electrode (width of electrode is the same as b_B)

Figure 3-4: Side view schematic of cantilever beam

4.1 Material Properties

All calculations are presented in standard SI units (m, kg, N, s, etc.). Specific values used in the calculations are:

- Elastic Modulus
    - (Si) <100>: 1.295 x 10^{11} N/m^2 [93]
    - (Au)[†]: 6.13 x 10^{10} N/m^2 [94]
- Dielectric Constant
    - (Si)[‡]: 13.5 [94]
- Density
    - (Si)[‡]: 2,320 kg/m^3 [95]
    - (Au)[‡]: 19,300 kg/m^3

[†] Vacuum-evaporated polycrystalline film (300°C)
[‡] Bulk

~38~

4.2 Standard Beam Dimensions

Although multiple beam sizes have been designed and fabricated, for ease of discussion, a standard set of dimensions are assumed unless otherwise stated. This standard beam, as it will be referred to, allows discussion of analytical design and characterization without having to continually refer to the dimensions of the beam. Reference to Figure 3-4 presents a schematic of the device and the standard beam dimensions are outlined in Table 3-1 below:

Table 3-1: Standard Beam Schematics

	Standard Beam Dimensions
Length	200 μm
Width	25 μm
Beam Thickness	2 μm
Gap	2 μm
Electrode Size (l x w)	25μm x 25μm

4.3 Threshold Voltage Calculations

When a bias voltage is applied between the beam and the lower electrode, charge distributes in such a way that an electrostatic force occurs between them. The Coulomb forces bring the cantilever beam toward the bottom electrode, which creates an opposing force (in the form of a mechanical restoring force due to the stiffness of the beam) as the structure is bent.

When the applied voltage reaches a certain threshold value, V_{th}, the restoring force can no longer sufficiently counteract the electrostatic force. As a result, the cantilever spontaneously deflects the remaining distance, and contact between the beam and bottom electrode is made. If the magnitude of voltage is then reduced, the cantilever is released and is restored to its original position. There is a hysteretic effect with respect to voltage for the cantilever because the cantilever is released back to its original position at a lower voltage than the threshold voltage. Complete actuation is never utilized for a beam's use as a resonator because the beam is required to be free for vibrational motion. However,

~39~

the threshold voltage calculation is analyzed because bias voltages are often applied to the devices. By adjusting an applied DC-bias, compensation for variation from device-to-device during fabrication with respect to frequency is achieved [2]. Hence, by calculating at what voltage potential the beam will contact the bottom of the cavity, the limit for the applied bias voltage is found.

Generally, the threshold voltage is calculated by equating electrostatic force and the mechanical restoring force [96]. This can be solved for the deflection vs. applied voltage. When plotted as "Applied Voltage vs. Deflection" the maximum value formed the threshold voltage. This method is described in detail in the following discussion.

For the geometry in Figure 3-4, the application of a voltage between the bottom metal electrode and the beam creates the attractive electrostatic force, F_e. This force is found by considering the change in power stored in the capacitive beam with respect to the movement of the beam, x, and is shown as [97, 98]:

$$P_{stored,cap} \approx \frac{1}{2}V^2 C(x) \qquad \text{Equation 3-4}$$

This equation does not include fringing effects but they are considered to be negligible. The assumption is valid as long as the width of the beam is sufficiently larger than the spacing between the plates such as is the case of the standard beam in this work (i.e. the width of the beam is $25\mu m$ and the beam-to-substrate gap is $2\mu m$). In addition, Equation 3-4 assumes that the beam and bottom electrode are parallel to each other so this assumption is only valid for small displacements of the beam.

$$F_e = \frac{dP}{dx} = \frac{1}{2}V^2 \frac{dC(x)}{dx} = \frac{\varepsilon_o A V^2}{2(d_{BS} - x)^2} \qquad \text{Equation 3-5}$$

Where:
ε_o = Permittivity of air [F/m]
A = Effective parallel-plate area [m^2]
V = Applied voltage [V]
d_{BS} = Beam-to-substrate distance [m]

~40~

x = Deflection of beam at the tip [m]

This applied electrostatic force is then equated with the mechanical restoring force due to the stiffness of the beam, $F_{SP}=kx$.

$$\frac{\varepsilon_o A V^2}{2(d_{BS}-x)^2} = kx$$

Equation 3-6

Where the spring constant, k [N/m], for a force distributed from E_1 [m] to l_B [m] on a beam with Young's Modulus, E [N/m^2], and width, b_B [m], as shown in Figure 3-4, is given by [96]:

$$k = 2Eb_B\left(\frac{t}{l_B}\right)^3 \frac{1-\left(E_1/l_B\right)}{3-4\left(E_1/l_B\right)^3+\left(E_1/l_B\right)^4}$$

Equation 3-7

Solving Equation 3-6 for voltage yields:

$$V = \sqrt{\frac{2k}{\varepsilon_o(l_B - E_1)b_b}x(d_{BS}-x)^2}$$

Equation 3-8

Figure 3-5 is a plot of applied voltage with respect to a normalized deflection (x/d_{BS}) using Equation 3-8. It is seen that a maximum voltage occurs at $x = \frac{1}{3}d_{BS}$, and its physical importance is further described below.

~41~

Voltage vs. Normalized Deflection
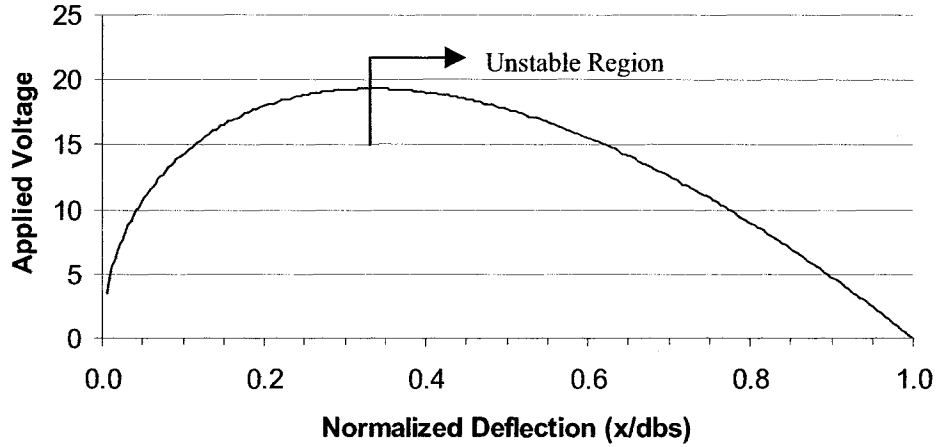
Figure 3-5: Voltage versus normalized deflection for a cantilever beam
Equation 3-7 and 3-8 used for plot. Normalized deflection is (x/d_{BS})

By substituting $x = \frac{1}{3}d_{BS}$ into Equation 3-8, an equation for the threshold voltage is:

$$V_{th} = V\left(\frac{1}{3}d_{BS}\right) = \sqrt{\frac{8k}{27\varepsilon_o\left(l_B - E_1\right)b_b}d_{BS}^{3}}$$ **Equation 3-9**

In practice, upon reaching an actuation voltage of, V_{th}, snapdown between the beam and the bottom electrode occurs spontaneously. It is impossible to hover a beam electrostatically beyond the distance of 1/3 d_{BS} because complete actuation always occurs once the threshold voltage is applied.

The standard beam's response to an applied voltage is calculated using the method described above. The method does not, however, include any intrinsic stress in either the cantilever or the top metal (Cr/Au). Using Equation 3-8 and shown below in Figure 3-6 is the applied DC voltage versus the displacement at the tip for this situation. As noted in the figure and calculated using Equation 3-9, the threshold voltage is 19.4V_{DC} for a standard beam (refer to Table 3-1 for standard beam dimensions).

~42~

Deflection vs. Applied Voltage for Standard Beam
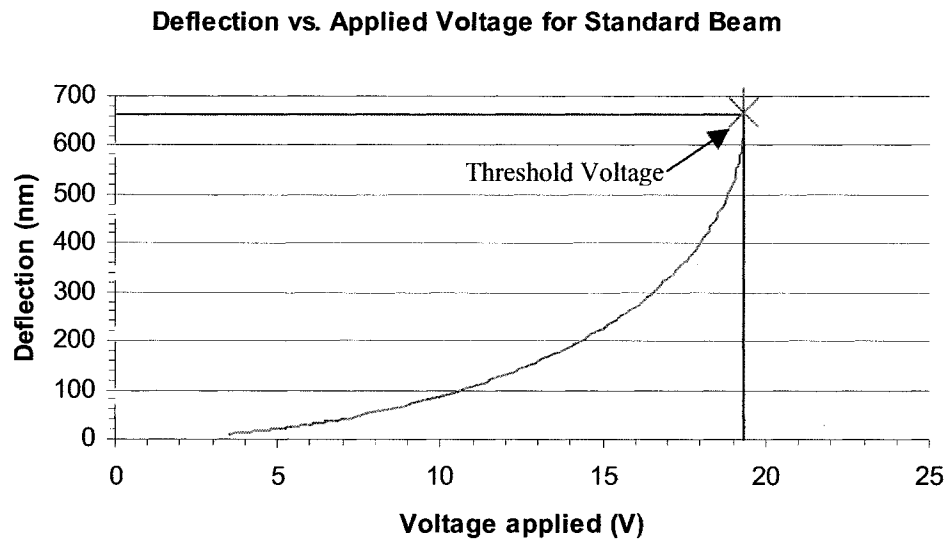
Figure 3-6: Calculating threshold voltage
Equation 3-7 and 3-8 used for the plot

4.4 Resonant Frequency Calculation

The differential equation for the lateral vibration of beam – the Euler Equation for beams – is found by summing the forces in the transverse direction about any point in the beam. The fourth-order differential equation for the vibration of a uniform beam is then found to be [99]:

$$\frac{d^4 x}{dl^4} - \rho \frac{\omega^2}{EI} x = 0$$

Equation 3-10

Where:
x = the transverse direction of the beam (Figure 3-4)
l = the direction along the length of the beam
ρ = Density of beam [kg/m^3]
E = Elastic modulus [N/m^2]
I = moment of inertia [m^4]

The natural frequencies of vibration of a uniform beam are found by equating a constant to $\rho \frac{\omega^2}{EI}$ in Equation 3-10 and solving for frequency [99]. The constant depends on the boundary conditions of the problem. The resonant frequency for transverse (or bending)

~43~

oscillations or the *fundamental frequency*, f_R [Hz], of a cantilever beam (refer to Figure 2-8 (a) or Figure 3-3 (a)) is found from the equation [94, 100]:

$$f_R = \frac{k_n^2}{2\pi}\sqrt{\frac{E_B I \cdot K}{\mu \cdot l_B^4}} = \frac{0.162 h_B}{l_B^2}\sqrt{\frac{E_B K}{\rho_B}}$$

Equation 3-11

Where:
k_n = constant of the nth mode of resonance (1.875 for the fundamental frequency)
I = moment of inertia
μ = weight per unit length of the beam [kg/m]
h_B = Beam height [m]
E_B = Elastic modulus of beam [N/m^2]
K = Relative contributions for a bi-material beam [*unitless*]
l_B = Beam length [m]
ρ_B = Density of beam [kg/m^3]

The relative contribution of the metal and the dielectric to the mechanical properties of the equivalent beam is accounted for via the expression for K', K", and K. These are shown below [94]:

$$K' = 4 + 6\cdot\left(\frac{h_M}{h_B}\right) + \left(\frac{E_B}{E_M}\right)\left(\frac{h_B}{h_M}\right) + 4\cdot\left(\frac{h_M}{h_B}\right)^2 + \left(\frac{E_M}{E_B}\right)\left(\frac{h_M}{h_B}\right)^3$$

Equation 3-12

$$K'' = \left[\left(1 + \frac{E_B h_B}{E_M h_M}\right)\left(1 + \frac{\rho_M h_M}{\rho_B h_B}\right)\right]^{-1}$$

Equation 3-13

$$K = K' K''$$

Equation 3-14

Where:
h_M = Top electrode thickness [m]
E_M = Elastic modulus of metal [N/m^2]

The fundamental resonant frequency is then calculated using Equation 3-11 and the standard beam dimensions and properties introduced at the beginning of this section. The result for the standard beam is found to be 54 kHz.

~44~

4.5 Quality Factor

The quality factor (Q-factor) is influenced by numerous losses as explained in Chapter 2. Every one of the loss mechanisms has an associated Q-factor and the overall quality factor Q_{tot} can be found from [101, 102]:

$$\frac{1}{Q_{tot}} = \sum_i \frac{1}{Q_i}$$

Equation 3-15

It is obvious from Equation 3-15 that this relationship indicates that the limitation of Q_{tot} comes from the lowest Q of all contributing factors. The following discussion focuses on the three most prominent of the mechanical energy losses, as introduced in Chapter 2 – (1) Thermoelastic energy dissipation (TED), (2) Support losses, and (3) Air damping [52]. All the individual Q factors are calculated in their respective sections and are combined to give a good idea as to the expected quality factor of the resonant beam. Other losses such as surface losses discussed in Chapter 2 are not included in this calculation as their influence is expected to be minimal.

4.5.1 Thermoelastic Energy Dissipation (TED)

As described in more detail in Chapter 2, TED is due to the inhomogeneous temperature gradients caused across the cross section of the beam due to tensile and compressive forces during the beam's movement. Analytical representation of the loss due to thermoelastic energy dissipation is reported by the literature using a model for the transversal vibration of a thin rod, whereby they replace the rod's diameter with the beam thickness. Thus, the Q factor of the ultra thin cantilever determined by thermoelastic loss is estimated as [103, 104]:

$$Q = 80 \frac{\chi}{fh_B^2} \frac{E}{\delta E}$$

Equation 3-16

Where:
f = is the resonance frequency [Hz]

~45~

E = is the isothermal Young's modulus [N/m²]

δE = is the difference between the adiabatic and the isothermal Young's moduli [N/m²]

h_B = is the thickness of the beam [m]

χ = is the thermal diffusivity [m²/s], which is defined as:

$$\chi = \kappa / (\rho C_p)$$

The thermal diffusivity describes the rate at which heat is conducted through a medium. It is related to thermal conductivity, κ [W/m·K], specific heat capacity, C_P [J/kg·K], and density, ρ [kg/m³].

The δE is the difference between the adiabatic and the isothermal Young moduli, and is given by [103, 104]:

$$\delta E = E_{ad} - E = \frac{E^2 T \alpha^2}{9 C_p}$$

Where:

α = thermal expansion coefficient [1/K]

T = absolute temperature [K]

adiabatic = refers to no heat transferred between the system (beam) and its surroundings

isothermal = the system (beam) remains at one temperature

The properties used for the numerical results for a standard beam are summarized below in Table 3-2.

Table 3-2: Properties Used for the Standard Beam TED Q Factor Calculations

Property Symbol	Property Name	Value	Units
ρ	Density	2320 [95]	kg·m⁻³
C_p	Specific heat capacity	705 [105]	J·kg⁻¹·K⁻¹
κ	Thermal conductivity	148 [105]	W·m⁻¹·K⁻¹
α	Thermal expansion coefficient	2.3×10^{-6} [52]	K⁻¹
E	Young's Modulus	1.295×10^{11} [93]	N·m⁻²
h_B	Thickness of cantilever beam	2×10^{-6} (Table 3-1)	m
f	Fundamental resonant frequency	53978 (Equation 3-11)	Hz

A summary of the calculated TED Quality factor for a standard beam is presented below.

$$\delta E = E_{ad} - E = \frac{E^2 T \alpha^2}{9c_p} = \frac{(1.295x10^{11})^2 \cdot (300) \cdot (2.3x10^{-6})^2}{9 \cdot (705)}$$ **Equation 3-18**

$$= 4.19x10^9 \, [\text{N} \cdot \text{m}^{-2}]$$

$$\chi = \kappa /(\rho c_p) = 148/(2320 \cdot 705) = 9.05E^{-5} \left[m^2 s^{-1}\right]$$ **Equation 3-17**

$$Q = 80\frac{\chi}{fH^2}\frac{E}{\delta E} = 80\frac{9.05E^{-5}}{(53978) \cdot (2E^{-6})}\frac{1.295E^{11}}{4.19E^9} = 1.04E^6$$ **Equation 3-16**

From the above sample calculations, the limiting Q due to thermoelastic loss is **1.04 x 10⁶** [unitless].

4.5.2 Support Losses

A second Q factor limiting loss is the loss through the anchors of the device. The anchors are the points at which the resonating mass is attached to the substrate. In the case of this work, this loss occurs at the base of the cantilever where it meets the substrate as shown in the left of Figure 3-4. Considering the support as an infinitely large elastic plate, the damping ratio caused by the loss to the support for the beam-type cantilever is given by · Hosaka *et al.*, and the support loss limited Q factor can be estimated from the following equation [106]

$$Q = 0.34\left(\frac{l_B}{h_B}\right)^3$$ **Equation 3-19**

It has been reported that if the ratio of length to thickness of a cantilever beam is less than 100, (l_B/h_B <100), the support loss is worth considering [52]. This is, of course, is a

~47~

subjective view and completely dependent on the quality factor desired by the designer. For this work, the standard beam's ratio of length to thickness is exactly 100, so the loss due to supports is included but is not expected to be the limiting factor in regard to the quality factor.

$$Q = 0.34\left(\frac{l_B}{h_B}\right)^3 = 0.34\frac{\left(200x10^{-6}\right)}{\left(2x10^{-6}\right)} = 3.40x10^5 \; [unitless] \qquad \textbf{Equation 3-19}$$

From the sample calculation, it is seen that the Q factor due to support losses is **3.4 x 10^5 [unitless]**, which is a bit lower than the TED, thus, is expected to be a more significant influence on the quality factor.

4.5.3 Air Damping

Finally, air damping is expected to be the dominant loss that limits the Q factor when testing micromechanical resonators in air. An estimate can be made of the effects of air damping in the molecular regime where the air damping is proportional to air pressure. This regime is used because no analytical solution exists in the viscous region - modeling in the viscous regime must entail interaction with each molecule present. In the molecular regime, the drag force can be determined by means of the kinetic theory of gases. Hence, for the molecular region the Q factor for a standard cantilever beam is given by [78]:

$$Q = \frac{2\pi f_n h_B \rho}{k_m P} = \frac{k_n^2}{k_m P}\left(\frac{h_B}{l_B}\right)^2 \sqrt{\frac{E\rho}{12}} \qquad \textbf{Equation 3-20}$$

Where:
f_n = resonance frequency of the nth mode [Hz]
ρ = density of the cantilever [kg/m^3]
P = pressure [Pa]
k_n = constant of the nth mode resonance [unitless]
h_B = thickness of the cantilever [m]
l_B = length of the cantilever[m]
R = universal gas constant [J/mol·K]
T = temperature [K]

~48~

k_m is defined for computation reasons as [78]:

$$k_m = \sqrt{\frac{32M}{9\pi RT}} \quad \left[s \cdot m^{-1} \right]$$

<div align="right">**Equation 3-21**</div>

Where:

M = mass of gas molecule [kg]

Actuation of the standard beam in atmospheric conditions means it is interacting with air that is considered part of the viscous damping regime (as was the assumption for Equation 3-1) and not the molecular region.   For length-to-height ratios of the beam, l_B/h_B = 482 in [52], the molecular/viscous boundary occurs at ~6mbar (0.6kPa); but for l_B/h_B =71 in [52], the boundary between the molecular region and the viscous region occurs at 40mbar (4kPa). It is seen that for the shorter or thicker beams, the barrier is located at a higher pressure than those of the longer or thinner ones [52]. The standard beam discussed in this work has a ratio of l_B/h_B =100; thus, at atmospheric conditions (101kPa), it is not in the molecular regime. In addition, by use of Equation 2-1, the Knudsen number is found to be 0.03 (where the mean free path in atmospheric conditions at sea level is 0.06μm and the characteristic length of the flow is the beam to substrate distance of 2μm), which is clearly in the viscous regime as is shown by Figure 2-6. However, the Equation 3-20 will be used as an estimate for the Q factor.

The properties used to calculate the quality factor with respect to air damping (Equations 3-20 and 3-21) are summarized below in Table 3-3. The constant for the fundamental frequency, k_o, is used as the value for the nth mode of resonance, k_n, introduced for Equation 3-21. All properties used in Equation 3-20 and 3-22 are summarized in Table 3-3 below.

Table 3-3: Properties Used for the Standard Beam Air Damping Q Factor Calculations

Property Symbol	Property name	Value	Units
k_o	Constant for fundamental frequency	1.875 [107]	*unitless*
R	Universal gas constant	8.314	$J \cdot mol^{-1} \cdot K^{-1}$
T	Absolute temperature	300	K
M (air)	Mass of air molecule	28.694×10^{-3}	kg
P	Atmospheric pressure	101325	Pa
ρ	Density of silicon	2320 [95]	$kg \cdot m^{-3}$

The constant, k_m, is found as:

$$k_m = \sqrt{\frac{32M}{9\pi RT}}, (s/m) = \sqrt{\frac{32 \cdot \left(28.964 \times 10^{-3}\right)}{9 \cdot \pi \cdot (8.314) \cdot (300)}} = 3.62 \times 10^{-3} \ \left[s \cdot m^{-1}\right] \qquad \text{Equation 3-21}$$

Thus, the Q due to air damping is:

$$Q = \frac{2\pi f_n h_B \rho}{k_m P} = \frac{2 \cdot \pi \cdot (53798) \cdot \left(2 \times 10^{-6}\right) \cdot (2320)}{\left(3.62 \times 10^{-3}\right) \cdot (101325)} = 4.28 \ [unitless] \qquad \text{Equation 3-20}$$

The Q factor due to air damping operated at atmospheric pressures is 4.28, which is two orders of magnitude lower than either the quality factors due to either TED or support losses.

4.5.4 Total Quality Factor

The final Q using Equation 3-15, and including the major sources of loss calculated above, is found as:

$$\frac{1}{Q_{tot}} = \sum_i \frac{1}{Q_i} = \left(\frac{1}{Q_{TED}}\right) + \left(\frac{1}{Q_{Support}}\right) + \left(\frac{1}{Q_{Air}}\right) = \left(\frac{1}{1.03 \times 10^6}\right) + \left(\frac{1}{3.40 \times 10^5}\right) + \left(\frac{1}{4.28}\right) = \frac{1}{4.28}$$

~50~

Shown by the above calculations, it is expected that the quality factor is limited by air damping. However, in vacuum (such as the case at 1mTorr) it can be seen that the quality factor is limited by support losses. At this pressure, the quality factor due to air damping is 3.6×10^6 (Equation 3-20) and due to support losses is 3.4×10^5 (Equation 3-19). The final quality factor using Equation 3-15 is then 2.4×10^5.

4.6 Induced Current Calculations

The derivation for the time-varying current induced on the bottom electrode to aid in the development of on-chip monitoring of the movement and resonance of the cantilever is outlined here. Considering the cantilever of Figure 3-4 to consist (electrically) of two parallel plates, a simple circuit representation is shown in Figure 3-7:

$$i(t) = \frac{dQ}{dt} = \frac{d(CV)}{dt} = C\frac{dV}{dt} + V\frac{dC}{dt}, \qquad \textbf{Equation 3-22}$$
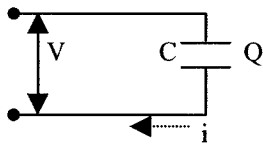
Plates spaced d apart, with effective area, A.
As the distance d changes, a current, i, is induced

Figure 3-7: Representation for induced current caused by moving cantilever beam

And, if the polarization voltage, V_p, is held constant, then:

$$i(t) = V_P\frac{dC}{dt} \qquad \textbf{Equation 3-23}$$

and since C varies only through x, assuming negligible deviation from linearity:

$$i(t) = V_P\frac{\partial C}{\partial x}\frac{dx}{dt} \qquad \textbf{Equation 3-24}$$

Where:
V_P = DC polarization voltage [V]
$\delta C/\delta x$ = Change in resonator-to-electrode capacitance per unit displacement [F/m] [25]

~51~

It is thus concluded that the vibration of the resonator creates a dc-biased, time-varying capacitor between the conductive resonator and output electrode, which then sources an output current given by Equation 3-24. A schematic representing the device during actuation and detection is shown below in Figure 3-8:
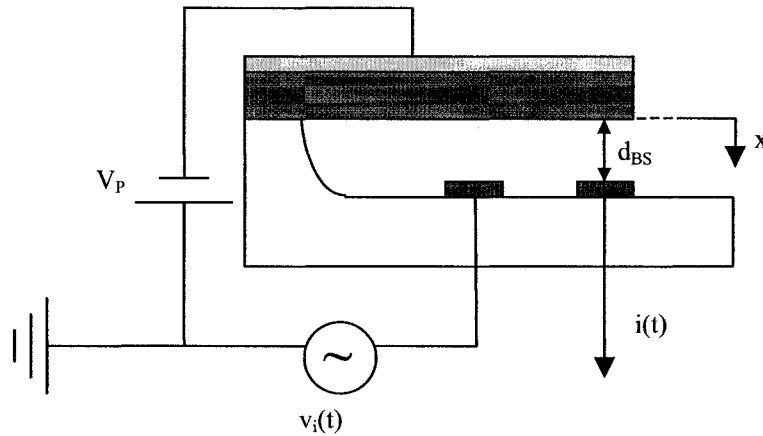
Figure 3-8: Schematic of electrostatically actuated, capacitively sensed micromechanical resonator

Ignoring fringing effects and for small displacements, the cantilever beam configuration is represented as a parallel-plate capacitor with the fringing of the field at the edges of the electrode area being negligible. The capacitance, C [F], is then:

$$C = \frac{\varepsilon_o A}{d}$$

<div align="right">**Equation 3-25**</div>

Where:
ε_o = Permittivity of air [F/m]
d - Distance between the plates
A - Electrode's area

For the situation of an electrostatically actuated cantilever beam represented in Figure 3-8, the capacitance, C [F], is then:

$$C = \frac{\varepsilon_o A}{d_{BS} - x}$$

<div align="right">**Equation 3-26**</div>

Taking the derivative with respect to the deflection at the tip of the beam, x, yields the change in electrode-to-resonator capacitance per unit displacement of the resonator, approximately given by (neglecting fringing fields & for small displacements so the parallel plates assumption is accurate):

$$\frac{dC}{dx} = \frac{\varepsilon_o A}{(d_{BS} - x)^2}$$

Equation 3-27

Where:
d_{BS} = Gap between the beam and the bottom electrode [m]
x = Displacement of the tip of the beam [m]

However, for small displacements of the beam (i.e. $x < 0.05 \cdot d_{BS}$), x can be ignored in Equations 3-27 & 3-28. The change in capacitance with respect to displacement of the beam tip is thus:

$$\frac{dC}{dx} = \frac{\varepsilon_o A}{d_{BS}^2}$$

Equation 3-28

From Equations 3-5 & 3-6, it is seen that the electrostatic force, F_e, is proportional to the voltage squared, $F_e \propto V^2$, and the mechanical restoring force is directly proportional to the displacement of the beam, x. Therefore, the displacement of the beam, x, is proportional to the square of the voltage, $x \propto V^2$. This assumption is valid for all values of $x < 0.05 \cdot d_{BS}$. The total voltage potential applied between the beam and the bottom electrode is represented by the addition of the polarization voltage, V_P, and the applied driving voltage, v_{AC}. By rearranging Equation 3-8 and utilizing the small displacements assumption, the time-varying displacement at the tip of the beam is:

$$x(t) = V^2 \cdot \frac{\varepsilon_o \cdot (l_B - E_1) \cdot b_B}{2 \cdot k \cdot d_{BS}^2} = (V_P + v_{AC}(t))^2 \cdot \frac{\varepsilon_o \cdot (l_B - E_1) \cdot b_B}{2 \cdot k \cdot d_{BS}^2}$$

Equation 3-29

Or,

$$x(t) = C_{OP} \cdot (V_P + v_{AC}(t))^2 \qquad \textbf{Equation 3-30}$$

Where:

$v_{AC}(t) = V_i \sin(\omega \cdot t)$ [m]

V_i = Maximum amplitude of AC input voltage [m]

And the constant of proportionality, $C_{op} = \dfrac{\varepsilon_o \cdot (l_B - E_1) \cdot b_B}{2 \cdot k \cdot d_{BS}^2}$

Where:

l_B = length of the beam [m]
b_B = width of the beam [m]
k = spring constant of the beam [N/m]
E_1 = distance to bottom electrode (actuation electrode) [m]

The change in the distance with respect to time using the triginometric double angle formula is then:

$$\frac{dx}{dt} = C_{OP} \cdot \left(2 \cdot \omega \cdot V_P \cdot V_i \cos(\omega \cdot t) + \omega \cdot V_i^2 \cdot \sin(2 \cdot \omega \cdot t)\right) \qquad \textbf{Equation 3-31}$$

Finally, by inputting all terms into Equation 3-24, the time dependent current, $i(t)$ [A], is shown as:

$$i(t) = V_P \left(\frac{\varepsilon_o A}{(d_{BS})^2}\right) \cdot C_{OP} \cdot \left(2 \cdot \omega \cdot V_P \cdot V_i \cos(\omega \cdot t) + \omega \cdot V_i^2 \cdot \sin(2 \cdot \omega \cdot t)\right) \qquad \textbf{Equation 3-32}$$

The polarization voltage used for all calculations is 9.7V_{DC} because this is about half of the threshold voltage of the standard beam. This ensures good comparison with all beams and, most importantly, with reasonably small V_P ensures that the beam does not snap under the DC voltage. The AC voltage is +/- 2V. The calculation is done near resonance (50kHz) but not directly at resonance. The amplitude at resonance would be higher, thus, increasing the signal. However, if the expected signal is high enough to be deemed detectable, the signal at resonance will have an even higher likelihood of being detectable. The calculation of the peak current using Equation 3-33 is summarized in the table below:

Table 3-4: Properties and Results of Induced Current Calculation

Property		Width, b_B [m]		
		10×10^{-6}	25×10^{-6}	50×10^{-6}
Polarization Voltage	V_p [V]	9.7	9.7	9.7
AC Voltage	V_i [V]	2	2	2
Frequency	F [kHz]	50	50	50
Electrode Area	A [m^2]	2.5×10^{-10}	6.25×10^{-10}	1.25×10^{-9}
Initial gap between the plates	d_{BS} [m]	2×10^{-6}	2×10^{-6}	2×10^{-6}
Spring Constant (Equation 3-7)	k [N/m]	0.35	0.875	1.75
Length of Bottom Electrode	(l_B-E_1) [m]	25×10^{-6}	25×10^{-6}	25×10^{-6}
Peak Current (Equation 3-32)	i_P [fA]	57.1	143	285

4.7 Alternate Induced Current Calculation

An alternate induced current calculation is performed assuming maximum displacement, which occurs at the threshold voltage (calculated in section 4.3). This provides an estimate for the maximum possible current through the device. The motivation for this calculation is to corroborate the previous calculation. The same formula presented as Equation 3-32 is used but with different assumptions. The assumptions are outlined as follows:

- A polarization voltage of ½ the threshold voltage is used to ensure one polarity swing of the beam. (~9.7V$_{DC}$ in the case of the standard beam). Refer to section 2 for explanation of the frequency-doubling phenomenon.
- An AC voltage of ½ the threshold voltage is assumed. (±~9.7V in the case of the standard beam)
- With these boundaries outlined, the voltage difference will oscillate between 0 and threshold (0 and ~19.4V).
- The displacement of the beam then varies between $x = 0$ and $x = \frac{1}{3}d_{BS}$ (~⅔μm for the standard beam with a gap of 2μm).

~55~

The result for the maximum expected induced current using the above assumptions is 941fA (Equation 3-32) where the previous result was 143fA. It would be expected that this calculation would result in a higher estimate because a higher AC voltage is assumed in this case (and hence, a larger AC induced deflection). In addition, it provides an expected range for the expected current induced due to the moving cantilever.

4.8 Extracted Signal Calculation

The extracted signal is the voltage drop across the wire traces, bonding pad, and oscilloscope probe due to the induced current calculated in the two previous sections. To evaluate whether or not on-chip monitoring is achievable, the extracted signal must be evaluated to ensure that the parasitic capacitance of the system is not so large as to prevent detection. The maximum change in charge, ΔQ, of the cantilever occurs when the beam moves from position at rest ($x=0$) to the threshold position that occurs when the threshold voltage is applied ($x= \frac{1}{3}d_{BS}$). This is using the same beam displacement as for the alternate induced current calculation in the previous section. This change in charge, ΔQ, is equal to the change in capacitance, ΔC, multiplied by the polarization voltage:

$$\Delta Q = \Delta C V_P \qquad \text{Equation 3-33}$$

The voltage drop across the test circuit (wire trace, bond pad, and oscilloscope probe) is equal to the change in charge described above divided by the equivalent capacitance of the test circuit.

$$\Delta V = \Delta Q / C_{eq} \qquad \text{Equation 3-34}$$

Where the equivalent capacitance is found by adding the capacitances (capacitors in parallel with respect to ground). The schematic for this setup and circuit equivalent is shown below in Figure 3-9.

$$C_{eq} = C_{WT} + C_{BP} + C_{PB} \qquad \text{Equation 3-35}$$

Where:

~56~

C_{WT} = capacitance of the wire trace [F]
C_{BP} = capacitance of the bonding pad [F]
C_{PB} = capacitance of the oscilloscope probe [F]
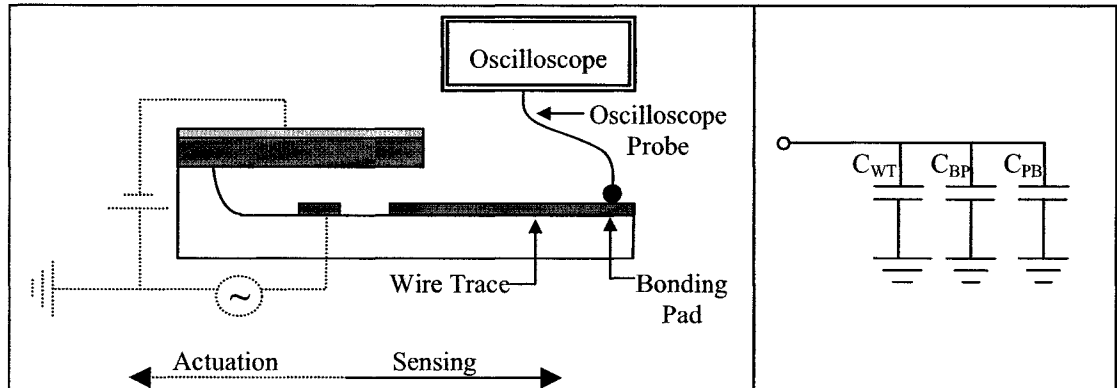
Figure 3-9: Schematic used for extracted signal calculation

Shown in Figure 3-10 is an overhead view of the cantilever (side view shown in Figure 3-9) beam as it appears on the chip. Shown in the figure are the wire traces extending from the bottom electrodes underneath the beam. These dimensions, as well as those for the contact pads, are used in the parasitic capacitance calculations. Contact is made to the pads with probes.
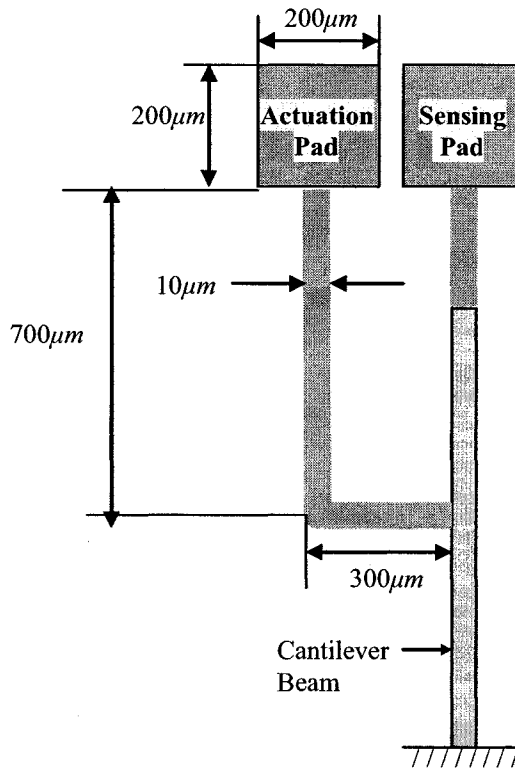
Figure 3-10: Overhead view of cantilever with wire traces

4.8.1 Charge in Beam

To find the maximum change in charge of the cantilever beam, the capacitance is calculated at a zero position and at the threshold position (⅓ the gap) with a constant voltage equal to the polarization voltage:

$$\Delta Q = \Delta C V_P \qquad \text{Equation 3-36}$$

$$= (\frac{\varepsilon_o A}{d_{zero}} - \frac{\varepsilon_o A}{d_{1/3}})V_P \qquad \text{Equation 3-37}$$

$$= (\frac{(8.854x10^{-12})(25x10^{-6})^2}{2.0x10^{-6}} - \frac{(8.854x10^{-12})(25x10^{-6})^2}{0.67x10^{-6}})(19.4)$$

$$=1.07x10^{-13} \ [C]$$

Where:

ε_o = Permittivity of air [8.854 x 10^{-12} F/m]
A = Effective sensing electrode area [625 μm^2]

~58~

V_P = Applied polarization voltage (using V_{th} = 19.4V$_{DC}$, maximum applied voltage possible)

d_V = Beam-to-substrate distance at applied voltage. [d_{zero} = 2μm, $d_{1/3}$ = 0.67 μm]

4.8.2 Set-up Capacitances

This calculation for the capacitance of the wire trace is based on the solution for a microstrip provided by "Foundations of Microstrip Circuit Design" [108]. A schematic is shown below in Figure 3-11 that outlines the variables used in the following discussion. These equations are presented in imperial units of inches. The capacitance of the wire trace is very small in comparison to the oscilloscope probe.
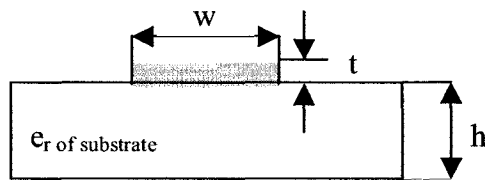
Figure 3-11: Schematic of a wire trace

Effective trace width (for $2\pi w < 2\pi h$):

$$WE\_SKNY(h,w,t) = w + \frac{1.25t}{\pi}(1 + \ln(\frac{4\pi w}{t}))$$

Equation 3-38

Effective relative permittivity (for w>h):

$$E\_SKNY(h,w,e_r) = \frac{e_r + 1}{2} + (\frac{e_r - 1}{2})\left[(1 + \frac{12h}{w})^{-0.5} + 0.04(1 - \frac{w}{h})^2\right]$$

Equation 3-39

Special adjustment for trace thickness:

$$EEFF(h,w,t,e_r) = E\_SKNY(h,w,e_r) - \frac{(e_r - 1)(\frac{t}{h})}{4.6\sqrt{\frac{w}{h}}}$$

Equation 3-40

Characteristic impedance as a function of trace geometry (Ω). Accuracy better than 2% is claimed if the following conditions are followed:

~59~

- $0 < t/h < 0.2$ (we have $0.25\mu m/500\mu m = 0.0005$)

- $0.1 < w/h < 20$ (we have $10\mu m/500\mu m = 0.02$) *

- $0 < e_r < 16$ (Pyrex 7740 = 4.6)

* With respect to the thickness of the metal line to thickness of the substrate ratio for the standard beam, the ratio is not within tolerance, so the calculations are not expected to be within 2%. It is, however, an estimate.

$$ZMS\_SKNY(h,w,t) = 60\ln(\frac{8h}{WE(h,w,t)} + \frac{WE(h,w,t)}{4h}) \qquad \text{Equation 3-41}$$

$$ZMSRIP(h,w,t,e_r) = \frac{ZMS\_SKNY(h,w,t)}{\sqrt{EEFF(h,w,t,e_r)}} \qquad \text{Equation 3-42}$$

Propagation delay (s/in):

$$PMSTRIP(h,w,t,e_r) = 84.72x10^{-12}\sqrt{EEFF(h,w,t,e_r)} \qquad \text{Equation 3-43}$$

Finally, the capacitance of microstrip (F/in):

$$CMSTRIP(h,w,t,e_r,x) = \frac{PMSTRIP(h,w,t,e_r)}{ZMSTRIP(h,w,t,e_r)} \qquad \text{Equation 3-44}$$

Utilizing Equations 3-37 through 3-43, the capacitance of the wire trace, C_{WT}, is found as **0.7pF/in** using the following parameters:

$h = 500\mu m = 0.019865$ [inches]
$w = 10\mu m = 3.94x10^{-4}$ [inches]
$t = 0.25\mu m = 9.8425x10^{-6}$ [inches]
$e_r =$ Effective relative dielectric constant of Pyrex = 4.6

~60~

The overall capacitance for a wire trace of $1000\mu m$ (3.937×10^{-2} [inches]), which is the length for a standard device between the bottom electrode and the bonding pad, is **16fF**. To corroborate, the maximum capacitance of a wire trace over the field oxide in a typical silicon gate CMOS process with the same dimensions as the wire trace used in this work is found to be [109]:

$$C_{WT} = w * l * C_{mf\_MAX} \qquad\qquad \textbf{Equation 3-45}$$
$$= 10\mu m * 1000\mu m * 0.3x10^{-4} \; pF/\mu m^2 = 0.3pF$$

Where:

w = width of wire trace [μm]
l = length of wire trace [μm]
C_{mf_MAX} = Maximum capacitance of metal over field (no fringing)

Although the device in this work uses a wire trace on Pyrex which is not exactly the same as the situation of a metal on the field oxide as in CMOS, the scenarios are similar enough (both metals on a glasslike material). The comparison of the two values is used to increase the confidence in the estimated extracted signal calculation. The value of the wire trace using the CMOS analogy is 0.3pF, which is also negligible with respect to the probe capacitance. Using either result will not impact the final voltage calculation of Equation 3-33 dramatically because it is not nearly the highest capacitance in the circuit's capacitance.

The capacitance of the bonding pad (gold on silicon), C_{BP}, for the $200\mu m$ x $200\mu m$ pad is found by using Equations 3-37 through 3-43 and is found as **29fF**. For comparison, the capacitance of the bonding pad (gold on silicon), C_{BP}, for a $75\mu m$ x $75\mu m$ has been reported as **80fF** [110] and by using the CMOS analogy (Equation 3-44), the value is 1.2pF.

The capacitance of the test probe, C_{TD}, for an oscilloscope probe (tek P6122) is **11pF** [§].

~61~

The equivalent capacitance for the test circuit is found using Equation 3-34 and the result is C_{eq} = 11.1pF. The final voltage drop across the equivalent capacitance for a standard beam (L=200μm x W=25μm) is then:

$$\Delta V = \Delta Q / C_{eq} \qquad\qquad \textbf{Equation 3-46}$$
$$= (1.07 \text{x} 10^{-13} \text{ C})/(11.1 \text{x} 10^{-12} \text{F})$$
$$= \textbf{9.7 mV}$$

A summary of all the beams in terms of voltage drop across the equivalent capacitance is shown below in Table 3-5. It is concluded from these calculations that the magnitude of the signal present lends to confidence that capacitive detection of the standard beam design should be feasible. However, it is noted that the above analysis assumes optimal conditions where the beam is traveling a maximum distance and operating just below the threshold where it will snap shut.

Table 3-5: Summary of Beams for Capacitive Sensing

Length (μm)	Electrode (width of beam x length along beam) All dimensions in μm	ΔV (mV)
200	10 x 25	4.3
200	25 x 25	9.7
200	50 x 25	19.3

4.9 Dimensional Considerations

Now that the equations are derived, it is obvious that in designing a micromechanical resonator, many dimensions must be considered and optimized to achieve the desired power and resonant frequency. The cantilever beam length, height, and gap are explored below in regard to their effect on the performance.

4.9.1 Beam Length

Both threshold voltage and resonance frequency depend inversely on beam length (from Equation 3-9 & 3-11, respectively). However, from Equation 3-19, the Q factor from support losses is directly proportional to the length cubed; but the Q with respect to air damping is inversely proportional to its square (Equation 3-20).

4.9.2 Beam Height

Increasing the beam height can increase resonance frequency and the Q factor with respect to air damping. Decreasing the beam height can decrease threshold voltage and the Q factor (from an increase in TED and support losses).

4.9.3 Beam-to-Substrate Separation

The threshold voltage can be reduced independently by minimizing the beam-to-substrate separation, d_{BS}. However, more importantly, the induced current also increases as the d_{BS} decreases because the change in capacitance with respect to deflection of the beam is proportional to the square of d_{BS}, as is shown by Equations 3-24 and 3-26. This is important when on-chip monitoring of the beam is desired. In addition, it is important that the gap must not exceed the maximum safe deflectable distance of the beam. The maximum safe deflectable distance is the maximum distance the beam can deflect prior to failure. In this regard, failure is designated as the maximum allowable stress, σ_{max}, that exceeds the material yield strength, σ_y. Beyond this, elastic deformation ceases and the material fails either catastrophically (ceramic and glasses) or plastically (metals). This is not usually a concern in the design of micromechanical resonators because, as previously mentioned, the gap is usually minimized to achieve low power consumption and high-induced current. In regard to sensing the change in capacitance, which the beam causes upon movement, this gap becomes increasingly important and is explored further in Chapter 5.

~63~

5 Summary of Calculations

These calculations are completed for all beams fabricated. Table 3-6 outlines the results of the calculations for beams of widths 10μm, 25μm, and 50μm. All the beams in this calculation have the same thickness of 2μm, gap sizes of 2μm, and wire trace and bond pad dimensions.

Table 3-6: Summary of Beam Calculated Results

Note: Beams are 200μm long.

Threshold Voltage (V) Equation 3-9			Resonant Frequency (kHz) Equation 3-11			Induced Current (fA) Equation 3-32			Quality Factor Equation 3-15		
Width (μm)			Width (μm)			Width (μm)			Width (μm)		
10	25	50	10	25	50	10	25	50	10	25	50
19.4	19.4	19.4	54	54	54	57.1	143	285	4.28	4.28	4.28

6 Comparison to Other Reported Beams

A very promising result is illustrated in Table 3-7. The calculations presented above for the fundamental frequency are used to compare to reported, tested cantilever beams from two sources. The reason these particular cantilever beams are chosen for the comparison is because they are composed of single-crystal silicon and their dimensions are similar to the beams in this work. Shown in the Table 3-7 below, the reported results for the beam's actual fundamental frequency compare within 5% with the calculated values when the dimensions of the cantilever were accurately known.

~64~

Table 3-7: Comparison of Calculations to Other Reported Beams

Switch	Thickness (μm)	Width (μm)	Length (μm)	Frequency Reported (kHz)	Pressure Tested	Chapter 3 Calculations (kHz) Equation 3-10	% Difference	Ref.
Single Crystal Silicon – (SCSi)	~5	40	300	58	Atmosphere	67.23	15.9%	[111]
SCSi	~5	40	800	10	Atmosphere	9.45	-5.5%	[111]
SCSi	6.5	20	700	15.94	1mTorr	16.05	0.7%	[75]
SCSi	4	20	500	19	1mTorr	19.36	1.9%	[75]
SCSi	5	20	500	24.59	1mTorr	24.20	-1.6%	[75]
SCSi	6	20	500	30.14	1mTorr	29.04	-3.6%	[75]

It is also interesting to note that the calculations seem accurate whether the beam is tested at atmosphere as in the first two cases or in a vacuum as the other examples. The assumptions presented for the calculation of Q factor with respect to air damping are, thus, deemed appropriate.

7 Multi-Physics Finite Element Analysis

As was briefly mentioned above, the cantilever beam will close at ⅓ the beam-to-substrate gap (the beam will make contact with the bottom electrode) at a threshold voltage; and upon reduction of the voltage, the beam will restore to its original state. The DC actuation voltage or threshold voltage and the restoring voltage are also found using multi-physics ANSYS. A 2D model was developed at initial stages of the development so as to aid in the final design.

The simulation couples the electrostatics with the structural solution to allow the actual electrostatic actuation of a MEMS device to be simulated, capturing the interdependencies of the physics. For example, as the cantilever beam is deflected, the electrostatic field distribution changes, as does the force generated. The finite element

analysis calculates an electrostatic force, transfers this to a structural analysis with the applied force, and calculates stress and displacement. When done in increments, the threshold voltage can be determined. When the voltage is then decremented, the restoring voltage is found. This analysis is done for a silicon cantilever beam assuming that the bottom electrode is the entire length of the cantilever beam (i.e. the electrostatic force is applied to the entire length of the beam). The beam used in the analysis has dimensions shown in Table 3-8 and the results of the analysis are shown in Figure 3-12.

Table 3-8: Beam Dimensions for ANSYS Simulation

	ANSYS Beam Dimensions
Length	$200 \mu m$
Width	N/A for 2D analysis
Beam Thickness	$4 \mu m$
Gap	$1.0 \mu m$
Threshold Voltage	$11.4 \, V_{DC}$
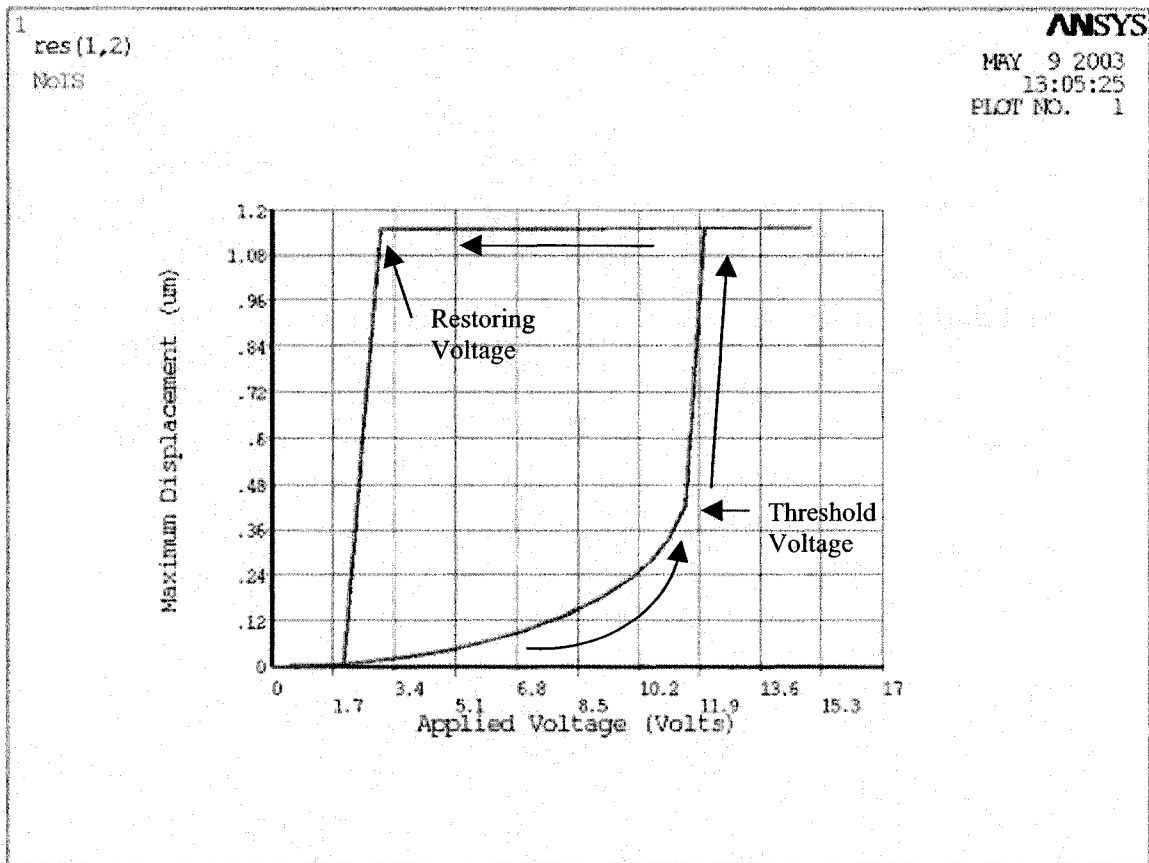
Figure 3-12: ANSYS simulation for DC behaviour

The arrows in the above figure show that the voltage is first incremented while the displacement is plotted; and once the threshold voltage is reached, the voltage is decreased while the displacement is plotted. The threshold voltage found using ANSYS is much lower to that predicted by Equation 3-9 ($\sim$11.4V_{DC} vs. 20.3V_{DC}, respectively), but the relationship of the beam movement with respect to voltage is expected to be similar. The reason there is such a discrepancy is because the ANSYS simulations assume that the electrostatic force is applied to the entire length of the beam (i.e. electrode is entire length of the beam) instead of just along the length of the beam over the bottom electrode as shown in Figure 3-4. This difference in bottom electrode length explains why a smaller applied voltage is required to snap the beam in the ANSYS simulations. Equation 3-9 can be used to calculate this same situation if the length to the

~67~

bottom electrode, E_1, is set to zero (Figure 3-4). A threshold voltage of $11.3V_{DC}$ is then found. Further detail of the ANSYS simulations is included in Appendix C.

8 Breakdown Voltage

Interestingly enough, the MEMS devices designed and simulated are not expected to exceed the voltage required for electrical breakdown even though their gap sizes are only $2\mu m$. The voltage for electrical breakdown depends on geometry of the electrode gap, the gas, and the pressure. The breakdown occurs between two parallel plates in air, at room temperature and at atmospheric pressure - if the electric field increases above roughly 3 MV m^{-1} [112]. Electrical breakdown refers to the discharge current that occurs when loosely bound electrons accelerate in the direction of the field (perpendicular to the plates) and pick up enough energy to ionize molecules upon collisions, causing further ionization. At this point, the insulating properties of air between the plates are broken down and the passage of high current occurs (i.e. a spark) [112].

It was found by Paschen that at a separation of several micrometers, the breakdown voltage reaches a minimum value [113]. When the electrode separation is reduced to less than several micrometers, the breakdown voltage and the breakdown field increase rapidly. It is for this reason that the gap sizes can be reduced beyond the point commonly thought to cause electrical breakdown. A plot of the breakdown voltage as a function of the product of electrode separation and pressure is known as Paschen's curve [114] and is represented in Figure 3-13. It is indicated by the curve that the breakdown voltage of the standard beam resonator examined (assuming a gap of $2\mu m$) is ~400V, which is nowhere near the threshold voltage to snap the beam closed ($19.4V_{DC}$).
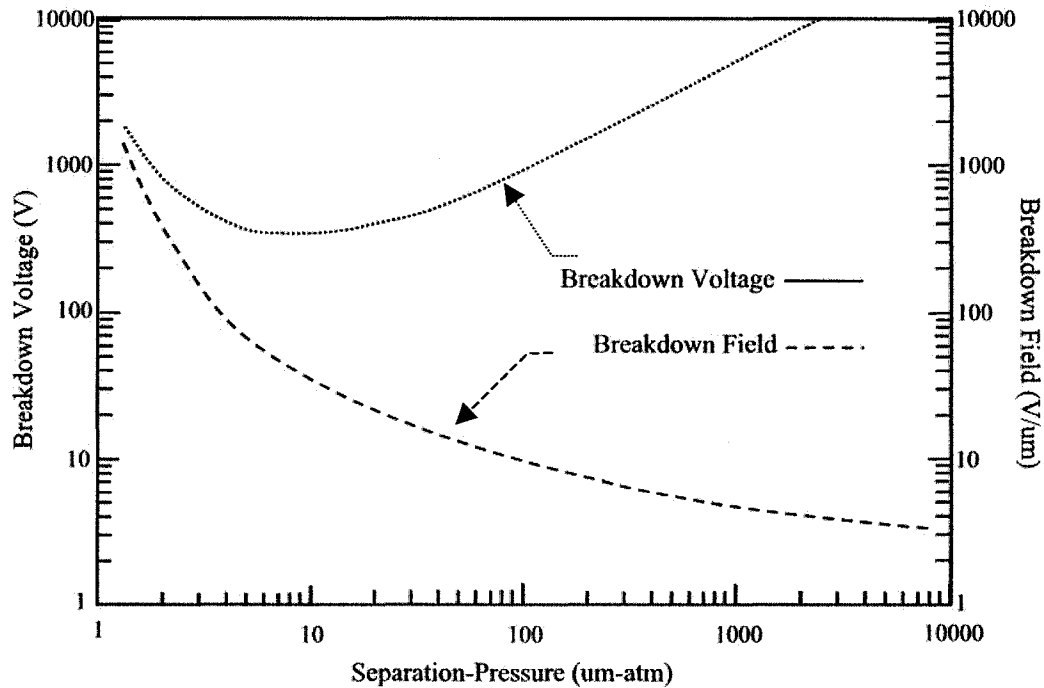
Figure 3-13: Paschen's curve
Representation of breakdown voltage and breakdown field at air and 1atm as a function of electrode separation - known as Paschen's curve [114]

Reported just under a half century ago, Germer explains that to the left of the minimum breakdown voltage in Pachen's curve, the applied voltage must increase drastically to cause the regenerative avalanche breakdown. This is because the mean free path of electrons in air is comparable with the gap distances and with no/few collisions, an ionization cascade does not occur, so no arc path forms [115]. Therefore, in this regime much larger electrostatic-energy densities can be attained. The fact that this is an advantage of microactuators over macroactuators was first identified by Bart *et al.* [116].

9 Conclusion

In this chapter equations are derived and expected results are explained for the design of a micromechanical resonator. Calculations for threshold voltage, resonant frequency, induced current, extracted signal, and quality factor are presented. For the standard beam, it is found that the threshold voltage is $19.4V_{DC}$, the resonant frequency is 54kHz, the induced current is 143fA, the extracted voltage drop across the system is 11mV, and the quality factor is between 4 and 5. ANSYS simulations are presented and, finally,

~69~

reasoning for why the electrical breakdown voltage is not exceeded in the MEMS design is given. This design chapter is used to theorize on expected outcomes. Upon presentation of the fabrication of the device, discussed in the next chapter, experimental set-ups, testing, and characterization are featured. The calculations presented in the chapter are often referred to and compared in the following chapters.

Chapter 4 – Fabrication

1 Introduction

Using a variation of the Micragem (Micralyne Generalized MEMS) process, the fabrication of the micromechanical resonators was completed by the candidate at Micralyne Inc.'s fabrication facility. The device was used as a prototype run for the development of the generalized process, Micragem. Micragem is a MEMS prototyping process currently under development at Micralyne Inc. in conjunction with the Canadian Microelectronics Corporation (CMC). The goal of Micragem is to offer a set fabrication outline in which a designer can submit a design, and for which as long as the designer has followed all rules and outlines, he will receive die weeks later.

2 General Process Flow - Micragem

A basic process description is shown in Figure 4-1 [117]. Shown in a), a 525μm thick 7740 Pyrex bonding wafer is patterned and etched to the specified depth to define the beam-to-electrode gap and grooves for electrode lines. The metal is patterned using lift-off so the substrate is lithographically patterned with the wire traces, electrodes, and bonding pads. This layer consists of 500Å titanium, 500Å platinum, and 200Å gold. Then, shown in b), a silicon-on-insulator (SOI) wafer is anodically bonded device side down to the patterned side of the Pyrex wafer. The SOI wafer consists of a 525 μm single crystal silicon "handle" and a single crystal "device" layer with a sufficiently thick buried oxide separating them. The thickness of the device layer corresponds to the thickness of the beam, 2μm in the case of the standard beam. Bond alignment is not required so no compensation in design is required between the membrane and the bottom metal. The handle and buried oxide portions of the wafer are etched away in a wet process, leaving the single crystal silicon membrane over the cavities/gaps (step c). A chrome/gold layer, consisting of 100Å Chrome and 750Å gold, is deposited on the silicon

surface, and lithographically patterned. The metals are then etched to expose the silicon using a wet etch process. Finally in step d), beam structures are patterned with a photoresist mask and released with a plasma etch technique referred to as Deep Reactive Ion Etching (DRIE) or Inductively-Coupled Reactive Ion Etching (ICPRIE), which will be explained in the detailed process description. Finally, the wafer is diced and the final devices are revealed. A more complete schematic outlining this process is shown in Figure 4-2.

(a) Pattern and etch Pyrex. Pattern Metal 1 and perform lift-off

(b) Anodically bond SOI wafer to Pyrex

Legend

Metal 1	SOI buried Oxide	SOI handle layer	SOI device layer	Metal 2

(c) Etch silicon backside.

(d) Remove buried SOI oxide.
Pattern and etch low stress Metal 2.
Pattern and DRIE etch Silicon membrane to release.
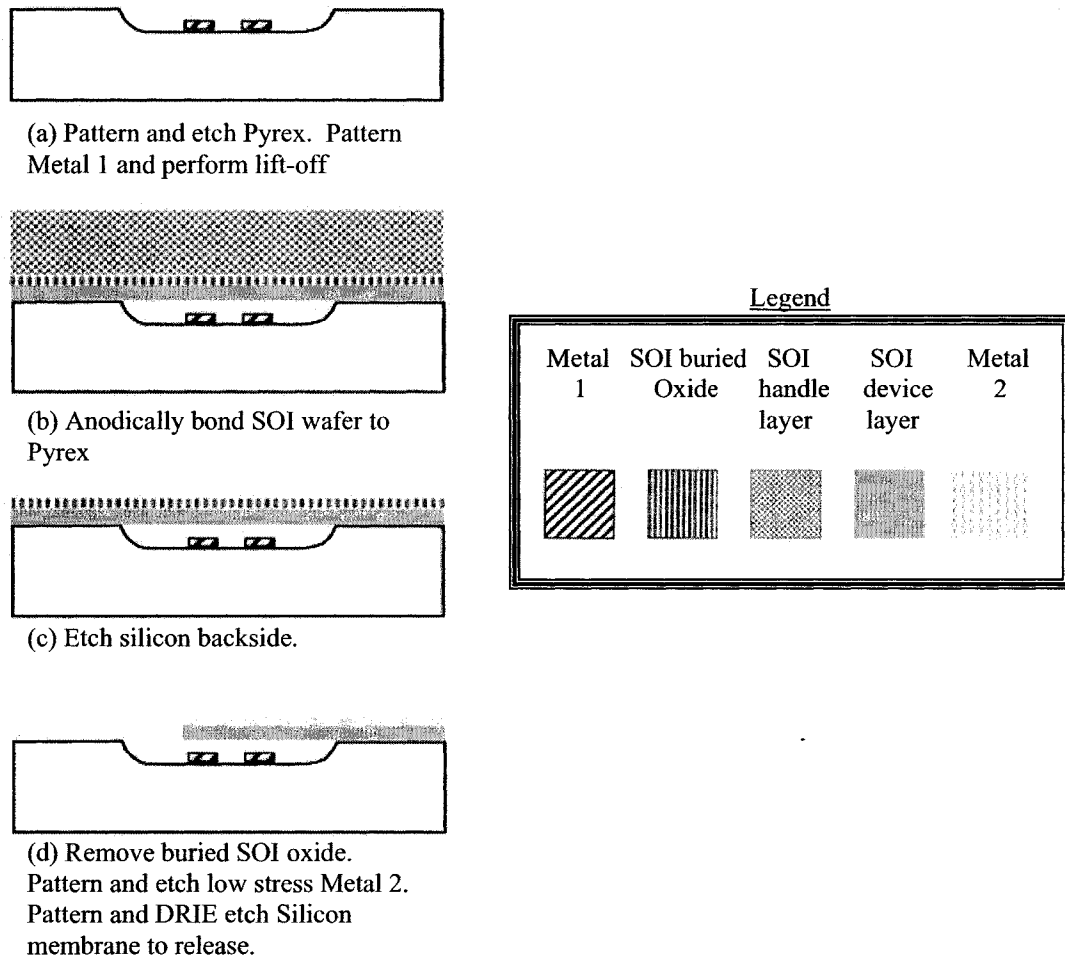
Figure 4-1: Micralyne's Micragem general process description

3 Advantages to Micragem

Single crystal silicon is a more attractive structural material for microresonators compared to polysilicon due to its low internal friction [75, 118, 119] and consequently

~72~

higher mechanical Q, low internal stress, and robustness in fabrication processes [75]. Internal friction results from a variety of physical mechanisms, including motion of lattice defects, thermoelastic dissipation (TED), phonon-phonon scattering, etc. [119].

1) Pyrex 7740
2) Wet Glass etch 2um
   -sinks metal for bond
   -creates 2um gap

3) Lift off Metal 1
   (bottom electrodes
   /wires/pads)

4) Silicon on insulater wafer
   (SOI) - ~2um device layer

5) Anodic bond glass
   to SOI device side

6) Remove handle wafer -
   wet etch (KOH)

7) Remove buried oxide
8) Sputter and pattern
   Metal 2 (top electrodes
   /wires/pads)

9) Plasma etch through device layer
   and release (ICPRIE)

Figure 4-2: Micragem process description for MEMS resonators

4 Detailed Process Description

The following section outlines the major steps within the process. Although the specific process details are proprietary to Micralyne, a generic description is included. Presented are explanations for the Pyrex cavity etch, patterning of the metal traces within the

~73~

cavities, the anodic bond, and thinning of the silicon membrane. Finally, the fully released, successful devices are unveiled.

4.1 Pyrex Etch

The ideal Pyrex etch is a wet isotropic etch, which means that the bulk etch is not preferential in any direction. However, the etch rate in the lateral direction along the surface of the glass is higher than the etch rate into the bulk. This has been attributed to film stress and adhesion effects in the etch mask layer. As illustrated in Figure 4-3, the process parameters used (with etch ratio 1~1:1.2) means that a 2.0μm etch will etch laterally ~2.4μm. Thus, with a feature size of 20μm in the Pyrex mask, the trench width is ~24.8μm.
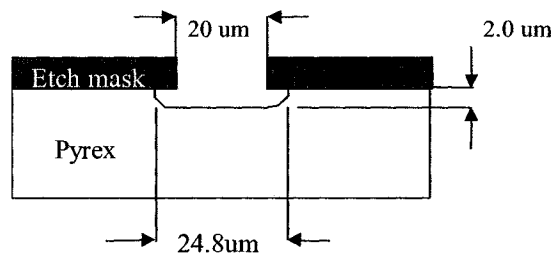
Figure 4-3: Schematic of the isotropic Pyrex etch

SEM photos of the Pyrex etch are shown below in Figure 4-4. The undercut was found to be 1:1.05 and the surface roughness is at the bottom of the etch is <10nm. This glass etch is deemed to be excellent in quality.
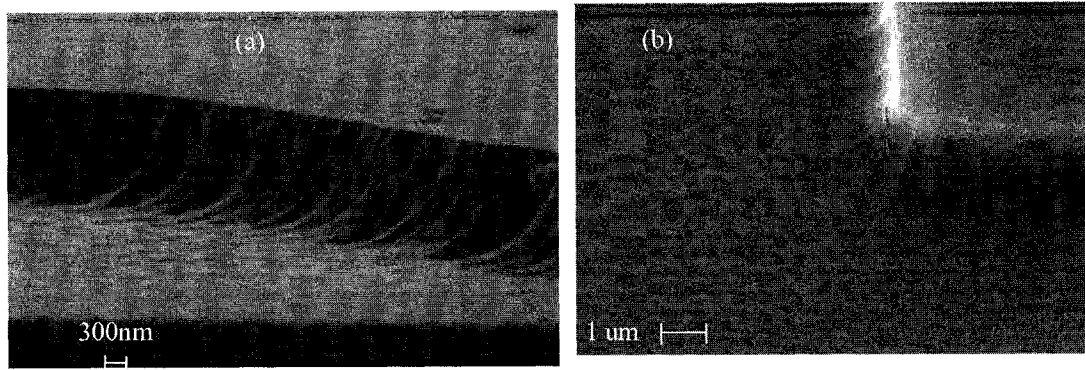
Figure 4-4: SEM photos of Pyrex etch
Photos taken with Leica Electron Optics, Model: Leo 435VP

Within the semiconductor manufacturing society there has been substantial effort devoted by researchers to studying the etching behaviour of silicon dioxide, quartz, and multicomponent glasses such as borofloat, Pyrex or soda lime glasses. The most commonly used etch chemistry is HF based [120] and different masking methods such as resist based [120-122] or Cr/Au metal combinations [123, 124] are utilized. The multicomponent glasses such as the Pyrex used in this work do not only contain SiO_2, but also contain NaO_2, CaO, MgO and small amounts of Al_2O_3 [120]. The presence of these constituents significantly increases the etching rate in HF-containing solutions [125].

4.2 Bottom Electrodes – Lift off

Figure 4-5 shows the steps of the lift-off process for the Metal 1 layer, which defines the bottom electrodes, wire traces, and bonding pads. Photoresist is patterned and Metal 1 is deposited via a sputtering process with an initial base pressure of 1.9×10^{-7} Torr. This base pressure is low enough to ensure good adhesion and to ensure that the metals do not oxidize as they travel from the target to the substrate (i.e. a good quality metal layer is expected.). The photoresist is then removed (partially removed in (a) and fully removed in (b) in the figure) and the metal edges taken off with a pressure washer (shown in (c) of the figure), leaving the patterned metal behind. As seen in the figure, the roughness of the patterned metal is due to the underlying roughness of the Pyrex and not from the metal because the metal is shown as very smooth on the patterned photoresist.

~75~
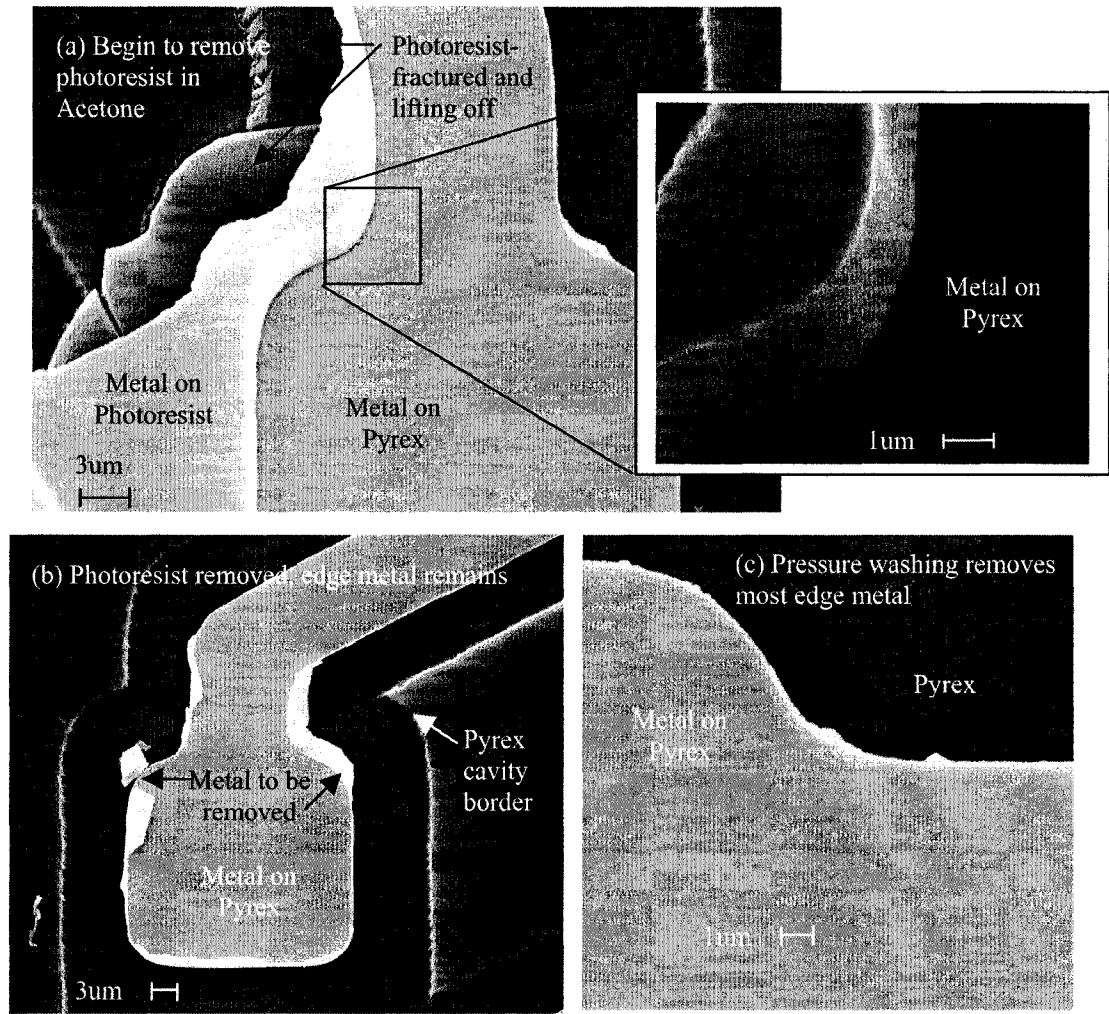
Figure 4-5:SEM of metal 1 "lift-off"
(a) Begin to dissolve photoresist after short immersion in acetone (b) Complete removal of photoresist (c) Pressure wash for edge metal removal. Photos taken with Leica Electron Optics, Model: Leo 435VP

SEM photos of the final Metal 1 patterning before bonding are shown below in Figure 4-6.
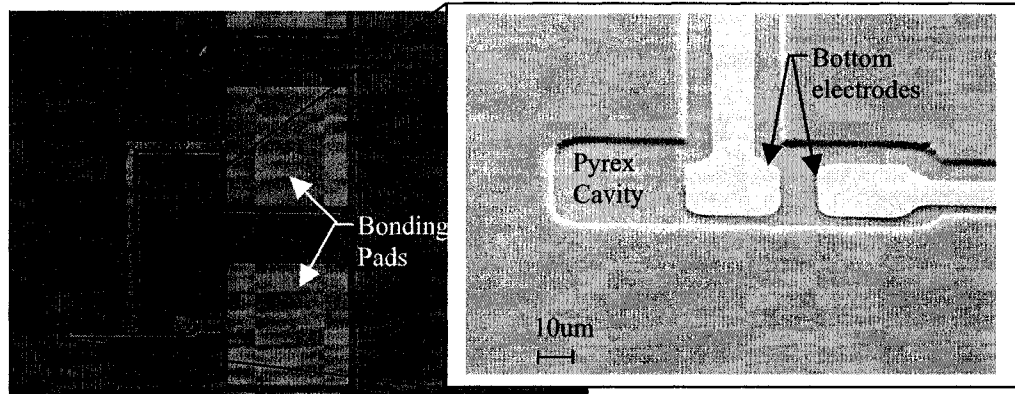
Figure 4-6: Completion of metal 1 lift-off
Photos taken with Leica Electron Optics, Model: Leo 435VP

4.3 Anodic Bonding

Anodic bonding is used to fuse the SOI wafer to the patterned Pyrex wafer.

4.3.1 General

Anodic bonding, also referred to as electrostatic bonding, bonds a conductive substrate (a SOI wafer, in this case) to a sodium-rich glass substrate (Pyrex, in this instance). The bond, assisted by an electric field and created at low temperature (350-450°C), results in low residual stress. The set-up for the bond is shown below in Figure 4-7.
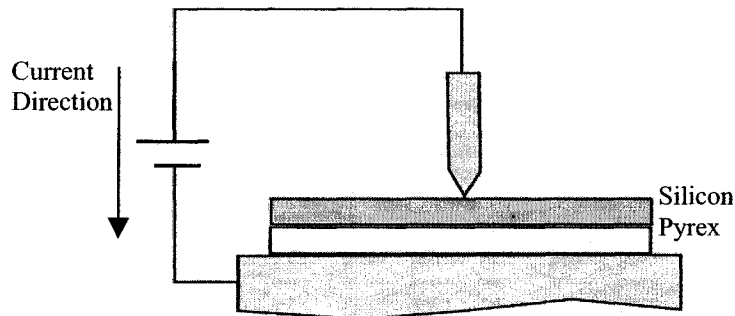
Figure 4-7: Set-up for anodic bond

Before the anodic bond is carried out, the substrates are put into direct contact, creating a "contact bond" through van der Waals forces between the Pyrex wafer and the silicon surface. This is done to tack the two wafers in place in order to ensure clean surfaces and a quicker, stronger anodic bond [126]. The bonded wafers are then placed on a

~77~

hotplate with the silicon side down and heated to ~300°C, which mobilizes the sodium ions in the glass. This temperature is also the crossover point for the thermal expansion between Pyrex 7740 and silicon [127]. A high voltage (500-1200V) is then applied between the two wafers with the negative on the glass, as shown in Figure 4-7 above. The sodium ions are repelled from the interface and an ion-depletion region is created (~1μm thick). In other words, positive ions migrate to the cathode, and negative oxygen ions toward the anode [127]. This creates an electrostatic pressure, which pulls the two substrates together. In areas where the silicon is in contact with the glass, oxygen produced during the anodic bonding process will oxidize the silicon into the glass and form the anodic bond [127].

4.3.2 Contact Bonding

It is well known that the more hydrophilic the surfaces before the contact bond, the stronger the bond will be. The hydrophilicity of a silicon surface can be measured by the contact angle between water and the surface. Figure 4-8 is a schematic of the concept of contact angle, θ. Different treatments of the surfaces before contact bond cause different levels of hydrophilicity, thus causing different contact angles. The more hydrophilic a surface, the lower the measured contact angle is.
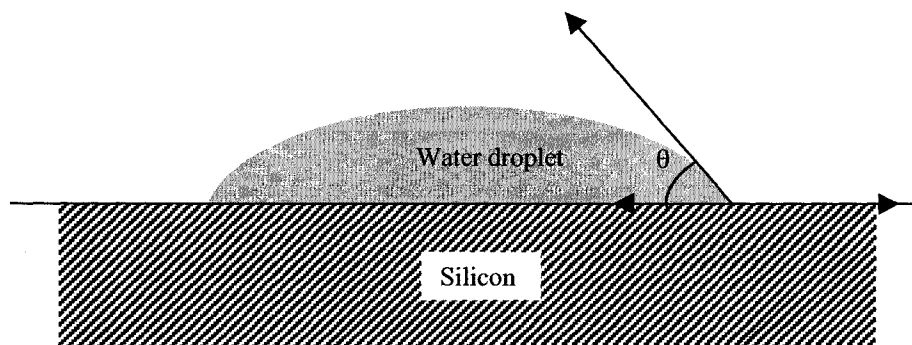
Figure 4-8: Concept of contact angle measurements for hydrophilicity

Shown below in Figure 4-9 is a representation of the measured contact angles for different surface treatments of silicon [128]. Potassium Hydroxide, KOH, is a good choice for a surface treatment because it is safe, effective, and etches silicon at a very low

~78~

rate at room temperature. KOH is the chosen surface treatment for the contact bond in the Micragem process for this reason.

Measured contact angle of water with Si surface prepared by various surface treatment methods
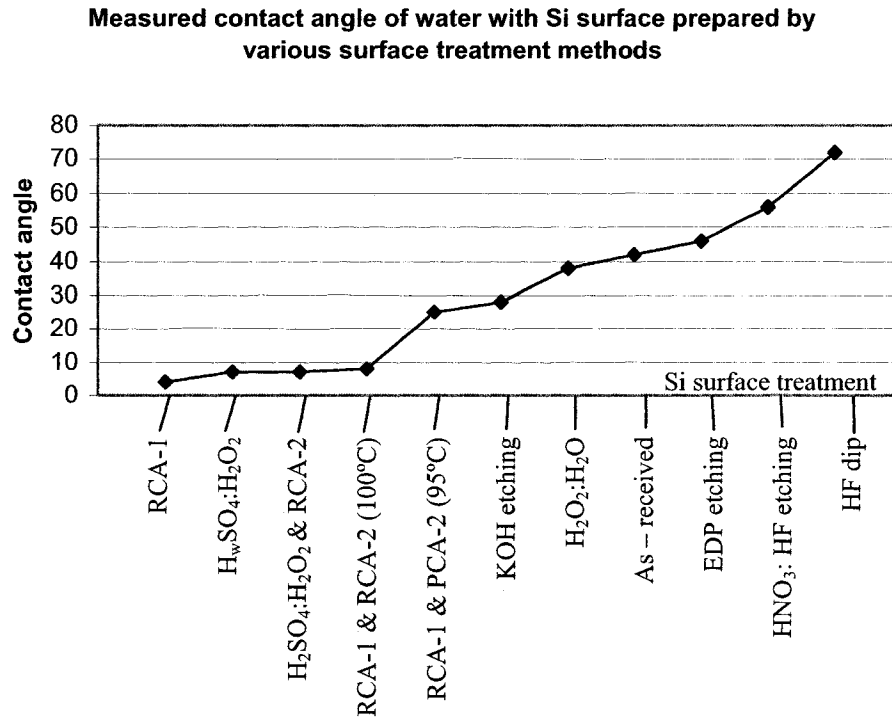
Figure 4-9: Representation of measured contact angle with Si surface prepared by various surface treatment methods
Graph recreated from [128]

4.4 Thinning of Silicon

4.4.1 Iteration #1

Initial fabrication of the beams, termed iteration #1, created 4μm thick beams, separated by a 1μm gap utilizing Micragem. However, to reduce costs, a 15μm-thick device layer SOI is thinned down with a wet etch process (refer to (c) of Figure 4-1) to achieve the desired 4μm thickness of the membrane. The undersides of the beams (inside the Pyrex cavities) are intended to be sealed from any chemicals during this stage; however, membranes broke during this processing step, exposing the undersides of the beams to further, multiple wet etching steps, leaving damage/debris between the beams and the bottom electrodes. Particles cause electrical shorts between the beam and bottom

~79~

electrode during actuation. Destruction of the devices is necessary in order to take pictures of the undersides of the beams. The beams were "pulled" off with conductive tape and SEM pictures of the undersides of some cantilever beams are shown below in Figure 4-10 and 4-11.
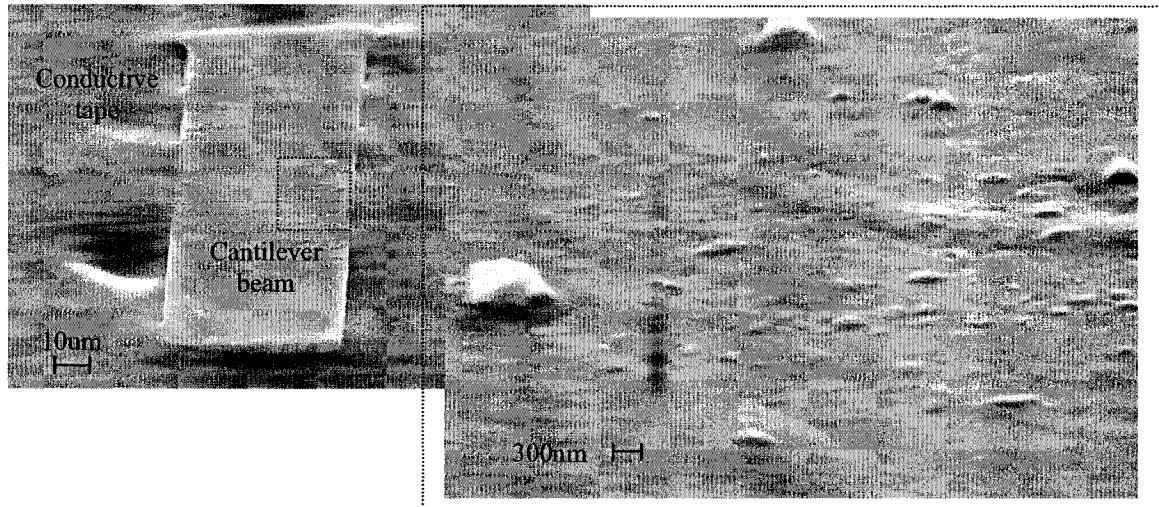
Figure 4-10: SEM of underside of the beam (b) close-up of debris
Photos taken with Leica Electron Optics, Model: Leo 435VP

This debris, although not on all devices of this fabrication run, causes a level of uncertainty during the troubleshooting of testing and characterization steps following the fabrication because it is impossible to tell which of the cantilevers are affected unless destruction of the device is done and the undersides analyzed in the SEM. Upon preliminary testing and partially due to this problem, it was decided to fabricate a second iteration using a 2μm SOI and a 2μm gap.

4.4.2 Iteration #2

The main reason for the second iteration was to increase the gap size to alleviate overdamping effects. This will be discussed with the experimental results of Chapter 8. However, by using a 2μm device layer SOI, the thinning step was thus eliminated and the problem removed. The "standard beams", referred to throughout this thesis, are from this

~80~

second fabrication run. The completed beams are shown in Figure 4-11. The surface shown in the figure is the underside of the beam and the sample was prepared similarly to that of Figure 4-10 where the beam was "pulled off" with conductive tape.
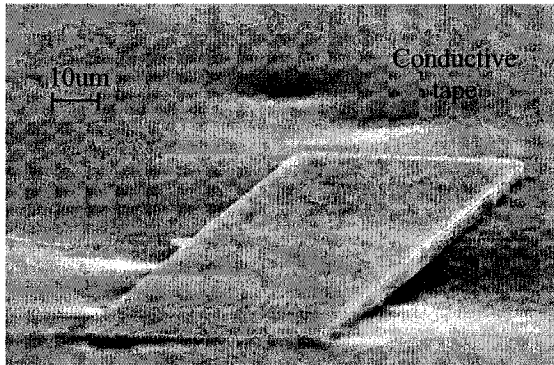
Figure 4-11: SEM of underside of clean beam
Photo taken with Leica Electron Optics,
Model: Leo 435VP

4.5 Final Release

Upon patterning of the top metal layer, the final silicon-masking layer is patterned and the exposed silicon etched in an Inductively-Coupled Reactive Ion Etcher (ICPRIE or DRIE). The ICPRIE is a high aspect ratio, deep trench silicon etching process. Also known as Bosch etching, the process relies on alternating cycles of ion-assisted chemical etching (SF_6) and polymer deposition (C_4F_8) to achieve parallel sidewalls. The main principle of the deep trench silicon process is the alternating of fluorine based etching and passivation of the structures. This results in sidewall profiles of nearly 90° and with aspect ratios of up to 40:1. The final, released cantilever beams are shown below in Figure 4-12. The left image shows the cantilever beam design and the right shows a fixed-fixed beam design. The fabrication of the cantilevers are deemed successful because they are not broken, are clean from particles (other than the debris caused by the prematurely leaking membranes on the first run), and there are no stiction effects. The static and dynamic testing of these devices is described in Chapter 5 and Chapter 8, respectively.
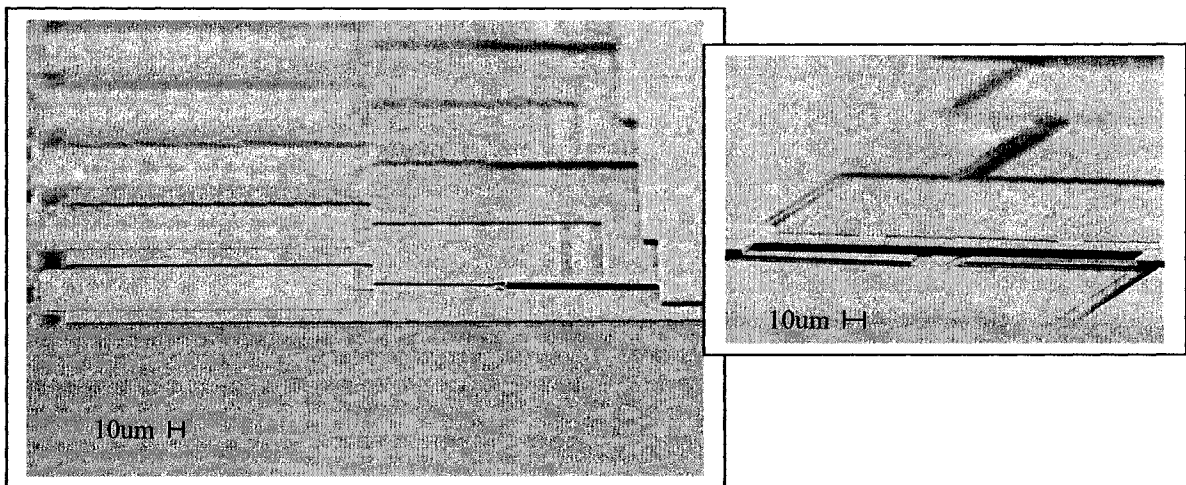
Figure 4-12: Final release of structures
Photos taken with Leica Electron Optics, Model: Leo 435VP

5 Characterizing Dimensions

Upon fabrication, characterization of the dimensions is essential to achieve accurate theoretical predictions. Fabrication variations, with respect to lithography, metal deposition, and etching, cause discrepancies in the intended mask and process design. For example, a difference in length of the cantilever beam of $5\mu m$ (due to lithography or etching undercut) can increase the resonant frequency by 3kHz.

5.1 Pyrex Etch Depth Measurements

The Pyrex etch depth is characterized in two ways. Profilometer measurements taken across the entire wafer give an across wafer variation measurement. Also, a cross section is analyzed in the SEM, as shown in Figure 4-13. In the figure, the metal trace within the cavity and the cavity cross sections are measured. The sidewall profile due to the isotropic Pyrex etch, discussed above in this section, is also apparent to the right. Both the profilometer and the SEM measurements agree with each other. However, the profilometer measurements are preferred over taking a SEM sample because they are non-destructive; thus, variations of the final etch depth across a wafer are found.

~82~
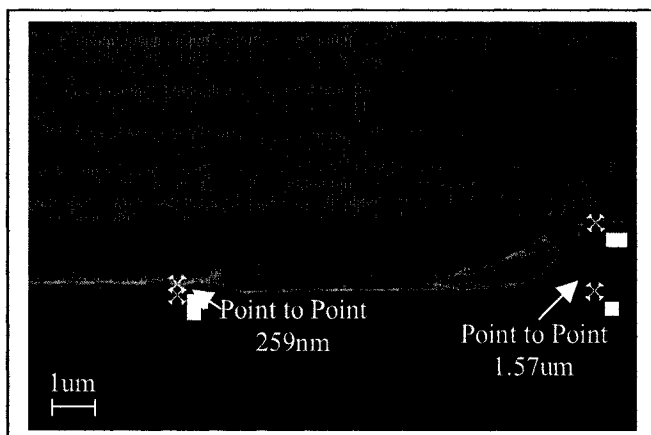
Figure 4-13: Side profile of metal 1 and Pyrex etch
Photo taken with Leica Electron Optics, Model: Leo 435VP

5.2 Layer-to-Layer Alignment

Mask alignment between Metal 1 and the Pyrex etch is characterized although it is not critical to the device performance. These numbers give an idea as to the alignment between the bottom electrodes and the cantilever beam as this alignment is difficult to analyze once the device is fabricated. As shown in Figure 4-14, the horizontal misalignment is 1.5μm and the vertical misalignment is 1.1μm, which is typical of optical lithography. The misalignment is characterized using the SEM.
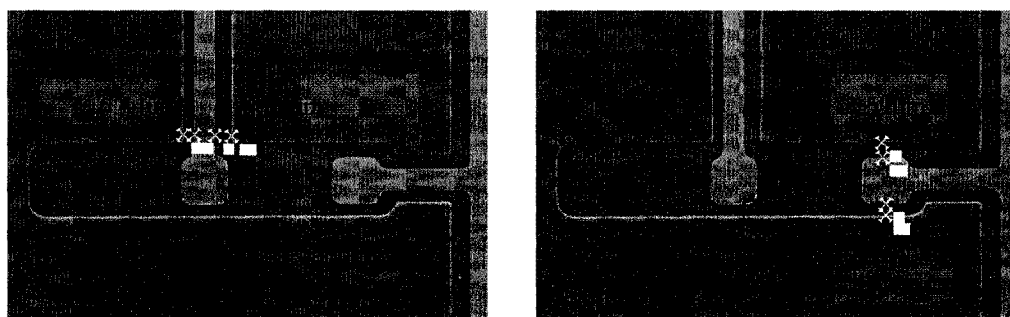
Figure 4-14: Misalignment characterization
Photos taken with Leica Electron Optics, Model: Leo 435VP

~83~

5.3 Thickness of Silicon

Completed devices are analyzed in the SEM for final gap and membrane measurements, as is shown in Figure 4-15. In the figure, the image's view is at the end of the beam. The membrane measurements are deemed to be accurate; however, the gap measurements are not accurate because charging within the SEM causes the beam to become attracted to the bottom electrodes and eventually, enough electrostatic force is accumulated to fully actuate the device. Because of this dynamic situation, another way to measure the beam-to-electrode dimension is required. This is solved by use of an optical profilometer and is further discussed in Chapter 5.
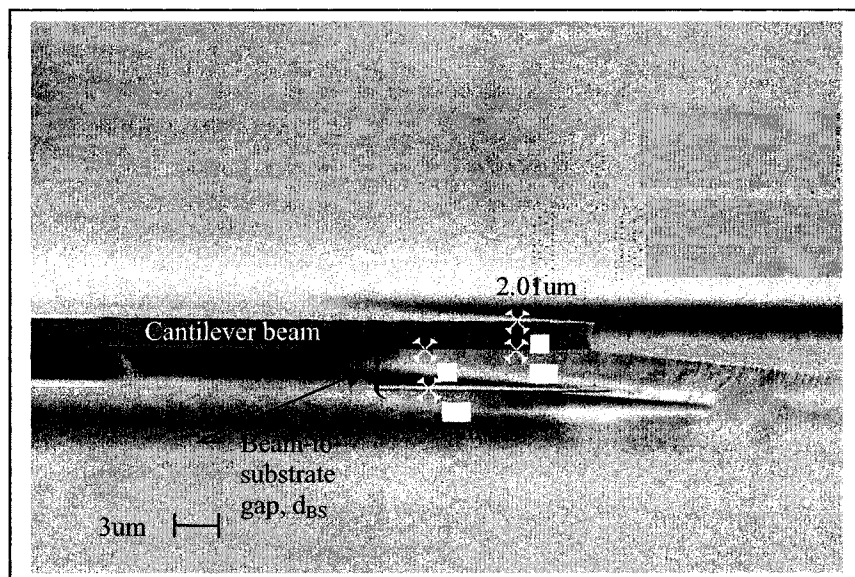
Figure 4-15: SEM profile taken at end of cantilever
Photos taken with Leica Electron Optics, Model: Leo 435VP

6 Conclusion

The fabrication of the devices discussed in this work was built using Micralyne's Micragem. As well, each major step is described in further detail with SEM photos illustrating the process. Micragem is now offered through the Canadian Microelectronics Corporation to academia across Canada. Micragem has been proven to be a reliable process, and with further development, has the potential to be a reliable prototyping process for both academic and industrial environments.

~84~

Chapter 5 – Beam Testing

1   Introduction

This chapter presents the initial testing of the cantilever beams. Static testing for characterization of the beam's movement with respect to the voltage potential is first presented, and the actuation voltage is found using this method. Attempts to measure the induced current due to the change in capacitance caused with the beam's motion (discussed in Chapter 3) are explained. Improvements to the electrical testing set-ups were numerous and are discussed in the chapter including reasons why electrical measurements are not possible with the current set-up. In addition, an equivalent electrical circuit is introduced, where an impedance analysis of the device is presented.

2   Static Testing

Actuation voltages are found by applying an increasing voltage potential between the beam and the bottom electrode while characterizing the movement with an optical profilometer.   The optical profilometer used is the Zygo New View 5000 at the University of Alberta's Nanofab. The Zygo was not fitted with electrical testing, so the equipment is retrofitted with probes.

2.1 Introduction to the Optical Profilometer (Zygo)

The Zygo NewView 5000 is a commercially available surface metrology tool based on scanning white-light interferometry. Light is split inside an interferometer with one beam being reflected off a stationary reference surface and the other off the sample. The reflected, recombined light produces destructive and constructive interference, which appears as light and dark lines (fringes) resulting from an optical path difference between the two light beams. The Zygo uses full three-dimensional aerial surface measurement, a precision vertical scanning transducer and camera to generate a three-dimensional interferogram of the surface. The interferogram is then processed by the computer and

~85~

transformed by frequency domain analysis, which results in a quantitative 3-D image[129]. It boasts a vertical resolution of 0.1nm! However, this tool is only useful for static measurements because of the time-consuming, calculation intensive approach to 3-D profilometry. Each measurement takes tens of seconds to analyze; thus, frequency response with respect to displacement measurements is not an option with this tool.

2.2 Calibration of the Zygo

To calibrate the instrument (Zygo), the height of the beam is measured and compared to the measurements taken with the SEM discussed in Chapter 4. The optical profilometer measurement of the iteration #1 device (4μm beam, 1μm gap) is shown in Figure 5-1. The scan is over the step from the glass surface to the silicon/metal 2 layer (its location is illustrated in (a)), and the results from the Zygo are traced and shown in (b). The bump in the scan on the silicon/metal 2 surface is thought to be a particle.
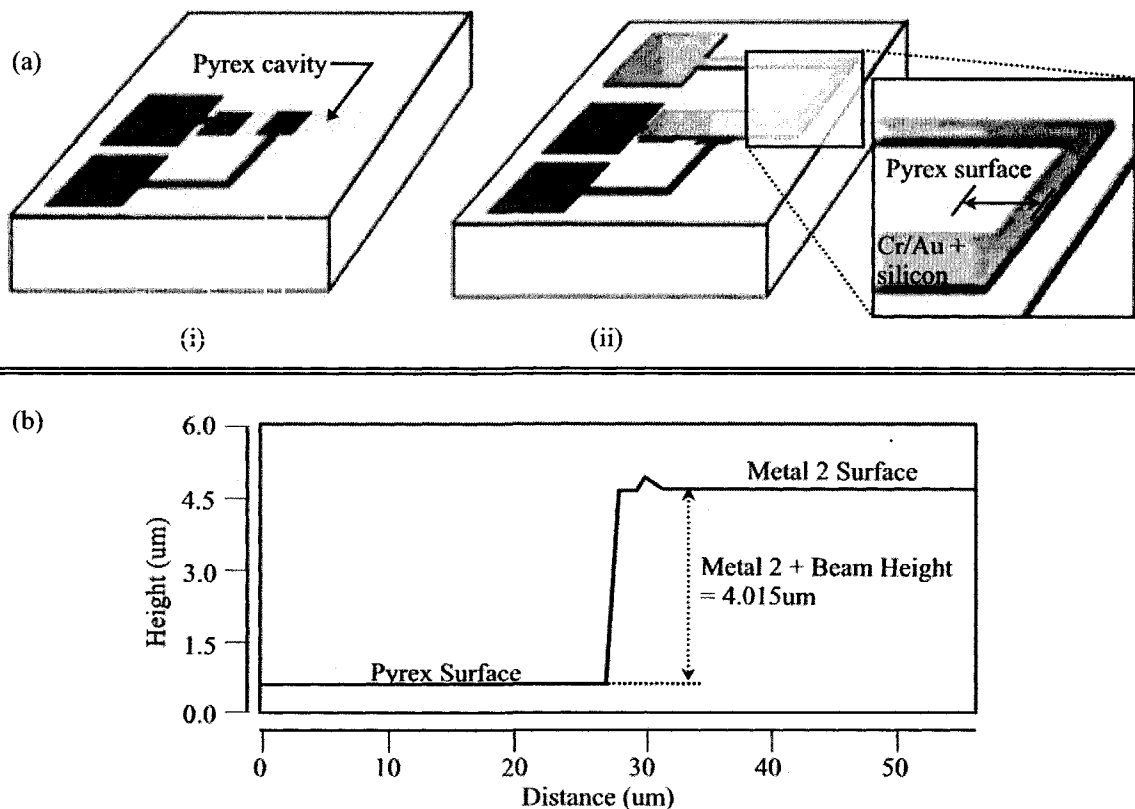
Figure 5-1: Optical profilometer (a) Scan location (b) surface profile results
(i) View of Pyrex cavity underneath Silicon layer (ii) Arrows indicate scan location from Pyrex surface to top of silicon / metal 2 layer

~86~

From Figure 5-1 (b), the measurement of the thickness of the silicon + metal 2 (Cr/Au) layers is 4.015 μm. When compared to the SEM image of the beam, shown in Figure 5-2, the thickness is found to be 4.12 ± 0.1 μm, and thus, the two measurements are consistent, so one may conclude that the Zygo provides accurate step heights. (However, in practice, measuring relative heights between different materials is difficult).
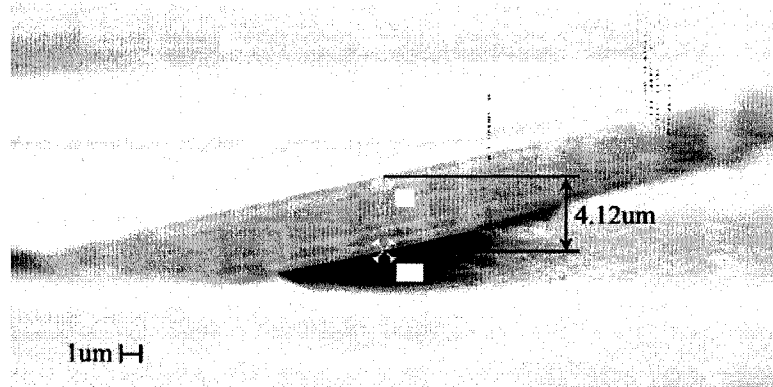
Figure 5-2: SEM of iteration #1 measuring beam thickness
Photos taken with Leica Electron Optics, Model: Leo 435VP

2.3 Film Stress Measurements

Film stress analysis is done for the Cr/Au reflective surface of the cantilever beams. Even though no external forces are applied to the cantilever, internal or residual stresses in the film cause the cantilever to bend. The stress values are extracted using the Stoney formula (see below) and measurements, such as Radius of Curvature (ROC) and tip displacement, taken with the Zygo. ROC measurements are a standard of measuring the curvature in a material (or stack of materials) as a way of measuring residual stresses in the material (Refer to Figure 5-3) and can also be related to displacement at the tip of the beam. Stress in the top Cr/Au film of this work is found from measuring either the radius of curvature or the deflection of the beam.

The free-body diagrams of the film and substrate composite beam with indicated end moments are shown in Figure 5-3. Further analysis shows an element of the composite

~87~

beam to have the net force vanishing on the film-substrate cross-section because of mechanical equilibrium, thus [130]:

$$F = \int \sigma dA = 0$$
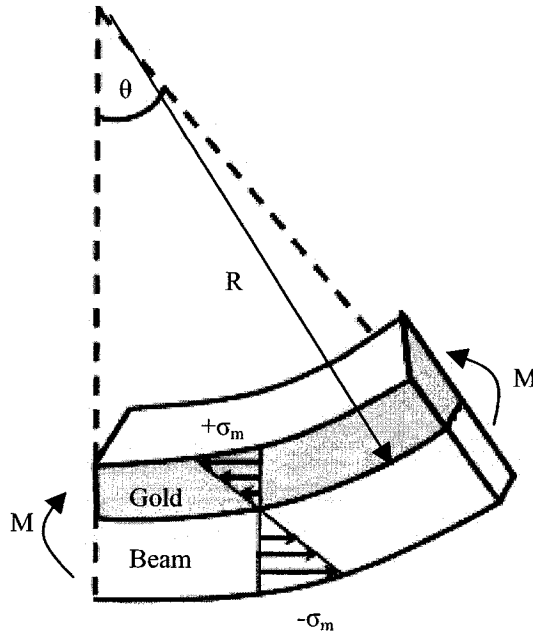
Where A is the sectional area and σ is the stress. Basically, at any cross section of the beam, the stress distribution across the beam must equal zero. From this, it is seen in the figure that the stress distribution across the section of the beam varies linearly from maximum tension $+\sigma_m$ at the top surface of the gold to maximum compression $-\sigma_m$ at the bottom of the beam. The neutral axis occurs at some point in the cross section and is the point of no stress.

Figure 5-3: Free body diagram and stress distribution of bi-material beam

Derivation of the Stoney formula is done with reference to Figure 5-3 and the assumption that the thickness of the thin film is less than that of the substrate. In addition, the cantilever's width-to-thickness ratio is considered large (~13) so the cantilever acts more like a plate, meaning biaxial stress must be assumed. To compensate for the plate-like behaviour, Poisson's ratio, v, is included and the elastic modulus, E, is replaced with $[E/(1-v)]$. By using a measured radius of curvature, R, and the Stoney formula, film stress, σ_f, is found by [130]:

$$\sigma_f = \frac{1}{6R} \frac{E_s d_s^2}{(1-v_s)d_f}$$

~88~

Where:

E_s = Young's modulus of substrate, 1.295 x 10^{11} Pa for Si

v_s = Poisson's ratio, 0.22 [*unitless*] for Si [95]

R = Radius of curvature [m]

d_s = thickness of substrate (silicon) [m]

d_f = Thickness of film (Cr/Au) (80 x 10^9 m for all beams)

The ROC measured by the Zygo is –3.04 x 10^{-2} m and is shown in the Figure 5-4, where (a) is the 3D image and (b) shows the side, surface profile of the beam along the length of the scan (noted along the beam in (a)). The ROC measurement from the Zygo is the distance from the surface of the beam to the centre of the curvature. This differs slightly from the assumption of the Stoney formula where R is measured to the neutral axis of the bi-material beam. However, because the film is much thinner than the beam, the difference between the surface and the neutral axis is negligible. For the 4μm thick standard beams (3.5μm measured thickness for beam used in calculation), and by using Equation 5-2, the film stress is 144 MPa ± 40 (tensile). The error in the value is found by incorporating the silicon thickness measurement error (±100nm), the thin film thickness measurement error (±10nm), and the ROC measurement error (±0.3cm).
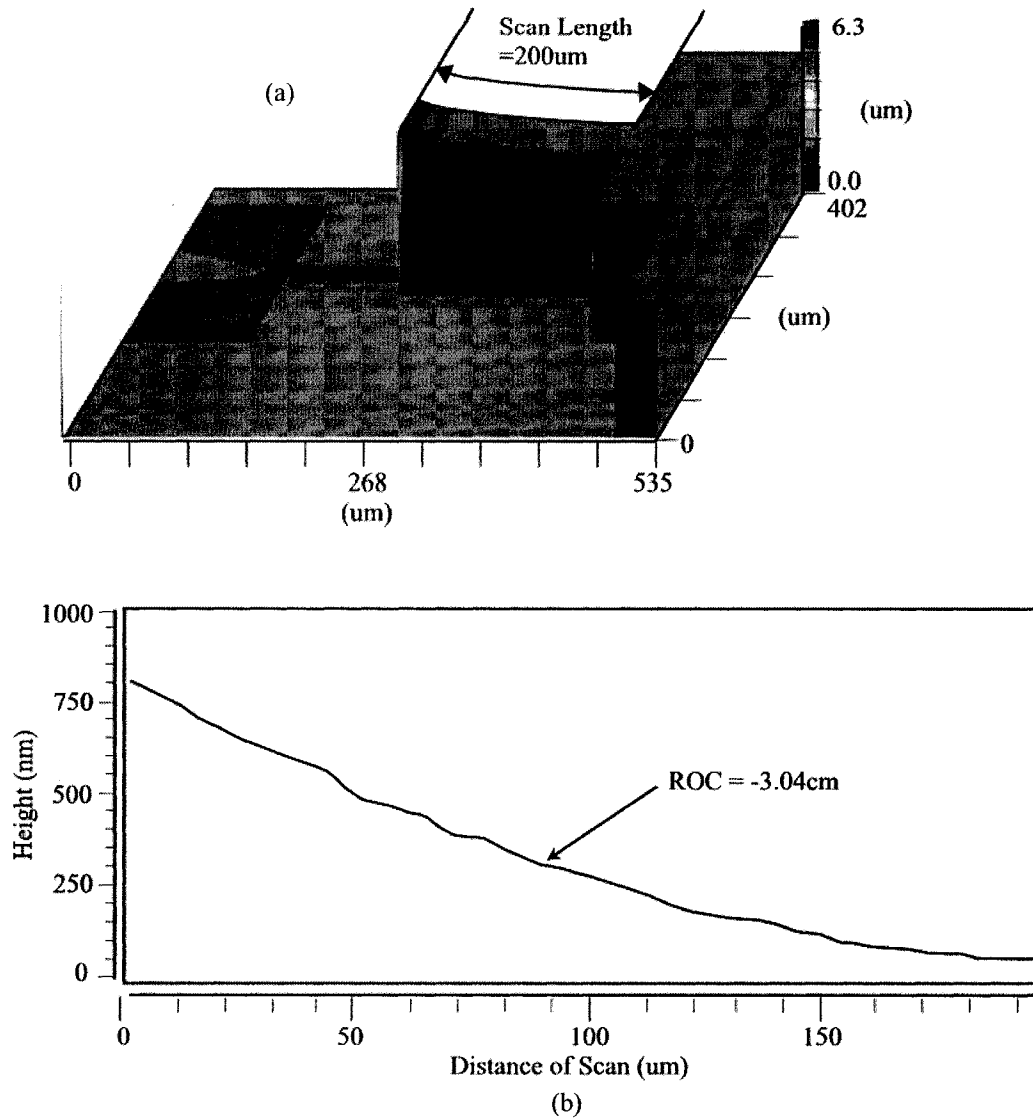
Figure 5-4: Radius of curvature measurement taken with the Zygo
(a) 3D plot of cantilever beam of t=4μm, l=200μm (b) Surface profile of cantilever beam

A second approach is used to determine the film stress using the fact that the ROC is related to the displacement at the tip of the beam by $\delta = l^2 / 2R$. The Stoney formula for film stress using deflection at the tip of a beam is [131]:

$$\sigma_f = \frac{\delta E_s d_s^2}{3l^2(1-v_s)d_f}$$

Equation 5-3

~90~

The Zygo is used to determine the deflection at the tip of the same beam that is shown in Figure 5-4. The side profile for a scan length 20μm longer than the beam's length is used to measure the deflection at the tip of the beam. The deflection of the tip of the beam due to film stress is found to be 817 ± 100 nm, and is shown below in Figure 5-5. Using the measurement shown in Figure 5-5 and Equation 5-3, the stress is calculated as 178 ± 46 MPa (tensile). The error in the value for this method is found by incorporating the silicon thickness measurement error (±100nm), the thin film thickness measurement error (±10nm), and the deflection measurement error (±60nm). The results of film stress methods of Equations 5-2 and 5-3 are comparable, and it is deemed that either method of analysis is acceptable for an estimation of film stress.
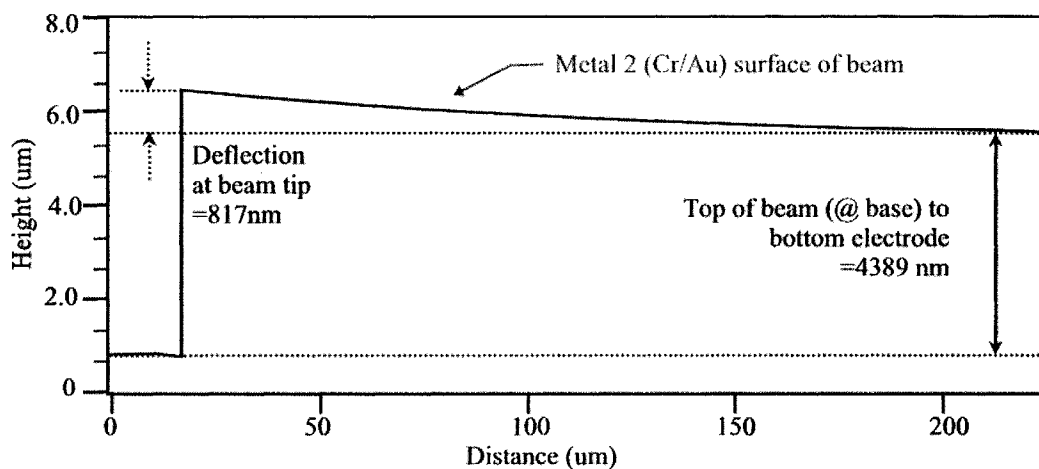
Figure 5-5: Surface profile of cantilever beam taken with the Zygo (t=4 μm, l=200 μm)

The deflection at the tip of the beam due to film stress is measured as 2847 ± 100 nm (Figure 5-6), and, by using Equation 5-3, the film stress is found to be 197 ± 49MPa (tensile). When comparing the two displacement methods for analysis, the film stress in the Cr/Au metal layer for the two iterations of beams (4μm thick and standard beams) is within error; thus, it can be deduced that the sputtering conditions are repeatable.
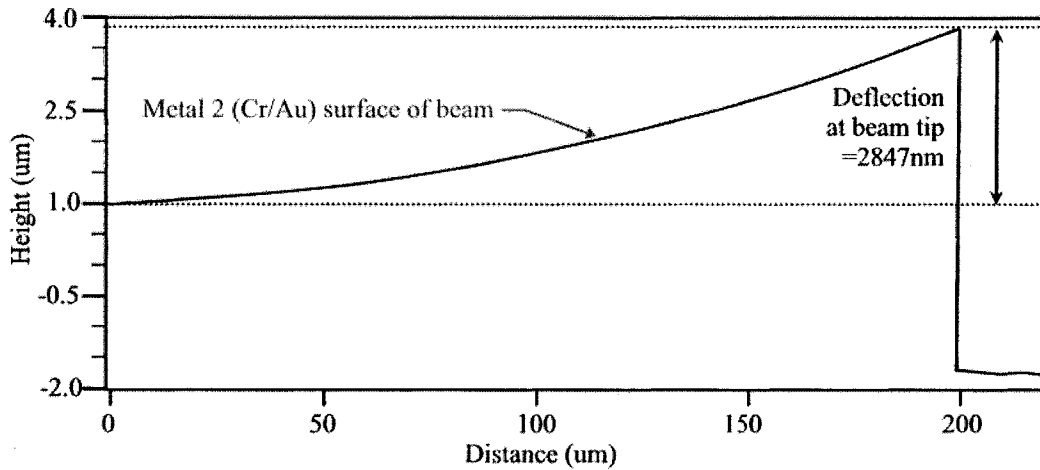
Figure 5-6: Surface profile of standard beam taken with the Zygo

2.4 Voltage Vs. Displacement Testing

Multiple beams are tested for static deflection, and they are found to sustain a maximum applied voltage potential between the beam and bottom electrode of between 21-25 ± 0.1V. The optical profilometer is used to take an image as the applied voltage is increased until actuation occurs. This *threshold voltage* (first introduced in Chapter 3) is found to be very much in accordance to the theoretical, expected value of 19.4V calculated in Chapter 3. Figure 5-7 below is a schematic of the set-up. Connection to the upper and lower electrodes is made with probes. Both the applied voltage and the voltage across the beam are measured by a Fluke 73 III Multimeter as a way to monitor current with increasing voltage, a concept discussed in the next section. Also, a 100kΩ resistor is in series with the beam to act as a current limiter to protect the device from rapid, high currents upon actuation. The resistor also acts as a way to monitor leakage current or shorts that may occur with the device.

~92~
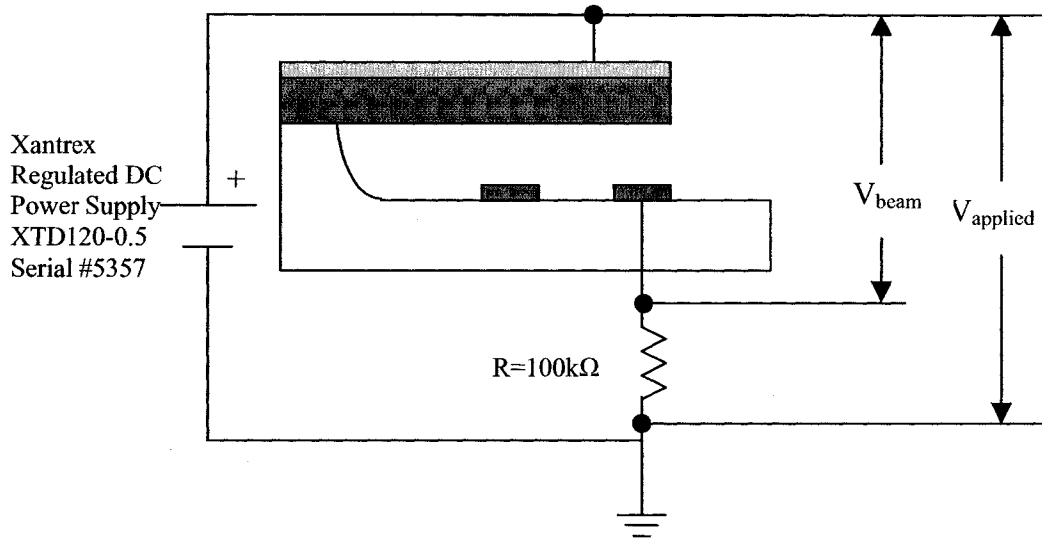
Figure 5-7: Schematic for DC testing

Figure 5-8 below is a graph of the distance measured between the tip of the beam and the bottom electrode with increasing applied voltage for a standard beam. These measured displacements are compared to the theoretical displacements calculated with Equations 3-8 & 3-9. Experimentally, the initial distance between the tip of the beam and the bottom electrode is expected to include the thickness of the upper electrode, the thickness of the beam, and the initial gap. This is expected to be ~5μm for iteration #1 and ~4μm for iteration #2 plus any initial stress causing deflection at the tip of the beam. The initial distance is found to be 5654nm for the iteration #1 beam and 5094nm for the standard beam (iteration #2). The deflection at each applied voltage is then found from the difference in this initial beam tip to bottom electrode distance at no applied voltage and increasing applied voltage.

2.4.1 Iteration #1

As was described in Chapter 4, the first iteration contained debris on the undersides of the beam, which caused problems during static testing. Shown in Figure 5-8, is the voltage versus displacement curve for a cantilever beam fabricated during iteration #1. The curve loosely follows the expected trend until ~40V_{DC}. However, upon additional applied voltage, the trend varies significantly. Complete actuation was not possible for beams

~93~

with debris. The explanation for this is that the debris on the underside of the beam makes contact to the bottom electrode before actuation and causes ever-increasingly leakage currents, reaching the limit of the power supply. It is difficult to deduce beam behaviour from the iteration #1 beams because the response in Figure 5-8 is representative of a typical result.

Deflection vs. Applied Voltage for Iteration #1
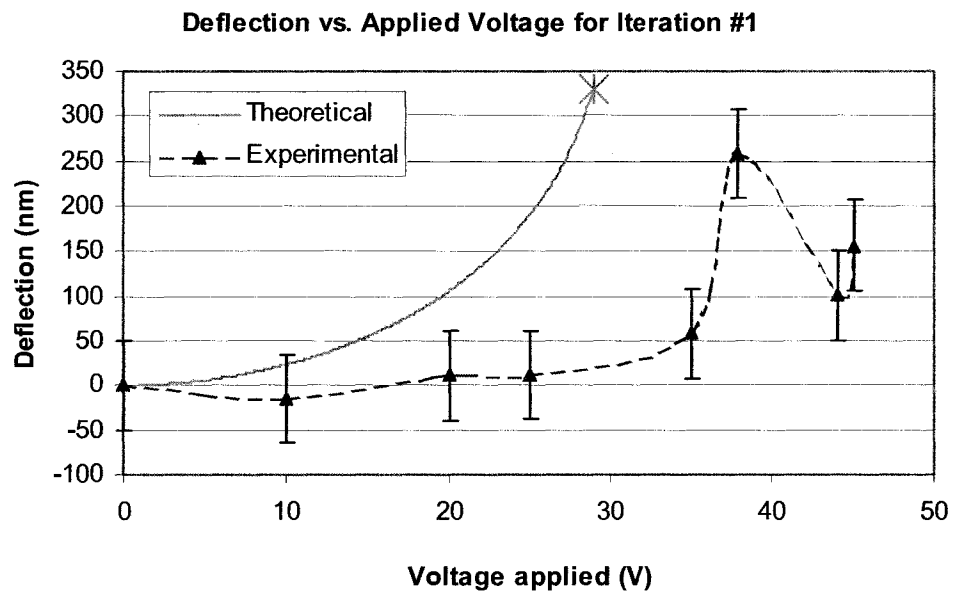
Figure 5-8: Deflection versus applied voltage for iteration #1
Theoretical graph from Equations 3-8 & 3-9

2.4.2 Iteration #2

The experimental result of Figure 5-9 is for the standard beam (iteration #2) and shows a similar trend as the analytical calculation (i.e. deflection increases with applied voltage). However, the threshold voltage is found to be 24V, which does not coincide within error to the analytical model (theoretical = 19.4V_{DC}), and actuation occurs at a deflection of 826nm from initial state (theoretical = 667nm). The fact that the beam starts out with a film stress-induced curvature and the analytical result did not account for any film stress is expected to be the difference in the threshold voltage. In addition, repeatability in the measurement was found to occur within 100nm with respect to displacement, and this is represented with error bars in the figure.

~94~

Deflection vs. Applied Voltage for Standard Beam
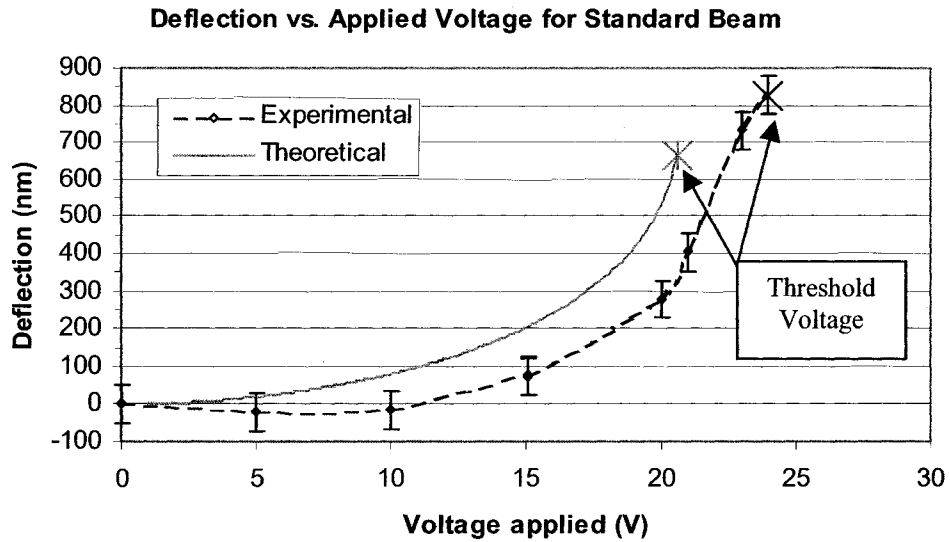
Figure 5-9: Deflection versus applied voltage for standard beam
Theoretical graph from Equations 3-8 & 3-9

Although the Zygo is thought to give accurate measurements with respect to the changing distance measured, the Pyrex surface is being measured inaccurately because of the difference in reflectance between the Pyrex (~3%) and the gold surface (~99%) of the cantilever beam. Shown below in Figure 5-10 is the Zygo measurement. The Pyrex surface is shown to be higher than the bottom wire trace, which is known to be false. However, because measurements were taken between the top surface and the bottom wire trace and because both surfaces are gold, the distances measured are thought to be accurate.

~95~
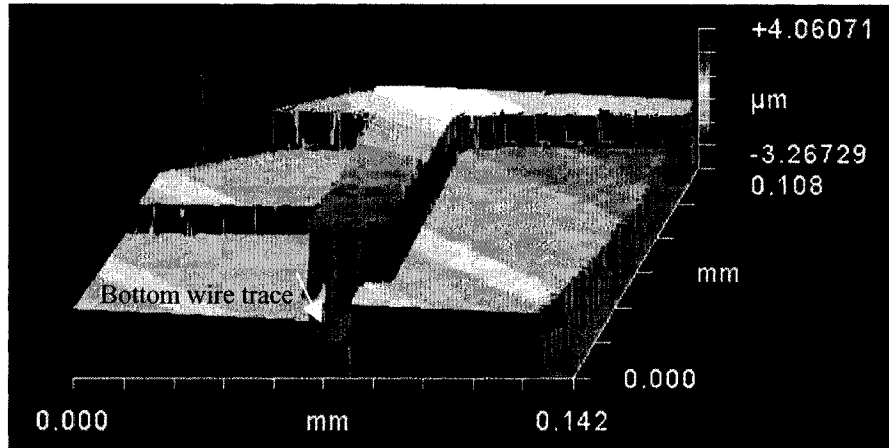
Figure 5-10: Optical profilometer image for standard beam with no applied voltage

The characterization method of using the Zygo is very good at determining the actuation voltage. Visually, with aid of the Zygo, it is very obvious when the beam deflects its full amount. A fully deflected cantilever is shown below in Figure 5-11 to be compared with the undeflected beam in Figure 5-10. Also, by monitoring the voltage drop across the resistor shown in Figure 5-7, (essentially, measuring the current through the circuit), the current increases rapidly when actuation occurs, creating a short. Monitoring current is discussed further in the next section.
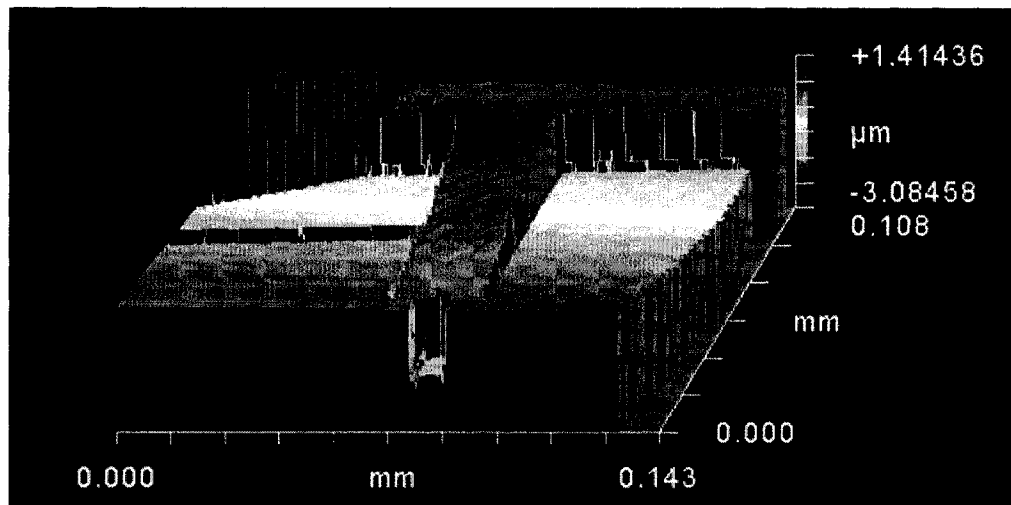
Figure 5-11: Optical profilometer image for actuated standard beam (V_{TH} applied)

~96~

2.5 Leakage Current

The leakage current is monitored through the circuit shown above in Figure 5-7. With each voltage applied, the voltage potential across the beam and the voltage drop across the resistor are measured for two standard beams. By monitoring the voltage applied across the beam and the voltage drop across the resistor, the current is deduced. Table 5-1 below shows the results for two standard beams. A standard error analysis is done for the current calculation. This includes the resistor $(97.9 \pm 0.59 \text{ k}\Omega)$[**] and the errors in the measurements of the voltages[††] (V_{Beam}, $V_{applied}$) with the Fluke 73 III multimeter.

Table 5-1: Voltage Monitor Across the Resistor for Static Deflections

Beam #1			Beam #2		
Voltage Applied (V ± mV)	Voltage across Beam (V ± mV)	Calculated Current	Voltage Applied (V ± mV)	Voltage across Beam (V ± mV)	Calculated Current
5.00 ± 25	4.95 ± 25	0.5 ± 0.5 μA	5.05 ± 25	4.99 ± 25	0.6 ± 0.5 μA
10.15 ± 404	10.06 ± 40	0.9± 0.8 μA	10.06 ± 40	9.97 ± 40	0.9 ± 0.8 μA
15.08 ± 55	14.94 ± 55	1.4 ± 1.1 μA	15.01 ± 55	14.87 ± 55	1.4 ± 1.1 μA
20.24 ± 71	20.03 ± 70	2.1 ± 1.4 μA	20.26 ± 71	20.06 ± 70	2.0 ± 1.4 μA
22.43 ± 77	22.25 ± 77	1.8 ± 1.6 μA	21 ± 73	20.96 ± 73	0.4 ± 1.5 μA
23.39 ± 80	23.14 ± 79	2.5 ± 1.6 μA	21.05 ± 73	Beam Actuated	
24.56 ± 84 V	24.31 ± 83	2.5 ± 1.7 μA			
24.62 ± 84 V	Beam Actuated				

The table shows very similar currents with respect to the applied voltage for both cases even though their actuation voltage differs by almost 4V. The open-beam currents ($<2.5\mu$A) could possibly be due to substrate or surface leakage currents. In one example, a maximum open-switch current of 10pA is reported [132]. The beams of this work do not show, experimentally, any correlation with changing humidity (40-70%) so surface

---

[**] Accuracy specifications are given for Fluke 73III Multimeter as: ± ([0.5% of reading]+[100Ω])
[††] Accuracy specifications are given for Fluke 73III Multimeter as: ± ([0.3% of reading]+[10mV])

leakage currents are ruled out as the source of leakage. The reason for the difference could be because the base substrate of the device is Pyrex, which contains sodium that may be causing charging effects and greater ion mobility than for the silicon-based devices. Although surface or substrate leakages can possibly be sources for leakage currents, no conclusion can be deduced because of the high level of error in the measurements. When factoring in the error in the measurement, the open-beam currents can be interpreted as being negligible.

2.6 Stiction

The devices are plagued by the very common problem of stiction. This term implies both friction and adhesion, occurring when internal restoring forces of microstructures cannot overcome surface adhesive forces such as capillary, hydrogen bonding, electrostatic, and van der Waals forces. Stiction can be categorized into two types: 1) release stiction and 2) in-use stiction. In microfabrication, structures are often built on a sacrificial layer that is dissolved as a final wet etch process to release the devices. Release stiction occurs during this process when the surface tension of the draining rinse liquid draws the microstructure to contact with the underlying substrate [133]. Because Micragem uses a dry release process and no sacrificial layers, release stiction is not a problem with the structures built in this work. In-use stiction refers to adhesion that occurs after the release stage, such as when the device is in operation, in storage or improperly handled. It is thought that the in-use stiction poses the greatest threat to MEMS reliability [134].

After actuation, 8 out of 10 beams do not restore to their original state once the applied voltage is removed. This is a well-known phenomenon explained as a contact welding phenomenon [135]. Robinson *et al.* explain that it may be due to the fact that charge is stored continuously with increasing voltage until actuation occurs. Upon actuation, there is immediate discharging, resulting in a large current density, melting the contact surfaces so that they are welded shut when cooled.

Physical methods that modify the surface are solutions for both release-related stiction and in-use stiction. One approach is to roughen the surface, but, as will become apparent

the application of hydrocarbon or fluorocarbon-based self-assembled monolayer (SAMs) can greatly improve the adhesion properties of micromechanical surfaces and greatly reduce the effect of stiction. The term self-assembled monolayer denotes the single layer of ordered molecules covalently assembled at an interface.

3 Dynamic Testing

Based on back of the envelope calculations in Chapter 3, the induced current caused by the moving cantilever is expected to be high enough to detect. However, after two iterations of amplification circuits used to detect the current, no current was detected. The basic test set-up is presented below in Figure 5-12 and the circuit layouts of the two electronic boards designed by an electronics technician, Ben Bathgate, for the testing are included in Appendix D for reference. The electronics technician was given the expected input signals (pA) and test frequencies (0-150kHz) as criteria for designing the board. In the first testing attempt, the electronic chip was attached to the side of the probing device and then wired to the probe tip holder. In this scenario, the chip was approximately 2cm from the MEMS device. It was thought that high capacitances in the wires connecting the chip to the MEMS device and a high capacitance in the ground wire – neither of which was included in the calculations of Chapter 3 - were the cause of the failed signal detection. A second operational amplifier design was made, including 45° bend, 12um radii, tungsten tips attached directly to the chip with sockets to reduce any losses that may occur through connecting wires. Also, this operational amplifier was also refitted with a gain of ~100 instead of the previous gain of ~4. However, still no signal was detected. The explanation presented as the reason for lack of signal detection is due to a low signal-to-noise ratio of the electronics board. This is explained in the following section.
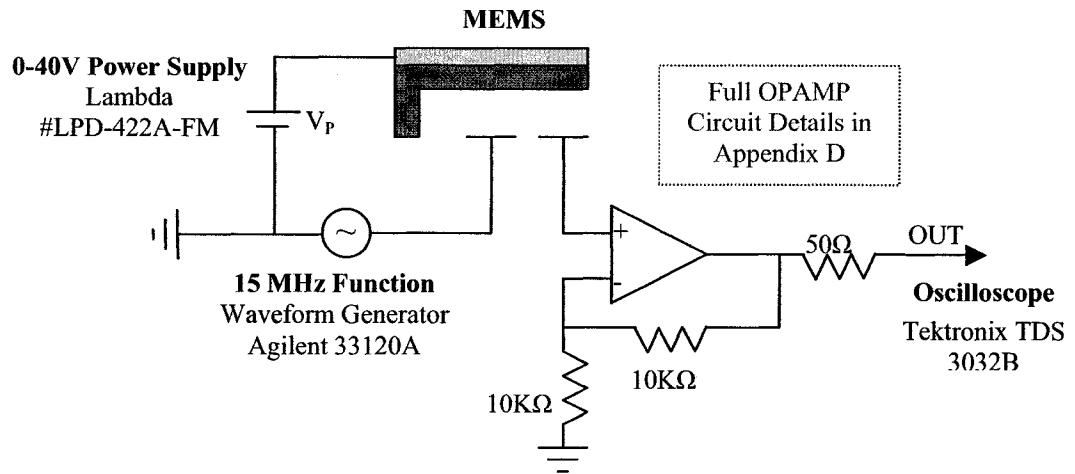
Figure 5-12: AC test layout

3.1 Signal-to-Noise Ratio of Electronics Board

Calculations in Chapter 3 estimated that the expected output voltage from the MEMS chip due to the change in capacitance caused by the maximum deflection of the beam is ~10mV across a combined capacitance of the wire traces, bonding pad and test set-up of 11pF. This calculation assumed optimal conditions because it was taken for maximum displacement of the beam where it operates near to the snap down point. However, for a 100nm displacement of the beam (caused by ~10V potential between the beam and the bottom electrode instead of the V_{TH}=19.4V assumed in the original calculation), the output voltage of the MEMS chip is reduced to 0.25mV. The noise level of the output of the second, improved board is found to be ~100mV as shown in Figure 5-13, and because the gain is 100, this corresponds to a minimum detectable signal of ~1mV. (For comparison, the first board had a noise level of ~120mV with a gain of 4.) The signal was observed for the set-up shown in Figure 5-12 for both boards, and for varying both the bias voltages and frequencies. The voltage across the device, as measured by the oscilloscope, was calculated in Section 4.8 of Chapter 3. By calculating the total amount of charge caused by the maximum displacement of the beam and dividing this by the equivalent capacitance of the device, a voltage of 9.7mV was calculated to occur across the device. It then follows that the expected signal-to-noise (SNR) of the estimated

~100~

signal calculated is 10. However, with the more likely displacement (100nm) than was assumed in the estimated calculations, the SNR would be 0.25. It is concluded that both the ideal calculations of Chapter 3 and a high noise level from the electronics board create a low signal-to-noise ratio, thus making it impossible to electrically detect the resonant device.

Noise Level of OpAmp Board
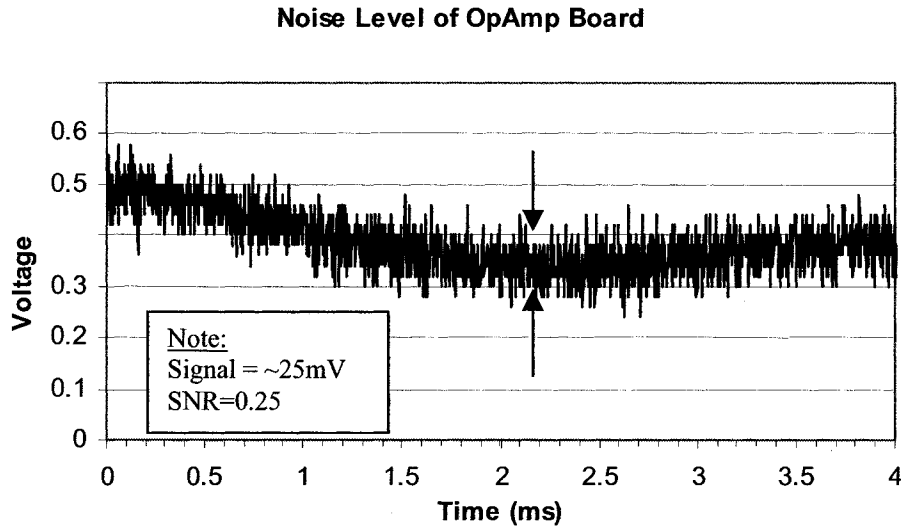
Figure 5-13: Noise level of operational amplifier board used for capacitive sensing

Attempts to reduce the noise in the circuit were made but none was successful. For example, all leads were kept as short as possible to reduce their antenna effects. In addition, the probe assemblies were eliminated because probe tips were connected to the circuit directly. This reduces the leads from ~30cm to 1cm for both the actuation and sensing pads. It should be noted that testing could not be done in a RF shielded cage because of the need for the probe station and microscopic alignment to the probe pads on the device. The electronics board detected many sporadic signals, including some that were very convincing. For example, on one occasion, one set of signals was intriguing because the frequency doubling behaviour discussed in Chapter 3 was thought to be detected. When the cantilever was driven with $6V_{p-p}$, a lower applied bias (<3.3V_{DC}) produced a signal $2f$ (Figure 5-14 (a)) than that of a higher applied bias (>3.7V_{DC}) (Figure 5-14 (b)). This was repeated numerous times during the testing on that occasion. However, upon further inspection it was deemed as signal pickup or parasitic oscillation because (1) it could not be repeated on other occasions and (2) was only seen for a small

~101~

range of frequencies which were far greater than was expected for resonance (~150kHz). The sets of signals are shown in Figure 5-14 below.
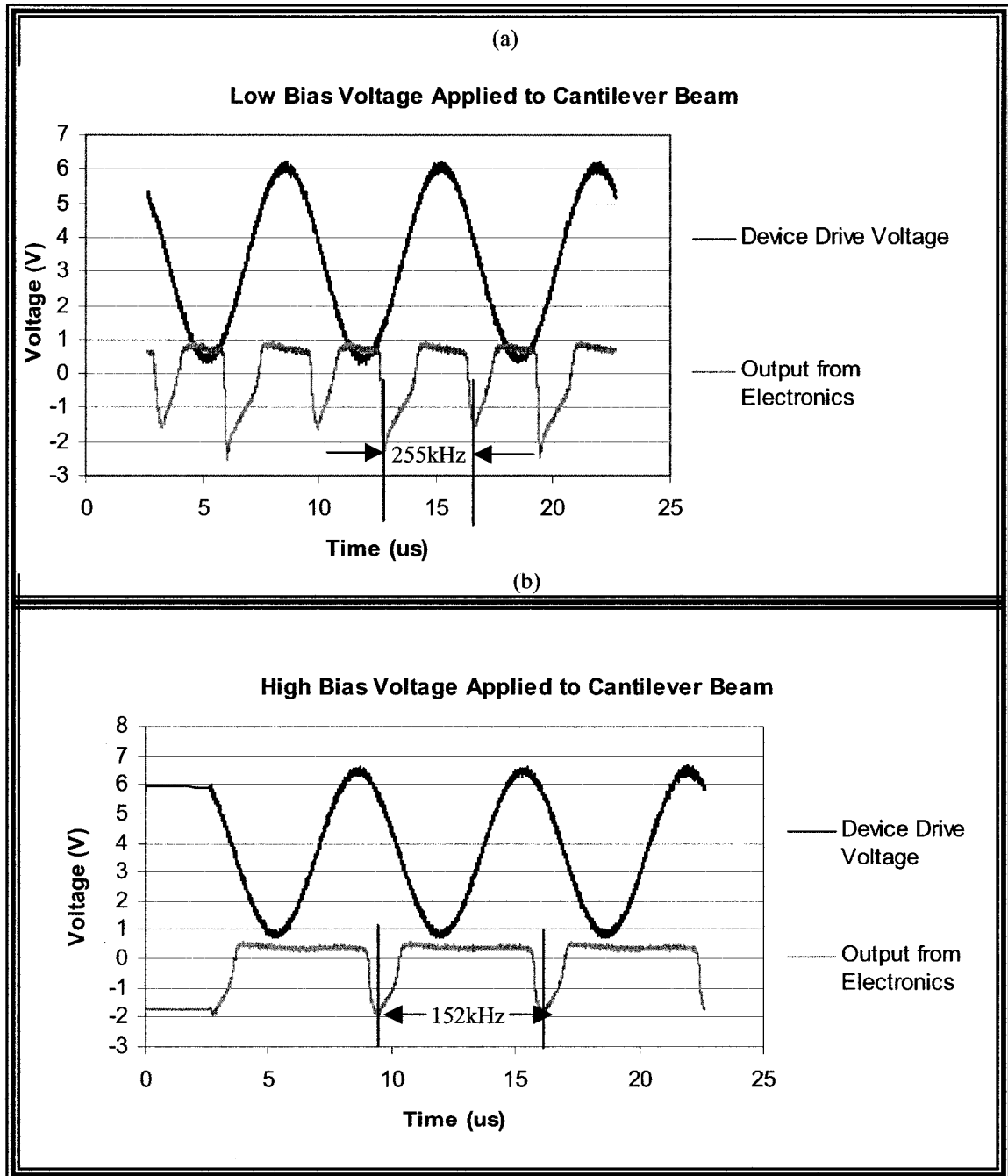
Figure 5-14: Output signal from electronics board #2 versus drive voltage for cantilever
(a) Lower Bias Voltage appears close to frequency doubling behaviour (255kHz) (b) Increasing bias shows sensed signal is same voltage as device driving voltage (152kHz)

~102~

3.2 Equivalent Electrical Circuit

As was first introduced in Chapter 3, the micromechanical resonator is analogous to an electrical RCL circuit [136]. Following an approach first introduced by Nguyen's group and shown below in Figure 5-15, the equivalent RLC circuit modeling a micromechanical resonator is presented in a form that separates the dynamic components from the static components [2, 90]. In this circuit, the dynamic components (termed the motional elements) R_x, L_x, and C_x model the resonant behaviour of the device, while the capacitor C_o models the static capacitance between the electrode and beam when at rest.
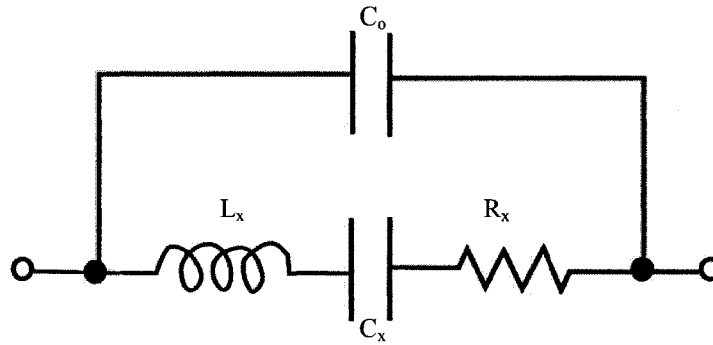
Figure 5-15: Electrical equivalent circuit for a micromechanical resonator

The equations for the circuit elements from the figure above are also introduced by [25, 90] and are as follows:

$$C_x = \frac{\eta^2}{k_r} \qquad\qquad \text{Equation 5-4}$$

$$L_x = \frac{m_e}{\eta^2} \qquad\qquad \text{Equation 5-5}$$

$$R_x = \frac{\sqrt{k_r m_e}}{Q\eta^2} \qquad\qquad \text{Equation 5-6}$$

$$\eta = V_P \frac{\delta C}{\delta x} \qquad\qquad \text{Equation 5-7}$$

Where:

C_x, L_x, R_x are referred to as motional capacitance, inductance, and resistance, respectively.
η = electromechanical coupling coefficient (defined below)
m_e = effective mass of the cantilever (Equation 2-1)

~103~

k_r = stiffness of the cantilever, which can be related to the natural angular frequency by [92]:

$$k = \omega_o^2 m_e$$ **Equation 5-8**

The values of the RLC circuit elements are dependent on the electromechanical coupling coefficient η, the effective mass m_e and stiffness k_r. The electromechanical coupling coefficient, also termed the transformer turns ratio, utilizes Equation 3-26 for $\delta C/\delta x$. This coefficient models the mechanical impedance transformation achieved by mechanically coupling to the resonator at a x location displaced from its centre [25]. The model is an ideal electromechanical transformer with a transformer ratio given by η [136]. The values for Equations 5-4 through 5-8 are summarized in Table 5-2 below:

Table 5-2: Summary of Electrical Equivalent Circuit Values

Values for a Standard Beam	
C_x	2.87×10^{-16} F
L_x	3.03×10^4 H
R_x	2.27×10^9 Ω
η	2.77×10^{-8} unitless
C_o (Equation 3-25)	2.77×10^{-15} F
V_P	20 V$_{DC}$
k_r	2.67 kg/s^2

The impedance of the system is found by utilizing the electrical equivalent circuit as is shown in Figure 5-15 and solving for the magnitude of the following equation:

$$Z = \left(jwC_o + \cfrac{1}{jwL_x + \cfrac{1}{jwC_x} + R_x} \right)^{-1}$$ **Equation 5-9**

Where:

$$Z_{static} = \frac{1}{j\omega \cdot C_o}$$ **Equation 5-10**

and,

~104~

$$Z_{motional} = jwL_x + \frac{1}{jwC_x} + R_x \qquad\qquad \textbf{Equation 5-11}$$

Solving for the magnitude of the impedance of the system with respect to frequency was done with the aid of Matlab 6.5. The program used to solve for the impedances is included in Appendix E, and the results for a standard beam are shown below in Figure 5-16.
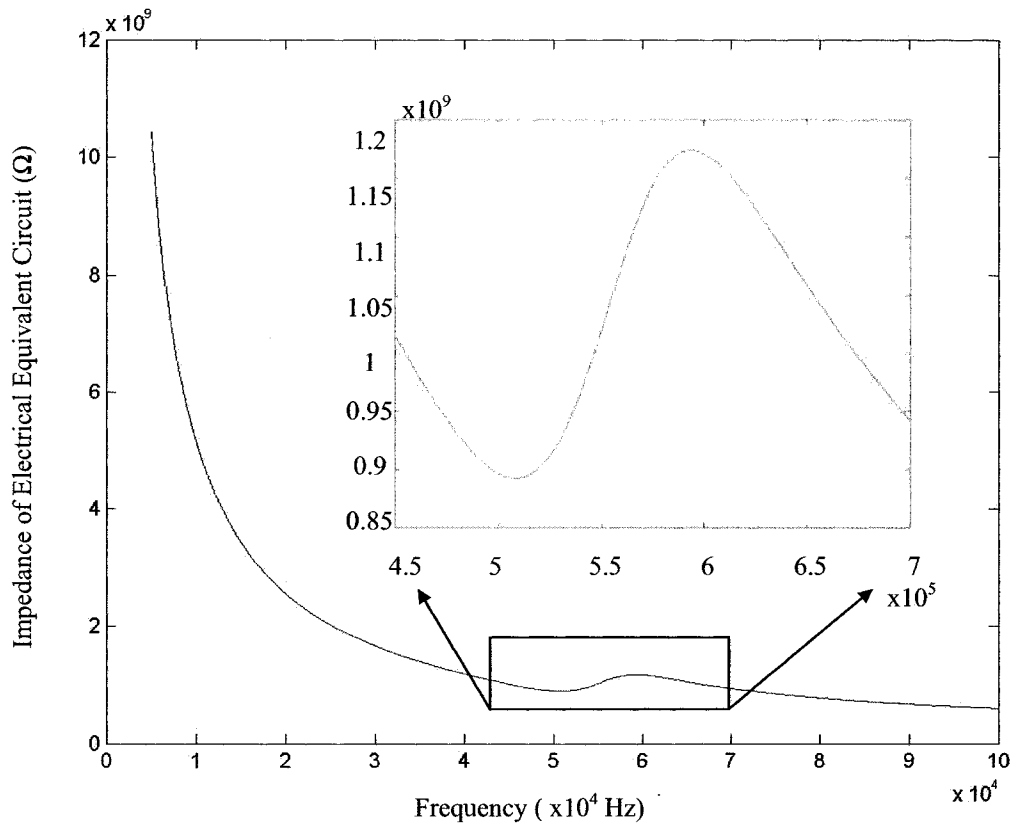
Figure 5-16: Impedance versus frequency for a micromechanical resonator

The impedances for the static and motional components of the electrical equivalent circuit are also found and are compared to the device's total impedance. This is shown below in Figure 5-17. It is seen in the figure that the motional components of the circuit (R_x, L_x, and C_x) have a much higher impedance than the impedance due to the static capacitance, C_o, of the device. Even though the impedance reaches a minimum at resonance, it is still much higher than that due to the static capacitance causing the static

~105~

capacitance to be the dominant arm in the circuit of Figure 5-15. The motional components are what are of interest when attempting to sense dynamic behaviour of the cantilever beam and because the RLC arm of the circuit is not dominant, it is not surprising that this electrical testing failed. The greatest contributor to the devices' impedance of $2.7G\Omega$ (Equation 5-9) is the motional resistance, which is $2.3G\Omega$ (Equation 5-6). Therefore, to reduce the device's impedance, the motional resistance must be reduced.
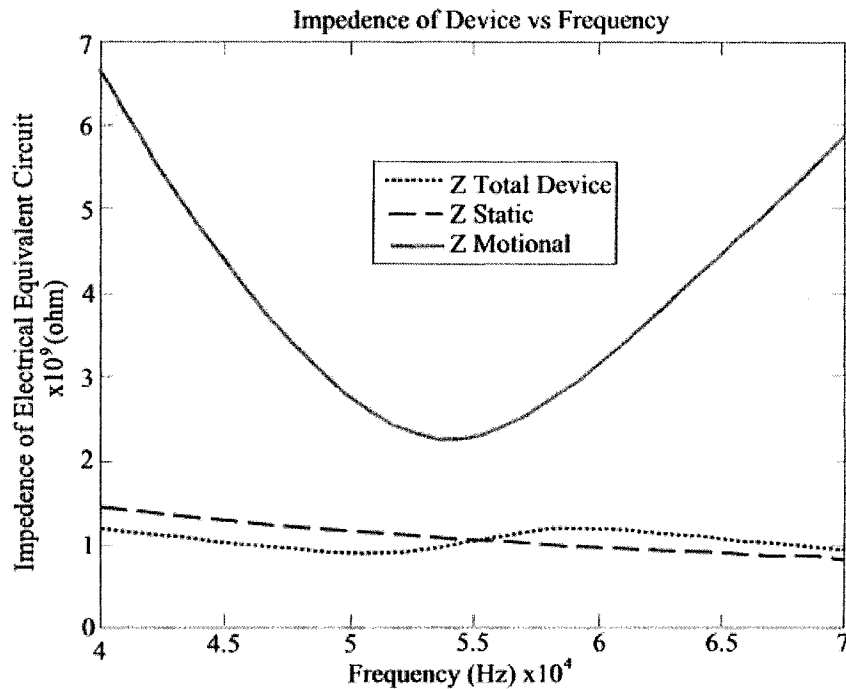
Figure 5-17: Comparing impedance of static & motional components to the device

In addition, the series motional resistance, R_x must often be minimized for impedance matching purposes [90]. For example, in micromechanical filter applications, the output resonator of the filter must see a matched impedance in order to reduce passband distortion [26]. (i.e. The filter response is made as flat as possible). Additionally, in applications where the resonator output is connected to antennas (as in the case with the harmonic radar tags), the output impedance must be matched between the two. According to Equations 5-4 through 5-8, the motional resistance for a standard beam is $2.3G\Omega$. For a given micromechanical resonator, the way to reduce the motional

~106~

resistance is through maximizing the dc-bias voltage, V_P, and the $\delta C/\delta x$ term. However, the maximum voltage can be limited by either the transistor technology supporting the resonator or the available the power supply [90]. In the case of the standard beam, V_P is increased to as much as 20V, but is limited by the threshold voltage, V_{TH}, of the device (21-25 V_{DC}). This leaves $\delta C/\delta x$, which varies with the thickness to the square of the gap (h_B/d^2) of the beam as the only adjustable parameter. Thickness directly changes the characteristics of the resonating beam, but decreasing the electrode-to-resonator gap spacing does not alter the resonating device. Since $\delta C/\delta x$ varies as ($1/d^2$), changes in d have a very strong effect on R_x, which are shown for the standard beam in Figure 5-18 as ($1/d^4$).
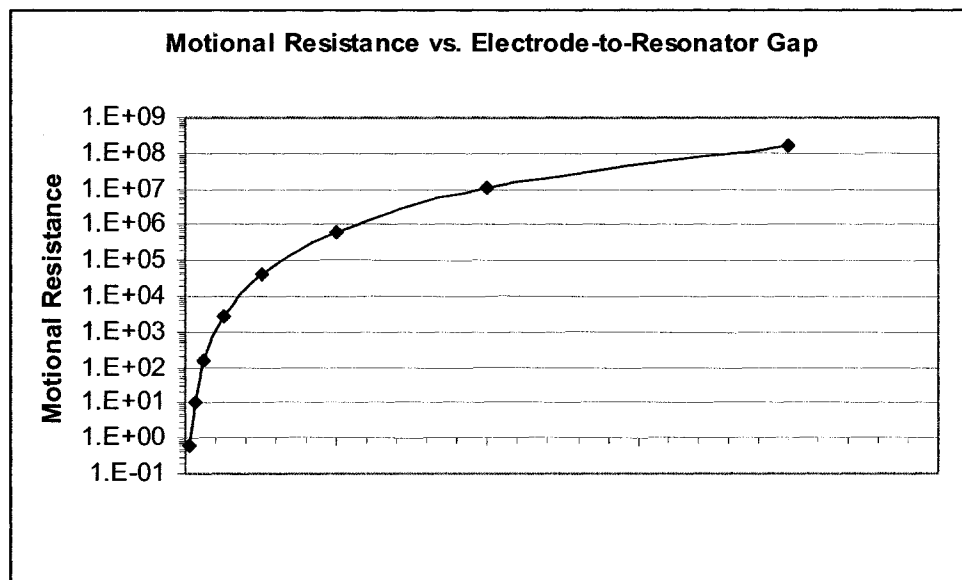
Figure 5-18: Beam-to-electrode dependence on motional resistance

From the figure above, it can be seen that to reduce the motional resistance an order of magnitude, the gap needs to be less than 1000Å, which is verified by reports for required small capacitive gaps [2, 25, 90].

Alternatively, the simplified electrical circuit of Figure 3-7 presents the cantilever/bottom electrode as being a capacitor that produces a charge, Q, and gives rise to a signal, V. This interpretation also confirms that decreasing the gap size produces an

increased signal for sensing. Shown by Equation 3-31 ($\Delta Q = \Delta C V_P$), as the original distance between the plates, d_{BS}, decreases, ΔC increases for the same deflection of the beam. ΔC for the displacement (x_1-x_2) of a cantilever beam is estimated (assuming parallel plates in both positions) as:

$$\Delta C = \frac{\varepsilon_o A}{(d_{BS} - x_1)} - \frac{\varepsilon_o A}{(d_{BS} - x_2)}$$
<div align="right">**Equation 5-12**</div>

From Equation 5-12, it is seen that for the same deflection of the beam, if the original distance between the plates is reduced, the charge, Q, also increases. For example, for a displacement of 10nm for the standard beam, the change in capacitance is 400 times less than for the same deflection but with a gap size of 1000Å. Fabrication techniques such as electron beam lithography [137] and sacrificial layers utilizing highly developed film thickness control technology in attaining the submicron gaps are reported [75, 90, 138, 139].

4 Conclusion

Both static and dynamic testing methods are presented in this chapter. Although the static testing method is not flawless, it is able to provide actuation voltage, leakage current, and shows the static deflection of the beam with respect to voltage potential between the beam and the electrode. For the standard beam, the actuation voltage is found to vary between 21–24 ± 0.1 V_{DC} with respect to the ground applied to the bottom electrode. These values do not agree within error with theoretical value of 19.4V estimated in Chapter 3. However, they are explicably higher because of the stress in the thin film was not taken into account in the analytical calculations. In addition to static testing, dynamic testing was attempted, which utilizes the technique of sensing the induced current caused by the varying capacitance of the beam as it moves. This was not successful and is explained through the low signal-to-noise ratio of the set-up. In addition, electrical testing is deemed possible if connections could be made closer such as would be possible if the device was directly attached to the electronics with wire bonds. The testing could then be carried out in a shielded environment where electronic pickup

would not interfere with testing. A stronger capacitive signal from the beam is also discussed as being an important improvement for successful electrical testing, which is possible if the distance between the beam and the bottom electrode is reduced (i.e. minimizing capacitive gaps). Finally, an equivalent electrical circuit is presented. The series motional resistance of a standard beam is the major contributing factor to a device impedance of $2.7G\Omega$, and the implications of this high impedance are discussed.

Chapter 6 – AC Measurement using Interferometry

1 Introduction

In this work, a modified Michelson interferometer is used to measure the sub-micron movement of cantilever beams. The Michelson interferometer, first described by Michelson in 1881, greatly affected modern physics because of its versatility, simplicity, and stability. This instrument laid the experimental foundations for the theory of relativity, evaluated a meter in light waves, measured the tidal effect of the moon on the earth, and, with slight modifications, has widespread use in optical workshops for lens and prism testing. It also forms the basis of the interference microscopes used for studying the microtopography of surfaces and has been used as a refractometer [140].

2 General Arrangement for a Michelson Interferometer

Simply put, interferometry uses the phase difference between a reference beam and an object beam for the detection of moving structures such as the cantilever beam in this work. The basic arrangement of a Michelson interferometer set-up is shown in Figure 6-1. In the figure, light from a source S is incident at 45° on a beam splitter mirror A. This mirror has a thin film of silver, which enables the mirror to transmit and reflect light equally. After the beam divides, half goes to M_1 and the other half to M_2. The beams then return to A, are recombined and interfere to form fringes at B.
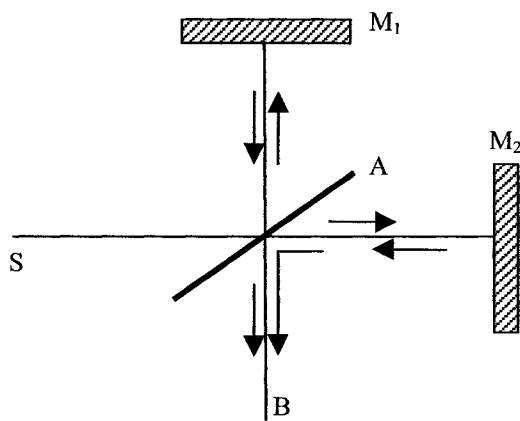
Figure 6-1: Basic arrangement of Michelson interferometer

This arrangement can be used to measure movement in the direction of the light path. If M_2 moves in the direction of the incident laser beam, the phase of the reflected laser beam is changed with respect to the beam reflecting off M_1. This phase difference alters the fringe pattern and is monitored at B. A more detailed explanation of this phase change with respect to the dynamics of the micromechanical resonator is given in Chapter 7.

3   Modified Set-up for Measuring MEMS

Optical measurement of the cantilever beam with an interferometer is utilized to characterize the time dependent movement at the tip of the beam. The amplitude of the beam (perpendicular to the substrate surface and in line with the laser path) is monitored as driving signals at varying frequencies are applied. The resonant frequency and quality factor are then deduced from this method. A schematic of the set-up is shown below in Figure 6-2. In general, a helium neon (HeNe) laser (λ=632.8nm) enters a beam splitter at (1) that splits the laser beam into a reference beam, which is just reflected back unchanged at (2), and an object beam that is focused through a lens at (4) into a spot on the end of the cantilever beam at (5). The reflected object light beam passes back through the lens at (4), the directional beam splitter at (3), enters the beam splitter at (2) where it is recombined with the reflected reference light beam, and both are focused onto the photo detector at (6). A fringe pattern is detected by the photodetector because the path lengths of the object and reference beam can interfere constructively or destructively

~111~

and are well within the coherence of the laser. So, when the cantilever beam moves, (in line with the object laser beam), the phase of the object beam changes relative to the reference laser light beam causing a time-varying fringe pattern related to the cantilever's frequency of movement.

There are additional components to the system such as the CCD camera set-up, the beam expander, the isolator, and the neutral density filter. These, as well as the photodetector circuit, are discussed in more detail below.
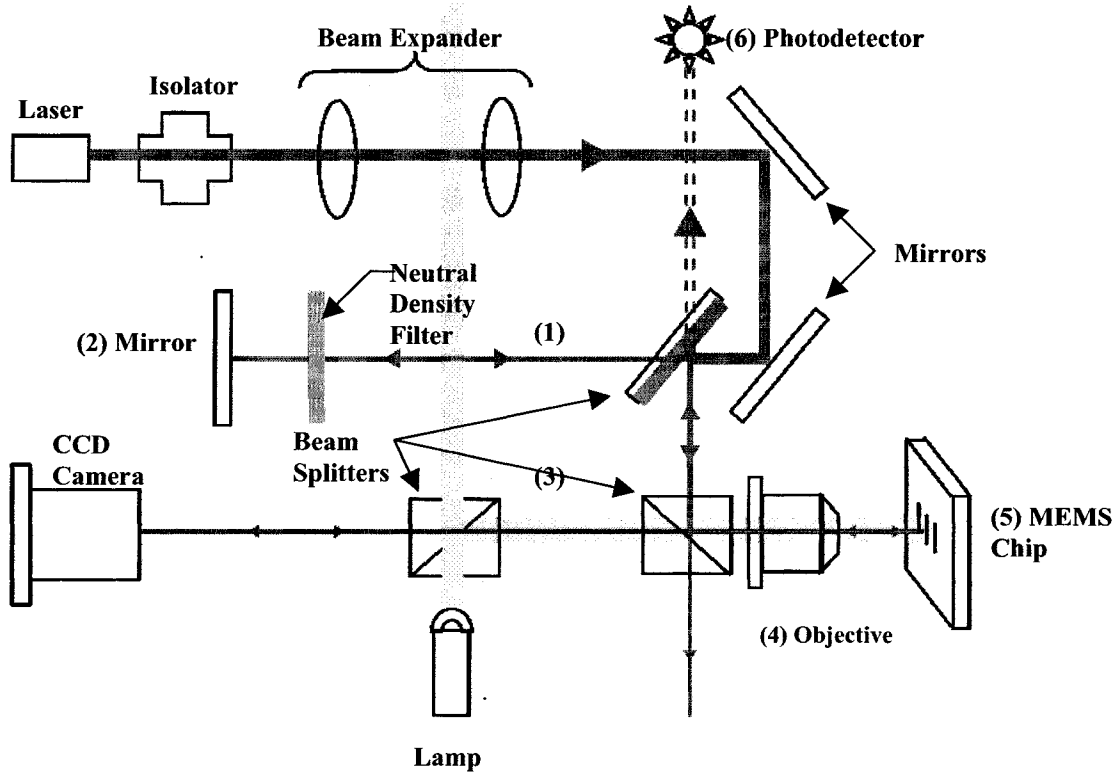
Figure 6-2: Schematic of interferometry set-up

3.1 The CCD Camera

The CCD camera set-up is used so the MEMS device can be imaged on a computer monitor. This is to facilitate aligning the probe tips to the pads for the driving signal and for aligning the laser spot onto the end of the cantilever beam.

~112~

3.2 The Beam Expander

The beam expander increases the spot size of the laser beam from 1mm to 5mm so that it can be more easily aligned and more finely focused by the objective.

3.3 The Isolator

The free-space optical isolator allows for precision alignment of the set-up without the reflected light causing parasitic oscillations of the laser light source. To explain, when the set-up is precisely aligned, the laser light is transmitted directly back into the laser cavity, which causes a non-cyclical flicker in power that is very disturbing to measurements. The optical isolator is a passive, non-reciprocal device that allows light to transmit in one direction only, and, when placed in front of the laser (Figure 6-2), inhibits the laser's transmission back into the laser cavity. The use of the optical isolator alleviates the flickering effects and stabilizes the laser in the set-up. The phenomenon of magneto-optic rotation is utilized. In other words, at the heart of the optical isolator used for 500-1100nm ranges is a Faraday Rotator using Terbium Gallium Garnet (TGG) single crystals. These, among other Faraday media, have the ability, when they are in an appropriate magnetic field, to rotate the plane of linearly polarized light by an amount proportional to its length.

3.4 Neutral Density Filter

Both the transmitted and reflected waves from the first beam splitter have lower amplitudes than the original. However, what may not be so obvious is that the reflected object beam is ¼ the amplitude of the reflected reference beam at the point of recombination. This is because the object beam passes through another beam splitter at (3) in Figure 6-2 before entering the objective, thereby cutting its amplitude in ½. The returning beam (after reflecting off the cantilever) then passes through this beam splitter again causing the returning beam to be ¼ the amplitude of the original object beam.

The clearest patterns exist when the interfering waves have equal or nearly equal amplitudes. The central regions of the dark and light fringes then correspond to complete destructive and constructive interference, respectively, yielding maximum contrast [141].

A neutral density filter is placed in the reference beam's path to reduce its amplitude to equal that of the returning object beam. The test that the correct neutral density filter is, in fact, chosen and that complete destructive interference is achieved, is presented in Section 7 of this chapter.

3.5 The Photodetector Circuit

A photodetector is a device that measures photon flux or optical power by converting the energy of the absorbed photons into a usable form. A photodiode is a type of photo detector, in which the absorption of photons results in an electronic transition to a higher energy level and the generation of mobile charge carriers. The device can be thought of as a current generator because under the effect of an electric field, these carriers move and produce a measurable electric current [141].

The photodetector circuit is designed to operate in three modes [142]: (1) photovoltaic, (2) short circuit, & (3) photoconductive. These three modes are shown in Figure 6-3. Photovoltaic (shown in (a)) acts as an open circuit and has an output voltage that is logarithmic as a function of incident light intensity. However, a linearly dependent response with respect to the incident radiation level is more desirable for this application because the photodetector is expected to be incident with a range of radiation levels with each passing fringe. Both the short circuit (shown in (b)) and the photoconductive circuits (shown in (c)) are linear in this regard. An advantage to the short circuit mode, shown simply in (b), is its ability to achieve sufficiently low load resistance and an amplified output voltage by feeding the photocurrent to an operational amplifier. Although this circuit is best in theory, the circuit used during testing does not have an optimal response, which is explained further in Section 5 of this chapter. Lastly, the photoconductive circuit, shown in (c), generates a voltage across a load resistor by the photocurrent produced by the diode. Although it was not the first choice, this mode is ultimately chosen as the test circuit because it gives the best frequency response of the output voltage and the clearest signals.

~114~
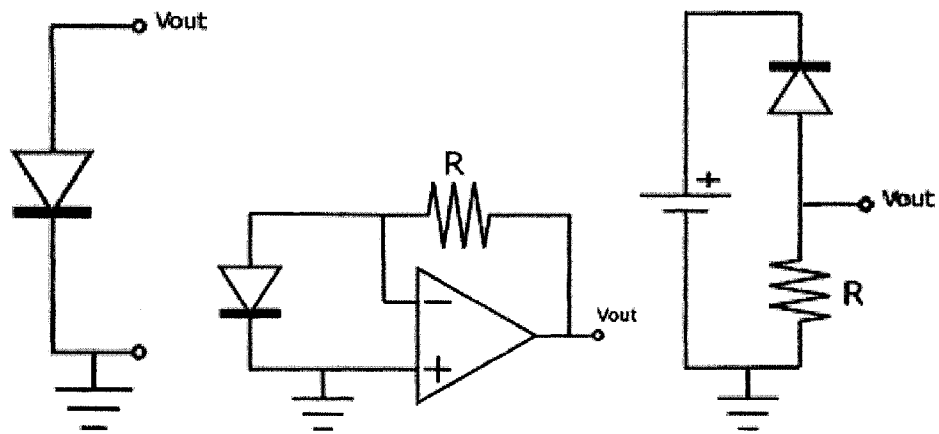
Figure 6-3: Photodetector schematics for various modes
(a) Photovoltaic; (b) Short Circuit with operational amplifier; (c) Photoconductive

Figures 6-4 & 6-5 show that all three circuits are on one board. As labelled in Figure 6-4, a switch is used to shift the circuit to either operate in short circuit mode or photoconductive mode. Also, in both modes are three resistors that allow for three different values of gain and are chosen by a jumper.
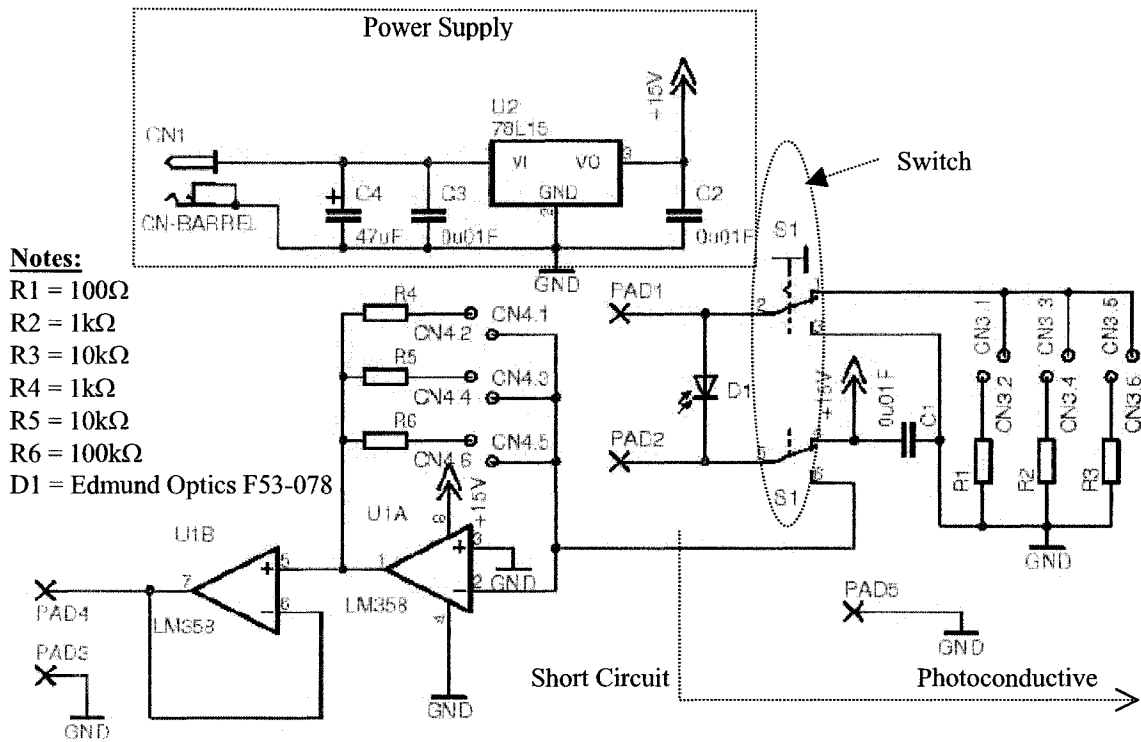
Figure 6-4: Photodetector circuit schematic
Circuit layout with jumper settings is described in Figure 6-5

Notes:
R1 = 100Ω
R2 = 1kΩ
R3 = 10kΩ
R4 = 1kΩ
R5 = 10kΩ
R6 = 100kΩ
D1 = Edmund Optics F53-078

Operational Mode Directions:

Pin 3 or 5 & 1: Photoconductive
Pin 3 or 5 & 4: Short Circuit
Pin 1 & 2: Photovoltaic
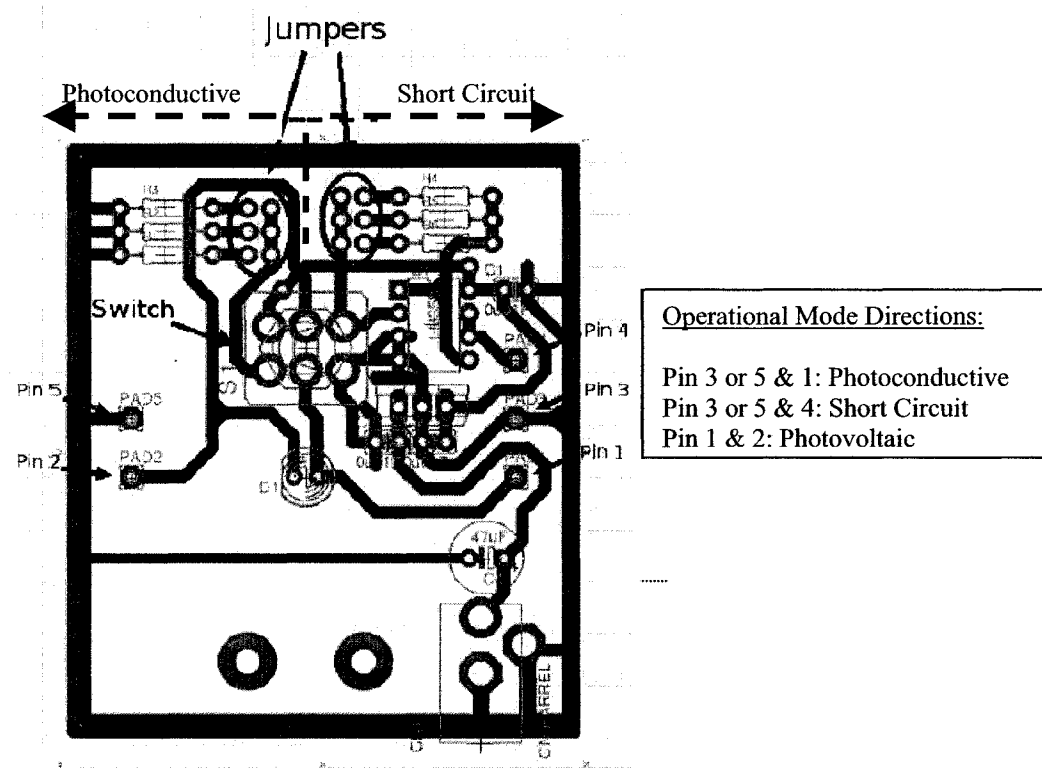
Figure 6-5: Photodetector circuit layout

~116~

4 Photodetector Frequency Response

The frequency response of the photodetector is analyzed for both the short circuit mode and the photoconductive mode for the circuit set-up shown in Figures 6-4 & 6-5. The different modes are achieved by probe attachments to pins outlined in Figure 6-5 for each respective mode being tested, and the results are monitored with an oscilloscope. With the assistance from a technician, Loi Hui, an LED is programmed as the input to the photodetector and its response is recorded. Programming an LED to turn on/off at the chosen frequency creates the square wave input signal, which is placed in front of the photodiode and detected by the photodetector. The LED is controlled with an I/O pin of the micro controller PIC16F877. The pin is set high (on), delayed, turned low (off) and delayed. The entire period (time on + time off) is set for frequencies ranging from 1kHz to 1MHz to examine the response of the photodetector circuits needed to test the micromechanical resonators. The input signal was checked with an oscilloscope and was, in fact, a square wave. Each instruction of the micro controller takes $\sim0.2\mu s$, thus limiting the frequency of testing to 2.5MHz.

The frequency responses of the short circuit and photoconductive modes are compared at increasing frequencies with the LED set-up just described. Their responses are shown in Figure 6-6 below. In the figure, it is seen that the frequency in short circuit mode (shown in (I) to the left) is unstable. Shown dramatically in (b) 10kHz is a modulated signal, from which it may be inferred that there are resonances in the circuitry in this range. However, the photoconductive Circuit shown in (II) has an excellent response to the square wave input and does not seem to have difficulties responding quickly enough until it reaches frequencies in the MHz range (shown in (II-d) in the figure). This is inconsequential for testing the micromechanical resonators in this work because the upper range required for the testing is 100kHz.
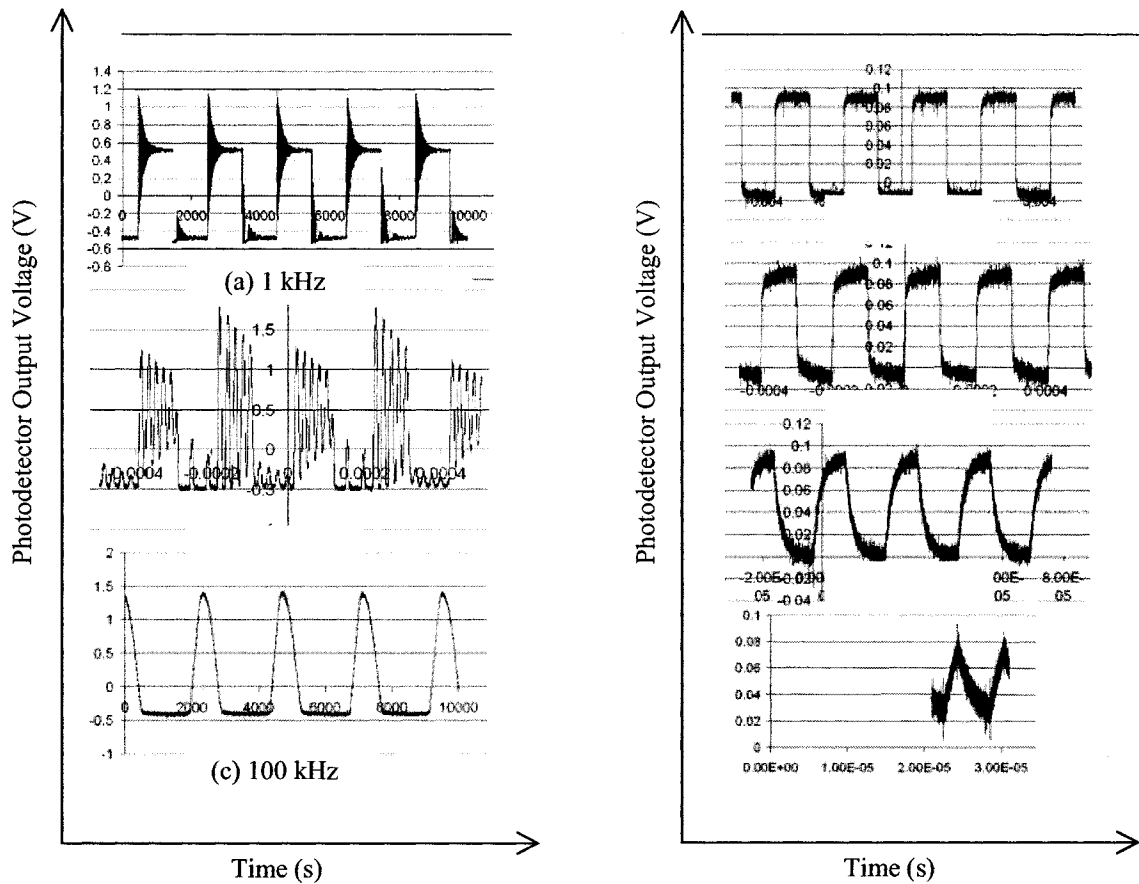
Figure 6-6: Photodetector circuit frequency response testing
(I) Short Circuit Mode Frequency Responses – (a) 1kHz, (b) at 10kHz, (c) at 100kHz; (II)
Photoconductive Mode Frequency Responses - (a) at 1kHz, (b) at 10kHz, (c) at 100kHz, (d) 1MHz –
Although is a partial trace, it is representative

The photoconductive mode outperforms the short circuit mode of the photoconductor circuit and is subsequently chosen for the testing. To increase the amplitude of the signal, which can be seen as almost 10 times less than the short circuit mode in Figure 6-6 above, an additional 100kΩ resistor was placed in series to the existing resistor (10kΩ). This increases the voltage drop created by the photocurrent of the diode and thus the gain of the circuit but was not expected to affect the frequency response of the circuit. (Refer to Figure 6-3 (c) for the schematic.)

~118~

5   Alignment and the Nature of Fringes

Reliable results from an interferometry set-up require that the circuit does not have any noise characteristics that may confuse the results. A good interferometry set-up must also have very accurate alignment in order to make good results possible. How precision alignment was achieved for this set-up is described.

During alignment of the reference and object beams, two distinct fringe patterns are observed at the location of the photodetector and utilized to aid in alignment of the system. The set-up is first aligned without the focusing lens and MEMS in the system ((4) and (5) in Figure 6-2). Instead of the MEMS chip, a mirror is used. Upon first recombination of the laser beams, a fringe pattern of parallel lines of constructive and destructive interference as illustrated below in Figure 6-7 (a).

(a)   (b)
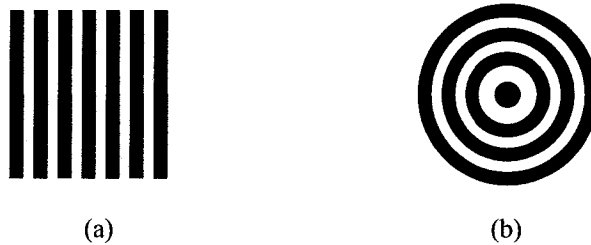
Figure 6-7: Fringe patterns (a) Localized linear fringes (b) Concentric circular fringes

Fringes of this type are found where the reflected reference beam and reflected object beam intersect. This crosover position is the position of zero path difference and is a straight line of intersection [140]. Fringes appear and will always be seen as either vertical or horizontal straight lines with this alignment (depending on which plane they are misaligned) and are parallel to the line of intersection. An illustration of this misalignment is shown in Figure 6-8 below. Lines representing the peaks illustrate the waves of the laser (note the peaks all line up in a monochromatic, coherent laser source as in the case of the HeNe laser used in the set-up). Shown in the figure are two laser beams at the point of intersection. In (a), the beams are misaligned by 10° from the central axis. At the point of the photodetector (placement is perpendicular to the page),

~119~

there are 3 bright and dark vertical fringes similar in presentation to those illustrated in Figure 6-7 (a). It is found that, as the beams are brought closer in alignment, the fringes increase in width and decrease in number. Shown in (b) are beams that are misaligned by 5° from the central axis. The width of the fringes is shown to have increased from those seen in (a), and the number of bright and dark vertical fringes has reduced to 2.
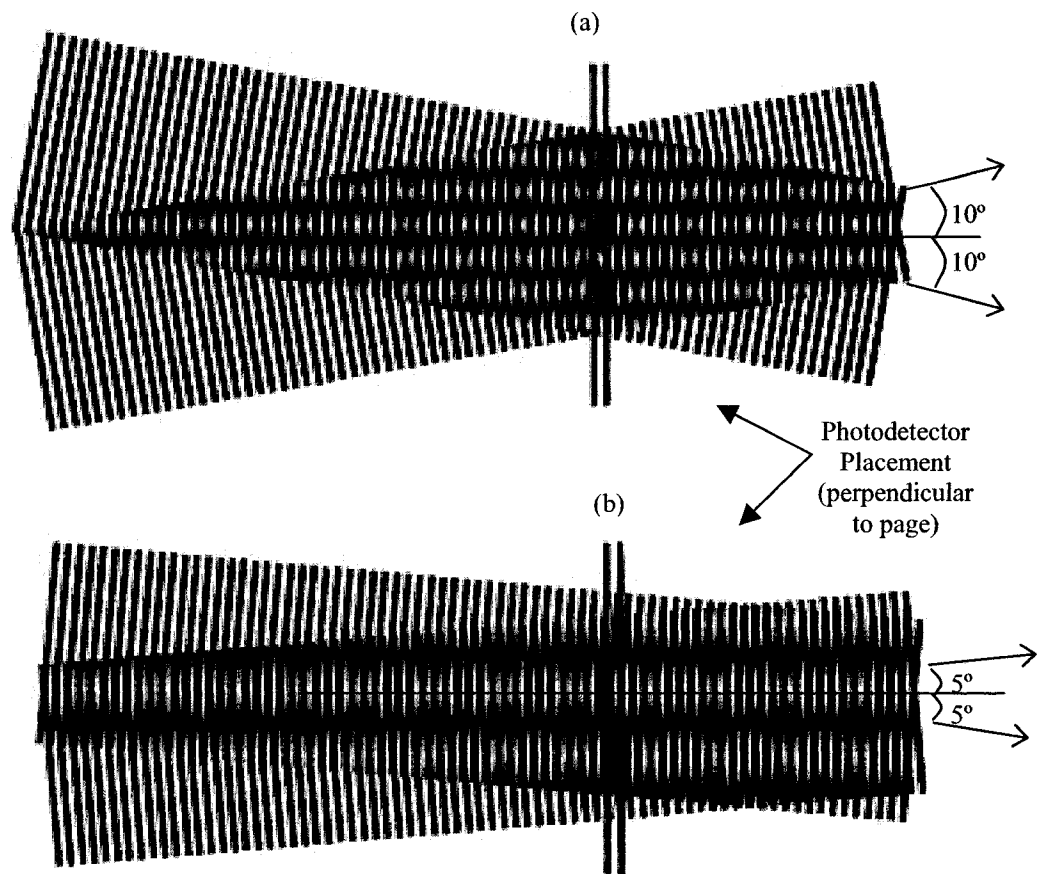
Figure 6-8: Misalignment of laser beams

The width of the fringes increases until the laser beams are collinear and just either one bright or dark fringe is seen at the point of the photodetector. Also, noted when misaligned, the fringes are localized to the region of overlapping beams, and this increases as the beams are brought closer to sharing a central axis.

~120~

Once the beams are completely collinear, the lens (Refer to (4) in Figure 6-2) is placed in the set-up. Concentric circles then appear as the fringe pattern at the point of the photodetector as shown in (b) of Figure 6-7 and photographed in Figure 6-9. A concentric ring fringe pattern, according to the literature, means that the reflected reference and the reflected object beam are parallel [140]. This means the light beams are equivalent to sources in line behind each other, which is what was achieved with the alignment described above. However, the concentric fringe
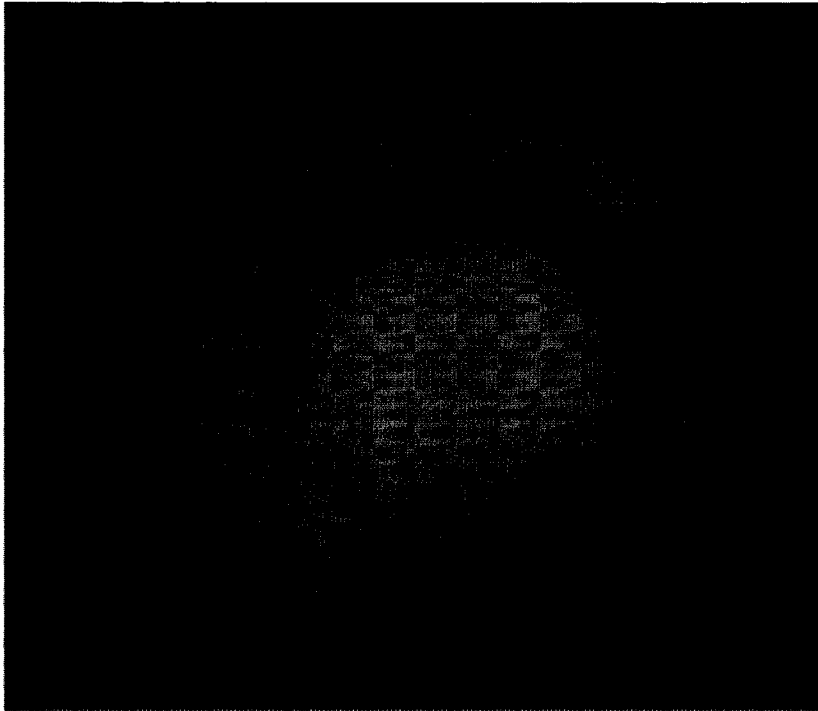
Figure 6-9: Photograph of fringe pattern at the photodetector beam

pattern also means that at least one of the laser beams is changing in size with respect to the other laser beam. As the beams are made the same size (by adjusting the focusing lens in the path of the laser beam), the centre fringe grows in size and the number of concentric fringes reduces until just one either dark or bright fringe is shown. Alignment of the two lasers is then complete.

6 Proof of Complete Destructive Interference

Shown below in Figure 6-10 is the photodetector signal in photoconductive mode, representing the voltage difference between laser on and the laser off. The voltage is expected to be higher for the laser incident on the photodiode and lower when the laser is turned off as is shown in the figure. When the laser is off, the only light incident on the photodiode is due to room lighting. In time, an oblique object is placed in and out of the

~121~

path of the recombined laser beam to imitate the laser on/off behaviour (between (1) and (6) in Figure 6-2) leading to the pattern shown in Figure 6-10. This method is consistent with turning the laser on and off. It should be noted that there is nothing else dynamic in the laser paths to cause any other interference. It is seen that the signal to noise ratio is ~1; however, the change in signal with respect to time is what is of interest in this test. The voltage difference between the laser on and the laser off is then estimated as ~40mV.
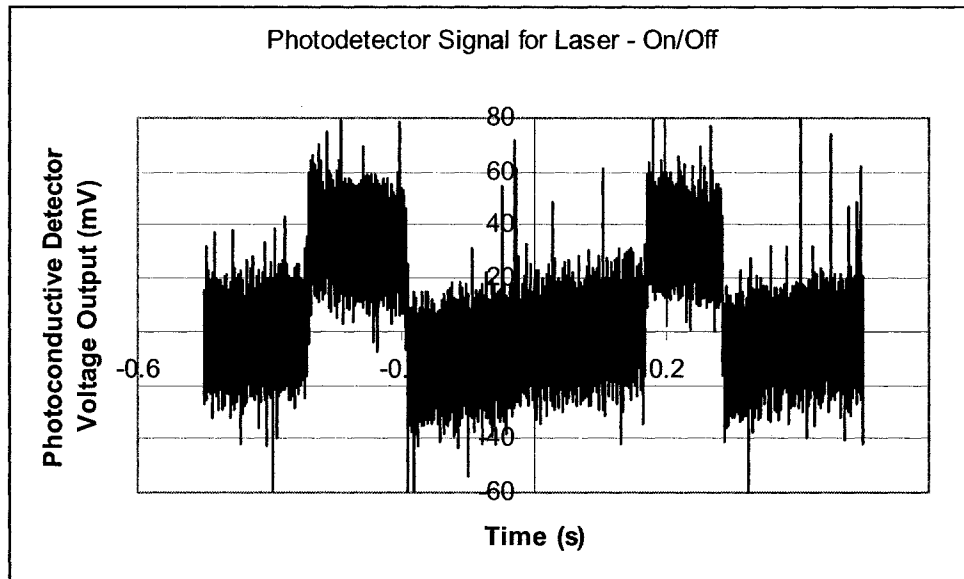
Figure 6-10: Photodetector signal for laser on/off

To test the voltage difference caused by the interference of a dynamic system, the reference mirror ((2) in Figure 6-2 above), is mounted on a translation stage. By moving the reference mirror, the phase difference needed for constructive/destructive interference between the reference and object beams is created. The oscillating light intensity caused by this movement is captured by the photodetector and is shown in Figure 6-11. The difference between constructive interference and destructive interference shown in the figure is ~40mV. Interestingly, this is the same as the difference in voltage for the on/off laser test discussed above in Figure 6-10. This leads to the belief that complete destructive interference occurs between the reference and the object laser beams and that the neutral density filter is correctly compensating for the reduced intensity of the object laser beam as first introduced in Section 3 of this chapter.

~122~
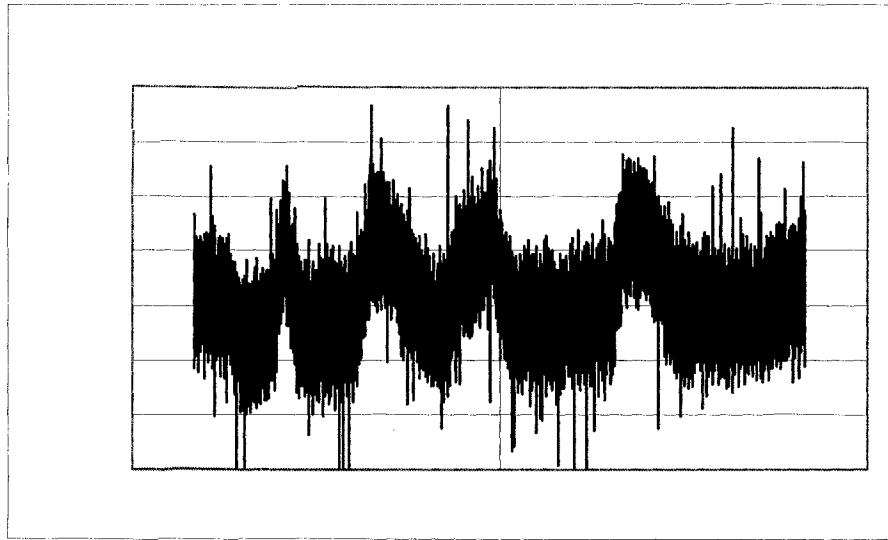
Figure 6-11: Photodetector signal to destructive and constructive interference

7 Change of Set-up

The signal above in Figure 6-11 is preliminary evidence that the interferometer set-up creates and detects constructive/destructive interference. However, no signal resembling this interference is found when the MEMS are integrated with the current set-up. As described below, the objective needs to be used in two ways, thereby introducing a dynamic alignment problem. It is thought that the reason for the set-up's inability to detect the motion of the resonators is because the focusing objective is in one position for the camera set-up, but then needs to be translated towards the MEMS chip in order to focus the laser. Once the laser is in focus, the chip is no longer in focus by the CCD camera, so it is not possible to verify that the laser spot is, in fact, focused at the correct location on the cantilever. Further explanation of the problem and alterations to the set-up are presented in the following section.

7.1 Motivation

Shown below in Figure 6-12 is a simplified set-up of a section of the interferometer set-up. This figure illustrates why the objective's function is twofold. In the figure, the objective is represented as a double convex lens. Shown in (a), the objective is used in position 1 to magnify the MEMS device (real image) by setting up a virtual image at the

~123~

end of the CCD camera lens. This creates a real-time image used for aligning the electrical probes to the contact pads (electrical contact to the chip is required because the resonators are electrostatically actuated). After alignment of the probes to the pads on the MEMS chip is complete, the lens is then moved to position 2 (shown in (b)) as this coincides its focal point with the tip of the cantilever beam. The two lines in (b) represent the width of the laser beam and show that the entire laser beam is focused at the focal point (tip of the cantilever). This is very important because the laser is collinear upon reflection and passes back through the objective, ensuring coincident laser beams and the concentric circular fringe pattern at the photodetector.
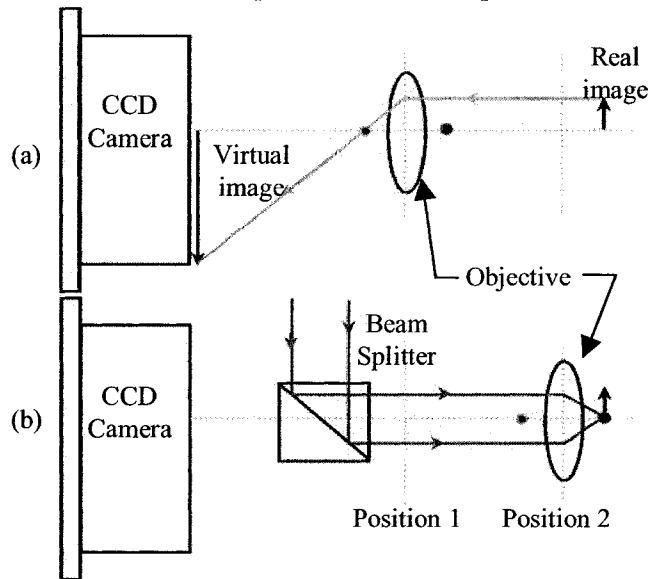
Figure 6-12: Dual function of objective in the interferometer set-up
(a) Objective in position 1 - used to magnify MEMS device (b) Objective in position 2 – used to focus laser beam on MEMS device

The problem with this set-up is that the laser spot can never be viewed with the CCD camera when it is focused on the end of the beam. This is a problem because if the objective is not positioned perfectly perpendicular to the laser beam (and keeps this position while being relocated), the focused spot size can move off of the intentioned location (i.e. the middle of the beam and the tip of the beam).

7.2 New Set-up

The objective in the set-up is replaced with a fixed lens and an external multiple-axis microscope replaces the CCD camera used as a visual aid. Also, the beam splitter cube is replaced with a 50/50 thin-film splitter to eliminate parasitic cube-face reflections in the path of the laser beam. The changes made to the set-up are shown in Figure 6-13 with (a)

being the original design (part of the schematic of Figure 6-2) and (b) illustrating the changes.
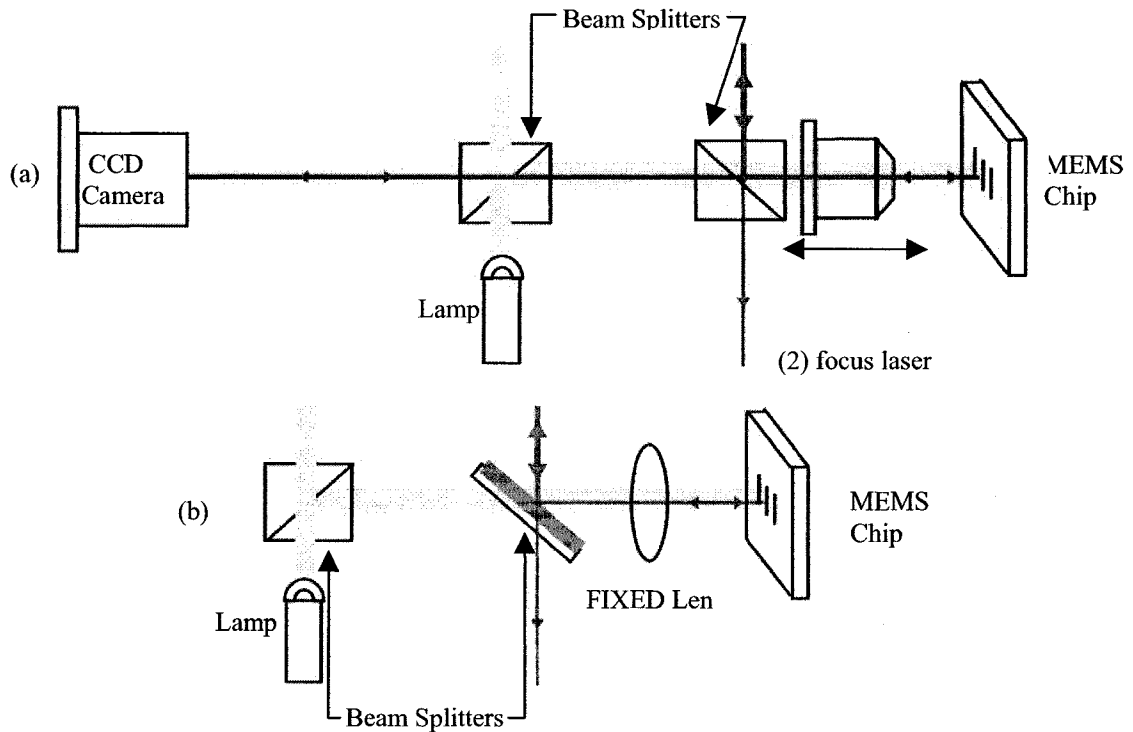
Figure 6-13: Schematic depicting change in interferometer set-up
(a) Original Set-up with CCD camera & translating objective; (b) New Set-up using an exterior microscope and fixed lens

A digital photo of the new set-up is shown in Figure 6-14 (for comparison to the set-up depicted in Figure 6-2 with changes of Figure 6-13 (b)) and the complete parts list is included in Appendix F.
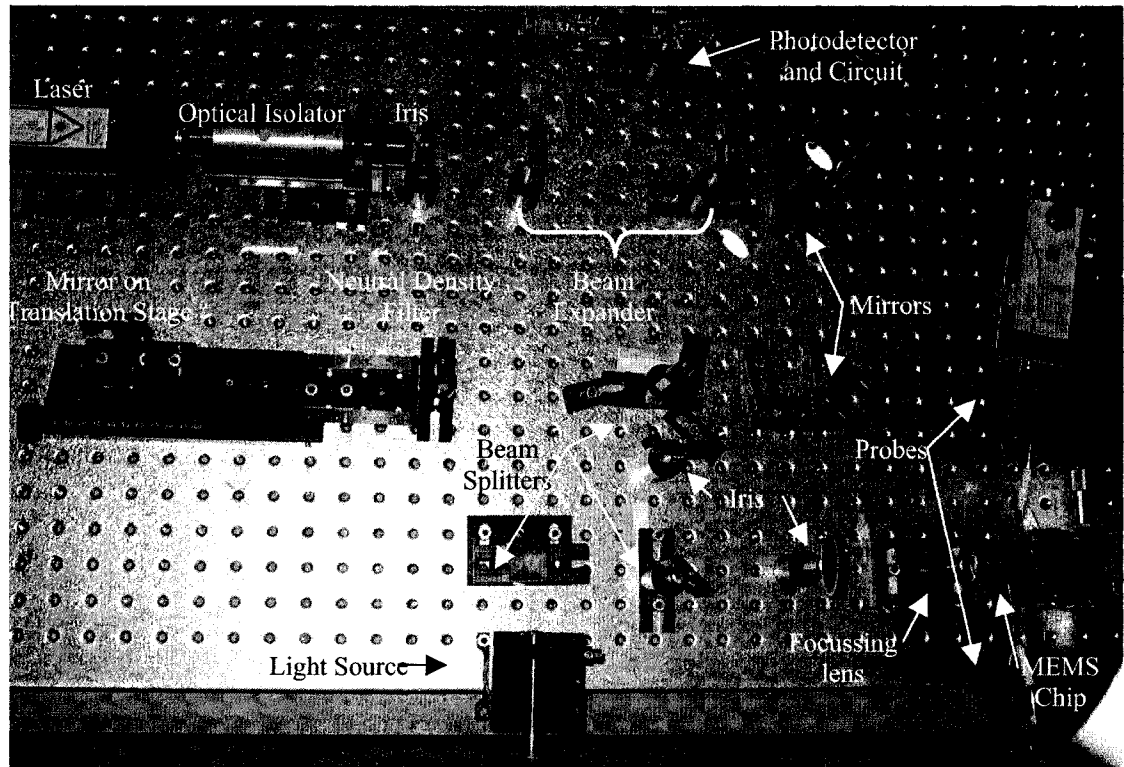
Figure 6-14: Digital photo of new set-up

Figure 6-15 (a) shows the multiple axis microscope and (b) shows the probes on translation stages and the tilt adjustment of the MEMS. The multiple axis microscope is very useful for aligning the probe tips to the actuation pads on the chip. The MEMS chip is also equipped with translations stages in 3 directions and tilt adjustment so that fine alignment can achieve perpendicular reflection. The set-up is now optimized for fine measurement like the movement of resonating cantilever beams in this work.

~126~
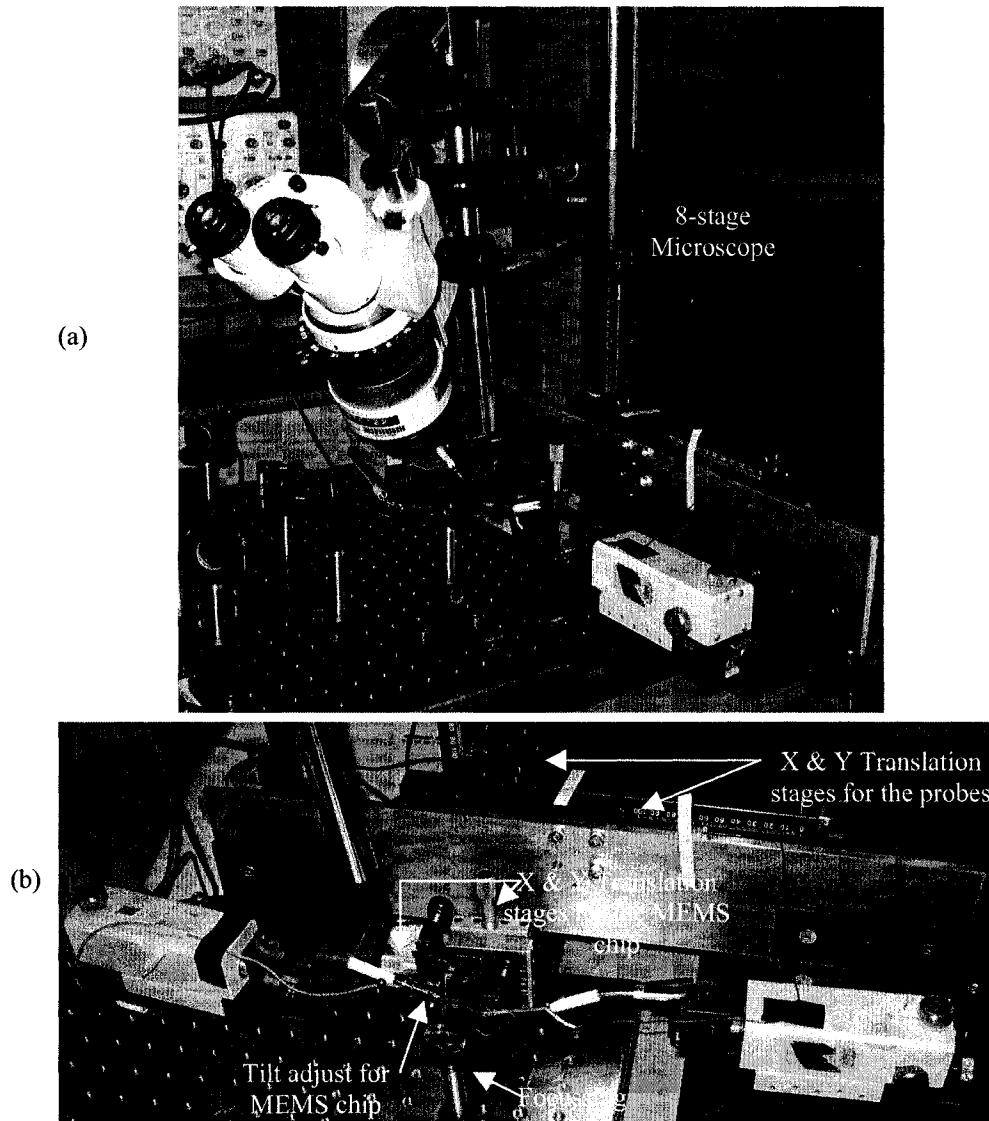
Figure 6-15: Close-up digital photos of set-up (a) Microscope in view (b) Probes in view

8 Conclusion

The set-up of an interferometer set-up used for the dynamic characterization of micromechanical resonators is presented in this chapter. Circuitry is tested to ensure that its usage in the frequency range required is acceptable. As well, many improvements are made to the interferometer not only to ensure that the interference pattern of the laser is correct, but also to ensure that this fringe pattern is maintained throughout the entire alignment, actuation, and characterization of the tested device. The following chapter

~127~

focuses on the characterization of the interferometer, and Chapter 8 unveils the results found for the micromechanical resonators used in this work.

Chapter 7 – Characterization of the Interferometer

1 Introduction

Characterization of the interferometer set-up introduced in Chapter 6 is presented in the following chapter. Expected interferometric signals are presented and their use to measure both displacement and resonant frequency of systems are explained. Following the theory for interferometric testing of dynamic structures, test devices and cantilever beams are used as independent methods for characterization of the set-up. These ensure that the photodetector circuit and method are giving accurate responses. Upon testing and characterization of the interferometer outlined in this chapter, the photodetector signals are analyzed and the quality and damping factors of the micromechanical resonators are presented in Chapter 8.

2 Expected Photodetector Signals

The expected signal sensed by the photodetector resembles a modulated signal because two separate phenomena are occurring simultaneously. The displacement of the beam causes it to pass through multiple interference minima/maxima (its displacement is greater than the wavelength of the laser). In addition, the beam is moving in a sinusoidal manner, which is controlled by the driving voltage frequency.

It is important to note that the photodetector is, in fact, only sensing one laser signal and not two signals, although the appearance of the signals resembles this situation. It is actually the movement of the beam that affects both the modulated frequencies. The beam moves a given distance at the driving frequency, where the displacement could be more than one fringe (resulting in a frequency of passing fringes that is within the driving frequency of the cantilever). The two situations influencing the change in intensity are further detailed below.

~129~

2.1 Change in Light Intensity – Interference Fringes

The intensity of light at the photodetector is expected to be a sinusoid with respect to movement of the object beam, directly related to the cantilever by which it is reflected. To most clearly explain interference fringes, the cantilever is first presented as moving with the same frequency as the applied voltage (i.e. without the doubling frequency phenomenon described in Chapter 3). The equation for the intensity of light at the photodetector is then [54]:

$$I = I_{max}[(1 + R) + 2\sqrt{R}\cos(2\pi\frac{\Delta x}{\lambda/2})] \qquad \textbf{Equation 7-1}$$

Where:

$I_{max} = (1 + \sqrt{R})^2$

R = net percentage of the reflected object beam (at photodetector)

Δx = change in displacement of the sample (perpendicular to the object beam)

λ = wavelength of the laser

The net percentage of the reflected object beam at the photodetector is expected to be roughly half of the reflected reference beam because of the neutral density filter explained in Chapter 6. Full destructive interference (or fringe minima) is then assumed to occur and constructive interference (or fringe maxima) occurs when [54]:

$$\Delta x = n * \frac{\lambda}{2}; \text{ Where n= 1,2,3, ...} \qquad \textbf{Equation 7-2}$$

Equation 7-2 establishes that as x varies (i.e. as the cantilever moves in the same path as the incident object laser beam), the photodetector detects successive maxima and minima with passing fringes at a distance of ½ the wavelength of the laser utilized. To clarify, if a cantilever beam is displaced 632nm in an interferometer set-up utilizing a HeNe laser (λ=632nm), two periods of intensity with respect to displacement occur, which are further referred to as two fringes occurring each time this displacement occurs.

~130~

2.2 Change in Light Intensity – Cantilever Movement

The sinusoidal function of interference fringes occurs within the time period of the cyclical movement of the beam. As was explained at the beginning of this section, each oscillation of the beam passes through multiple interference fringes. This affects the signal to the photodetector because within each period of movement (with respect to the frequency of the driving voltage), the cantilever reaches a maximum displacement, x_{max}, at ½ the period and then returns the same distance, x_{max}. For example, the cantilever reaches its maximum displacement at the maximum voltage potential difference (the peak of the driving signal sinusoid) and then returns the same distance to the beginning position at the minimum potential difference (the valley of the driving signal sinusoid). This displacement, as was first introduced in Chapter 3 is characterized as:

$$x(t) = C_{OP} \cdot (V_P + v_{AC}(t))^2$$

Equation 3-30

Where:

$v_{AC}(t) = V_i \sin(\omega \cdot t)$ [m]

V_i = Maximum amplitude of AC input voltage [m]

And the constant of proportionality, $C_{op} = \dfrac{\varepsilon_o \cdot (l_B - E_1) \cdot b_B}{2 \cdot k \cdot d_{BS}^2}$

Where:
l_B = length of the beam [m]
b_B = width of the beam [m]
k = spring constant of the beam [N/m] (Equation 3-7)
E_1 = distance to bottom electrode (actuation electrode) [m]

Now, if Δx is assumed to occur from $x = 0$, a sinusoidal movement, $\Delta x = x_{max} \sin(\omega \cdot t)$ for Δx in Equation 7-1. This is represented as:

$$I = I_{max}[(1 + R) + 2\sqrt{R} \cos(\frac{2\pi}{\lambda/2} \cdot x_{max} \cdot \sin(\omega \cdot t))]$$

Equation 7-3

~131~

Alternatively, for an electrostatically-actuated cantilever beam, where the displacement is affected by both a DC and AC applied voltage, Δx can be replaced by Equation 3-30, and the theoretical interferometry signal for the beam of this work is presented as:

$$I = I_{max}[(1 + R) + 2\sqrt{R}\cos(\frac{4\pi}{\lambda} \cdot C_{OP} \cdot (V_P + v_{AC}(t))^2)] \qquad \text{Equation 7-4}$$

In summary, the signal detected by the photodetector is manipulated by both the signal due to the passing of maxima and minima of fringes and the signal from the sinusoidal physical movement of the cantilever beam.

2.3 Examples of Interferometric Output

To illustrate, the expected photodetector signal output described above, a representation of Wylde and Hubbard's results are shown in Figure 7-1 below for two periods of movement [54]. In this experiment, the authors used interferometry to measure the displacement of micromachined beams. The exciting signal is shown in (a) and photodetector signals for two amplitudes are illustrated in (b) and (c) of the figure.

Period $T = 2\pi/\omega_s$
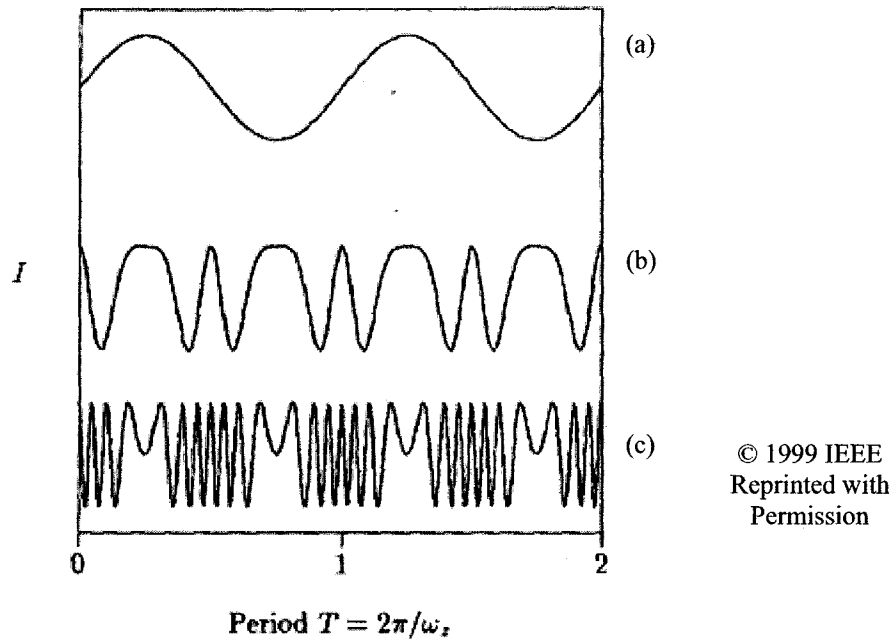
Figure 7-1: Input/output signal versus time for varying beam height, $x=x_{max}sin(w_2*t)$
(a) Exciting signal (b)Detector signal with low amplitude (c)Detector signal with a higher amplitude
[54]

The two influences on the signal are clearly shown in the above figure. Two periods are shown for the driving signal, and in (b) and (c) it can be seen that the displacement of the micromachined beams follows these periods but moves multiple fringes back and forth within each period of movement, creating the appearance that the interferometer signal is modulated on top of the sinusoidal movement of the cantilever beam. Because a HeNe laser is utilized in this experiment (λ=632nm), the authors report displacements as (b) 2 fringes or (2* 316nm/fringe) = ~0.6μm and in (c) 6.5 fringes or (6.5*316nm/fringe) = ~1.9μm. The authors compare the number of peaks and valleys of both (b) and (c) to the drive signal in (a); thus, they count the number of fringes and report use of Equation 7-2 for conversion to actual displacement representation. Utilizing Equation 7-3, Wylde and Hubbard's signals can be theoretically calculated shown below in Figure 7-2. Equation 7-3 thus accurately depicts the experimental interferometric signals of resonating microdevices.

~133~

Theoretical Interferometric Signals for Varying Beam Height
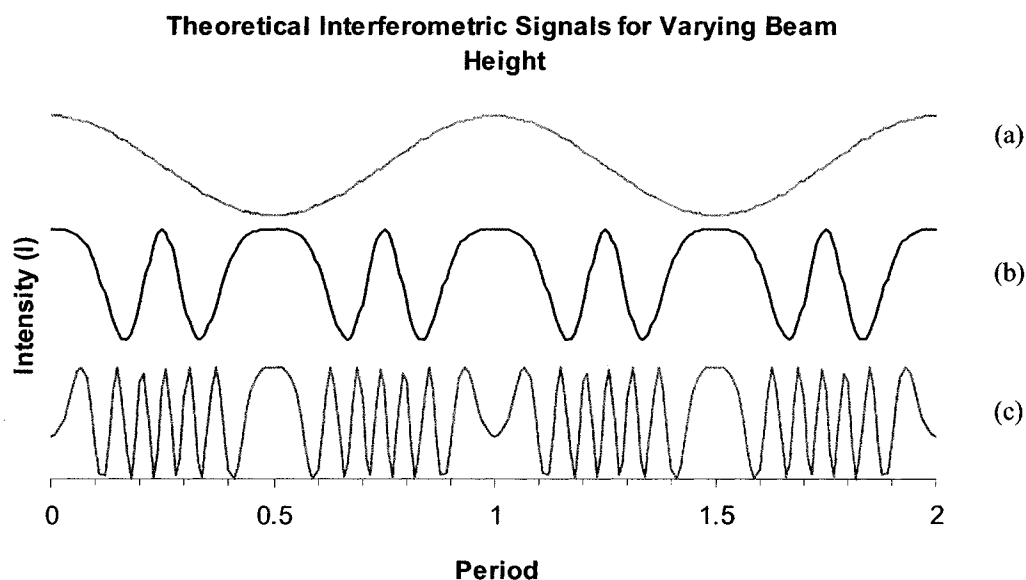
Figure 7-2: Input/output signal versus time for varying beam height, x.
(a) Exciting signal (b) Detector signal with amplitude = 2 Fringes (c) Detector signal with amplitude =
6.3 Fringes

The interferometry method is further expanded to characterize the resonant frequency of the samples. To explain, for a given amount of energy at a certain frequency, an oscillator moves with a particular amplitude. For the same amount of energy at the resonant frequency of the device, the oscillator will move with increased amplitude. Monitoring the amplitude of the oscillator at different frequencies for the same input energy is a well-suited technique for isolating at which frequency a resonance occurs. In Figure 7-3, Annovazzi-Lodi *et al.* presented the displacement of an oscillator at different frequencies by showing their respective, interferometric outputs [143]. Shown in Figure 7-3, the maximum amplitude of oscillations occurs at 6183.0Hz, indicating a resonance at that frequency, and diminishes with increasing or decreasing frequency from the resonance, as indicated by the number of fringes occurring within each period of the driving signal. It is also noted that the amplitude of the signal used to excite the frequencies tested.

~134~
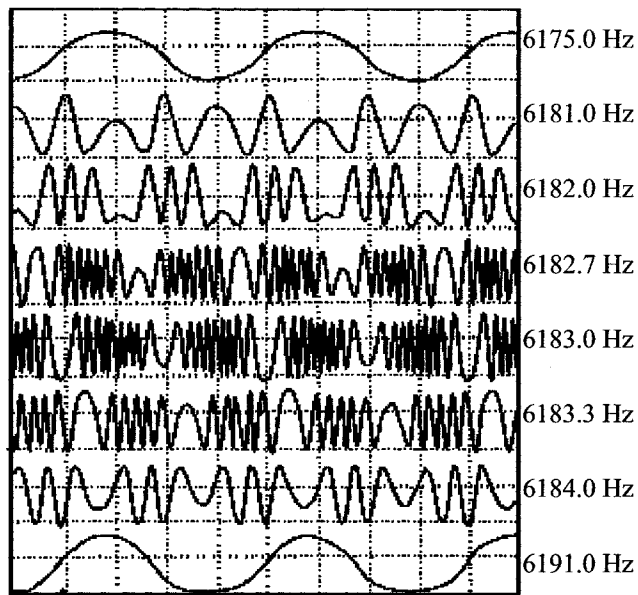
Figure 7-3: Representation of resonance characterized by interferometry
Increased displacement is shown by increased modulation of signal [143]

Similar results, as illustrated in Figure 7-3, are expected to occur for testing of the micromechanical resonators. Presented in the following section, are the results for the testing and characterization of the interferometer set-up with respect to displacement and frequency.

3 Characterization of Interferometer

Before the system is utilized to obtain amplitude of oscillation displacements or resonant frequencies of the micromechanical resonators in this work, there are two important functions of the interferometer in need of characterization: (1) the output with respect to resonance and whether or not the circuitry is able to respond within the required frequency range, and (2) how much movement is required to cause one fringe. Theoretically, it is expected that for deflections beyond 316nm, a second fringe begins to form. This claim is in need of verification to validate the analysis and experimental set-up.

~135~

3.1 Amplitude: Characterizing Fringes in Terms of Displacement

Shown below in Figure 7-4 is the side profile (i.e. along the length) of a $2\mu m$-thick, $200\mu m$-long standard cantilever beam taken with a Zygo optical profilometer. The graph in the figure shows a measurement of $5.1\mu m$ taken from the tip of beam to the surface of the bottom electrode. The measurement correctly measures a beam with a $2\mu m$-thick silicon layer, a $2\mu m$ fabricated gap, and an addition $\sim 1\mu m$ of the gap at the tip caused by the stress of the surface gold (refer to Section 2.3 of Chapter 5 for the stress analysis of the gold film).
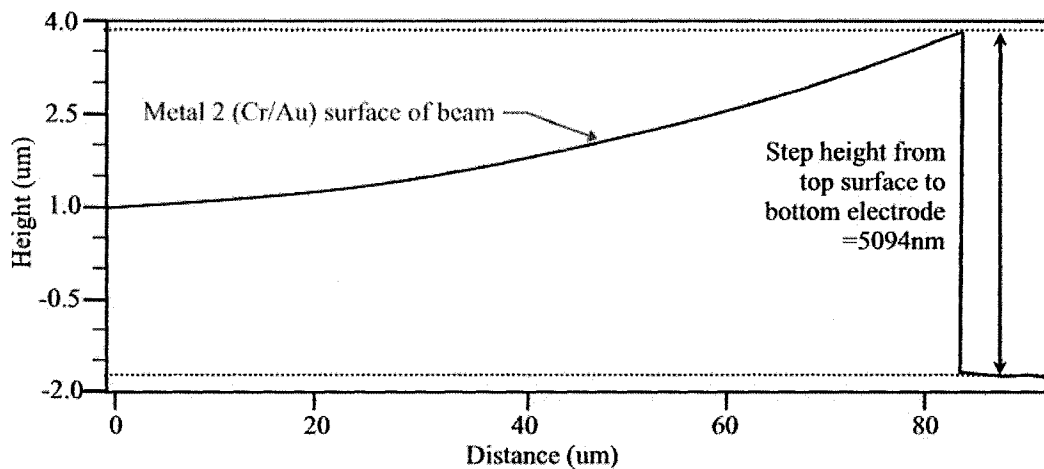
Figure 7-4: Side profile of $2\mu m$ thick, $200\mu m$ long cantilever with no applied voltage

Voltage of $21V_{DC}$ is applied to the top metal of the beam while the bottom electrode is held at ground. With a potential of $21V$, Figure 7-5 below shows a Zygo measurement from the tip of the beam to the surface of the bottom electrode as being $4.7\mu m$. Comparing this result with the previous figure, one may derive a conclusion that a voltage potential of $21V$ causes a deflection of 400nm for a standard beam.
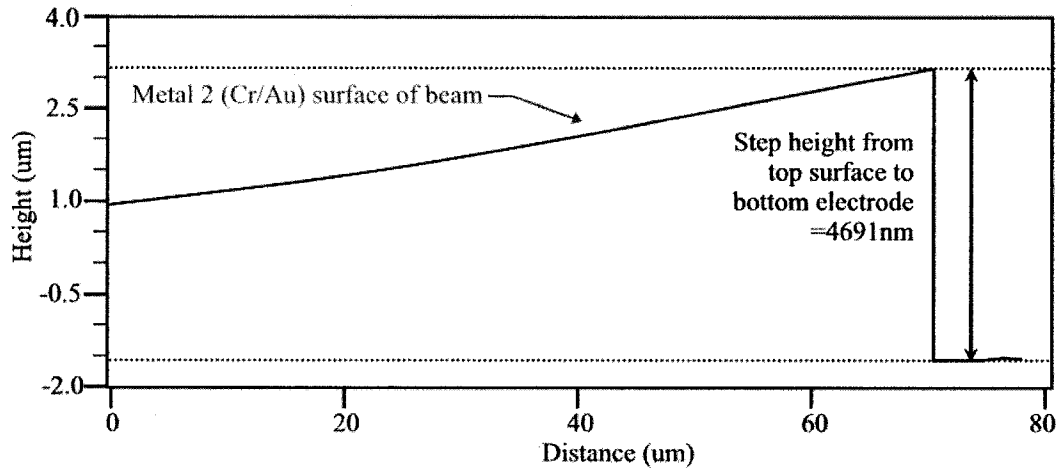
Figure 7-5: Side profile of 2μm thick, 200μm long cantilever with 21V applied voltage

This is a very important result because it can be used to characterize the amplitude change in the interferometer set-up. Recall from the previous section that one fringe represents 316nm of displacement. The theoretical signal for a beam driven by a biased driving voltage of $V_{beam} = 4V_{DC} + 20V_{p-p}$ is shown in Figure 7-6. Shown in the figure is (a) the intensity of the signal as measured by the photodetector calculated with Equation 7-4; (b) the voltage potential applied between the beam and bottom electrode; (c) the expected displacement at the tip of the beam for the applied voltage shown in (b), which is calculated using Equation 3-30. Since the AC voltage has a magnitude of 10V, the magnitude of the total voltage can be as large as 14V and as low as 0V. The amplitude of the photodetector response reaches a maximum when 14V potential is applied and a second, lesser maximum when a potential of 6V is applied. It is clear from the graph that a smaller signal results when a smaller voltage potential is applied because the beam's deflection is less for less potential. It is important to point out that both potentials cause a displacement less than 316nm because the signal remains less than one fringe.

~137~
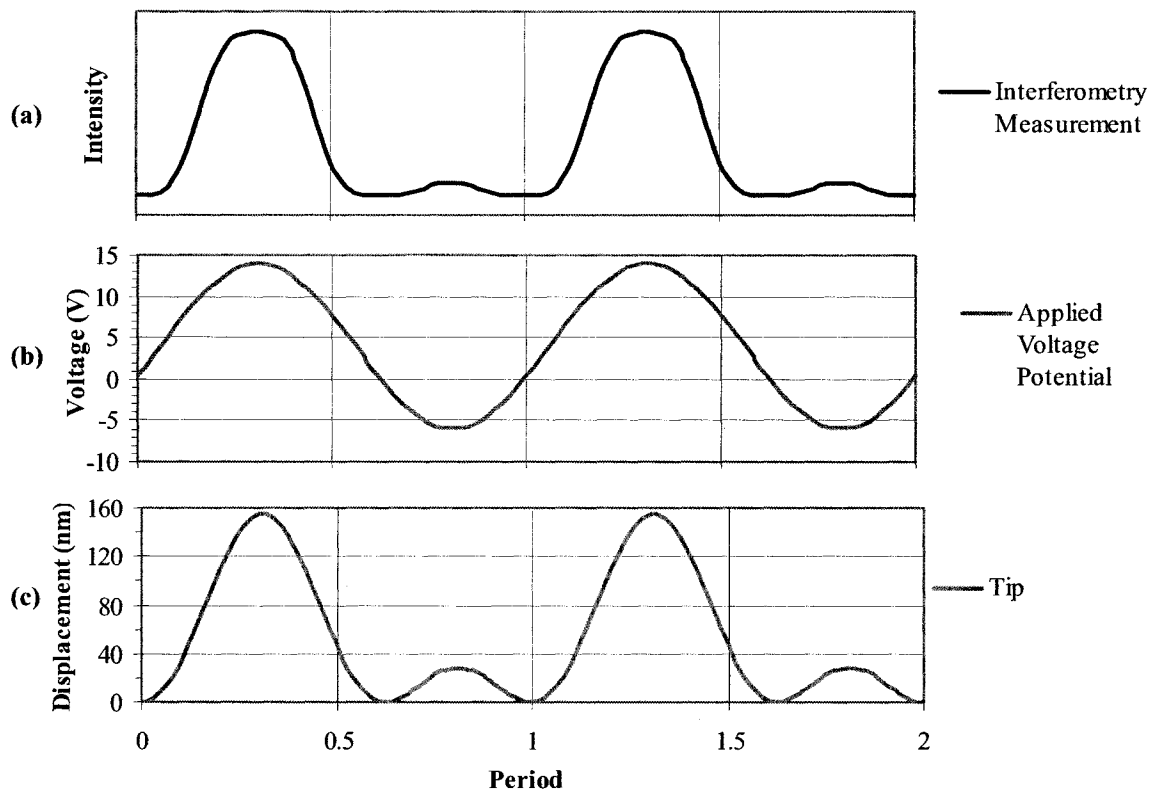
Figure 7-6: Theoretical dynamic signals for standard beam
(a) Intensity of signal at the photodetector (Equation 7-4) for moving beam; (b) Applied voltage potential between beam and bottom electrodes (4 V_{DC} + 20V_{p-p}) (c) Expected displacement at the tip of the beam with applied voltage from (b) (Equation 3-30)

Now, shown below in Figure 7-7 is the experimental photodetector response for a standard beam driven with 20V_{p-p} at 1kHz with a bias of +4V_{DC}, i.e. V_{beam} = 4V_{DC} + 20V_{p-p}. The signal's trend is very much represented by the expected signal shown in (a) of Figure 7-6. There is indeed a difference in the amplitude of the intensity between the two maximas caused by the applied voltage potentials of +14V and –6V. However, the difference in the amplitude of the two peaks is much smaller in the experimental results. This can be attributed to the fact that the cantilever does not move entirely perpendicular to the incident laser beam during movement. The greater the cantilever is displaced, the greater the angle of reflection for the laser beam. Alignment of the interferometer was done with the cantilever in rest position so the displacement from this alignment, causes a reduction of the recombined signal (shown by intensity at the photodetector).

~138~

Beam Response to +14V/-6V @ 1kHz
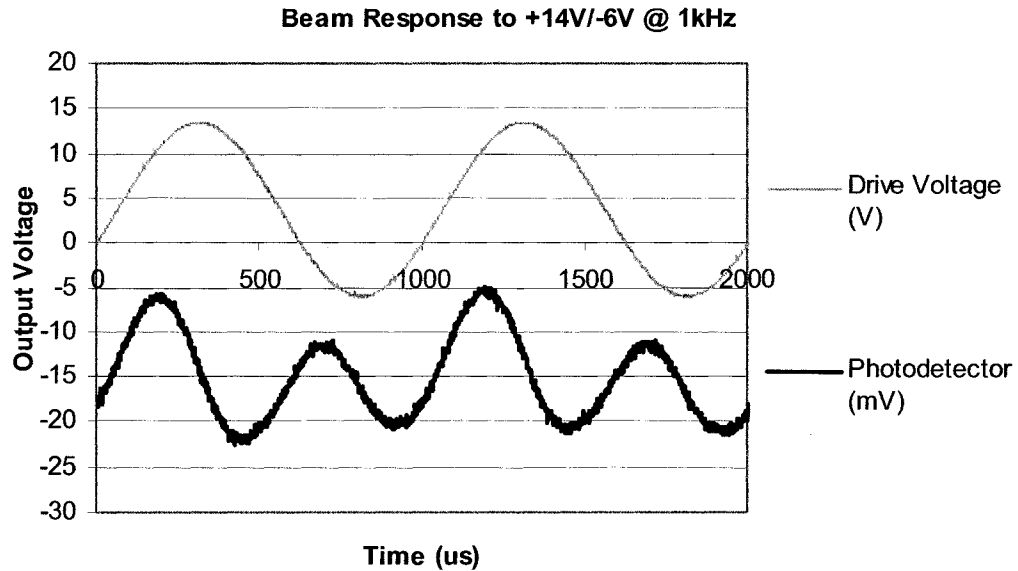
Figure 7-7: Experimental photodetector signal for standard beam (x=<200nm)
Displacement is shown to be less than one fringe as shown by the photodetector signal coincident
with each period of beam movement

This same beam is tested with the interferometer under the same applied voltage (20V_{p-p} at 1kHz) but the bias is increased to 10V_{DC} from 4V_{DC}. This increases the maximum voltage potential to 20V at a frequency of 1kHz and the amplitude of the cantilever has one maxima at this same frequency. The photodetector response expected for this situation is shown below in (a) of Figure 7-8. However, the experimental result, shown in Figure 7-9, exhibits a response that more closely follows the situation of an applied voltage of ~15V_{p-p} (using Equation 7-4 and shown in (b) of Figure 7-8) or a displacement of ~250nm (using Equation 7-3 and shown in (c) of Figure 7-8 for each period of the exciting signal. The difference between the expected signals due to an applied voltage and the actual signals is because more voltage is required to displace the beam than was expected because of the intrinsic film stress in the beam's Cr/Au film. This was explained in Chapter 5 and illustrated in Figure 5-9. The theoretical signal for a displacement (Equation 7-3) is deemed a more appropriate way to predict and compare interferometric results because of the discrepancy between the expected response due to an applied voltage and the actual displacement.

~139~
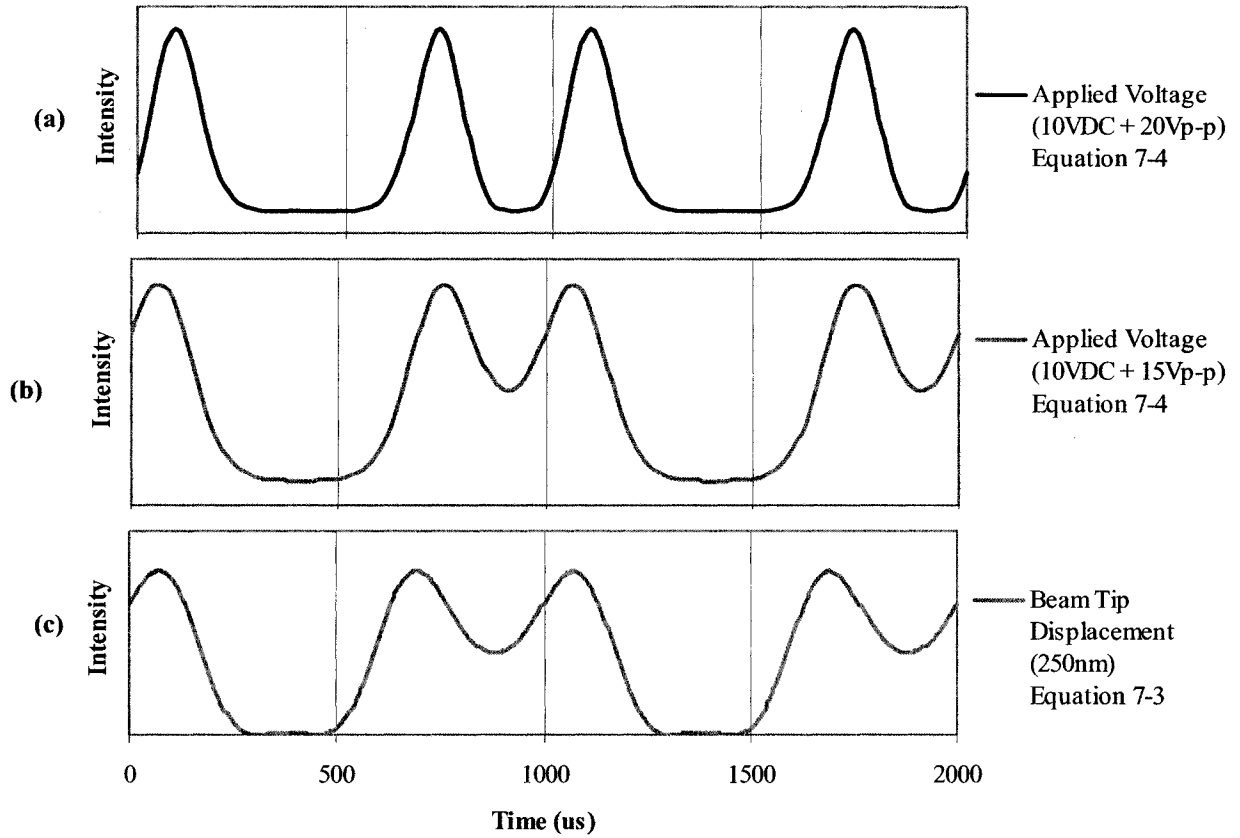
Figure 7-8: Theoretical photodetector signals using either applied voltage or displacement
(a) Intensity of signal at the photodetector (Equation 7-4) for applied voltage potential between beam and bottom electrodes (10 V_{DC} + 20V_{p-p}) (b) Intensity of signal at the photodetector (Equation 7-4) for applied voltage potential between beam and bottom electrodes (10 V_{DC} + 15V_{p-p}) (c) Intensity of signal at the photodetector (Equation 7-3) for beam moving x_{max} = 250nm

~140~

Beam Response to 20VPP @ 1kHz
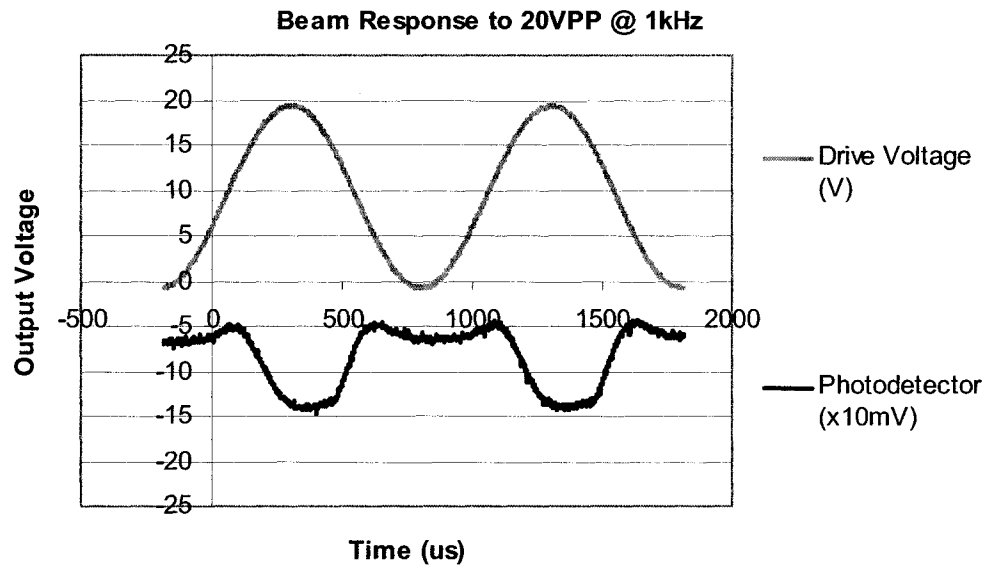
Figure 7-9: Experimental photodetector signal for standard beam driven at 20V$_{PP}$
Displacement is shown to be ~250nm when compared to Figure 7-8, inferred by the second valley in
the photodetector signal present for each period of beam movement

It is concluded that the beam's amplitude at a voltage potential of 20V is ~250nm. Independent results from the optical profilometer (Zygo) and the interferometer yield this same result. It is also noted that this test is done at a frequency that is far enough away from the expected resonance (i.e. expected resonance = 58kHz; characterization = 1kHz); thus, no increased amplitude due to resonant behaviour factors into the photodetector response during characterization. A preliminary demonstration of applicability of the interferometer is done with a commercially available, easy to align, piezoelectric buzzer and is discussed below.

3.2 Resonance: Measuring a Piezoelectric Buzzer

To demonstrate the applicability of our system and theory to a dynamic system, a commercial Piezoelectric Buzzer is used (Radio Shack, model 273-059). This buzzer contains a piezoelectric disk inside its casing that resonates at an audible frequency of ~2.7kHz with applied DC voltage. The disk offers a relatively large reflecting surface in order to characterize resonant behaviour. Unfortunately, we were unable to successfully disassemble the device to independently characterize displacement with respect to applied voltage (such as with the Zygo), and this hindered a more detailed description. In

~141~

addition, no schematics of this circuitry are available but all included specifications are shown in Table 7-1 below.

Table 7-1: Specifications of the Piezoelectric Buzzer

Manufacturer	Radio Shack
Manufacturer's Part Number	273-059
Voltage Range	$3.0\text{-}20\text{V}_{DC}$
Rated Voltage	12V_{DC}
Current Consumption	10mA max. @ 12V_{DC}
Sound Pressure Level	76dB min. @ $30\text{cm}/12\text{V}_{DC}$
Resonant Frequency	$2700\pm500\text{Hz}$
Operating Temperature	-20°C to +60°C
Mounting Centres	29mm (1 9/64")

As the voltage is increased to the buzzer, the audible signal becomes louder, thus indicating that the disk inside is moving with an increased amplitude. For the experiment, the buzzer is mounted vertically and the laser is focused inside the casing onto the piezoelectric disk inside. The buzzer is then adjusted in all axes so that the piezoelectric disk is perpendicular to the laser. This ensures that the laser reflects back onto itself, maintaining good alignment within the set-up, creating
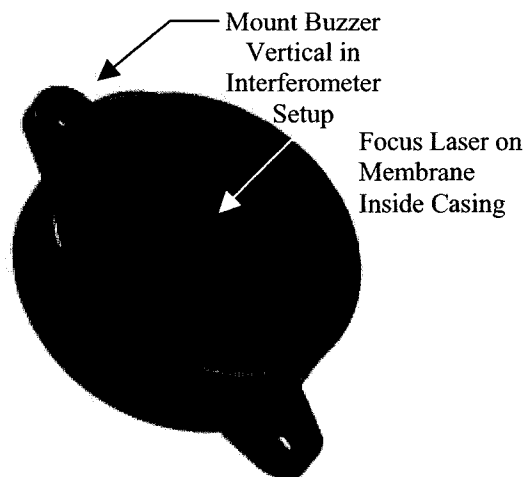
Mount Buzzer Vertical in Interferometer Setup

Focus Laser on Membrane Inside Casing

Figure 7-10: Picture of piezoelectric buzzer

a concentric fringe pattern at the photodetector (see Chapter 6, Section 7 – "Nature of Fringes" for additional explanation). A DC signal is then applied to the buzzer and a repeating pattern of fringes is found to occur at 2672Hz, which is the resonant frequency. This assumption is further proven because as the voltage (V_{DC}) is increased (increasing the amplitude), the fringe pattern still repeats at a frequency of 2672Hz, but the number

~142~

of fringes within the pattern increases. The resonant frequency is thus 2672Hz and is within the specifications of the device. The results for a variety of applied voltages are shown below in Figure 7-11. For each voltage shown in the table, one period of the resonating disk is displayed.

Figure 7-11: Photodetector output for a resonating piezoelectric buzzer

Drive Voltage (V)	Photodetector Output for a Resonating Piezoelectric buzzer with Applied V_{DC}: x-axis (µs) y-axis (mV)
(a) 0.815	
(b) 1.045	
(c) 1.384	
(d) 1.799	
(e) 2.054	
(f) 2.759	
(g) 3.541	
(h) 4.180	
(i) 5.152	
(j) 6.032	

~143~
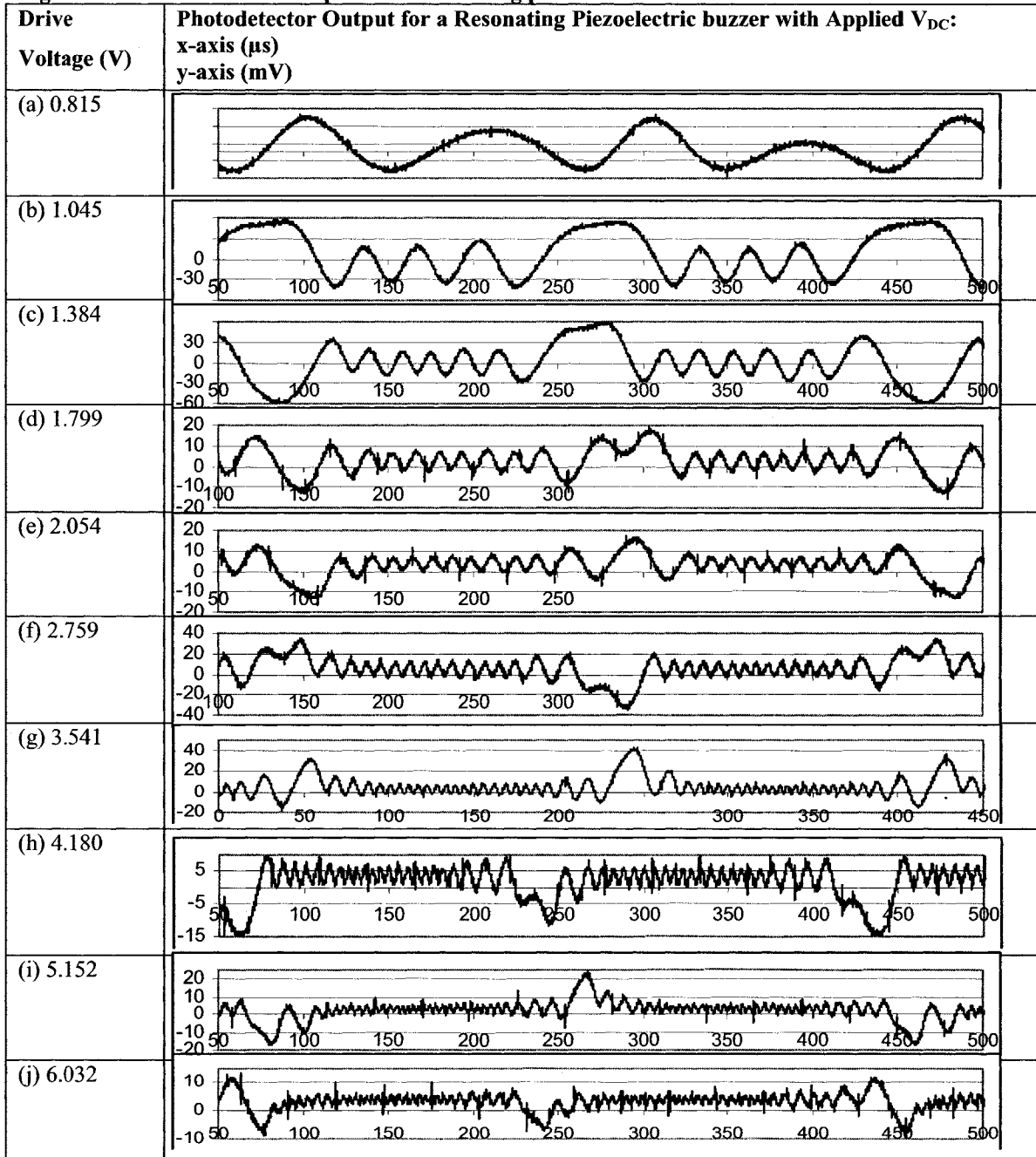
Further examining the table and using Equation 7-2, one deduces that an applied voltage of (a) $0.815V_{DC}$ causes an amplitude, $x_{max} = 2\lambda$; (g) $3.541V_{DC}$ an amplitude, $x_{max} = 24\lambda$; and (j) $6.032V_{DC}$ an amplitude of $x_{max} = 32\lambda$. Because a red laser ($\lambda=632$nm) is used, this represents a deflection of (a) 1.26μm, (g) 15.17μm, and (j) 20.22μm.

Although the buzzer resonates at a lower frequency than the standard beam to be tested (2.6kHz vs. an expected 54kHz), these results verify two important points:

(1) With increased amplitude of the test device, there is corresponding increase in the number of fringes, which is the same qualitative behaviour as was expected (e.g. as in Figure 7-1).

(2) As shown in (j) of Table 7-2, the photodetector can detect at least an amplitude change of 64 wavelengths (32 increasing and 32 decreasing) for each period at 2.7kHz. Assuming this is the maximum speed at which the photodetector operates, by using a simple ratio, the maximum displacement at any frequency can be found. For example, 64 wavelengths are detected at 2.7kHz and this is equated to solve for the number of wavelengths possible at a frequency of 54kHz. It is thus found that a minimum detection of 3.2 wavelengths is possible at 54kHz. This equates to a 2μm deflection, which corresponds to the maximum distance the cantilever beam can travel before it reaches the bottom of the gap. The photodetector circuit is thus verified as being capable of detecting the increased number of fringes at resonance of the cantilever beams.

4 Threshold Accelerometer Testing

To aid in the troubleshooting and characterization of the interferometer, devices with multiple fringe motion are utilized. Prototype threshold accelerometers borrowed from Micralyne Inc., manufactured in 1990, are chosen because they are a series of different length cantilevers with large open cavities underneath them. These cavities do not restrict movement of the beam, so large displacements, represented by multiple fringes, are achievable. The device is shown below in Figure 7-12.

4.1 Theoretically Predicting Resonance

The same calculations as explained in Chapter 3 are used to calculate the theoretical resonance of the eight cantilevers on a die. The material of the cantilever beams is SiO_2 and the electrodes are made of gold. Because no dimensions are documented for the device, characterization of both the thickness and lengths are necessary, in accordance with the method provided below.
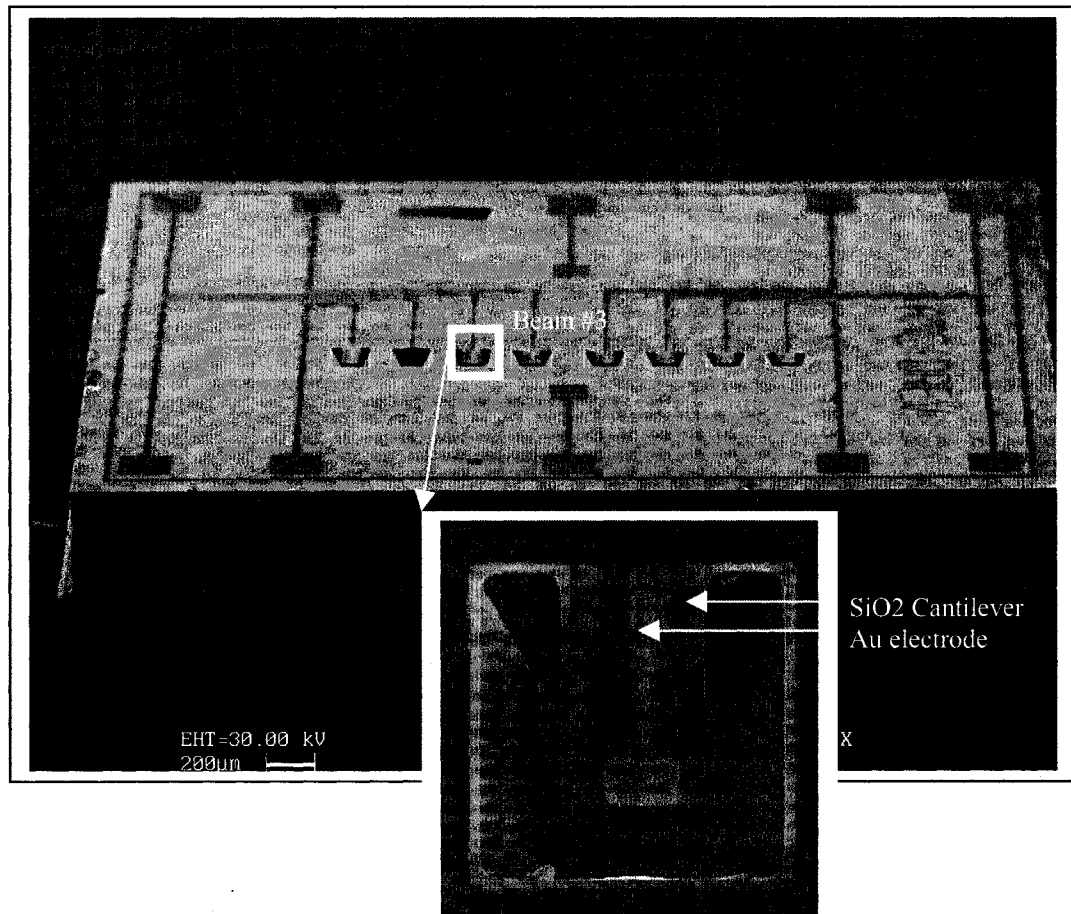
Figure 7-12: Layout of prototype threshold accelerometer
Photos taken with Leica Electron Optics, Model: Leo 435VP

4.1.1 Determining Thickness

The thicknesses are determined from a SEM photo taken at 84° shown in Figure 7-14. Measurements are then adjusted to represent more accurately the actual thickness by converting the thickness as if measurements are taken at 90°. A schematic representing this calculation is shown to the left in Figure 7-13.

~145~
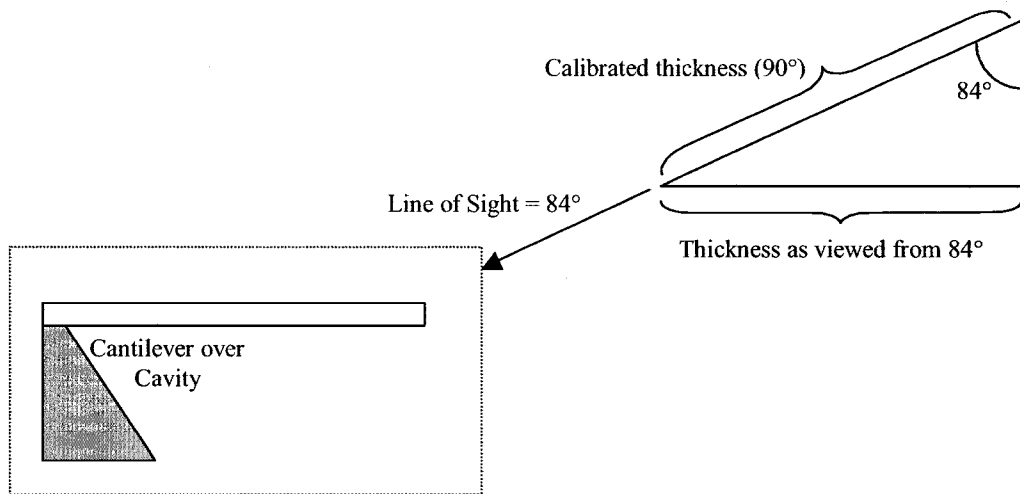
Figure 7-13: Calibrating thickness measurements taken at an angle
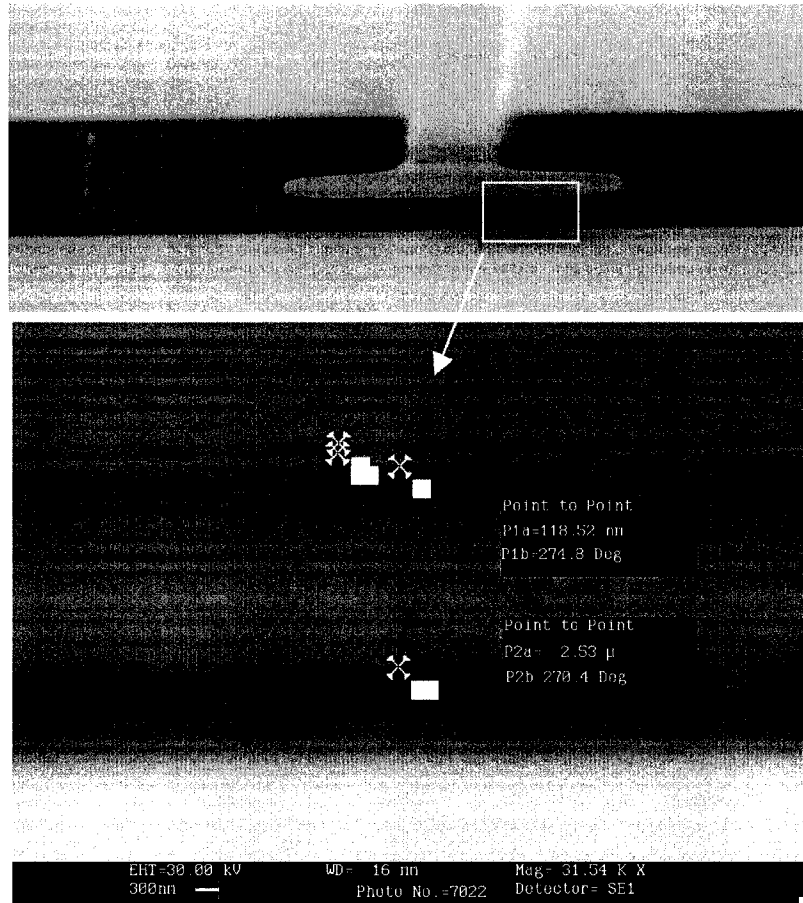
Figure 7-14: SEM cross section of cantilever beam
(a) Picture of beam taken at 84° (b) Close-up of section noted
Photos taken with Leica Electron Optics, Model: Leo 435VP

~146~

The calibrated thicknesses for the top metal layer and the SiO_2, respectively, are:

$$T_{90°} = \frac{T_{84°}}{\sin 84°} = \frac{118nm}{\sin 84°} = 119nm$$

$$T_{90°} = \frac{T_{84°}}{\sin 84°} = \frac{2.53\mu m}{\sin 84°} = 2.54\mu m$$

4.1.2 Determining Length of Beams

The lengths are also measured using the SEM from a direct overhead view. An example is shown below for beam #4 in Figure 7-15.
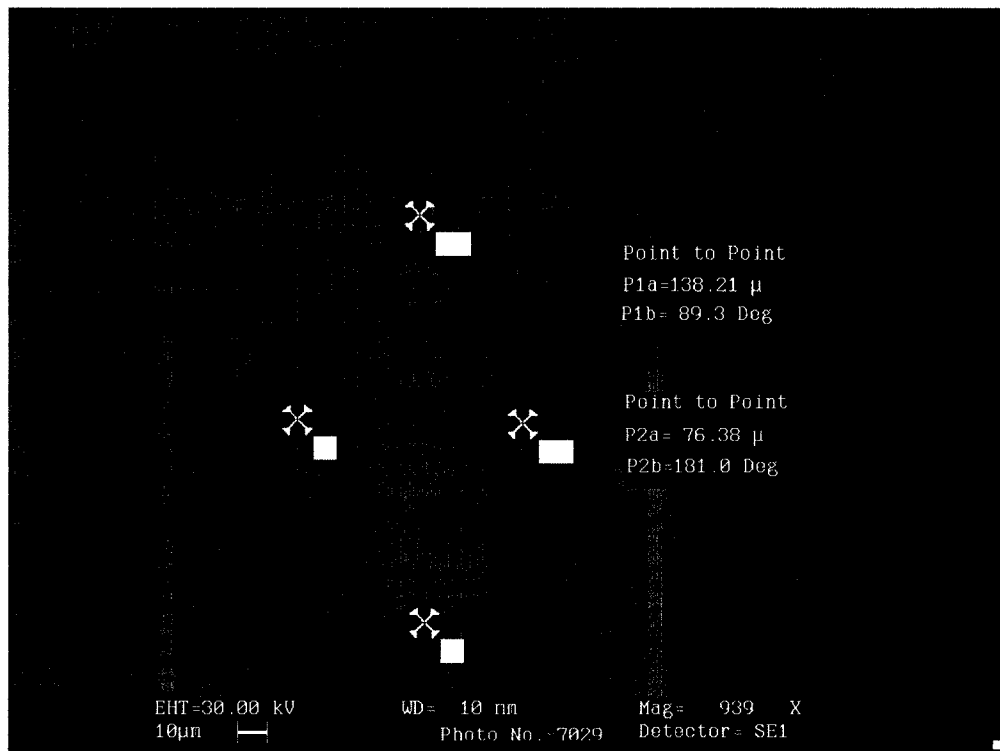
Figure 7-15: Overhead SEM of a cantilever for measurement
Photos taken with Leica Electron Optics, Model: Leo 435VP

The calibrated measurements and the material properties used in the calculations are summarized below in Table 7-2.

~147~

Table 7-2: Properties Used in Resonance Calculations

Elastic Modulus (Au)	6.13×10^{11} N/m^2
Elastic Modulus (SiO$_2$)	7.17×10^{10} N/m^2
Density (SiO$_2$)	2200 kg/m^3
Thickness of Au	119 nm (adjusted from 84°)
Thickness of SiO$_2$	2.54 ± 0.1 μm (adjusted from 84°)
Length of Beams (μm):	Beam #1 = 168.61
(Note: measured ± 0.5 μm)	Beam #2 = 158[‡‡]
	Beam #3 = 149.12
	Beam #4 = 138.21
	Beam #5 = 128.95
	Beam #6 = 119.02
	Beam #7 = 108.46
	Beam #8 = 97.33

4.2 Measurement of Resonance with Interferometer

The prototype threshold accelerometer chip was mounted perpendicular to the incident object beam and each of the eight cantilever beams is tested. Each beam tip is aligned to the laser spot, actuated at different frequencies, and the photodetector response recorded. Methods of actuation and alignment, as well as the results, are discussed below.

4.2.1 Set-up

The cantilevers on the prototype threshold accelerometer chip do not have bottom electrodes; thus, one cannot electrostatically activate them. However, mechanical actuation is a method available and is achieved by using a piezoelectric tube. The set-up is shown in Figure 7-16 below.

[‡‡] Used 158μm as a best guess effort because beam broke during testing.

~148~
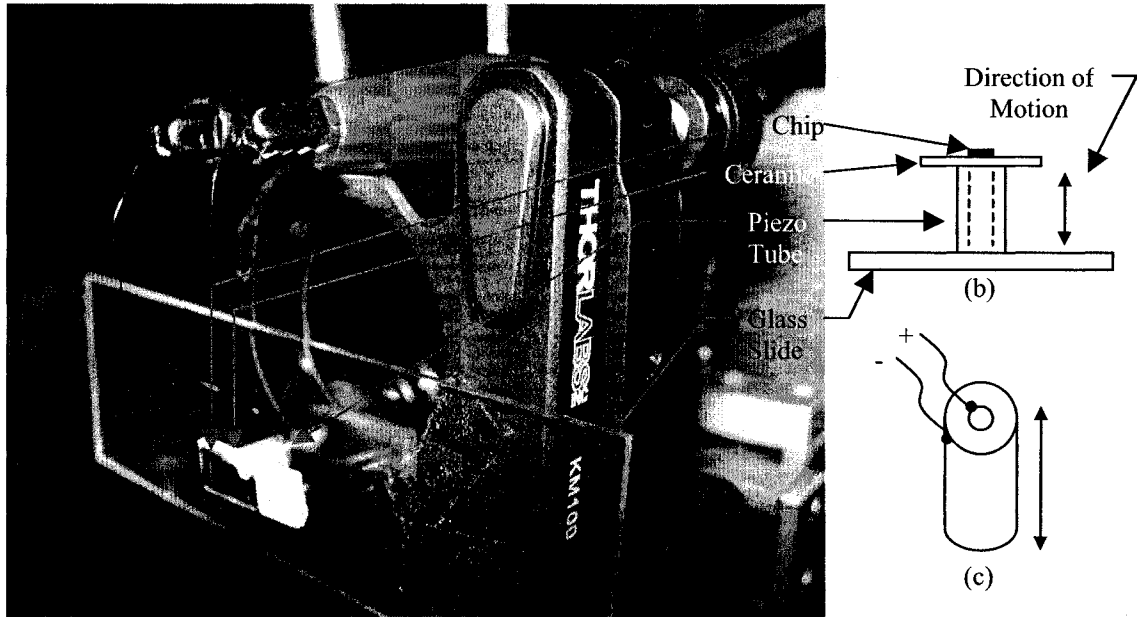
Figure 7-16: Set-up for actuation of prototype threshold accelerometer chip
(a) Digital photo of actual set-up (b) Schematic (c) Piezoelectric tube[§§] (illustrating the wire
connections). Photos taken with Leica Electron Optics, Model: Leo 435VP

Referring to both the (a) and the schematic shown in (b) of the above figure, the actuation set-up is explained. On a glass slide, a piezoelectric tube[§§] is connected upright; a ceramic slide is then glued to the other end of the piezoelectric tube, and the test chip attached directly to the ceramic slide. The piezoelectric tube is made from a ceramic material that changes shape when a voltage is applied to it. Movement in the longitudinal direction of the tube is produced when a voltage is applied to the entire interior electrode surface relative to the voltage on the entire outer voltage. A schematic illustrating the wire connections to the piezoelectric tube is illustrated in (c) of the above figure. Because the inner and outer surfaces have to be isolated from each other, attaching the silicon chip directly to the top surface causes a short. The ceramic slide is used for its isolating properties to alleviate this.

[§§] Model # unavailable, Dimensions: OD=4mm, ID=2mm, Height=7mm

~149~

When an AC signal is applied to the leads, the tube vibrates at the same frequency as the driving signal. Before the mechanical actuation method is applied to the cantilevers, the frequency with which the piezoelectric tube is swept from 1-100 kHz with an actuation voltage of $3V_{p-p}$[***]. The interferometer is used to characterize the movement of a solid, reflective surface attached to the end of the piezoelectric tube instead of the MEMS chip (Figure 7-16). This test is necessary to eliminate any parasitic resonances caused by the piezoelectric tube in this frequency range that could lead to misleading results. Basically, if peaks, resonances, or any other irregularities had been found, they could have confused resonances caused by the cantilever beams. However, no resonance of the piezoelectric tube was found in the range of 1-100kHz as is shown in Figure 7-17 because the intensity of the signal at the photodetector remains stable. If a resonance were present, an increase in intensity of the signal would be seen at the photodetector because the driving voltage of the tube caused a signal less than one fringe. In other words, the displacement of the tube caused less than the maximum intensity of the signal and any increase in displacement (due to a resonance) would cause an increase in the intensity. The piezoelectric tube was not calibrated further with respect to displacement because of the confidence in Equation 7-4 to assess the amplitude of movement. Upon the satisfactory frequency response of the piezoelectric tube, the above actuation method is applied to the test die of cantilever beams and the displacement with respect to frequency of each of the cantilevers is monitored. At resonance of a cantilever, the amplitude of the beam is far greater than the motion created by the piezoelectric tube. The results are presented below.

[***] 15 MHz Function Waveform Generator Agilent 33120A
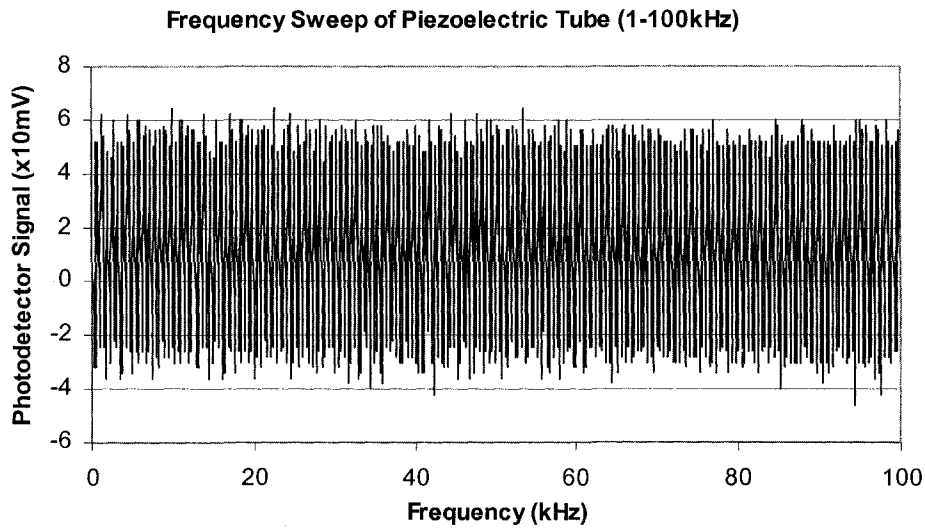
Figure 7-17: Piezoelectric tube amplitude response with frequency

4.2.2 Results

Figure 7-18 below displays a series of photodetector responses to driving frequencies. The response is similar to Figure 7-3, and, thus, the expected signal for a resonating cantilever is achieved. From the table, the maximum number of fringes occurs at 72.8 kHz, thus indicating a maximum displacement at that frequency, and implying resonance. Using Equation 3-11, the theoretical resonance is valued at 73.8 kHz and the measured result is only 1.3% lower. In addition, when compared, all the results are within the uncertainty of the calculation. The uncertainty in the theoretical calculation is due to the uncertainties in the measurement of the thickness ($\pm$ 0.1μm) and length ($\pm$ 0.5μm) of the beam.

~151~

Figure 7-18: Resonance of SiO₂ beam characterized by interferometry

Drive Frequency (kHz)	Photodetector Output 1st beam at $3V_{p-p}$: x-axis (μs) y-axis (mV)
70.8	
71.5	
72.0	
72.4	
72.6	
72.8	
73.1	
73.3	
73.8	
74.2	

~152~
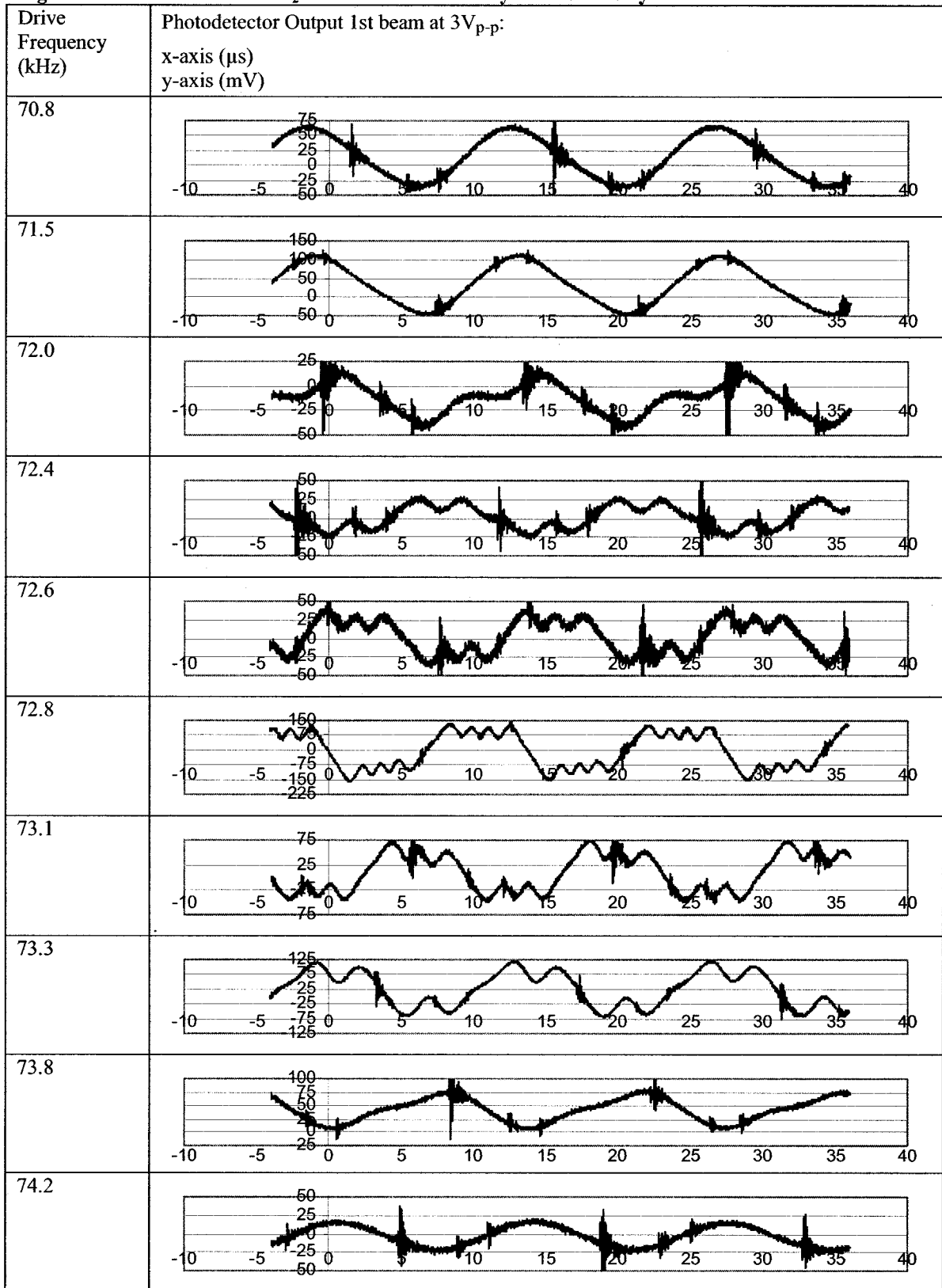
A summary of the 8 cantilever beams is shown below in Table 7-3. The measured resonance for each beam is compared with the expected, calculated resonance. They are all within error.

Table 7-3: Summary of Cantilever Resonances for Threshold Accelerometer

Beam Length (μm)	Calculated Resonance (kHz)	Measured Resonance (kHz)
168.61 ± 0.5	73.8 ± 3	72.8 ± 0.2
158[†††] ± 0.5	84.1 ± 4	81 ± 0.2
149.12 ± 0.5	94.4 ± 4	93.4 ± 0.2
138.21 ± 0.5	109.9 ± 5	107 ± 0.2
128.95 ± 0.5	126.2 ± 6	123.8 ± 0.2
119.02 ± 0.5	148.2 ± 7	145.3 ± 0.2
108.46 ± 0.5	178.4 ± 9	171.7 ± 0.2
97.33 ± 0.5	221.6 ± 11	205.9 ± 0.2

5 Conclusion

This chapter presents the testing and characterization of the interferometer discussed in the previous chapter. Independent methods measuring movement of the standard cantilever beam are used to verify that one fringe, in fact, measures half a wavelength of the laser utilized. A piezoelectric buzzer is used to verify the fact that increasing displacement causes increasing fringes while a test chip with eight lengths of cantilever beams is tested for their resonances. The interferometer set-up is deemed adequately tested and characterized and is ready for the testing of the micromechanical resonators. This work is presented in the following chapter.

[†††] Used 158μm as a best guess effort because beam broke during testing.

Chapter 8 - Measurements with Interferometry

1 Introduction

This chapter includes the interferometric results that evaluate the damped mechanical oscillator, referred to as the micromechanical resonator. Steady state and transient behaviours are analyzed resulting in the resonant frequency, the quality factor (Q), and the damping coefficients for $10\mu m$ and $25\mu m$ wide standard beams.

2 Equation of Motion for Micromechanical Resonator

The equation of motion of the micromechanical resonator was first introduced in Chapter 3 and is again presented here, but now in terms of resonant angular frequency and damping coefficient instead of its constituent mechanical components. Utilizing Newton's second law, it is written:

$$\sum F_x = -kx - bv = ma_x$$

Then,

$$-kx - b\frac{dx}{dt} = m\frac{d^2x}{dt^2}$$

And because $\gamma = \frac{b}{m}$ and $\omega_o = \sqrt{\frac{k}{m}}$, it is found:

$$-\omega_o^2 x - \gamma\frac{dx}{dt} = \frac{d^2x}{dt^2}$$

The equation is then [91, 92]:

$$\frac{d^2x}{dt^2} + \gamma\frac{dx}{dt} + \omega_o^2 x = 0 \qquad \text{Equation 8-1}$$

where:

$\gamma = \frac{b}{m}$ is the damping coefficient [1/s]

~154~

$\omega_o = \sqrt{\dfrac{k}{m}}$ is the natural frequency of the system [Hz]

b – damping force constant [kg/s]
k – spring constant of the system [N/m]
m – mass of the system [kg]
x – direction of displacement [m]

The mass (or cantilever) is driven by a sinusoidal force or forcing function, $F_o \cdot \cos \omega t$, because the input signal to the cantilever is a sinusoidal voltage, which induces a sinusoidal electrostatic force between the beam and the bottom electrode. Equation 8-1 then becomes [1,2]:

$$\frac{d^2 x}{dt^2} + \gamma \frac{dx}{dt} + \omega_o^2 x = F \cos \omega t \qquad \textbf{Equation 8-2}$$

where:

$F \cos \omega t$ - driving force
$F = F_o/m$ (F_o is the magnitude of the applied force)

If the system lacked the driving and damping forces, the system would exhibit simple harmonic motion and the masses would oscillate around their equilibrium position indefinitely. This state is also achieved when the driving force is sufficient to overcome the losses caused by any damping forces; and after a sufficiently long period of time, when the energy input per cycle equals the energy lost per cycle, a steady-state condition is reached in which the oscillations proceed with constant amplitude. Once this constant motion or steady-state is achieved, the solution to Equation 8-2 is [144]:

$$x = A \cos(\omega t + \phi) \qquad \textbf{Equation 8-3}$$

where:

ϕ = Depends on initial conditions

$$A = \frac{F_o/m}{\sqrt{\left(\omega^2 - \omega_o^2\right)^2 + (\gamma \omega)^2}} \qquad \textbf{Equation 8-4}$$

~155~

This solution of Equation 8-3 indicates that the mass oscillates as a sinusoid with the same frequency (ω) as the driving force. The size of the oscillation depends on the ratio of the driving frequency to the resonant frequency (ω_o), on the magnitude of the driving force, and on the amount of damping in the system (γ). It is shown by Equation 8-4 that as the forcing function's frequency approaches the natural frequency of the system, the amplitude becomes large. This is resonance. Also noted from Equation 8-4, if there is no damping present in the system and $\omega \rightarrow \omega_o$, the amplitude approaches infinity [144]. This is, of course, impossible as there are always retarding forces in a system. It does, however, illustrate that the larger the damping force, the more rapidly the oscillations of the system die out.

Basically, a steady state solution exhibits resonant behaviour at a certain frequency (ω) if the system displays maximum response with little response away from the frequency as shown with the cantilevers in Chapter 7. The "width" of the resonance - the range of frequencies over which there is sizable motion of the mass - depends on the Q-factor.

2.1 Transient Solution

The transient solution represents what happens when there is no steady driving force but the mass has been disturbed momentarily. The mass oscillates with a frequency ω, but the size of the oscillations decays exponentially with time because of damping forces. Therefore, Equation 8-1 represents the equation of motion for this situation. The retarding force observed when an object moves through a gas is proportional to the speed and acts in the direction opposite the motion [144] as was explained in Chapter 3. The restoring force of the system, the spring k, also acts in the direction opposite to the motion.

The solution of Equation 8-1 is valid if the restoring force is greater than the damping force, that is, if there is oscillating, decaying amplitude. If the damping force were equal to the restoring force, there would be no oscillations at all. With that noted, the solution is [92, 144]:

~156~

$$x = A\cos(\omega t + \phi)e^{-\frac{\gamma}{2}t}$$

<div align="right">**Equation 8-5**</div>

Where:

$$\omega^2 = \omega_o^2 - \frac{\gamma^2}{4}$$

<div align="right">**Equation 8-6**</div>

As is shown by Equation 8-6, if the damping constant is small, its effects on the natural frequency are negligible and the resonance frequency is approximately equal to the natural frequency.

2.2 Damping Coefficient

To reiterate, the natural frequency is the frequency at which a system would oscillate without the presence of any external forces. When damping is added to the system, it creates forces in the direction opposite to those of the cantilever beam's motion. In the case of a standard beam tested at atmospheric pressure, the damping force is caused by air molecules and is referred to as air damping or "squeeze film damping". This external force causes the system to dissipate energy exponentially until there is a loss of all the energy and the beam ceases oscillating. It affects the steady-state motion and the frequency of the system. The damping constant can be deduced from measure of the motion of the damped system over time. It is calculated by drawing an exponential curve along the top amplitudes of the transient solution. The envelope of the curve represents the exponential damping factor [144]. The transient responses of the standard beams are analyzed in this manner to calculate the damping coefficient. Assuming the validity of the situation depicted in Equation 8-2, the equation of the decay of the envelope of Equation 8-5:

$$x = A_o e^{-\frac{\gamma \cdot t}{2}}$$

<div align="right">**Equation 8-7**</div>

Where:
A_o = is the maximum amplitude [*unitless*]
γ = is the damping constant [1/s]

2.3 Quality Factor

The quality factor, (Q), first introduced in Chapter 2, is found from both the steady state and transient responses. For steady state, the amplitude with respect to frequency is found and plotted. A Gaussian function is then fit to the data points. By calculating $A_{max}/\sqrt{2}$ and then finding Δf at that amplitude, the quality factor (Q) is determined. The well-known bandwidth/centre frequency definition is shown as [145]:

$$Q = \frac{f_{res}}{f_{+\frac{1}{\sqrt{2}}} - f_{-\frac{1}{\sqrt{2}}}}$$

Equation 8-8

This Q is dependent on the damping and refers to the width of the curve. The quality factor becomes larger for smaller damping forces. For transient responses, it demonstrates how rapidly the amplitude falls off to zero. From the measured γ value described above, the value of Q is calculated with the equation [92]:

$$Q = \frac{\omega_o}{\gamma} = \frac{\left(\omega^2 + \frac{\gamma^2}{4}\right)^{1/2}}{\gamma}$$

Equation 8-9

3 Movement of Micromechanical Resonators

Characterization of dynamic motion of the micromechanical resonators is now presented. After a brief review of expected motion, one observes that the displacement of a standard beam with respect to applied voltage, bias, and frequency is presented.

3.1 Theoretical Movements

Theoretical movement of the cantilever beam is explained in Chapter 3. A brief summary of expected phenomena is outlined below:

- The beam's displacement is proportional to the absolute value of voltage potential between the beam and the bottom electrode. Therefore, an AC signal input with

~158~

- no bias creates movement of the beam at twice the frequency of the driving signal.

- At the resonant frequency of the micromechanical resonator, an increased number of fringes are expected to occur as the photodetector response measures increased displacement. Fundamental resonance is expected to occur at 54kHz for the standard beam.

3.2   Effect of Bias on Beam's Displacement

The testing set-up for the interferometer measurements of the cantilever beams is shown below in Figure 8-1. A resistor is placed in series on the power side of the cantilever beam to limit a large, possibly destructive current if contact is made between the cantilever beam and the bottom electrode with increasing applied voltage. Also, the drive voltage, V_{drive}, is measured after the resistor with respect to ground, which measures the voltage potential across the cantilever beam. For example, if $20V_{p-p}$ is applied across the cantilever beam and there is a leakage current, then this will be detected at the resistor, thus, resulting in a measured voltage.
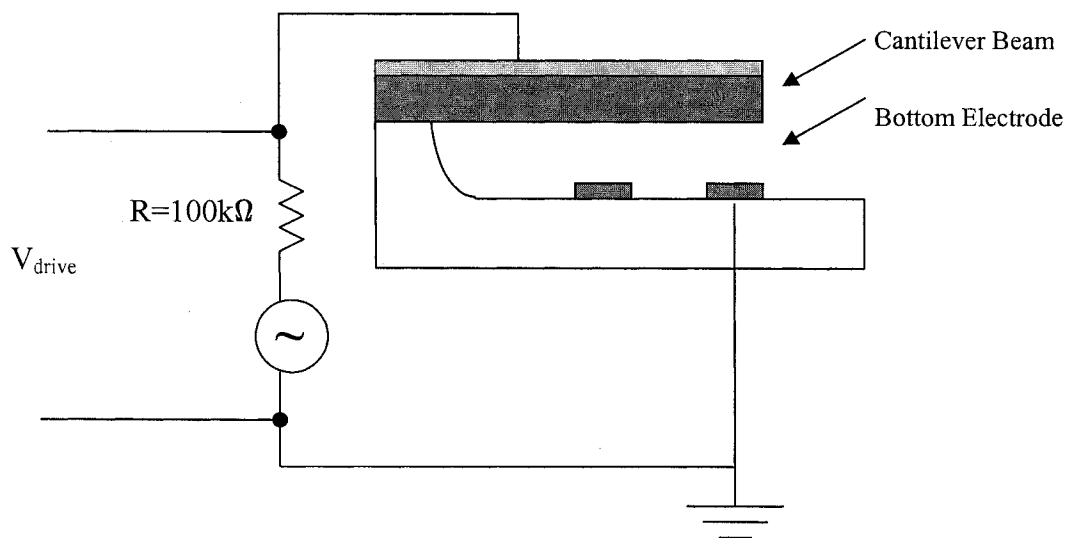
Figure 8-1: Interferometer measurement test set-up
V_{drive} **is measured by an oscilloscope (Tektronix TDS 3032B)**

~159~

Contact is made to the chip with contact probes and is carried to the cantilever beam and bottom electrodes through thin film gold wires. The impedance of the measurement probes used is 1.5MΩ, so by using a resistor with a value of 100kΩ, the apparent resistance is still 93.75kΩ, indicating that the measurement probes have a very small effect on the system.

With the test set-up explained in Figure 8-1, $10V_{p-p}$ at 1kHz is applied to the top surface of the cantilever and the bottom electrode is held at ground. The photodetector response is observed as the bias is changed to +5 V DC and –5 V DC to observe the frequency-doubling phenomenon discussed in Section 2 of Chapter 3. Figure 8-2 illustrates the drive signal and photodetector response for these scenarios. It is noted that the maximum voltage potential for these cases is 10V, so the displacement is not greater than what is represented by one fringe. To expand, an applied $10V_{DC}$ was shown to produce a deflection <100nm both analytically and experimentally (Figure 5-8), and the theoretical interferometric signal for <100nm (Figure 7-6) shows no formation of a second fringe. This is an important note to ensure the frequency-doubling of the signal is due to the frequency of the beam's movement and not from the amplitude of its motion (i.e. its motion passing through two fringes creating a signal that is twice the driving frequency).

As was expected from the discussion in Section 2 of Chapter 3, it is observed from the figure that with no applied bias, the photodetector response is twice that of the driving signal with respect to frequency. It is concluded that the beam reaches a maximum displacement at both the peak (+5V) and the valley (-5V) of the driving signal. However, with either polarity of applied bias, the photodetector response is at the same frequency as the driving signal. It is concluded that the beam reaches a maximum displacement at the peak of the driving signal (±10V) and a minimum at 0V. Further evidence that the signals are representing the displacement of the beam is the amplitude of the signals. For the 'no bias' case, the amplitude is 20mV; but when bias is applied, the amplitude of the photodetector response is 200mV[‡‡‡], indicating increased displacement of the beam.

[‡‡‡] As measured across the resistor in Figure 6-3 (C) by an oscilloscope (Tektronix TDS 3032B)

~160~

Figure 8-2: Photodetector output with respect to bias (50μm-wide standard beam)

	Photodetector output for 50μm -wide standard beam: x-axis (ms) y-axis (x10mV)
10V$_{p-p}$, 0 bias, 1kHz	
10V$_{p-p}$, -5V$_{DC}$ bias, 1kHz	
10V$_{p-p}$, +5V$_{DC}$ bias, 1kHz	
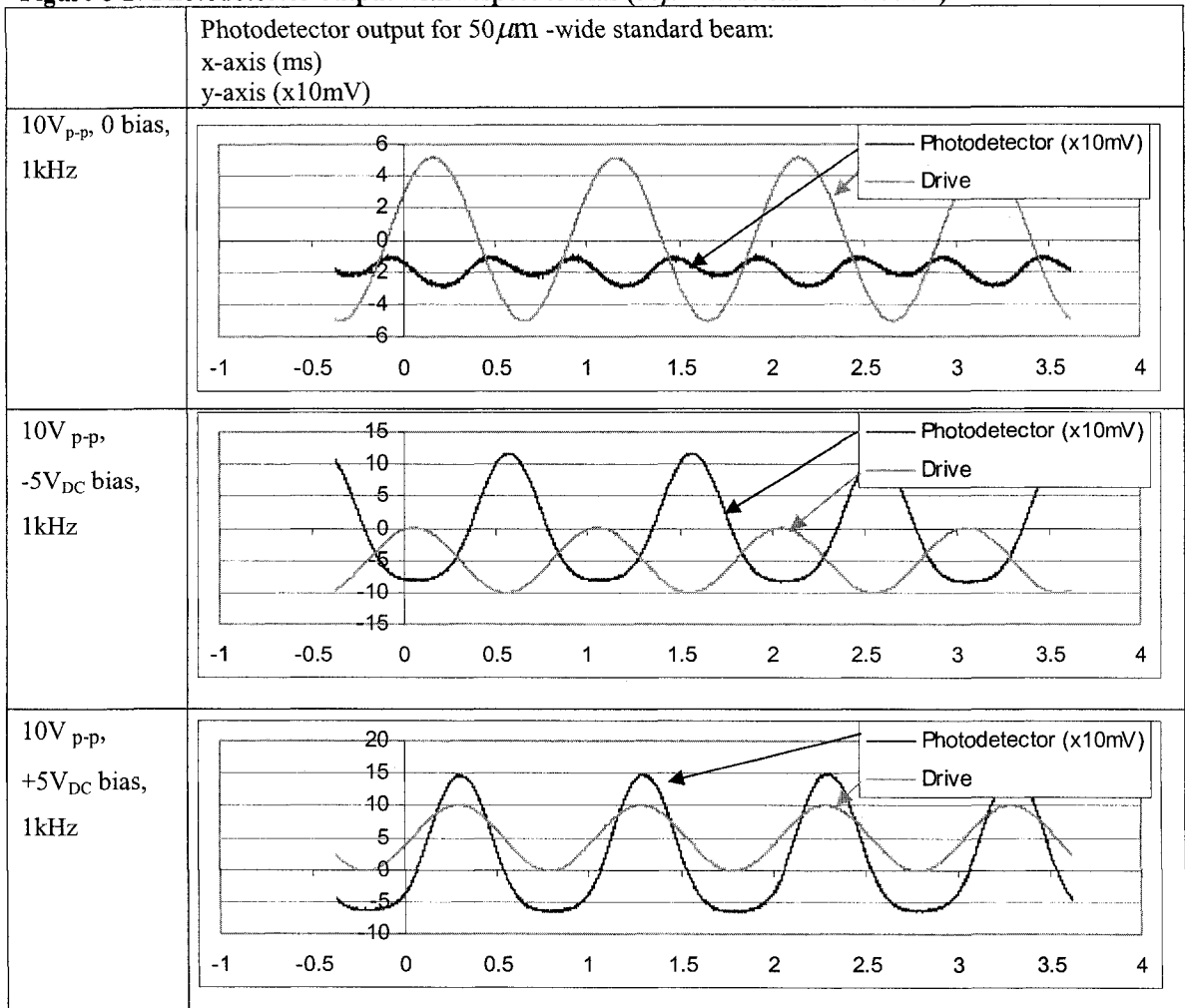
A bias is then applied but not great enough for the driving signal to appear completely in one polarity. Shown below in Figure 8-3 is the photodetector responses for ±2V$_{DC}$-applied bias compared to the no bias case for the same set-up as above.
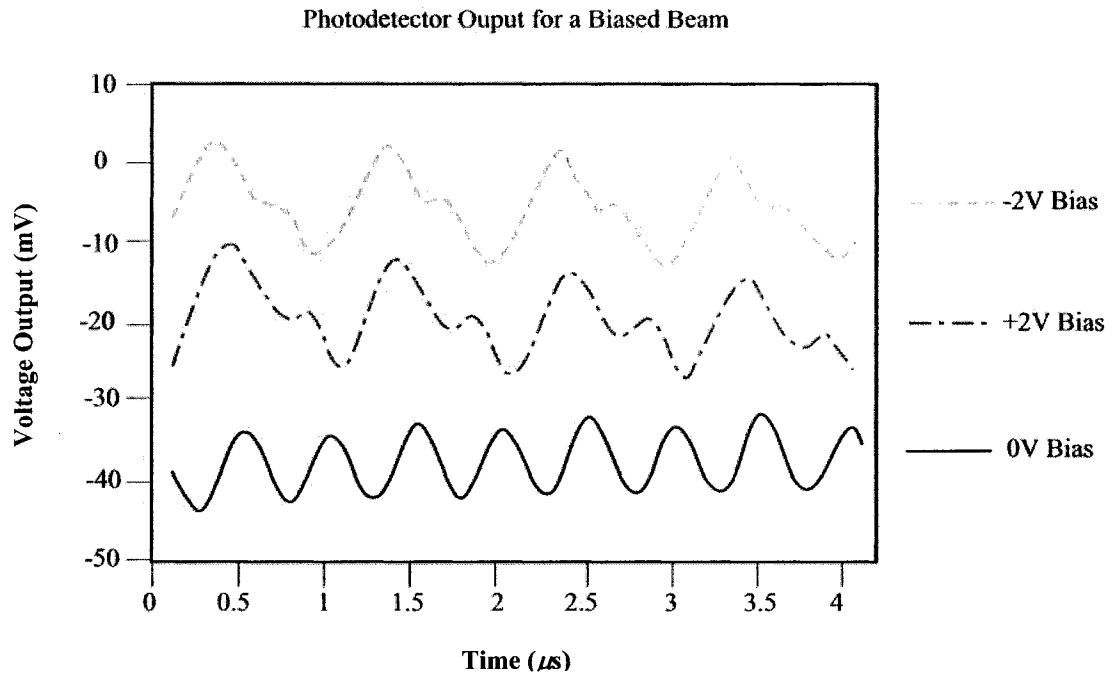
Figure 8-3: Asymmetrical amplitudes due to partial applied bias (@1kHz)

The figure clearly represents an asymmetry in the response of the cantilever beam. The maximum amplitude occurs at the maximum potential of ±7V and the second maximum occurs when the voltage potential is ±3V.

3.3 Testing to Ensure Interference

An obvious, simplistic test for further evidence supporting the interference signal is included for the sake of completeness. As shown by Figure 8-4, by driving the cantilever with a biased AC signal and moving the laser just off the tip of the beam, it is noted that the photodetector response becomes a flat line. There is no movement of the object beam and, therefore, no moving interference pattern at the photodetector. This test is also used as a way to ensure that the laser beam is focussed on the tip of the beam and not further towards the anchor, which moves with a smaller amplitude.

~162~

Laser Beam Focused off 10um Wide Beam @58kHz

Drive Voltage (V)

Photodetector (x10mV)
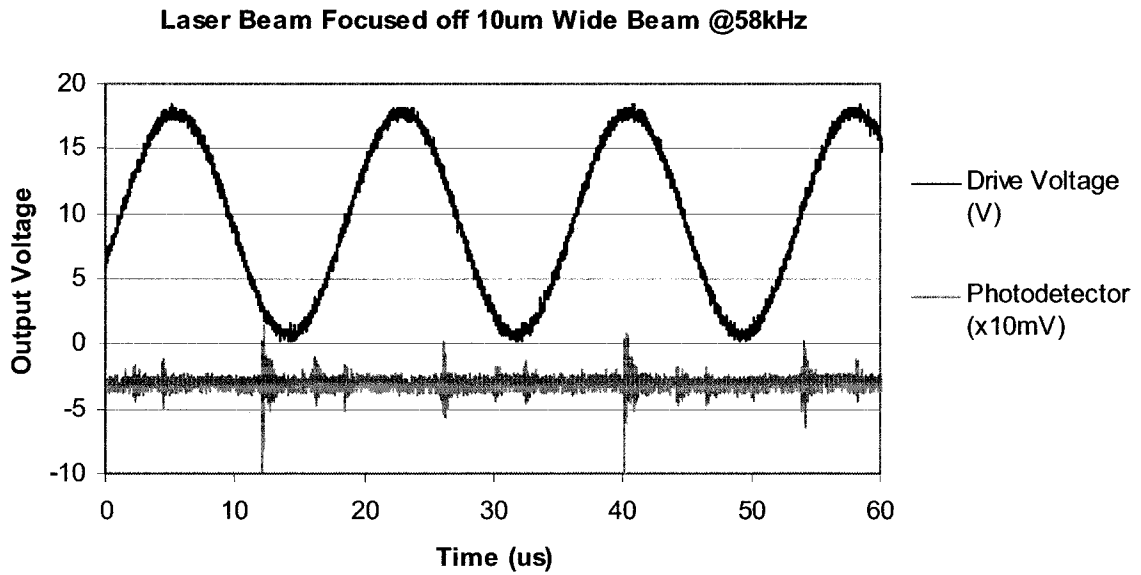
Figure 8-4: Photodetector response to laser spot focussed off a 10µm wide beam @ 58kHz

3.4 Current Measurements

Current through the system is monitored, as well. The set-up to measure current is shown in Figure 8-5. The resistor is placed in series with the resonating beam. The voltage across the 100kΩ resistor is monitored. As an example, a $20V_{p-p}$ signal with a 10DC bias was applied to a standard beam and the photodetector response monitored. The resulting voltage drop across the resistor shown in Figure 8-5 was ±0.75V, equalling a maximum current of ±7.5µA.
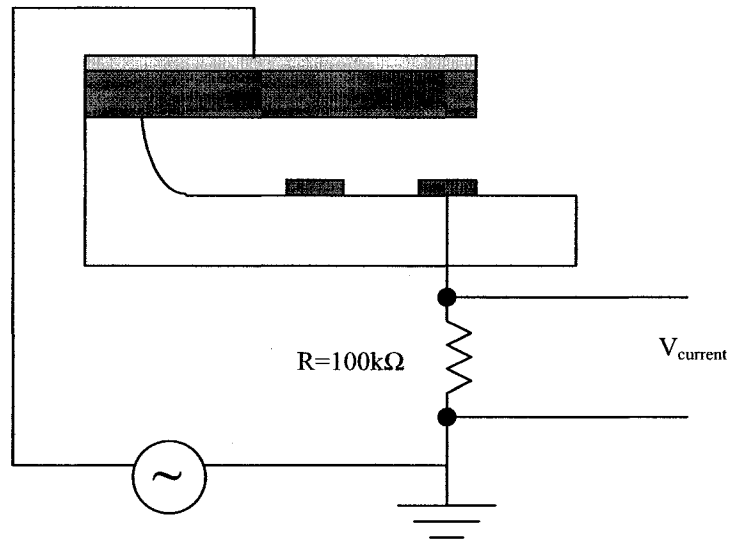
Figure 8-5: Schematic for measuring current in the system
$V_{current}$ **is measured with an oscilloscope (Tecktronix TDS 3032B)**

3.5 Modification of Waveform Generator
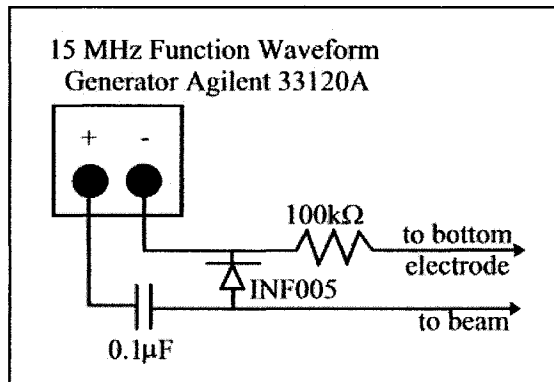
Figure 8-6: Schematic of voltage multiplier

Mentioned above is the applied voltage of $20V_{p-p}$ with an applied bias of $10V_{DC}$. The maximum voltage output of the waveform generator used is 20V. This means that at maximum output (20V) no bias is possible. A voltage multiplier is used in conjunction with the waveform generator to create a

maximum applied voltage of 20V but with the middle line with no applied bias voltage at 10V. This creates much more flexibility because the maximum voltage potential achievable is 20V (instead of the 10V without the voltage multiplier), which is enough to displace the tip of the beam by at least one fringe. A schematic of the voltage multiplier is shown in Figure 8-6 and an experimental voltage signal using the voltage multiplier is

~164~

shown in Figure 8-7. As shown in Figure 8-6, there are two leads exiting the voltage multiplier setup. One lead is connected to the cantilever beam (via the 100kΩ resistor shown in Figure 8-1) and the other to the bottom electrode (also shown in Figure 8-1).

Drive Signal 20Vpp Using Voltage Multiplier
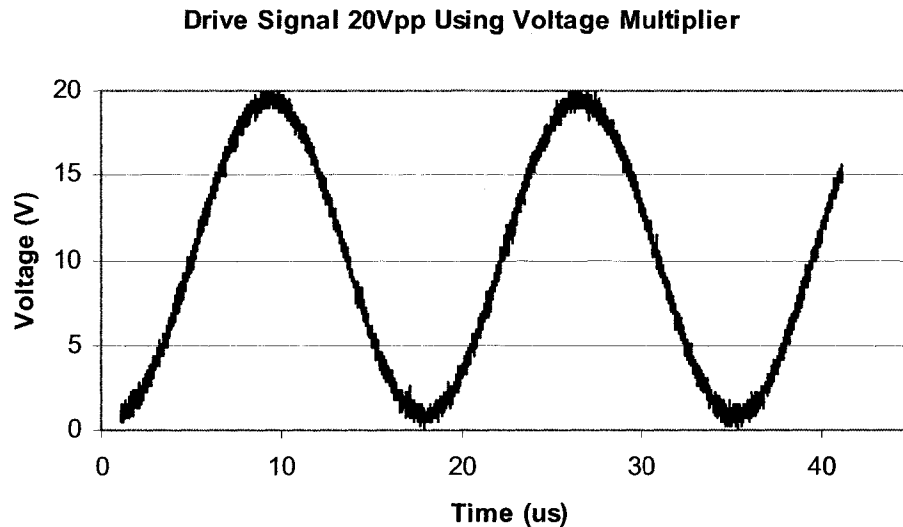
Figure 8-7: Voltage output of the waveform generator using the voltage multiplier
Schematic of voltage multiplier is shown in Figure 8-6

3.6 Resonance of 10μm & 25μm Wide Beams

Using the set-up of Figure 8-1 in conjunction with the voltage multiplier of Figure 8-6, an applied driving signal of $20V_{p-p}$ is applied with a $10V_{DC}$ bias using an Agilent 33120A 15MHz function waveform generator with the voltage multiplier modification described above. The voltage is applied to the cantilever while the bottom electrode is held at ground. This creates a situation where the beam responds at the same frequency of the driving signal and reaches a maximum displacement at the maximum voltage potential of 10V. Increasing frequencies are applied to the set-up, while never altering the laser spot alignment or focus, and the photodetector responses recorded. The responses for the 10μm and 25μm wide standard beam are presented in Figure 8-8 and 8-10, respectively. No significant response at or near resonance is seen for the 50μm wide standard beam.

~165~

Figure 8-8: Resonance of 10μm wide, 2μm thick, and 200μm thick beam by interferometry

Drive Frequency (kHz)	# Fringes for x_{max}, (Equation 7-3)	Photodetector Output 10μm beam at 20V_{p-p}: x-axis (μs) y-axis (mV)
48	1.5	
52	2.1	
54	2.5	
56	3.25	
57	3.25	
58	3.5	
60	3.5	
62	2.5	
64	1.6	
66	1.5	
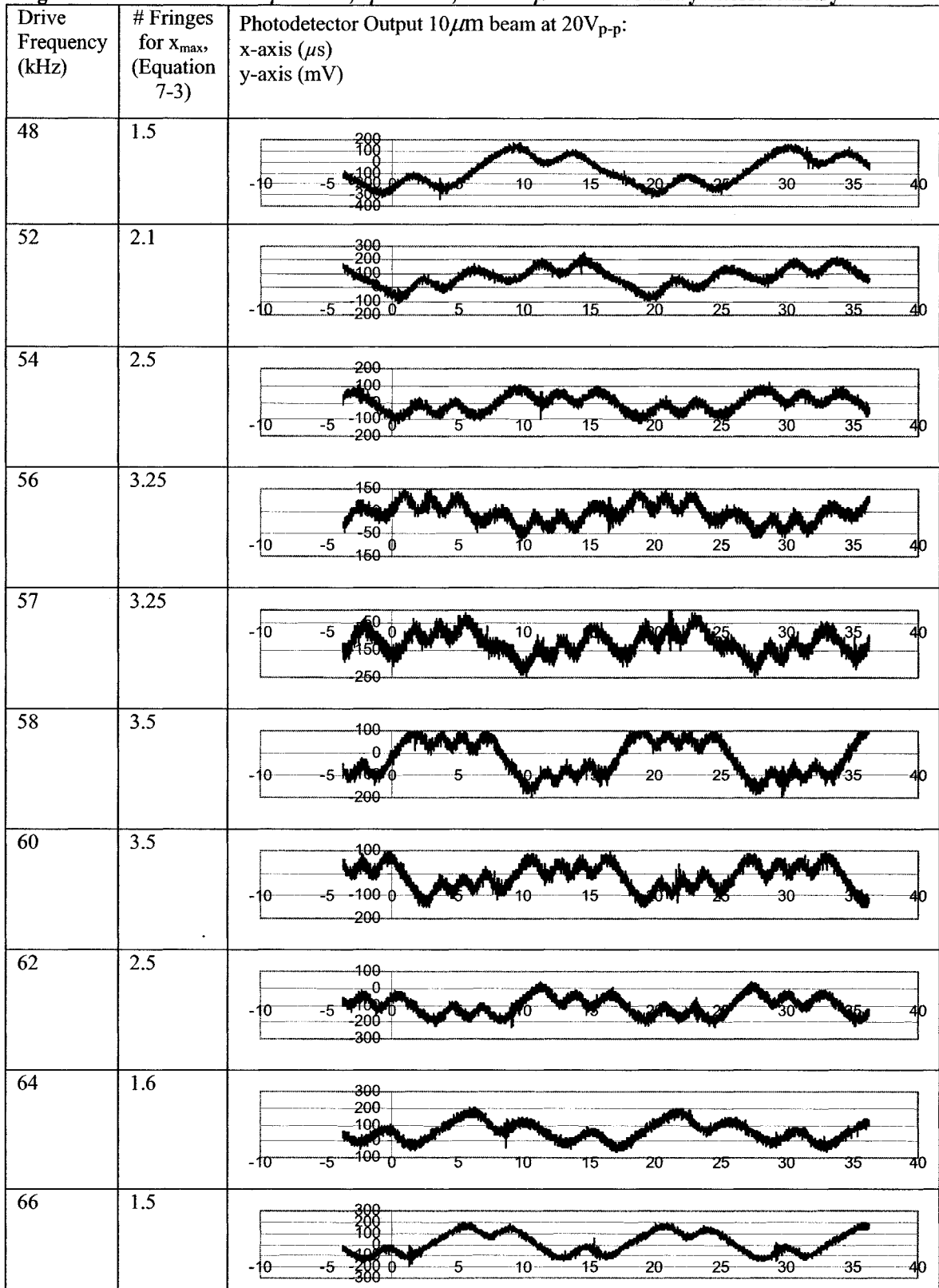
It is shown in the above figure that the photodetector response at 48kHz is 1.5 ± 0.1 fringes (using Equation 7-3). Shown below in Figure 8-9 is an example of how Equation 7-3 is used to determine the # of fringes ± 0.1. In the figure, the theoretically calculated signals at the photodetector are shown for 1.4, 1.5, and 1.6 fringes. The signal at 48kHz from Figure 8-8 is compared to the signals and its fringe pattern closely parallels that of 1.5 fringes. An error of ± 0.1 is found because above or below 1.5 fringes, a peak either begins to form or starts to diminish as is labelled in the figure. Using this comparison method, the number of fringes can be determined within 0.2 fringes. Preliminary review of the literature indicates this method for theoretically predicting the interferometer signals for a micromechanical resonator is original work. Once the number of fringes is determined, using Equation 7-2, the displacement is calculated. For example, at 48kHz, the 1.5 fringes represents a 475nm displacement. The oscillatory amplitude increases to 3.5 ± 0.1 fringes (1.1μm) between 58-60kHz, and finally, settling back down to 1.5 ± 0.1 fringes at 66kHz. It is then concluded that the resonance occurs between 58kHz and 60kHz. A Gaussian function is fit to the data points, whereby the resonant frequency and Q are extracted. This is presented in the next section.

Equation 7-4 to Determine # Fringes
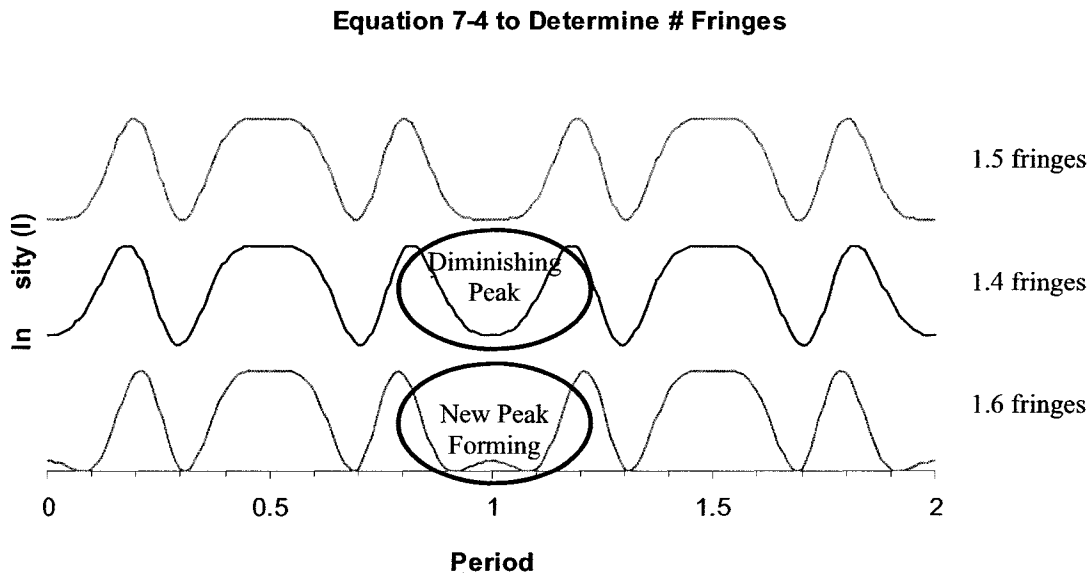
Figure 8-9: Using Equation 7-3 to Determine # of Fringes

~167~

Figure 8-10 presents the resonant characteristics of a 25μm wide cantilever that is more damped because the system does not increase its displacement as drastically at resonance as is found for the 10μm wide beam. In other words, the difference between the displacements off and on resonance for the 25μm wide beam is far less than the 10μm wide beam just described above even though the laser spot is also focussed at the tip of the cantilever. The maximum displacement occurs at 53-56kHz, but the displacement is only 2 ± 0.1 fringes (0.6μm) whereas the maximum displacement for the 10μm wide beam is double this value at resonance. Either side of the resonant frequency, the displacement reduces to a similar displacement at the 10μm wide beam described above, which shows that the beam is driven similarly.

Figure 8-10: Resonance of 25μm wide, 2μm thick, and 200μm long beam by interferometry

Drive Frequency (kHz)	# Fringes for x_{max}, (Equation 7-3)	Photodetector Output 25μm beam at 20V$_{p-p}$: x-axis (μs) y-axis (mV)
45	1	
46	1.2	
49	1.4	
51	1.5	
53	1.5	
56	1.4	
57	1.4	
64	1.1	
67	1	
68	1	
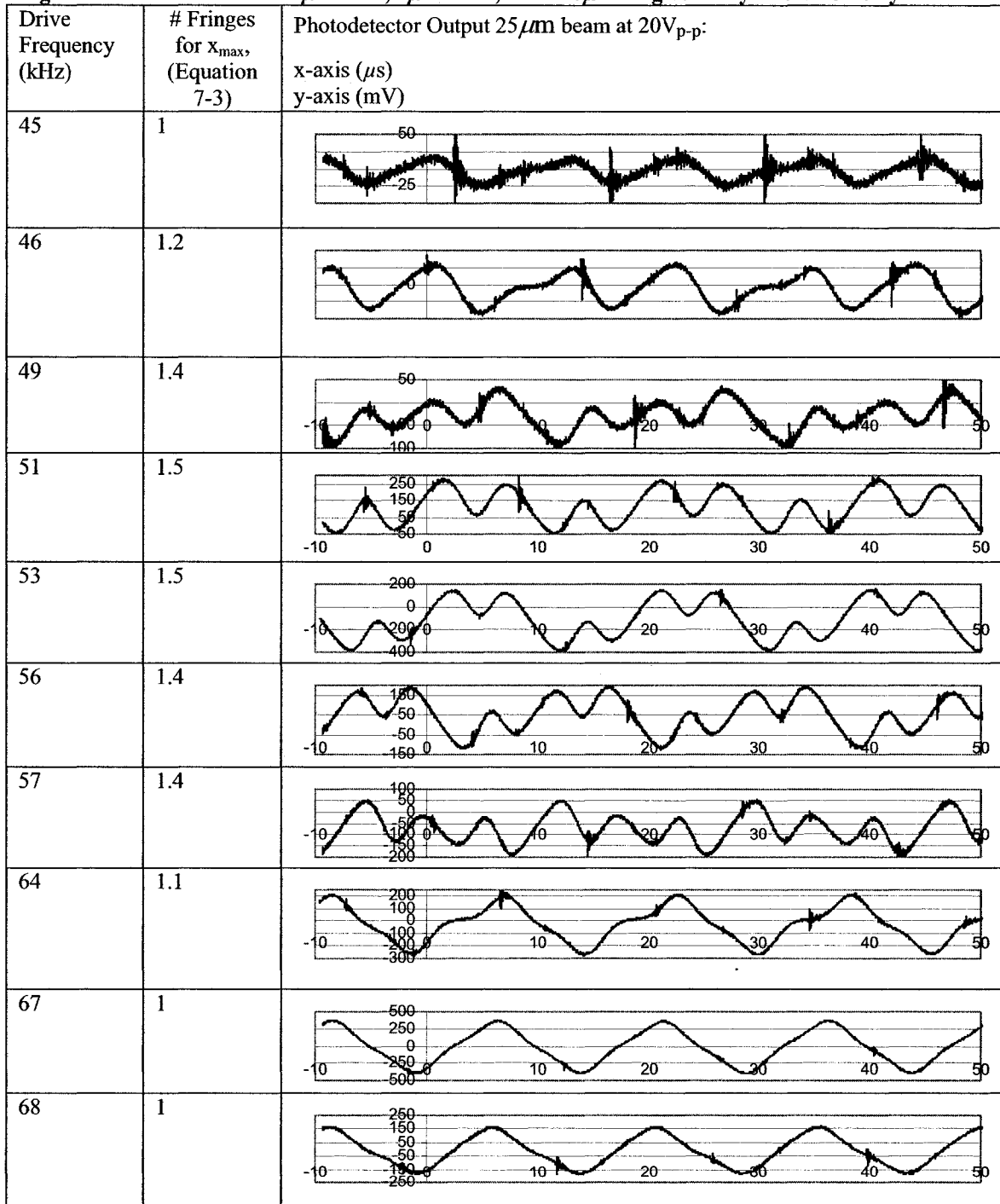
3.7 Calculating Q-Factor

The signals from the interferometer are used to calculate a Q-factor. The number of fringes is directly proportional to the amplitude of the cantilever. Therefore, the number

~169~

of fringes is plotted with respect to frequency, a Gaussian function is fit to the data points, and the Q-factor calculated with Equation 8-10.

A Gaussian function takes on the form:

$$y = a_o \exp\left[-\ln(2)\left(\frac{x - a_1}{a_2}\right)^2\right]$$

<div align="right">**Equation 8-10**</div>

Where:
a_o = the maximum height of the peak (at $x=a_1$) [*unitless*]
a_1 = the position of the centre of the peak [Hz]
a_2 = half width at half maximum of the peak [Hz]

The signals of Figure 8-8 are plotted with the drive frequency on the x-axis and the number of fringes on the y-axis. Fringe counting is accurate to within a quarter fringe or ~80nm and is done by comparing to theoretical signals using Equation 7-3. Fringes are counted as the maximum displacement the beam travels. This distance is travelled twice in each period. (i.e. (1) the beam is attracted toward the bottom electrode and (2) returns to original state.) The number of fringes plotted with respect to displacement is the number of peaks on either the peak or the valley of the signal. For example, in Figure 8-8, at 58kHz, there are 7 fringes per period so the maximum amplitude travelled is 3.5 fringes. The data point is then (3.5, 58kHz).

The data points are then analyzed with a freeware non-linear curve-fitting and data analysis software program called *fityk* [146], in which a standard non-linear least-squares routine (Levenberg-Marquardt method) is utilized for optimization (i.e. minimize the chi-squared). The program specializes in non-linear fitting of analytical functions such as the common peak-shaped functions like Gaussian, Lorentzian, Pearson 7, and Voigt to experimental data points. The data points taken from Figure 8-8 are shown with the Gaussian fit function below in Figure 8-11. The chi-square, χ^2, of the fitted function given as output from fityk is 0.7. Using the criteria for n data points, if χ^2 is of order n or less, then we have no reason to doubt that our measurements are distributed as a Gaussian [147]. However, it should be noted that the method used by fityk to calculate χ^2 is uncertain.

~170~
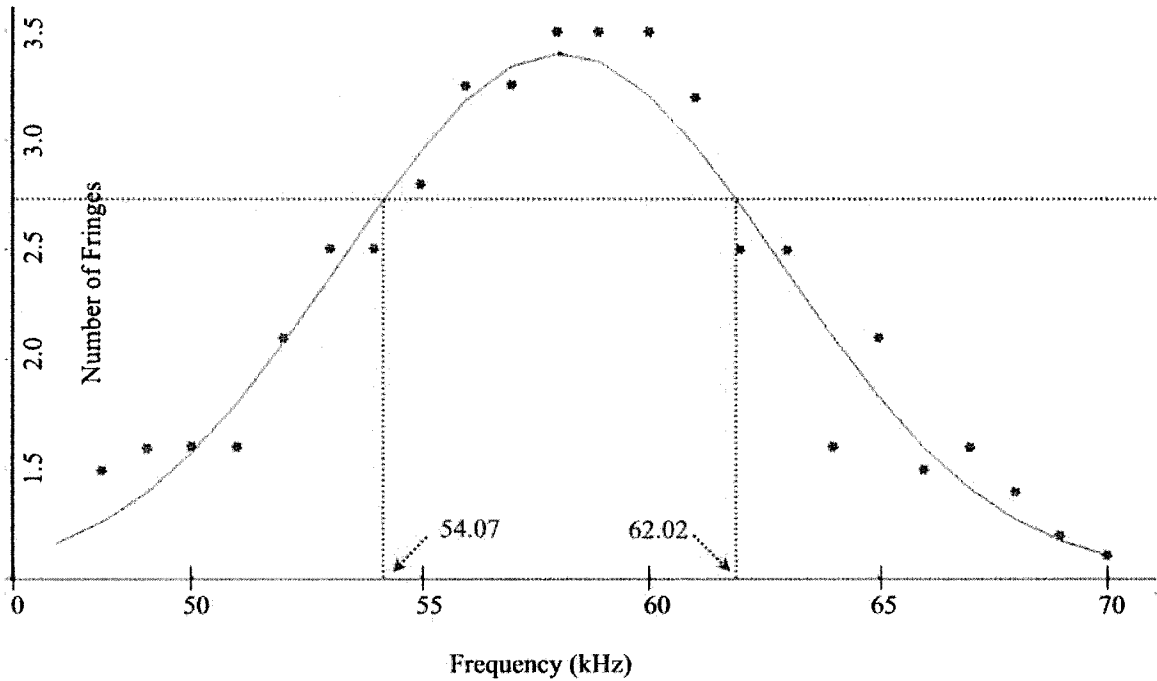
Figure 8-11: Gaussian fit of frequency versus amplitude data for 10μm -wide beam
Points represent the interferometry measurement at respective frequencies, and are taken from
Figure 8-8.

The Gaussian function is of the form in Equation 8-10 with the coefficients summarized in Table 8-1 below (found by Fityk). The software does not include uncertainty predictions for parameters so 10 data sets were generated based on the original data set. Fityk was used to analyze the data sets using random values of y ± 0.1, where y is the # of fringes. Because the signals were compared to the theoretically calculated signals found using Equation 7-3, the accuracy to which the comparison can be made is ± 0.1. This was illustrated in Figure 8-9. The difference between the maximum and minimum values of a_0, a_1, a_2, found by running the 10 data sets, is deemed the error in each respective coefficient; and these are presented in Table 8-1 below. On the original data set, the centre frequency, a_1, is found to be 58.0 ± 0.2 kHz, which is 7.4% higher than the theoretical value found in Chapter 3 of 54kHz. As described in Section 2.3, the frequencies at $A_{max}/\sqrt{2}$, are calculated and shown in the above figure. Using Equation 8-10, the Q-factor for a 10μm standard beam is found to be 7.30 ± 0.5. The error in the Q is found by the same method as described above – the range of Q factors from the randomly generated data sets is deemed the error in the original data set.

~171~

Table 8-1: Coefficients for Gaussian Fit Function for 10μm wide beam
(For Equation 8-10)

a_o	Max. Amplitude, A_{max}	3.39 ± 0.1 fringes
a_1	Centre	58.05 ± 0.2 kHz
a_2	HWHM	5.62 ± 0.4
Q	Quality Factor	7.30 ± 0.5

For the 25um wide beam, data points taken from Figure 8-10 are shown with the Gaussian fit function below in Figure 8-12. The chi-square, χ^2, of the fitted function of Figure 8-12 is 0.1. Using the same criteria as was presented for the 10μm case, the fit is not at all unreasonable. Again, it should be noted that the method used by fityk to determine χ^2 is uncertain. The curve is of the form of Equation and the Gaussian coefficients are presented in Table 8-2.
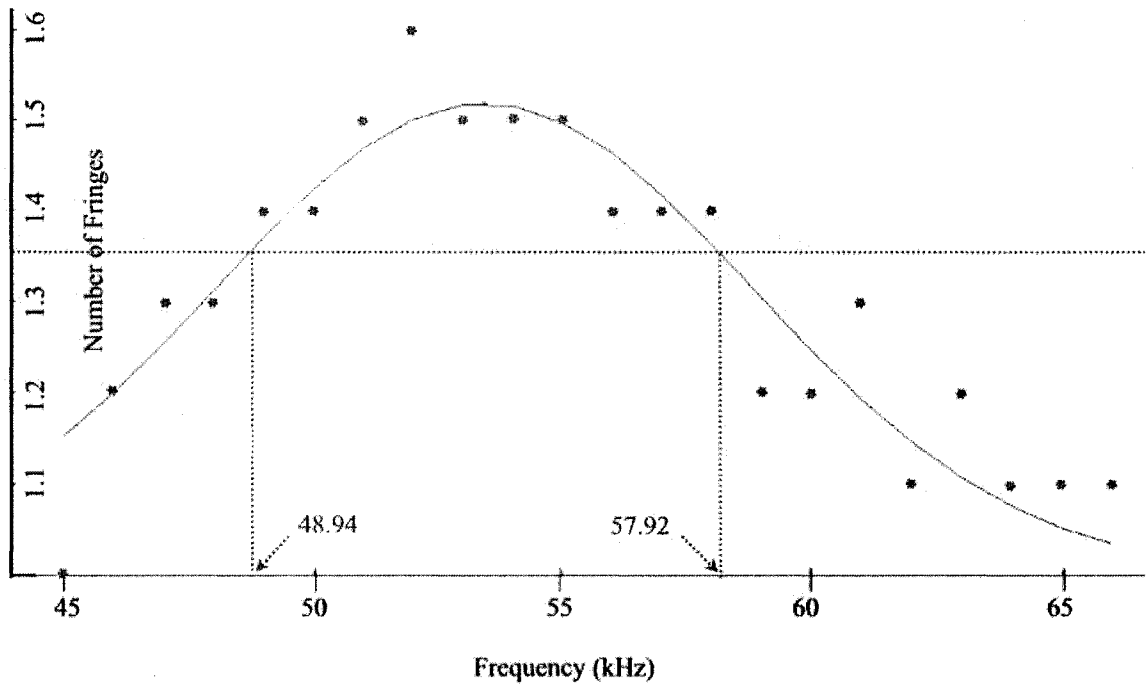
Figure 8-12: Gaussian fit of frequency versus amplitude data for 25μm-wide beam
Points represent the interferometry measurement at respective frequencies, and are taken from
Figure 8-10.

Table 8-2: Coefficients for Gaussian Fit Function for 25μm Wide Beam
(For Equation 8-10)

a_0	Max. Amplitude, A_{max}	1.52 ± 0.1 fringes
a_1	Centre	53.43 ± 1.1 kHz
a_2	HWHM	6.35 ± 1.3
Q	Quality Factor	5.95 ± 1.2

The centre frequency is found to be 53.4 ± 1.1 kHz, which is only 1.1% higher than the theoretical value found in Chapter 3 of 54kHz. The frequencies at $A_{max}/\sqrt{2}$ are calculated and shown in the above figure. Using Equation 8-10, the Q-factor for a 25μm standard beam is found to be 5.95 ± 1.2.

3.8 Transient Responses

The transient response of the cantilevers is analyzed for two reasons: (1) to calculate the damping factor for comparison between the 10μm-wide and 25μm-wide beams, and (2) to

~173~

calculate the Q-factor directly from the damping factor and compare to the interference fringe method described above.

The transient response of the cantilever is found using the same interferometer set-up as before. In order to remove the complications produced by the presence of multiple fringes, the maximum voltage potential is kept to 15V to ensure that the deflection of the cantilever is below one fringe. A square wave is used as the driving signal input to the cantilever beam while the bottom electrode is held at ground using the set-up of Figure 8-1 in conjunction with the voltage multiplier of Figure 8-6. A square wave of $15V_{p-p}$ at 5kHz with a bias of $7.5V_{DC}$ is utilized and the photodetector response is monitored for $10\mu m$, $25\mu m$, and $50\mu m$ wide standard beams. However, no significant transient response is found for the $50\mu m$ wide standard beam.

Shown below in Figure 8-13 is the transient response for the $10\mu m$ wide beam. A close up of the response for a potential of 15V is shown. An important note is that the input square wave (measured as shown in Figure 8-1) shows no electrical transients or irregularities. At a frequency of 5kHz, the beam is allowed to ring for 0.1ms, which is enough time for 5 oscillations at the cantilever beam's resonance. The average of the first 4 oscillations is 58kHz, which coincides with the measured resonance of these beams explained above with the fringe method in Figure 8-11.

The decay of the response is then examined for the damping factor and, ultimately, the quality factor utilizing the method explained in Section 2 of this chapter.

Transient Response for 5kHz @15VPP
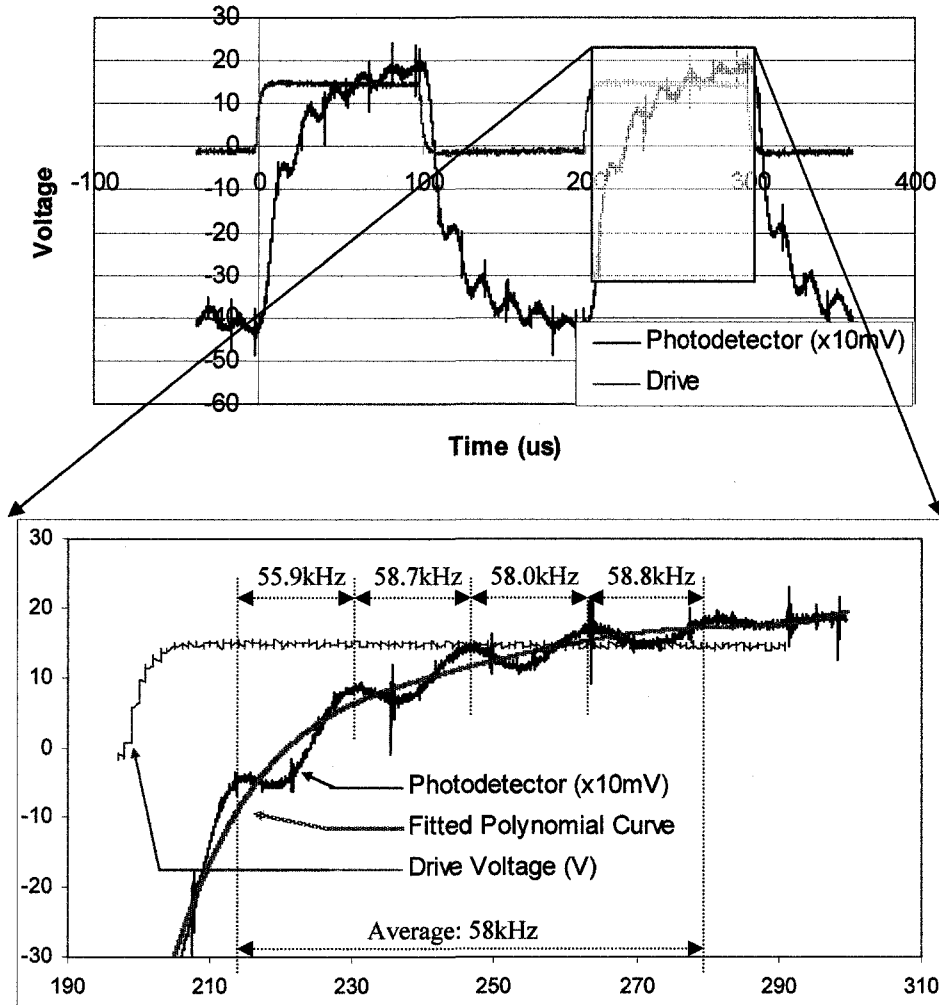
Figure 8-13: Transient response for 10μm wide, 2μm thick, and 200μm long beam (TOP) Beam driven 15V$_{p-p}$ @ 5kHz (BOTTOM) Close-up of resonance

Fityk (first introduced in Section 3.7 of this chapter) is used to fit a polynomial function to the photodetector response due to the input of a square wave. The function represents the response time of the photodetector to the square wave and the middle axis of the transient behaviour of the cantilever beam. A fifth degree polynomial function is fit to the response and is shown as the dotted line in the close-up of Figure 8-13. The general form of the function is:

~175~

$$y = a_o + a_1 x + a_2 x^2 + a_3 x^3 + a_4 x^4 + a_5 x^5 \qquad\qquad \textbf{Equation 8-11}$$

where:

      y – the photodetector response [V]

      x – time [μs]

      $a_o, a_1, ..., a_5$ – coefficients of the function [*unitless*]

The coefficients for the polynomial function of Equation 8-11 fit to the photodetector response shown in Figure 8-13 are as follows:

Table 8-3:Coefficients for polynomial fit function for 10um wide beam

a_o	-845.632 [V]
a_1	$1.63046e^7$ [V/μs]
a_2	$-1.25586e^{11}$ [V/μs^2]
a_3	$4.83123e^{14}$ [V/μs^3]
a_4	$-9.27923e^{17}$ [V/μs^4]
a_5	$7.11692e^{20}$ [V/μs^5]

The difference between the polynomial fit function and the photodetector response for Figure 8-13 are then plotted and the decaying behaviour of the beam is more clearly shown. This is illustrated in Figure 8-14.
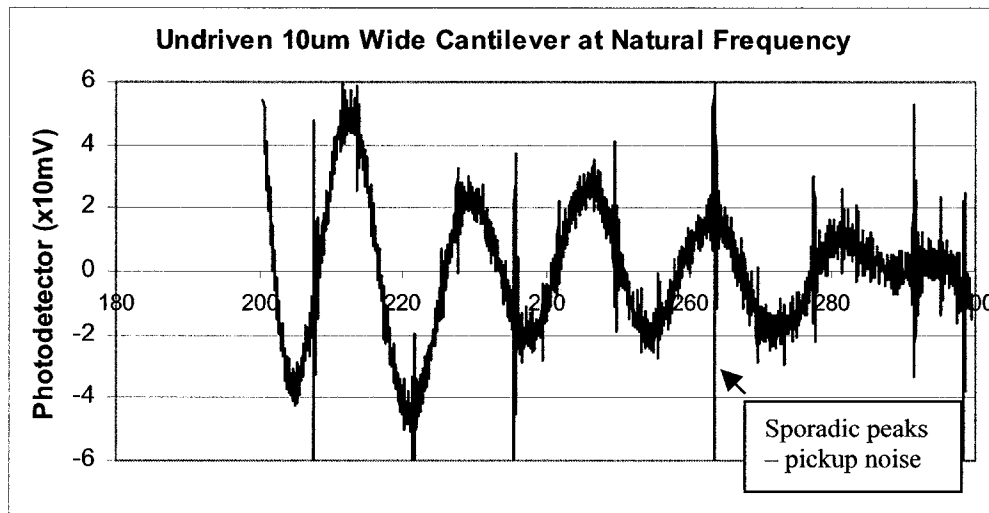
Figure 8-14: Decaying behaviour - transient response for 10μm wide standard beam
Sharp peaks are sporadic and are assumed to be pick-up noise

The maximum amplitudes (both peaks and valleys of the photodetector response in Figure 8-14) are then plotted as data points with respect to time. These data points were found at each peak by taking a line average (256 times) of the photodetector signal and determining the voltage from the photodetector at each maxima or minima. The error in the y-value (photodetector response) is deemed to be the height of the signal before averaging (±5mV). Time is shifted to start at zero for the beginning of the decaying response instead of the absolute time of 200μs shown in Figure 8-14. An exponential curve was fit to these decaying amplitudes of the transient solution and is shown in Figure 8-15. The envelope of the curve represents the exponential damping factor.

~177~

Maximum Amplitude with Time of 10um Wide Cantilever - Transient Response

$x=0.0535e^{-23581t}$
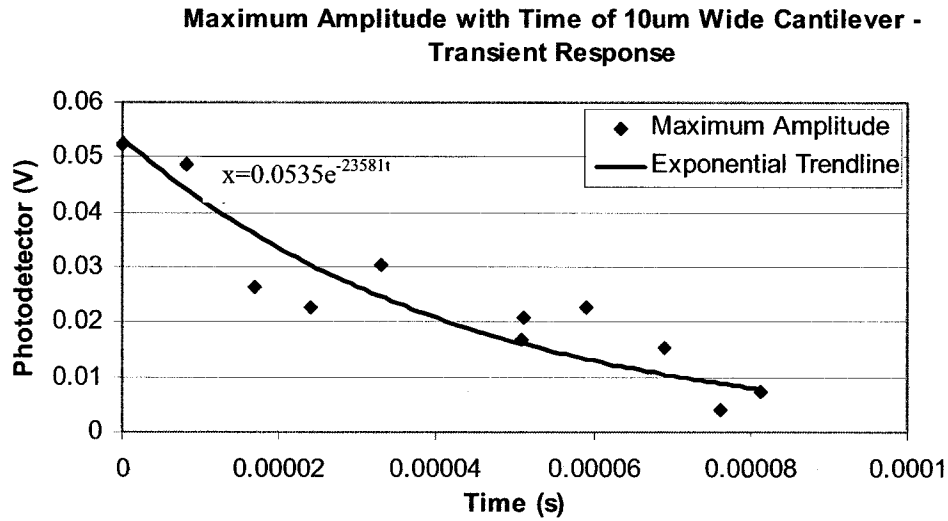
Figure 8-15: Envelope curve for decaying behaviour of $10\mu m$ wide standard beam

The fit to the data is shown in Figure 8-15 and when compared to Equation 8-7 above, the damping factor, γ, is found to be 47162 ± 2400 [unitless]. This calculation is demonstrated below:

$$x = A_o e^{-\dfrac{\gamma \cdot t}{2}} = 0.0535e^{-23581t} = 0.0535e^{-\frac{47162 \cdot t}{2}} , \therefore \gamma{=}47162 \pm 2400 \qquad \textbf{Equation 8-7}$$

The error in γ is found by taking dx/dy of Equation 8-7 and shown in Figure 8-15 and solving for dy at each data point. As described previously, the error in x (or photodetector signal in Figure 8-14) is ± 5mV. The error in γ was then determined as the maximum error in the data set. The damping factor is then used in Equation 8-9 using the centre frequency of 58.05 ± 0.2 kHz found from Figure 8-11. This calculation is demonstrated below:

$$Q = \frac{\omega_o}{\gamma} = \frac{\left(\omega^2 + \dfrac{\gamma^2}{4}\right)^{1/2}}{\gamma} = \frac{\left((2\pi * 58050)^2 + \dfrac{47162^2}{4}\right)^{1/2}}{47162} = 7.75 \pm 0.1 \qquad \textbf{Equation 8-9}$$

~178~

The Q-factor is found to be 7.75 ± 0.1 using this method and is 6.2% higher than the Q-factor using the fringe method described above. The methods are consistent since the values for both methods are within error.

The same method is applied to the $25\mu m$ wide standard beams and the transient response is shown in Figure 8-16. Visually, a higher damping factor and lower Q-factor are expected for this beam because the response decays at a much quicker rate than seen in Figure 8-13 for the $10\mu m$ wide standard beam.

Transient Response for 5kHz @15VPP
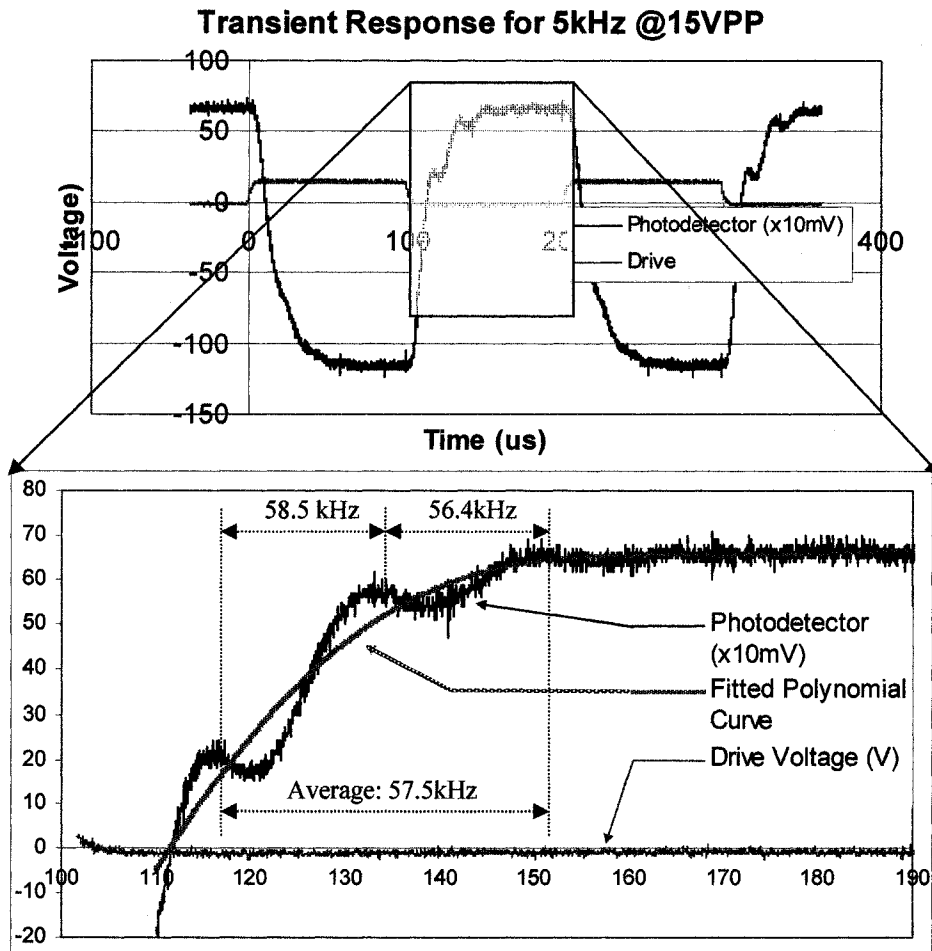
Figure 8-16: Transient response for $25\mu m$ wide, $2\mu m$ thick, $200\mu m$ long beam (TOP) Beam driven $15V_{p-p}$ @ 5kHz (BOTTOM) Close-up of resonance

~179~

The coefficients for the polynomial function of Equation 8-11 fit to the photodetector response in Figure 8-16 are shown below in Table 8-4:

Table 8-4: Coefficients for Polynomial Fit Function for 25μm Wide Beam

a_o	35.6823 [V]
a_1	-1.49413e^6 [V/μs]
a_2	2.27915e^{10} [V/μs^2]
a_3	-1.63156e^{14} [V/μs^3]
a_4	5.60361e^{17} [V/μs^4]
a_5	-7.47488e^{20} [V/μs^5]

Again, the difference between the polynomial fit function and the photodetector response from Figure 8-16 is plotted and the decaying behaviour of the beam is shown in Figure 8-17.
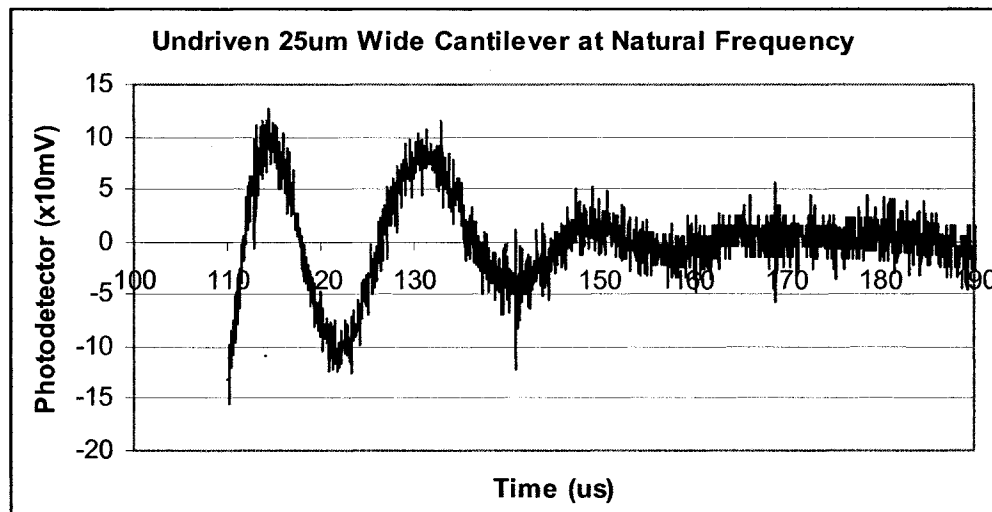
Figure 8-17: Decaying behaviour - transient response for 25μm wide standard beam

The peaks of Figure 8-17 are plotted as data points with respect to time zeroed from the start of decay. The points, as well as the fitted exponential function, are shown below in Figure 8-18.

~180~

Maximum Amplitude with Time of 25um Wide Cantilever - Transient Response
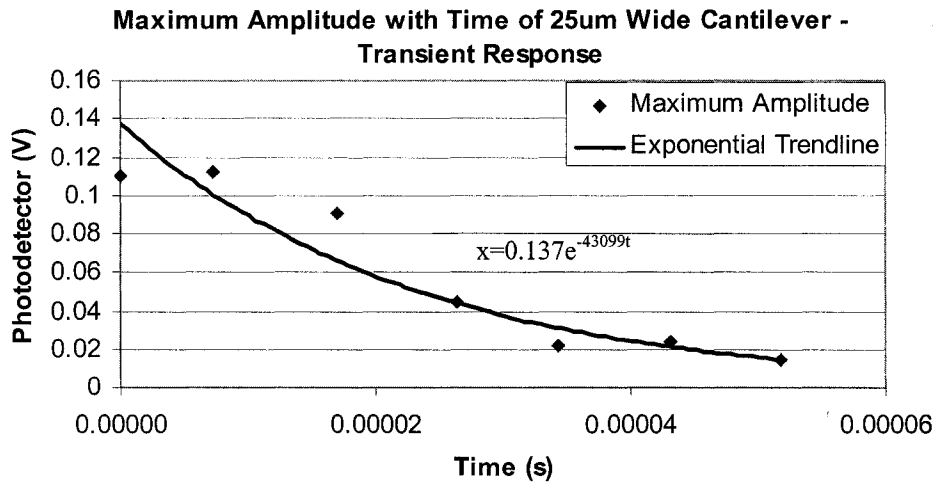
Figure 8-18: Envelope curve for decaying behaviour of 25μm wide standard beam

Using the same method as for the 10μm wide standard beam above (i.e. Equations 8-7 & 8-9) and the resonant frequency of 53.43 ± 1.1 kHz from Figure 8-12, the damping coefficient is found to be 86198 ± 2800 and the Q-factor 3.93 ± 0.1 for the 25μm wide standard beam. The error in the damping coefficient is found the same as was for the 10μm wide beam where $dx/d\gamma$ of Equation 8-7 (shown in Figure 8-18) is taken. The Q-factor is found to be much lower than was found for the 10μm wide beam using the transient method. However, when comparing the Q factors found for the two methods (fringe and transient), they are not consistent because they do not match within error. The transient method is deemed as more representative of the actual response from the cantilever because the error in the Q factor is much less than was found for the fringe method.

All resonant systems will exhibit transient behaviour from any disturbance to the system. The transient behaviour will decay in time in about:

$$t = \frac{6Q}{\omega_o} \approx \frac{Q}{f_o}$$
<div style="text-align:right">Equation 8-12</div>

~181~

Using Equation 8-12, the average of the two Q-factors and the resonant frequency found with the steady state method, the expected time for decay for the 10μm wide is 120μs. Because the driving square wave is at 5kHz, the beam is allotted only 100μs to ring. The response in Figure 8-14 shows that the transient response is nearly faded out by the end of the 100μs. Similarly, from Equation 8-12, for the 25μm wide beam, the expected time for complete decay is 85μs. In Figure 8-17, the decay is complete after 80μs. It is thus concluded that Equation 8-12 is accurate for the results found in this chapter.

4 Discussion of Results

Air damping has been highlighted throughout the thesis as being the major source of energy losses in the micromechanical resonator and the main reason for low Q factors. It was estimated from the analytical calculations in Chapter 3 that the Q factor be dominated by air damping and was calculated as ~4.3 for the standard beam. The analytical calculations were, however, only an estimate and not expected to match the experimental results closely because assumptions made during the calculations were not for air in a viscous regime and did not model air at atmospheric conditions. Another important fact is, analytically, the width of the beam does not affect the effect of air damping. It is found experimentally that, although the Q factors matched quite well to the estimations, they were dependent on width. The quality factor is found to increase with decreasing width of the beam. Standard beams of 50μm, 25μm, and 10μm width are found to have Q factors of overdamped, ~4, and ~7, respectively. Also, the first iteration of devices had a beam-to-substrate distance of 1μm (instead of the 2μm for the standard beam) and no resonance was found, possibly due to an overdamped structure. The first iteration was designed with the fact that the distance between the capacitor plates should be minimized and the area of the electrode be maximized in order to optimize the sensitivity of capacitive detection and reduce the voltage required for actuation. Under such conditions, however, damping dominated. When electrical testing failed, these requirements were then relaxed, and the distance between the beam and the bottom electrode, d_{BS}, was doubled in iteration #2.

The cantilevers tested are believed to be affected by a more complicated phenomenon than conventional air damping, which is termed 'squeeze film damping'. Newell first reportedly observed squeeze film damping when he discussed the effect of the surrounding air on the Q of a resonator. He observed that the ever-present damping due to the ambient surroundings increased when the resonator was brought near to a second surface [148]. He explained this as the pumping action of the gas between the surfaces. It has also been explained by Neyheh that the viscosity of the fluid resists the movement of the fluid underneath the plate. This interaction gives rise to a pressure gradient underneath the plate, which may act as a spring and/or a damping force against the plate [149]. In other words, squeeze film damping refers to air that becomes increasingly trapped and is not free to move out of the way of an impinging MEMS device.

The problem for squeeze-film is commonly described with a two-dimensional linearized Reynolds equation, solved by Blech [150] for a rectangular geometry. The Reynolds equation is derived from the Navier-Stokes equations and the continuity equation. The main assumption is that the gas in the gap can be treated as a continuum [149]. The continuum model breaks down when beams are operated at low pressure or nanoscale beams are operating at atmosphere. The validity of this assumption depends on the so-called Knudsen number, K_n, [151] defined as the molecular mean free path of the gas divided by the characteristic variable distance between the two plates. The mean free path is inversely proportional to the pressure of the ambient. Therefore, as pressure is decreased, the distance that a gas particle travels between collisions (mean free path) increases, and the K_n increases.

It has been reported that resonator vibration damping is dominated by squeeze-film damping for small recess depths (15μm or less) and that a pressure below 1 mbar is needed to achieve Q-factors of more than 3000 [152]. The devices fabricated for this work are, in fact, recessed cavities, 1 or 2μm in depth, and this certainly falls below the 15μm limit Corman et al. present. The squeeze film damping effect is an obvious reason why there was no measurable Q factor in the first iteration of devices (1μm gap) but how squeeze film damping can be the explanation for the Q factor's dependence on width in

~183~

the second iteration (2μm gap) is not so obvious. An explanation is presented for how squeeze film damping is the cause for Q factor's width-dependence.

Shown in Figure 8-19 is a side view of an electrostatically actuated cantilever beam like the ones used in this work. In the figure, (a) depicts the situation most appropriate for the Q factor calculations with respect to air damping as performed in Chapter 3. However, the side views illustrated in (b) and (c) depict the standard beams of 25μm and 10μm widths. In the design, the widths between the edges of the Pyrex etch and the edge of the cantilever beam is kept the same. This means that there are 12.0μm lateral gaps between the edge of the cantilever and the wall of the Pyrex etch for air to flow. There is higher volume of air escaping with the wider beam through the same pathway so a higher level of resistance to this airflow is expected. It is, therefore, expected that the narrower beam (10μm) have a higher quality factor than the wider beam (25μm) and a possible explanation as to why no measurable quality factor resulted from the widest beams (50μm).
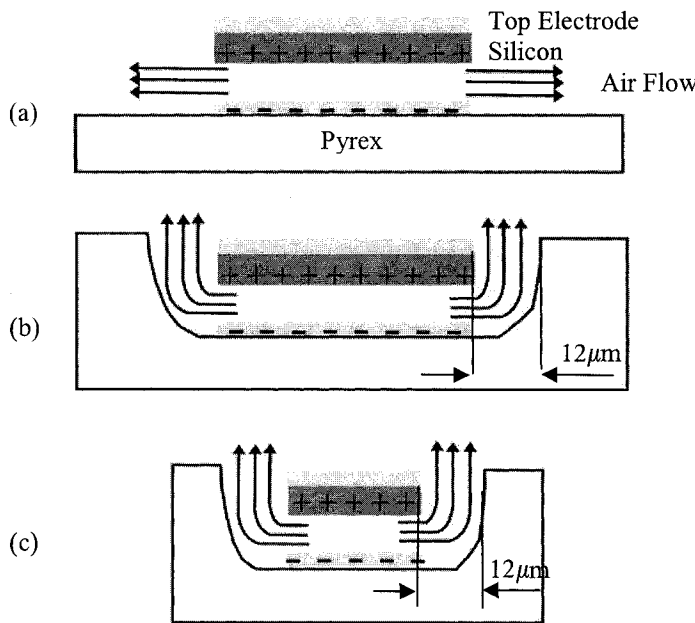
Figure 8-19: Squeeze film damping airflow schematics

To reduce the squeeze film damping effect, it is desired that the flow be in the free molecular regime instead of the viscous regime as was shown in Figure 2-6. To be in this regime, K_n must be greater than 10. With the current design, K_n is 0.03 (Equation 2-1). One way to increase K_n is to decrease pressure because this will increase the mean free path. To achieve a K_n of 10, the pressure must be reduced to 250 Torr (0.3 atm) when

~184~

keeping the distance between the plates to 2μm. However, the second way to achieve free-molecular flow is by reducing the distance between the plates. At atmospheric conditions, the distance between the plates required to achieve free-molecular flow is 70nm. Although this is not necessarily plausible, it shows that by reducing the distance between the plates, the vacuum requirements needed to achieve adequate damping factors can be reduced.

5 Conclusion

In this chapter, the dynamic motion of the cantilever is analyzed with the interferometer presented and characterized in Chapters 6 & 7. General movements such as the beam's effect with applied bias and characteristics such as current and increasing applied voltages between the beam and the bottom electrodes are presented. The beam's resonance is explored with both steady state and transient behaviours. The steady-state method utilizes fringe counting at different applied frequencies while the transient method utilizes a reduced-frequency square wave to induce a decaying, response of the beam. The resonant frequencies, Q-factor, and damping factors are found with these methods. In addition, a discussion of results and explanation of squeeze film damping effect observed during tested is presented. A summary of the results found in this chapter is presented in Table 8-5 below:

Table 8-5: Summary of Results for Standard Beam

	10μm wide (Std. Beam)	25μm wide (Std. Beam)
Theoretical Resonant Frequency	53.98 kHz	53.98 kHz
Resonant Frequency	58.0 ± 0.1 kHz	53.4 ± 1.1 kHz
Quality factor (steady-state response)	7.30 ± 0.5	5.95 ± 1.2
Quality factor (transient response)	7.75 ± 0.1	3.93 ± 0.1
Damping Factor (γ)	47162 ± 2400	86198 ± 2800

Chapter 9 – Improvements & Future Directions

1   Introduction

This chapter presents improvements to both the testing set-up and to the design and a discussion of future directions. A fibre optic interferometer is developed by Brian Moore and in collaboration with him, is made to suit the MEMS dynamic testing of this work (paper submitted). The discussion includes explanation of the design and comparative results for a resonant MEMS cantilever to the bench top interferometer introduced in Chapter 6. Secondly, a design is proposed that will virtually eliminate support loss but which allows for processing options to reduce capacitive gaps to submicron dimensions. Lastly, future directions are discussed with respect to applications requiring high Q factors and/or on-chip dynamic movement sensing.

2   Utilization of a Fibre Optic Interferometer

A non-destructive, contactless optical technique for the testing of small displacements and MEMS structures is developed in collaboration with Brian Moore, a PhD. Candidate in the same group.   Together, Brian's design is adapted to measure micromechanical resonators with far less alignment, cost, and time than the bench-top interferometer design presented in Chapter 6. This technique uses standard single mode optical fibres and low cost laser sources to achieve submicron measurements. The technique provides a sensor interface that does not require electrical or ohmic contact with the mechanically active elements and is capable of detecting very small displacements at high speed with minimal power requirements, no design layout changes, and virtually no area overhead. This technique facilitates characterization under harsh environmental conditions including vacuum, high pressure, high temperature, etc. A paper has been submitted to IEEE Sensors for this work [153].

2.1 Design

The principle of operation of the single fibre interferometer is similar to the Michelson interferometer introduced in Chapter 6. The reference light beam is created by the reflection of the first fibre-air interface, and is reflected back into the sensing fibre before entering or traversing the cavity. The object beam passes the fibre-air interface and is incident on the surface to be measured where it is then reflected back into the fibre. The two beams then recombine and their interference is monitored with a photodetector attached downstream to the fibre. The interference between the reference and object beams alters as the reflective surface alters. Figure 9-1 shows how the reference, measurement, and source beams are carried in the fibre and the cavity for the single fibre case.
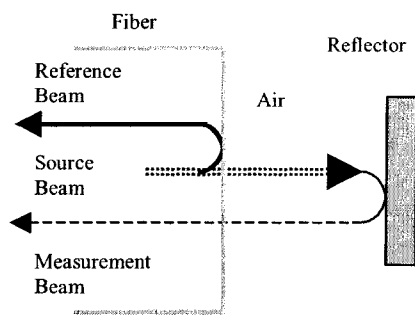
Figure 9-1: Single fibre interferometer optical beams

How does one use a single fibre to act as a source and a detector? Recently, optical circulators have been created for fibre optic telecommunications applications. Although small, these devices are sophisticated from an optics viewpoint. In one device, termed a circulator, are polarization separation, $\frac{1}{4}$ wavelength plates, GRIN lenses, combiners and polarizers - all in a package 5 cm long, .5 cm diameter and featuring polarization independence! A fibre circulator is a 3-port device that is used to couple laser light to fibre 1, couple detection light onto fibre 2 (i.e. fibre 2 is incident on the sample being measured), and use the fibre 3 as the sensor in the interferometer. The circulator results in light energy transfer in one direction only. For example, from fibre 1 to 2, 2 to 3, and 3 to 1. In this design, port 1 to 2 is used to bring the source light to the sample to be measured, and port 2 to 3 brings the reflected, recombined light to a photodetector. Port 3 to 1 is not utilized in this design. A parts list for the fibre interferometer is presented in Appendix f. This set-up successfully measured active MEMS structures, as is discussed in the following section.

2.2 Results

The beams used to characterize the bench top interferometer in Chapter 7 are used for the same purpose with the fibre interferometer. The 168.6 ± 0.5 μm long beam with expected, analytical resonant frequency of 73.8 ± 3 kHz and a measured resonant frequency of 72.8 ± 0.2 kHz (measured using the bench top interferometer & excited mechanically with a piezoelectric tube, both introduced in Chapter 6). Figure 9-2 shows the single-fibre interferometer response of MEMS structure (flexural beam) to the actuation frequency sweep. In this set-up, the stimulation of the cantilever is swept over a range of frequencies. The width of the signal is a combination of noise in the system and the interferometer sensing motion. Clearly shown in the figure is a resonance peak of the MEMS structure at about 72.8 ± 0.2 kHz, which corresponds precisely to the measured resonance presented in Table 7-3 using the bench top method.

Resonance of Cantilever Detected by Fibre Interferometer
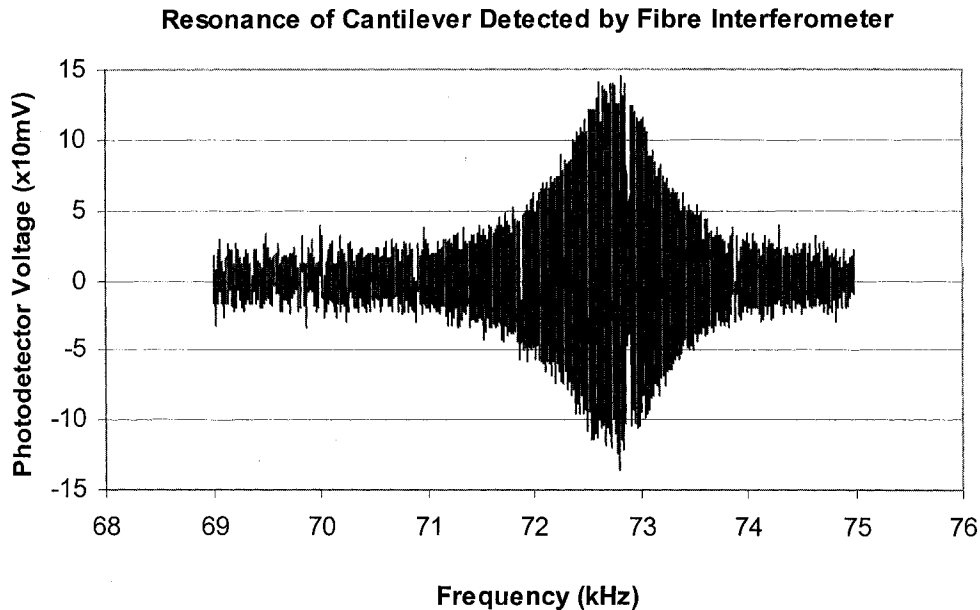
Figure 9-2: Response of micromechanical resonator measured by a fibre interferometer

3 Improvement of Support Loss

In addition to improvements to the testing aspect of this work, a proposed design for a micromechanical resonator is presented. It has been discussed that the Q of a micromechanical resonator is limited by viscous losses in the gas surrounding the

~188~

resonator (i.e. air or squeeze film damping) when actuated in atmospheric or near-atmospheric environments. However, at lower pressures, the Q is controlled by material losses such as through the supports. For example, consider the first mode of vibration for a free-free bar. As labelled in Figure 9-3, the nodes, n, occur near the end of the bar with the antinode in the middle. There is movement at the end of the bar; therefore, if the bar is constrained (i.e. motion is inhibited) at these points, there are energy losses. This is the same situation occurring with the cantilever beams in this work.

Support losses can be reduced if the attachments are made at the nodes of vibration. (A real life example is the xylophone.) Notes are achieved by hitting a free-free bar and allowing for the vibration of the bar to move the air so the audible tone is heard.
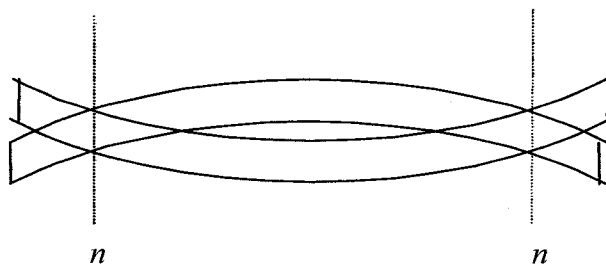
n n

Figure 9-3: Principal mode of free-free bar

The note rings for seconds because there is minimal damping and low support loss. The low support loss is achieved because the bar rests on pegs situated at the nodes. This same technique can be applied to micromechanical resonators. This is reported by Wang *et. al.* through supporting, what the author terms as "free-free" mechanical beams, at their flexural node points by four torsional beams, each of which is anchored to the substrate by rigid contact anchors [85]. Also, Clark *et al.* fabricated a disk resonator which utilizes the same strategy. The motion of the disk is radial so the centre corresponds to a motionless nodal point during vibration [90]. This technique contributes to obtaining Q factors as high as 8400 at 30-90 MHz for the beam and 9400 at 160 MHz for the disk (both in vacuum). It should be noted that the high frequency is also achievable because of the high stiffness of the design, which is not usually possible because, usually, the support losses increase with increased stiffness. Presented below is a preliminary design idea which further extends the musical analogy and incorporates the technique of minimizing energy losses by supporting at vibrational nodes.

~189~

3.1 Tuning Fork Design

The tuning fork is a well-known frequency-tuning device. The fork is used in many applications as a tuning device because of its great purity of tone. The tuning fork is considered from the point of view of a free-free bar as shown above in Figure 9-3. The nodes are situated at n, n and when the bar is gradually bent at the middle the nodes approach each other [154]. When two limbs are parallel and connected at one end, the arrangement forms a tuning fork. There is also an antinode at the centre of the bend connecting the two limbs. When a stem is added at the location of the bend, it has the effect of adding mass at the antinode, thus increasing the stiffness at that point [154]. The result is that the prongs have much greater amplitude of vibration than the antinode, as shown in the figure below. Although the fork is usually used known for its principal mode, there is another mode of vibration predicted by theory, called the "clang" mode. The fundamental mode and clang mode are illustrated in Figure 9-4 where the arrows point to nodal locations. The clang mode occurs at a much higher frequency (nearly three octaves higher in a typical fork) [155].
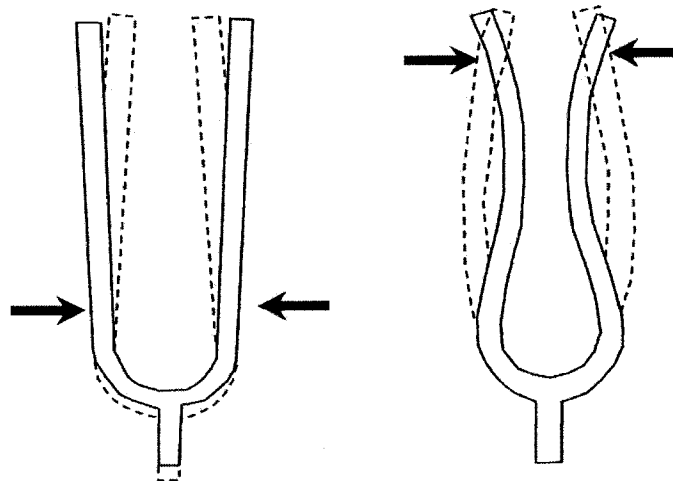
Figure 9-4: Representation of vibrations of a tuning fork:

(a) Principal mode; (b) "Clang" mode [155]

In their normal motion, the bars pivot about two nodes marked by arrows in the figure above, causing the handle to move up and down. Evidence of a moving handle is

~190~

presented when the handle of a vibrating tuning fork is pressed against another object like a piece of sheet metal, causing that object to act as a sounding board. This result implies that the handle of a tuning fork design for a micromechanical resonator may be an undesirable place to constrain. Attaching the fork by the nodes would be the obvious solution, but accurately predicting the placement of the nodes may be difficult because of microfabrication variation. This then leads to exploration of the second, less known "clang" mode, which seems to have a node at the handle.

3.2 Modelling a Tuning Fork

A tuning fork is modeled to explore the modes and vibrations at the handle. The note A above middle C produces a principal resonance of 440Hz which is used in this model to illustrate the idea. The "clang" mode is expected to occur around three octaves above the principal mode so the frequency for the nth octaves is $2^n * f$, and three octaves above the principal mode for this tuning fork is $2^3 * 440Hz = 3520Hz$. It is expected that the principal mode be ~440Hz and the "clang" mode be in and around 3500Hz. The tuning fork is modeled in a finite element-modeling (FEM) program called Pro Engineer WildFire Mechanica. This program allows modeling of the tuning fork with extremely accurate geometry. For example, rounding of corners typically found in machined devices is easily implemented. The tuning fork is modeled utilizing a modal analysis without any forces or constraints applied to the model and the first 6 modes of vibration are shown in the Table 9-1 below.

Table 9-1: Unconstrained Modes of a 440Hz Tuning Fork

Displacement Mag (WCS) (mm) Deformed Max Disp +1.0000E+00 Scale 1.1977E+01 Loadset:Mode 1, +4.2682E+02 — mode 1 426.82Hz	**Principal Mode**
Displacement Mag (WCS) (mm) Deformed Max Disp +1.0000E+00 Scale 1.2014E+01 Loadset:Mode 2, +7.6850E+02 — mode 2 768.50Hz	**Rigid Body Twisting**
Displacement Mag (WCS) (mm) Deformed Max Disp +1.0000E+00 Scale 1.2199E+01 Loadset:Mode 3, +1.2398E+03 — mode 3 1239.8Hz	
Displacement Mag (WCS) (mm) Deformed Max Disp +1.0000E+00 Scale 1.2085E+01 Loadset:Mode 4, +1.4494E+03 — mode 4 1449.36Hz	**Rigid Body Bending**
Displacement Mag (WCS) (mm) Deformed Max Disp. +1.0000E+00 Scale 1.2142E+01 Loadset:Mode 5, +2.6868E+03 — mode 5 2686.78Hz	**Clang Mode**
Displacement Mag (WCS) (mm) Deformed Max Disp +1.0000E+00 Scale 1.2498E+01 Loadset:Mode 6, +3.1805E+03 — mode 6 3180.49Hz	**2nd Mode Rigid Body Bending**

~192~

The principal mode is found at 427 Hz, instilling confidence in the fact that the model is accurately drawn[§§§], and that the analysis details such as the model's mesh, convergence criteria, etc. are also accurate in this range of frequencies. Theory predicts the two modes (principal and clang), but other modes are shown in the result of the analysis. This is explained by rigid body motion. It should be noted that the displacements have been scaled for visual effect and that the prongs are not actually touching at the antinode of the clang mode. Also, as mentioned above, the clang mode is expected to be ~3 octaves. The result predicts the clang mode to be 2.7 times higher (2.7kHz) than the principal mode (440Hz), which is what was predicted by theory. The number of octaves the clang mode is excited above the principle mode for the tuning fork in this model is calculated as:

$$\#Octaves = \frac{\log(\frac{2686.78Hz}{426.82})}{\log(2)} = 2.65 \qquad \text{Equation 9-1}$$

A close-up image of the handle for the principal and clang mode is shown in Figure 9-5. The original shape is overlaid on the result as a semi-transparent blue. It is most importantly noted that the handle moves in x (horizontal in the figure) at the fundamental frequency, as expected. If anchored at the handle (as would be in a MEMS design), this would result in energy loss from the handle. However, the handle does not move at all while resonating at the clang mode so no energy loss is expected at the handle. Although higher order modes do not usually resonate with as high of a Q as the fundamental frequency, if the fundamental frequency is limited by support damping, the clang mode may exhibit a much higher Q.

[§§§] Tuning fork model created by Dr. Roger Toogood from Mechanical Engineering, University of Alberta

~193~

Displacement Mag (WCS)
(mm)
Deformed
Max Disp +1.0000E+00
Scale 1.1977E+01
Loadset:Mode 3, +4.269IE+02

9.000e-01
8.000e-01
7.000e-01
6.000e-01

No movement
in handle

Displacement Mag (WCS)
(mm)
Deformed
Max Disp +1.0000E+00
Scale 3.6096E+01
Loadset:Mode 1, +4.2682E

9.000e-01
8.000e-01

Movement
illustrated at
handle

Unconstrai

(a) Clang Mode   (b) Principle Mode
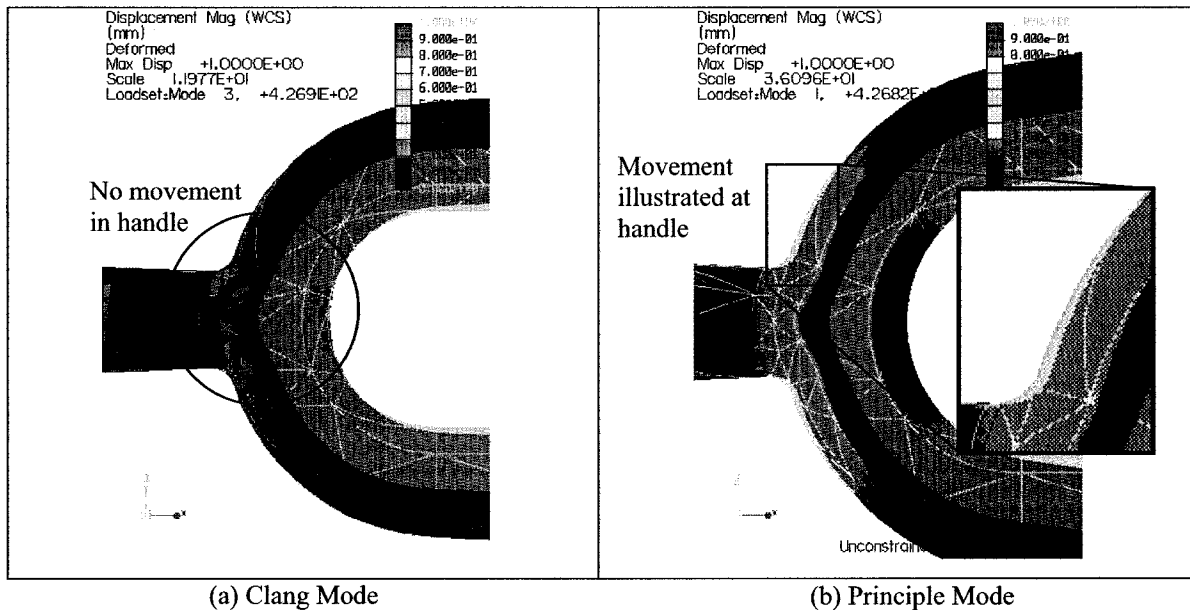
Figure 9-5: Close-up of the handle of a tuning fork in its principal mode:
(a) "Clang mode" showing no displacement of the handle (b) Principle mode showing displacement of the handle.

4 Targeted Applications for Future Directions

Improvements in the test set-up and design have been proposed in this chapter. Additionally, improvements and discussions on increased performance have also been presented. For example, the need for increased frequencies and decreased damping for targeted applications have been main themes. The following section outlines applications with respect to their most important performance criteria. Included are discussions for high Q and on-chip sensing. The improvements required and the applications targeted for these areas are mentioned as a way to clearly outline possible future directions.

4.1 High Quality Factor Required

Biological mass sensing has been one of the targeted applications for this work. Although a higher frequency is not necessarily required, a high quality factor is vital. As was seen by the Q factor calculation in Chapter 3 (verified experimentally in Chapter 8), the main cause for damping in this work is caused by 'squeeze film damping'. It has been discussed that operating a micromechanical resonator in vacuum will mostly

~194~

alleviate these effects. For the standard cantilever beam discussed throughout this work operating at 1mTorr, a quality factor of 2.4×10^5 (Equation 3-15) is expected (compared to the ~4 calculated in air). It is also important to note that at this pressure, the quality factor is limited by support losses and the quality factor due to air damping alone is 3.6×10^6 (Equation 3-20). This concludes that for a cantilever design, the Q factor could be increased by 3 orders of magnitude at low pressures if support losses could be alleviated.

Biological mass sensing usually takes place in a laboratory environment so the systems do not have to be self-contained with vacuum packages and on-chip device monitoring but can be used in proper vacuum systems with optical motion sensing systems such as the fibre interferometer described above. However, even operating the design in UHV does not assume a lossless design. As was noted, other losses such as support losses play a more dominant role in reducing the quality factor of the device. TED and surface losses are also other sources of loss for a mechanical resonator but are difficult to design around. However, the support losses can be practically alleviated with design approaches such as the tuning fork design which is attached to the substrate at a nodal (or non-moving) location, as discussed in this chapter.

The second most common application for micromechanical resonators discussed is for use as filters in wireless communication circuits. Resistors, capacitors, and inductors are the most common passive circuit elements, and filters can be constructed with these three elements only. For example, a RCL bandpass filter is formed from a high pass filter followed by a low pass filter, provided that the cut-off frequency of the high pass filter is lower than that of the low pass filter. A schematic of the set-up is shown in Figure 9-6.
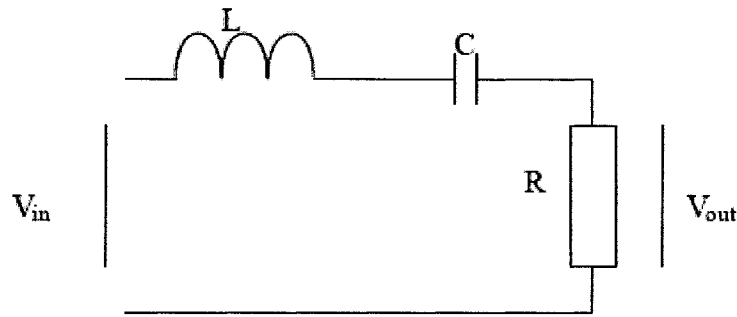
Figure 9-6: Schematic of a passive resonant circuit

This is often referred to as a passive resonant circuit, used to pass select frequencies while removing unwanted frequencies. These passive filters were first popularized in 1910-1920, during the advent of the era of radio, to remove unwanted static from the signal to improve the reception. As was discussed in Chapters 3, 5, and Appendix B, the micromechanical resonator presented in this work is a physical representation of the RCL passive, resonant circuit. It can, therefore, be used as a filter itself and, ideally, replace the RCL circuit directly. A switched-filter front-end is proposed by Nguyen in lieu of the tuneable filter used today [26]. Obvious advantages are the micromechanical resonator's fabrication compatibility with integrated circuits. Currently, most passive components in a circuit such as capacitors, resistors, and inductors are difficult to integrate into circuitry and must be fabricated separately and assembled on the board as "off-chip" components. This is a labour intensive, and therefore, expensive part of the fabrication which could be eliminated through the use of micromechanical resonators. Secondly, tuneable filters are achieved in a RCL circuit by varying the value of either the capacitor or the inductor and this will change the resonance of the circuit. Adjusting dimensions such as length alters the resonant frequency of the micromechanical resonator which is easily done with lithographic techniques so that many different frequency selective filters can be made simultaneously. The last advantage is the potential for high quality factors of micromechanical resonators versus their electronics counterparts. As just discussed, the quality factor of micromechanical resonators can reach into 10^5 compared to under 75 for integrated circuits [4]. However, reliable packaging techniques which maintain vacuum are not only difficult and an active area of research [32, 156], but are also expensive. In order to reduce these costs, methods such as the fibre interferometer developed during

~196~

this work become increasingly important. As briefly mentioned, devices can be tested on chip with this method without the need to dice the chips and bond or probe. Assembling and packaging only the devices that test within specification avoids needless packaging and therefore, needless cost.

4.2 On-Chip Sensing Necessary

On-chip sensing is required in applications such as filters for wireless communications and passive harmonic radar tags where a complete, integrated system is important. These applications have been discussed throughout this work. In short, micromechanical resonators used as filters take advantage of the fact that they are easily integrated with current ICs and they have high Q factors. Harmonic radar tags utilize a different frequency for the transmitting signal as the receiving signal. Both the harmonic generation expected of the beam in this work or using the higher order mode of a tuning fork design ("clang" mode) can be used as designs that create the differentiating signals.

Many typical micromechanical resonator designs employ a parallel-plate capacitor in which one of the plates is electrostatically actuated and, where on-chip sensing is necessary, its motion is detected by capacitive changes. In order to decrease the voltage required to create motion and to improve the sensitivity of detection, small capacitive gaps (Chapter 5) and large electrode areas are necessary. In addition, small capacitive gaps are required to reduce the impedance of the device so matching to other components such as antennas is possible. Under these conditions, however, the 'squeeze film damping' effect (Chapter 8) is pronounced. In order to reduce these effects while still being able to have small capacitive gaps, packaging in low-pressure cavities is required (Chapter 2).

Although the MEMS resonator has the potential to outperform the existing technology in the fields of filters and harmonic radar tags, if the motion cannot be detected on chip, its feasible is questioned because optical testing is as bulky as the off-chip components MEMS is trying to replace. Although not demonstrated in this work, capacitive sensing is a successful approach to sensing the dynamic motion of electrostatically actuated

~197~

MEMS [26, 157]. Under the right circumstances, such as with the MEMS device completely integrated with the electronics (CMOS-MEMS integration) or in close proximity of the electronics (wire bonds instead of probes), the signal is more easily sensed because the capacitance external to the device is reduced and electronic pickup can be shielded.

5 Conclusions

Future directions and improvements are outlined in this chapter. A fibre optic interferometer is introduced, which can be used as a wafer level characterization device without the need for expensive, large, bench top interferometry. Also, a tuning fork design is presented using a little known mode of vibration to eliminate support losses. The utilizing of a tuning fork design, driven at the "clang" mode, is thus presented as a possibility for future directions. Because the design resonates in plane with the substrate surface, more options for decreasing the gap size are available. (i.e. e-beam lithography or novel sacrificial layer techniques). Lastly, targeted applications are discussed through the development of achieving higher quality factors and on-chip sensing.

Chapter 10 – Conclusion

The work presented here encompasses an investigation of perhaps the simplest MicroElectroMechanical Systems (MEMS) example – the cantilever beam - from design and fabrication to experimental analysis. More specifically, an electrostatically actuated micromechanical resonator is designed, fabricated, tested and characterized. The work was done as part of a Natural Sciences and Engineering Research Council of Canada Industrial Postgraduate Scholarship (NSERC IPS) in collaboration with Micralyne Inc. to further develop a generalized MEMS fabrication process, Micragem, while laying the groundwork for future work in the field of Radio Frequency MEMS (RF MEMS).

A 2μm thick cantilever beam is designed with a resonance in the low kHz range, is gold coated, and is separated by a 2μm gap from its bottom electrodes. The standard beam discussed throughout the work is 200μm long and 25μm wide. When a voltage potential exists between the beam and the bottom electrode, an electrostatic force is created, causing a deflection of the beam towards the electrode. In addition, when a sinusoidal potential is applied across the gap (between the beam and bottom electrode), the beam deflection also moves in a sinusoidal manner. Analytical calculations for the standard beam found that at 54kHz, there is a great increase in deflection amplitude because of the fundamental resonance that occurs at this frequency. The efficiency of this increased amplitude, termed the quality factor (Q), is partially inherent to the physical design and dimensions of the beam but also due to the environment in which it is actuated. The analytical Q factor is found to be ~4.5 and is dominated by air damping (i.e. its environment).

Successful devices were fabricated with Micralyne's Micragem process; and, following this work, in collaboration with the Canadian Microelectronics Corporation, the generalized process has been offered as a prototyping service across Canada.

Analyzing the beams turned into a very complex task. The original intent was to test the beams dynamically by sensing the induced current produced due to the change in capacitance from the varying distance of the beam with respect to the bottom electrode. Analytical, "back of the envelope" calculations estimated an induced current in the fA-pA range and a voltage signal in the mV range when including the capacitances of the wire traces, connection pads, probes, etc. After two operational amplifier circuit designs and numerous attempts, no induced current signal was detected. It was deemed that if the electronic pickup could be reduced and the connections to the operational amplifier detection circuit could be minimized, the electrical testing would be possible. For example, if the chip was designed so wire bonds to the detection circuit were possible, the need for probes and a probe station would be eliminated and the testing could take place in a shielded environment.

The beams were also characterized for dimensions and actuated statically. Zygo, a commercially available surface profiler based on interferometry, was used as a tool to characterize the beam's deflection with respect to applied voltage. The beam snapped shut at a threshold voltage, ranging between 21V-25V for beams. These values compared well to the expected, calculated threshold voltage of 19.4V when taking into account that the analytical model did not include film stress. It was then concluded that the beams are, in fact, completely released and motion was proven.

Although the electrical testing of the dynamic motion of the micromechanical resonators failed, it was demonstrated that they were actuating and behaving as expected. The available equipment (i.e. the Zygo) was not capable of dynamic characterization. A bench top interferometer based on Michelson interferometry was designed, assembled, and characterized as an alternative method for dynamic testing and characterization of the devices. Various techniques were used to develop and characterize the interferometer

~200~

and photodetector circuitry such as other resonant devices and frequency response testing of the circuitry. Upon satisfactory results from the characterization of the set-up, the micromechanical resonators presented in this work were tested. It was found that they resonate between 55-58kHz with quality factors between 4-8, as expected. Most interestingly, the width was found to have an extremely important influence on the damping and, thus, the quality factor of the devices. In short, the wider the beams are, the greater the "squeeze-film damping" effect and the lower the efficiency of resonance of the beam. The effect became so prominent in the 50μm-wide standard beams that no detectable resonance was found. The 25μm-wide beams had quality factors in the range of 4 and the narrowest beam's quality factor was in the range of 7. This was an unexpected phenomenon because all calculations were width independent.

Upon analyzing the result of the testing of a micromechanical resonator, improvements were a necessary and inevitable part of the work. In collaboration with Brian Moore, a doctoral candidate in electrical engineering who has been developing non-contact characterization methods, the candidate developed and applied a single fibre optic interferometer for detecting dynamic, submicron movement of MEMS devices. The appeal of this approach is its low cost, assembly time, and adaptability to a manufacturing wafer-level testing method. The method was proven by testing the resonance of some cantilever beams and compared to the bench-top design presented in this work. Secondly, a design of a micromechanical resonator is presented for future directions. The low quality factor due to air damping presented a case for actuation within a vacuum environment. As discussed in this thesis, the next most crucial energy loss mechanism is due to the attachment of the device to the substrate. In the case of the tuning fork design, and unlike the cantilever beam, the point at which the device attaches to the substrate is a nodal point, so it does not move at resonance. This creates an opportunity for a greatly increased quality factor, which is the major limiting concern for a device's applicability for biological mass sensing applications. Modeling of the device is thus presented and pursuing this endeavour is encouraged as a future direction because its lateral movement presents greater opportunities in possible fabrication processes to reduce the capacitive gap size. This greatly increases the chance of integrating the device with on-chip

~201~

monitoring and makes it a feasible approach for wireless communication applications or lab-on-a-chip biological mass sensing approaches.

The micromechanical resonators presented in this work are in need of further development before they are candidates to replace any off-chip components in the circuits in wireless communications or used as mass sensors in the biological field. Further, to be used as a harmonic radar tag, the advantage of the device over present methods is only apparent if the frequency of the device is higher and the output impedance lower so that integrated, on-chip antennas can be incorporated. Increasing the frequency is also necessary for its applicability for wireless communications but also (and more importantly for use as a biological mass sensor), the Q factor needs to be much higher than 10. In order for the Q factor to increase dramatically, the device needs to be packaged in a vacuum. This is currently the major stumbling block for micromechanical resonators worldwide because packaging at vacuum with long-term stability is challenging.

In summary, this work was done on an NSERC IPS with Micralyne Inc. and the University of Alberta. In it we present the design, fabrication, and testing of a micromechanical resonator operating in the kHz range. In this work, the candidate further developed the commercial microfabrication prototyping process, Micragem, to the point that it is now offered commercially across Canada. Micragem now enables high quality fabrication of devices for a range of MEMS applications.

Bibliography

[1]   S. Y. No, A. Hashimura, S. Pourkamali, and F. Ayazi, "Single-crystal silicon HARPSS capacitive resonators with submicron gap-spacing," presented at Solid-State Sensor, Actuator and Microsystems Workshop, Hilton Head Island, South Carolina, 2002.

[2]   W.-T. Hsu, W. S. Best, and H. J. D. L. Santos, "Design and Fabrication Procedure for High Q RF MEMS Resonators," *Microwave Journal*, vol. 47, pp. 60-74, 2004.

[3]   T. Ono, X. Li, and H. Miyashita, "Mass sensing of adsorbed molecules in sub-picogram sample with ultrathin silicon resonator," *Review of Scientific Instruments*, vol. 74, pp. 1240-1243, 2003.

[4]   J. V. d. Tang and D. Kasperkovitz, "A low phase noise reference oscillator with integrated PMOS varactors for digital satellite receivers," *IEEE Journal of Solid-State Circuits*, vol. 35, pp. 1238-1243, 2000.

[5]   C. T.-C. Nguyen, L. P. B. Katehi, and G. M. Rebeiz, "Micromachined devices for wireless communications," *Proceedings of the IEEE*, vol. 86, pp. 1756-1768, 1998.

[6]   M. L. Roukes, "Nanomechanical systems," presented at 2000 Solid-State Sensor and Actuator Workshop, Hilton Head Island, SC, June 4-8, 2000.

[7]   J. P. Cleveland, S. Manne, D. Bocek, and P. K. Hansma, "A nondestructive method for determining the spring constant of cantilevers for scanning force microscopy," *Review of Scientific Instruments*, vol. 64, pp. 403-405, 1993.

[8]   A. Hierlemann, O. Brand, C. Hagleitner, and H. Baltes, "Microfabrication Techniques for Chemical/Biosensors," *Proceedings of the IEEE*, vol. 91, pp. 839-863, 2003.

[9]   J. K. Gimzewski, C. Gerber, E. Meyer, and R. R. Schlittler, "Observation Of A Chemical-Reaction Using A Micromechanical Sensor," *Chemical Physics Letters*, vol. 217, pp. 589-594, 1994.

[10]   H. Jensenius, J. Thaysen, A. A. Rasmussen, L. H. Veje, O. Hansen, and A. Boisen, "A microcantilever-based alcohol vapor sensor-application and response model," *Applied Physics Letters*, vol. 76, pp. 2615-2617, 2000.

[11]   T. Thundat, G. Y. Chen, R. J. Warmack, D. P. Allison, and E. A. Wachter, "Vapor detection using resonating microcantilevers," *Analytical Chemistry*, vol. 67, pp. 519-521, 1995.

[12]   M. Maute, S. Raible, F. E. Prins, D. P. Kern, H. Ulmer, U. Weimar, and W. Gopel, "Detection of volatile organic compounds (VOC's) with polymer-coated cantilevers," *Sensors and Actuators B*, vol. 58, pp. 505-511, 1999.

[13]   H. P. Lang, R. Berger, F. Battiston, J. P. Ramseyer, E. Meyer, C. Andreoli, J. Brugger, P. Vettiger, M. Despont, T. Mezzacasa, L. Scandella, H. J. Guntherodt, C. Gerber, and J. K. Gimzewski, "A chemical sensor based on a micromechanical cantilever array for the identification of gases and vapors," *Applied Physics A-Materials Science & Processing*, vol. 66, pp. S61-S64, 1998.

[14]   J. Fritz, M. K. Baller, H. P. Lang, H. Rothuizen, P. Vettiger, E. Meyer, H. J. Guntherodt, C. Gerber, and J. K. Gimzewski, "Translating biomolecular recognition into nanomechanics," *Science*, vol. 288, pp. 316-318, 2000.

[15]   F. M. Battiston, J. P. Ramseyer, H. P. Lang, M. K. Baller, C. Gerber, J. K. Gimzewski, E. Meyer, and H. J. Guntherodt, "A chemical sensor based on a microfabricated cantilever array with simultaneous resonance frequency and bending readout," *Sensors and Actuators B*, vol. 77, pp. 122-131, 2001.

[16]   Z. J. Davis, G. Abadal, O. Kuhn, O. Hansen, F. Grey, and A. Boisen, "Fabrication and characterization of nanoresonating devices for mass detection," *Journal of Vacuum Science & Technology B*, vol. 18, pp. 612-616, 2000.

[17]   A. Hierlemann, D. Lange, C. Hagleitner, N. Kerness, A. Koll, O. Brand, and H. Baltes, "Application-specific sensor systems based on CMOS chemical microsensors," *Sensors and Actuators B*, vol. 70, pp. 2-11, 2000.

[18]   D. Lange, C. Hagleitner, A. Hierlemann, O. Brand, and H. Baltes, "Complementary metal oxide simiconductor cantilever array on a single chip: Mass0sensitive detection of volatile organic compounds.," *Analytical Chemistry*, vol. 74, pp. 3084-3095, 2002.

[19]   A. Boisen, J. Thaysen, H. Jensenius, and O. Hanson, "Environmental sensors based on micromachined cantilevers with integrated read-out," *Ultramicroscopy*, vol. 82, pp. 11-16, 2000.

[20]   B. Ilic, D. Czaplewski, H. G. Craighead, P. Neuzil, C. Campagnolo, and C. Batt, "Mechanical resonant immunospecific biological detector," *Applied Physics Letters*, vol. 77, pp. 450-452, 2000.

[21]   H. P. Lang, M. K. Baller, R. Berger, C. Gerber, J. K. Gimzewski, F. Battiston, P. Fornaro, J. P. Ramseyer, E. Meyer, and H. J. Guntherodt, "An artificial nose based on a micromechanical cantilever array," *Analytica Chimica Acta*, vol. 393, pp. 59-65, 1999.

[22]   K. L. Ekinci, Y. T. Yang, and M. L. Roukes, "Ultimate limits to inertial mass sensing based upon nanoelectromechanical systems," *Journal of Applied Physics*, vol. 95, pp. 2682-2689, 2004.

[23]   M. Su, S. Li, and V. P. Dravid, "Microcantilever resonance-based DNA detection with nanoparticle probes," *Applied Physics Letters*, vol. 82, pp. 3562-3564, 2003.

[24]   X. M. H. Huang, C. A. Zorman, M. Mehregany, and M. L. Roukes, "Nanoelectromechanical systems: Nanodevice motion at microwave frequencies," *Nature*, vol. 421, pp. 496, 2003.

[25]   F. D. Bannon, J. R. Clark, and C. T.-C. Nguyen, "High-Q HF microelectromechanical filters," *IEEE Journal of Solid-State Circuits*, vol. 35, pp. 512-526, 2000.

[26]   C. T.-C. Nguyen, "Transceiver front-end architectures using vibrating micromechanical signal processors (invited)," presented at Topical Meeting on Silicon Monolithic Integrated Circuits in RF Systems, Ann Arbor, MI, USA, 2001.

[27]   N. Tredennick, "MEMS and the Cell Phone," *Dynamic Silicon*, vol. 1, pp. 1-7, July, 2001.

[28]   D. Eddy and D. Sparks, "Application of MEMS technolgy in automotive sensors and actuators," *Proceedings of the IEEE*, vol. 86, pp. 1747, Aug. 1998.

[29]   H. Henmi, S. Shoji, Y. Shoji, K. Yoshimi, and M. Esashi, "Vacuum packaging for microsensors by glass-silicon anodic bonding," *Sensors and Actuators A*, vol. 43, pp. 243-248, 1994.

[30]   D. Sparks, G. Queen, R. Weston, G. Woodward, M. Putty, L. Jordan, S. Zarabadi, and K. Jayakar, "Wafer-to-wafer bonding of nonplanarized MEMS surfaces using solder," *Journal of Micromechanics and Microengineering*, vol. 11, pp. 630-634, 2001.

[31]   S. Mack, H. Baumann, U. Gosele, H. Werner, and R. Schlogl, "Analysis of bonding-related gas enclosure in micromachined cavities sealed by silicon wafer bonding," *Journal of Electrochemical Society*, vol. 144, pp. 1106-1110, 1997.

[32]   D. R. Sparks, S. Massoud-Ansari, and N. Najafi, "Chip-level vacuum packaging of micromachines using NanoGetters," *IEEE Transactions on Advanced Packaging*, vol. 26, pp. 277-282, 2003.

[33]   B. Lee, S. Seok, and K. Chun, "A study on wafer level vacuum packaging for MEMS devices," *Journal of Micromech Microengineering*, vol. 13, pp. 663-669, 2003.

[34] Y. Jin, Z. Wang, L. Zhao, P. C. Lim, J. Wei, and C. K. Wong, "Zr/V/Fe thick film for vacuum packaging of MEMS," *Journal of Micromech Microengineering*, vol. 14, pp. 687-692, 2004.

[35] D. Sparks, R. Smith, R. Schneider, J. Cripe, S. Massoud-Ansari, A. Chimbayo, and N. Najafi, "A variable temperature, resonant density sensor made using an improved chip-level vacuum package," *Sensors and Actuators A*, vol. 107, pp. 119-124, 2003.

[36] G. Boiteau and B. G. Colpitts, "Electronic tags for the tracking of insects in flight: Effect of weight on flight performance of adult Colorado potato beetles," *Entomologia experimentalis et applicata*, vol. 100, pp. 187-193, 2001.

[37] D. Mascanzoni and H. Wallin, "The harmonic radar: A new method of tracing insects in the field," *Ecological Entomology*, vol. 11, pp. 387-390, 1986.

[38] J. R. Riley and A. D. Smith, "Design considerations for an harmonic radar to investigate the flight of insects at low altitude," *Computers and Electronics in Agriculture*, vol. 35, pp. 151-169, 2002.

[39] J. Roland, G. McKinnon, C. Backhouse, and P. Taylor, "Even smaller radar tags on insects," *Nature*, vol. 381, pp. 120, 1996.

[40] B. Colpitts and G. Boiteau, "Harmonic Radar Transceiver Design: Miniature Tags for Insect Tracking," *IEEE Transactions on Antennas and Propagation*, vol. 52, pp. 2825-2832, 2004.

[41] D. Williams, G. Li, and R. Gao, "Tracking movements of individual Anoplophora glabripennic (Coleoptera: Cerambycidae) adults: Application of harmonic radar," *Environmental Entomology*, vol. 33, pp. 644-649, 2004.

[42] J. J. Yao and N. C. MacDonald, "A micromachined, single-crystal silicon, tunable resonator," *Journal of Micromechanics Microengineering*, vol. 5, pp. 257-264, 1995.

[43] J. M. Sulima, "Developments Towards Manufacturable Nanoelectronics and Applications," in *Electrical and Computer Engineering*. Edmonton: University of Alberta, 2004.

[44] S. J. Gross, S. Tadigadapa, T. N. Jackson, S. Trolier-McKinstry, and Q. Q. Zhang, "Lead-zirconate-titanate-based piezoelectric micromachined switch," *Applied Physics Letters*, vol. 83, pp. 174-176, 2003.

[45] S. Zurn, M. Hsieh, G. Smith, D. Markus, M. Zang, G. Hughes, Y. Nam, M. Arik, and D. Polla, "Fabrication and structural characterization of a resonant frequency

PZT microcantilever," *Smart Materials and Structures*, vol. 10, pp. 252-263, 2001.

[46] C. Niezrecki, D. Brei, S. Balakrishnan, and A. Moskalik, "Piezoelectric Actuation: State of the Art," *The Shock and Vibration Digest*, vol. 33, pp. 269-280, 2001.

[47] S. E. Park and T. R. Shrout, "Ultrahigh strain and piezoelectric behavior in relaxor based ferroelectric single crystals," *Journal of Applied Physics*, vol. 82, pp. 1804-1811, 1997.

[48] R. Hickey, D. Sameoto, T. Hubbard, and M. Kujath, "Time and frequency response of two-arm micromachined thermal actuators," *Journal of Micromechanics and Microengineering*, vol. 13, pp. 40-46, 2003.

[49] A. N. Cleland and M. L. Roukes, "Fabrication of high frequency nanometer scale mechanical resonators from bulk Si crystals," *Applied Physics Letters*, vol. 69, pp. 2653-2655, 1996.

[50] C. T.-C. Nguyen, "An integrated CMOS micromechanical resonator high-Q oscillator," *IEEE Journal of Solid-State Circuits*, vol. 34, pp. 440-455, 1999.

[51] J. Yang, T. Ono, and M. Esashi, "Surface effects and high quality factors in ultrathin single-crystal silicon cantilevers," *Applied Physics Letters*, vol. 77, pp. 3860-3862, 2000.

[52] J. Yang, T. Ono, and M. Esashi, "Energy dissipation in sub-um thick single crystal silicon cantilevers," *Journal of Microelectromechanical Systems*, vol. 11, pp. 775-783, 2002.

[53] R. E. Mihailovich and N. C. MacDonald, "Dissipation measurements of vacuum-operated single-crystal silicon microresonators," *Sensors and Actuators A*, vol. 50, pp. 199-207, 1995.

[54] J. Wylde and T. Hubbard, "Measurement of MEMS displacements and frequencies using laser interferometry," presented at IEEE Canadian Conference on Electrical and Computer Engineering, Edmonton, Alberta, May 9-12, 1999.

[55] P. B. Chu, P. R. Nelson, M. L. Tachiki, and K. S. J. Pister, "Dynamics of polysilicon parallel-plate electrostatic actuators," *Sensors And Actuators A-Physical*, vol. 52, pp. 216-220, 1996.

[56] D. W. Carr, L. Sekaric, and H. G. Craighead, "Measurement of nanomechanical resonant structures in single-crystal silicon," *Journal of Vacuum Science & Technology B*, vol. 16, pp. 3821-3824, 1998.

[57] J. A. Walker, K. W. Goossen, and S. C. Arney, "Fabrication of a Mechanical Anitreflection Switch for Fiber-to-the-Home Systems," *Journal of Microelectromechanical Systems*, vol. 5, pp. 45, 1996.

[58] W. R. Wiszniewski, R.E.Collins, and B. A. Pailthorpe, "Mechanical light modulator fabricated on a silicon chip using SIMOX technology," *Sensors and Actuators A*, vol. 43, pp. 170, 1994.

[59] D. W. Carr and H. G. Craighead, "Fabrication of nanoelectromechanical systems in single crystal silicon using silicon on insulator substrates and electron beam lithography," *Journal of Vacuum Science & Technology B*, vol. 15, pp. 2760, 1997.

[60] W.-T. Hsu, J. R. Clark, and C. T.-C. Nguyen, "A sub-micron capacitive gap process for multiple-metal-electrode lateral micromechanical resonators," presented at IEEE International Micro Electro Mechanical Systems Conference, Interlaken, Switzerland, Jan. 21-25, 2001.

[61] C. T.-C. Nguyen, "Frequency-selective MEMS for miniaturized low-power communication devices," *IEEE Transactions on Microwave Theory and Techniques*, vol. 47, pp. 1486-1503, 1999.

[62] Y.-H. Park and K. C. Park, "High-fidelity Modeling of MEMS resonators - Part 1: Anchor loss mechanisms through substrate," *Journal of Microelectromechanical Systems*, vol. 13, pp. 238-247, 2004.

[63] Y.-H. Cho, A. P. Pisano, and R. T. Howe, "Viscous damping model for laterally oscillating microstructures," *Journal of Microelectromechanical Systems*, vol. 3, pp. 81-81, June 1994.

[64] W. Ye, X. Wang, W. Hemmert, D. Freeman, and J. White, "Air damping in lateral oscillating micro resonators: a numerical and experimental study," *Journal of Microelectromechanical Systems*, vol. 12, pp. 557-566, 2003.

[65] T. Veijola and M. Turowski, "Compact damping models for laterally moving microstructures with gas-rarefaction effects," *Journal of Microelectromechanical Systems*, vol. 10, pp. 263-273, 2001.

[66] S. Hutcherson and W. Ye, "On the squeeze-film damping of micro-resonator in the free-molecule regime," *Journal of Micromechanics and Microengineering*, vol. 14, pp. 1726-1733, 2004.

[67] Y.-H. Cho, B. M. Kwak, A. P. Pisano, and R. T. Howe, "Slide film damping in laterally driven microstructures," *Sensors and Actuators A*, vol. 40, pp. 31-39, 1994.

[68]   Y. H. Park and K. C. Park, "Coupled substrate-resonator-electrostatic simulation and validation of high-Q MEMS resonator performance," presented at Nanotech 2003, The Nanotechnology Conference and Trade Show, San Francisco, CA, Feb. 24-26, 2003.

[69]   M. C. Cross and R. Lifshitz, "Elastic wave transmission at an abrupt junction in a thin plate with application to heat transport and vibrations in mesoscopic systems," *Physical Review B*, vol. 64, pp. 1-22, 2001.

[70]   R. Lifshitz and M. L. Roukes, "Thermoelastic damping in micro and nanomechanical systems," *Physics Review B*, vol. 61, pp. 5600-5609, 2000.

[71]   Z. Hao, A. Erbil, and F. Ayazi, "An analytical model for support loss in micromachined beam resonators with in-plane flexural vibrations," *Sensors and Actuators A*, vol. 109, pp. 156-164, 2003.

[72]   J. R. Vig and Y. Kim, "Noise in microelectromechanical system resonators," *IEEE Transactions on Ultrasonics, Ferroelectrics, and Frequency Control*, vol. 46, pp. 1558-1565, 1999.

[73]   C. Zener, "Internal friction in solids I: Theory of internal friction in reeds," *Physical Review*, vol. 52, pp. 230-235, 1937.

[74]   C. Zener, "Internal friction in solids II: general theory of thermoelastic internal friction," *Physical Review*, vol. 53, pp. 90-99, 1938.

[75]   S. Pourkamali, A. Hashimura, R. Abdolvand, G. K. Ho, A. Erbil, and F. Ayazi, "High-Q Single Crystal Silicon HARPSS Capacitive Beam Resonators with Self-Aligned Sub-100nm Transduction Gaps," *Journal of Microelectromechanical Systems*, vol. 12, pp. 487-496, 2003.

[76]   K. Y. Yasumura, T. D. Stowe, E. M. Chow, T. Pfafman, T. W. Kenny, B. C. Stipe, and D. Rugar, "Quality factors in micron- and submicron-thick cantilevers," *Journal of Microelectromechanical Systems*, vol. 9, pp. 117-125, 2000.

[77]   R. V. Roszhardt, "The effect of thermoelastic internal friction on the Q of micromachined silicon resonators," presented at IEEE Solid State Sensor and Actuator Workshop, Hilton Head Island, SC, June 4-7, 1990.

[78]   F. R. Blom, S. Bouwstra, M. Elwenspoek, and J. H. J. Fluitman, "Dependence Of The Quality Factor Of Micromachined Silicon Beam Resonators On Pressure And Geometry," *Journal Of Vacuum Science & Technology B*, vol. 10, pp. 19-26, 1992.

[79]   G. N. Patterson, *Introduction to the Kinetic Theory of Gas Flows*. Toronto: University of Toronto Press, 1971.

[80]   J. D. Zook, D. W. Burns, H. Guckel, J. J. Sniegowski, R. L. Engelstad, and Z. Feng, "Characteristics of polysilicon resonant microbeams," *Sensors and Actuators A*, vol. 35, pp. 51-59, 1992.

[81]   S. Pourkamali and F. Ayazi, "Fully single crystal silicon resonators with deep-submicron dry-etched transducer gaps," presented at IEEE International Micro Electro Mechanical Systems Conference (MEMS '04), Maastricht, Netherlands, Jan. 15-29, 2004.

[82]   A.-C. Wong, J. R. Clark, and C. T.-C. Nguyen, "Anneal-activated tunable, 65 MHz micromechanical filters," presented at 10th International Conference on Solid-State Sensors and Actuators, Sendai, Japan, June 7-10, 1999.

[83]   Y.-H. Park and K. C. Park, "High-fidelity modeling of MEMS resonators - Part II: Coupled beam-substrate dynamics and validation," *Journal of Microelectromechanical Systems*, vol. 11, pp. 248-257, 2004.

[84]   W.-T. Hsu, J. R. Clark, and C. T.-C. Nguyen, "Q-optimized lateral free-free beam micromechanical resonators," presented at Transducers '01: 2001 International Conference on Solid-State Sensors and Actuators: digest of technical papers, Munich, Germany, June 10-14, 2001.

[85]   K. Wang, "VHF free-free beam high-Q micromechanical resonators," *Journal of Microelectromechanical Systems*, vol. 9, pp. 347-360, 2000.

[86]   T.-R. Hsu, *MEMS & Microsystems*, 1st ed. NY: McGraw-Hill, 2002.

[87]   M. Roukes, "Nanoelectromechanical Systems Face the Future," in *Physicsweb (http://physicsweb.org/article/world/14/2/8)*, 2001.

[88]   J. Yang, T. Ono, and M. Esashi, "Investigating surface stress: Surface loss in ultrathin single-crystal silicon cantilevers," *Journal of Vacuum Science & Technology B*, vol. 19, pp. 551-556, 2001.

[89]   S. Y. No and F. Ayazi, "The HARPSS process for fabrication of nano-precision silicon electromechanical resonators," presented at IEEE Conference on Nanotechnology, 2001.

[90]   J. R. Clark, W.-T. Hsu, and C. T.-C. Nguyen, "High-Q VHF micromechanical contour-mode disk resonators," presented at IEEE International Electron Devices Meeting, San Francisco, California, 2000.

[91]   K. U. Ingard, *Fundamentals of Waves and Oscillations*. Cambridge: Cambridge University Press, 1990.

[92] A. P. French, "Vibrations and Waves," in *The M.I.T. Introductory Physics Series*. New York: W. W. Norton & Company, 1971, pp. 83.

[93] J. C. Greenwood, "Silicon in Mechanical Sensors," *Journal of Physics E, Scientific Instrmentation*, vol. 21, pp. 1114-1128, 1988.

[94] H. Santos, *Introduction to Microelectromechanical (MEM) Microwave Systems*. Norwood, MA: Artech House, 1999.

[95] M. J. Madou, *Fundamentals of Microfabrication: The Science of Miniaturization*, 2nd ed. Boca Raton: CRC Press LLC, 2002.

[96] G. M. Rebeiz, *RF MEMS: Theory, Design, and Technology*. Hoboken, New Jersey: John Wiley & Sons Inc., 2003.

[97] M. Zahn, *Electromagnetic Field Theory: A Problem Solving Approach*. New York: John Wiley and Sons, 1979.

[98] M. A. Plonus, *Applied Electromagnetics*. New York: McGraw-Hill, 1978.

[99] W. T. Thomson and M. D. Dahlah, "Theory of Vibration with Applications." Upper Saddle River, NJ: Prentice Hall, 1998, pp. 271-276.

[100] K. E. Petersen, *IEEE Transactions on Electronic Devices*, vol. 25, pp. 1241-1250, 1978.

[101] H. A. C. Tilmans, M. Elwenspoek, and J. H. J. Fluitman, "Micro resonant force gauge," *Sensors and Actuators A*, vol. 30, pp. 35-53, 1992.

[102] G. Stemme, "Resonant silicon sensors," *Journal of Micromechanical Microeng*, vol. 1, pp. 113-125, 1991.

[103] N. Garcia, A. P. Levanyuk, S. A. Minukov, and V. T. Binh, "Estimation of the characteristics of GHz range nanocantilevers: Eigenfrequencies and quality factors," *Surface Science*, vol. 328, pp. 337-342, 1995.

[104] L. D. Landau and E. M. Lifshitz, *Theory of Elasticity*. Oxford, UK: Pergamon, 1967.

[105] D. R. Lide, *CRC Handbook of Chemistry and Physics*, 76 ed. Boca Raton, FL: CRC, 1995-1996.

[106] H. Hosaka, K. Itao, and S. Kuroda, "Damping characteristics of beam-shaped micro-oscillators," *Sensors and Actuators A*, vol. 49, pp. 87-95, 1995.

[107] S. Timoshenko, D. H. Yound, and J. W. Weaver, "Vibration Problems in Engineering," 4th ed. New York: Wiley, 1974, pp. 415-431.

[108] T. C. Edwards, *Foundations of Microstrip Circuit Design*. New York: John Wiley, 1981.

[109] N. Weste and K. Eshraghian, *Principles of CMOS VLSI Design - A Systems Perspective*: Addison-Wesley Publishing Company, 1985.

[110] T. S. Tan, D. M. Braun, T. L. Bagwell, C. P. Kocol, J. Straznicky, and S. R. Sloan, "Flip-chip photodetector for high-speed communications instumentation - Technology Information - Techinical," *Hewlett-Packard Journal*, vol. 10, pp. 1-10, 1997.

[111] J. Brugger, N. Blanc, P. Renaud, and N. F. d. Rooij, "Microlever with combined integreated sensor/actuator functions for scanning force microscopy," *Sensors and Actuators A*, vol. 43, pp. 339-345, 1994.

[112] M. J. Madou, "Fundamentals of Microfabrication: The Science of Miniaturization," 2nd ed. USA: CRC Press LLC, 2002, pp. 84-85.

[113] F. Paschen, *Ann. Physik*, vol. 37, 1889.

[114] A. R. v. Hippel, "Molecular Science and Molecular Engineering." New York: The Technology Press of M.I.T. and John Wiley & Sons, 1959, pp. 39-47.

[115] L. H. Germer, "Electrical Breakdown between close electrodes in air," *Journal of Applied Physics*, vol. 30, pp. 41-47, 1959.

[116] S. F. Bart, T. A. Lober, R. T. Howe, J. H. Lang, and M. F. Schlecht, "Design considerations for micromachined electric actuators," *Sensors and Actuators*, vol. 14, pp. 269-292, 1988.

[117] T. Zhou, P. Wright, J. Crawford, G. Mckinnon, and Y. Zhang, "MEMS 3D Optical Mirror/Scanner," presented at The 2003 international Conference on MEMS, NANO and Smart Systems, Banff, Canada, 2003.

[118] R. A. Buser and N. F. D. Rooij, "Very high Q-factor resonators in monocystalline silicon," *Sensors and Actuators A*, vol. A21-A23, pp. 323-327, 1990.

[119] V. B. Braginsky, *Systems with Small Dissipation*. Chicago, IL: University Chicago Press, 1985.

[120] M. Stjernstrom and J. Roeraade, "Method for fabrication of microfluidic systems in glass," *Journal of Micromechanics and Microengineering*, vol. 8, pp. 33-38, 1998.

[121] C.-H. Lin, G.-B. Lee, Y.-H. Lin, and G.-L. Chang, "A fast prototyping process for fabrication of microfluidic systems on soda-lime glass," *Journal of Micromechanics and Microengineering*, vol. 11, pp. 726-732, 2001.

[122] A. Grosse, M. Grewe, and H. Fouckhardt, "Deep wet etching of fused silica glass for hollow capillary optical leaky waveguides in microfluidic devices," *Journal of Micromechanics and Microengineering*, vol. 1, pp. 257-262, 2001.

[123] M. Bu, T. Melvin, G. J. Ensell, J. S. Wilkinson, and A. G. R. Evans, "A new masking technology for deep glass etching and its microfluidic application," *Sensors and Actuators A*, vol. 115, pp. 476-482, 2004.

[124] P. C. Simpson, A. T. Woolley, and R. A. Mathies, "Microfabrication technology for the production of capillary array electrophoresis chips," *Journal of Biomed Microdevices*, vol. 1, pp. 7-26, 1998.

[125] Spierings, "Compositional effects in the dissolution of multicomponent silicate-glasses in aqueous HF solutions," *Journal of Material Science*, vol. 26, pp. 3329, 1991.

[126] D.-J. Lee, B.-K. Ju, J. Jang, K.-G. Lee, and M.-H. Oh, "Effects of a hydrophilic surface in anodic bonding," *Journal ov Micromech. Microeng.*, vol. 3, pp. 313-318, 1999.

[127] T. Rogers and J. Kowal, "Selection of glass, anodic bonding conditions and material compatibility for silicon-glass capacitive sensors," *Sensors and Actuators A*, vol. 46-47, pp. 113-120, 1995.

[128] Q.-Y. Tong and U. Gosele, *Semiconductor Wafer Bonding: Science and Technology*: John Wiley & Sons, Inc., 1999.

[129] Zygo, "www.zygo.com," Laurel Brook Road Middlefield, CT 06455-0448.

[130] M. Ohring, "The Stoney Formula," in *Material Science of Thin Films*, 2nd ed. San Diego: Academic Press, 2002, pp. 727-730.

[131] M. Ohring, "Techniques for Measuring Internal Stress in Films," in *Material Science of Thin Films*, 2nd ed. San Diego: Academic Press, 2002, pp. 735-737.

[132] Y. Loke, G. McKinnon, and M. J. Brett, "Fabrication and characterization of silicon micromachined threshold accelerometers," *Sensors and Actuators A*, vol. 29, pp. 235-240, 1991.

[133] J.-M. Kim, C.-W. Baek, J.-H. Park, D.-S. Shin, Y.-S. Lee, and Y.-K. Kim, "Continuous anti-stiction coatings using self-assembled monolayers for gold

microstructures," *Journal of Micromech Microengineering*, vol. 12, pp. 688-695, 2002.

[134] W. R. Ashurst, C. Yau, C. Carraro, C. Lee, G. J. Kluth, R. T. Howe, and R. Maboudian, "Alkene Based Monolayer Films as Anti-Stiction Coatings for Polysilicon MEMS," *Sensors and Actuators A*, vol. 91, pp. 239-248, 2001.

[135] C. Robinson, D. Overman, R. Warner, and T. Blomquist, "Problems encountered in the development of a microscale g-switch using three design approaches," presented at 4th International Conference Solid-State Sensors and Actuators (Transducers '87), Tokyo, Japan, June 2-5, 1987.

[136] H. A. C. Tilmans, "Equivalent circuit representation of electromechanical transducers: I. Lumped-parameter systems," *Journal of Micromech. Microeng.*, vol. 6, pp. 157-176, 1996.

[137] J. W. Weigold, A.-C. Wong, C. T.-C. Nguyen, and S. W. Pang, "A Merged Process for Thick Single-Crystal Si Resonators and BiCMOS Circuitry," *Journal of Microelectromechanical Systems*, vol. 8, pp. 3, 1999.

[138] S. Pourkamali and F. Ayazi, "Fully single crystal silicon resonators with deep-submicron dry-etched transducer gaps," presented at IEEE International Micro Electro Mechanical Systems Conference (MEMS '04), The Netherlands, 2004.

[139] S. Pourkamali and F. Ayazi, "SOI-based HF and VHF single crystal silicon resonators with sub-100nm vertical capacitive gaps," *Transducers '03*, pp. 837-840, 2003.

[140] S. Tolansky, *An Introduction to Interferometry*. London: Longmans, Green and Co Ltd, 1966.

[141] E. Hecht, *Optics*, 2nd ed: Addison-Wesley, 1990.

[142] B. Saleh and M. C. Teich, *Fundamentals of Photonics*. New York: Wiley, 1991.

[143] V. Annovazzi-Lodi, S. Merlo, and M. Norgia, "Characterization of Silicon Microstructures by Feedback Interferometry," *Journal of Optics A: Pure and Applied Optics*, vol. 4, pp. S311-S317, 2002.

[144] R. A. Serway, *Physics for Scientists and Engineers with Modern Physics*. Phiadelphia: Saunders College Publishing, 1996.

[145] K. M. Strohm, F. J. Schmuckle, B. Schauwecker, J.-F. Luy, and W. Heinrich, "Silicon micromachined RF MEMS resonators," presented at IEEE MTT-S Digest, 2002.

[146] M. Wojdyr, "Fityk," 0.4.3 ed: www.sourceforge.net, 2004.

[147] J. R. Taylor, *An Introduction to Error Analysis - The Study of Uncertainties in Physical Measurements*. Sausalito, CA: University Science Books, 1982.

[148] W. E. Newell, "Miniaturization of tuning forks," *Science*, vol. 161, pp. 1320-1326, 1968.

[149] A. H. Nayfeh and M. I. Younis, "A new approach to the modeling and simulation of flexible microstructures under the effect of squeeze-film damping," *Journal Of Micromechanics And Microengineering*, vol. 14, pp. 170-181, 2004.

[150] J. J. Bech, "On isothermal squeeze films," *Journal of Lubrication Technology A*, vol. 105, pp. 615-620, 1983.

[151] M. M. Khonsari and R. Booser, *Applied tribology: bearing design and lubrication*. New York: John Wiley, 2001.

[152] T. Corman, P. Enoksson, and G. Stemme, "Gas damping of electrostatically excited resonators," *Sensors And Actuators A-Physical*, vol. 61, pp. 249-255, 1997.

[153] B. Moore, H. Rourke, and C. Backhouse, "Innovative Optical Methods for MEMS Characterization," *IEEE Sensors Journal*, submitted in 2005.

[154] S. N. Sen, *Acoustics: Waves & Oscillations*. New Delhi, India: Wiley Eastern Limited, 1990.

[155] T. D. Rossing, *The Science of Sound*: Addison-Wesley, 1982.

[156] S. H. Choa, "Reliability of vacuum packaged MEMS gyroscopes," *Microelectronics and Reliability*, vol. 45, pp. 361-369, 2005.

[157] C. T.-C. Nguyen, "Vibrating RF MEMS for low power wireless communications (invited)," presented at Proceedings of 2000 International MEMS Workshop (iMEMS'01), Singapore, 2001.

[158] M. W. Putty, S. C. Chang, R. T. Howe, A. L. Robinson, and K. D. Wise, "One-port active polysilicon resonant microstructures," presented at Micro Electro Mechanical Systems Proceedings, 'An Investigation of Micro Structures, Sensors, Actuators, Machines and Robots'. IEEE, Salt Lake City, Utah, 1989.

[159] J. Yang, T. Ono, and M. Esashi, "Mechanical Behavior of Ultrathin Microcantilever," *Sensors and Actuators A*, vol. 82, pp. 102-107, 2000.

Appendix A - Other Reported Cantilevers

Table A-1: Other Reported Micromechanical Resonators

Switch	Thickness (um)	Width (um)	Length (um)	Frequency (kHz)	Q-factor	Vacuum	Reference
Single Crystal Silicon – (SCSi) Clamped-Clamped (C-C)	5.5	20	510	f_o-1st=164.5 f_3=1.03MHz	Q1=60400 Q3=10700	1mTorr	[1]
SCSi C-C	6.5	20	510	198.0	35000	1mTorr	[1]
SCSi C-C	7.5	20	510	217.0	27000	1mTorr	[1]
SCSi C-C	5.5	20	300	489.3	21500	1mTorr	[1]
SCSi C-C	6.5	20	300	528.0	17000	1mTorr	[1]
Polysilicon C-C	1	50	75	160		Atmosphere	[158]
Polysilicon C-C	1	50	100	100		Atmosphere	[158]
SCSi	~5	40	300	58	65	Atmosphere	[111]
SCSi	~5	40	800	10		Atmosphere	[111]
Calcs for Si	0.1	4	88.9	100kHz			[72]
Calcs for Si	0.1	1	28.1	1MHz			[72]
Calcs for Si	0.1	0.4	8.89	10MHz			[72]
Si_3N_4	V-shaped 0.6-0.8?	36	200	12.4			[7]
Si_3N_4	V-shaped 0.6-0.8?	22	120	37-54			[7]

~216~

Ti/Au on Si$_3$N$_4$	V-shaped 0.6	90	150	115			[23]
SCSi	0.17	1	6	3669.2	5000	10^{-5}Torr	[159]
SCSi	0.17	5	32.3	175.8	13762	10^{-5}Torr	[159]
SCSi	0.17	5.5	41.5	104.4	10878	10^{-5}Torr	[159]
SCSi	0.17	9.7	64.6	f_0-1st=46.6 f_2=291.8 f_3=817.4 f_4=1600.6	Q1=11882 Q2=11994 Q3=12234 Q4=13410	10^{-5}Torr	[159]
* SCSi Clamped-Clamped (C-C)	5	20	700	f_0-1st=80.3 f_3=490 f_5=1240	Q1=74000 Q3=23100 Q5=10700	1mTorr	[75]
SCSi C-C	4	20	500	117	67000	1mTorr	[75]
SCSi C-C	5	20	500	f_0-1st=116 f_3=720 f_5=1880	Q3=21300 Q5=7600	1mTorr	[75]
SCSi C-C	5.5	20	500	f_0-1st=164.5 f_3=1030	Q1=60400 Q3=10700	1mTorr	[75]
SCSi C-C	6.5	20	500	f_0-1st=198 f_3=1210	Q1=35000 Q3=8300	1mTorr	[75]
SCSi C-C	7.5	20	500	217	27000	1mTorr	[75]
SCSi C-C	7.5	20	900	f_0-1st=74.8 f_3=440	Q3=10400	1mTorr	[75]

SCSi C-C	4	20	300	$f_0\text{-}1^{st}=288$ $f_3=1710$ $f_5=4410$	Q1=43000 Q3=13900 Q5=8400	1mTorr	[75]
SCSi C-C	5.5	20	300	489.3	21500	1mTorr	[75]
SCSi C-C	6	20	300	$f_0\text{-}1^{st}=496$ $f_3=2720$	Q1=21900 Q3=6700	1mTorr	[75]
SCSi C-C	6.5	20	300	528	17000	1mTorr	[75]
SCSi C-C	5	20	200	$f_0\text{-}1^{st}=911$ $f_3=5050$	Q1=10000 Q3=5000	1mTorr	[75]
SCSi C-C	10	20	200	3200	4500	1mTorr	[75]
* SCSi	6.5	20	700	15.94	173800	1mTorr	[75]
* SCSi	4	20	500	19	178000	1mTorr	[75]
* SCSi	5	20	500	24.59	157400	1mTorr	[75]
* SCSi	6	20	500	30.14	154800	1mTorr	[75]

Appendix B – Mechanical/Electrical Oscillator Analogy

The discussion of forced, damped, harmonic mechanical oscillators in the field of Electrical Engineering warrants analogy to ensure full understanding and clarity is achieved.

Mechanical Oscillator	*Electrical Oscillator*
ξ = displacement	q = electric charge
$v = \dfrac{d\xi}{dt}$ = velocity	$I = \dfrac{dq}{dt}$ electric current
M = inertial mass	L = inductance
b = mechanical resistance coefficient	R = electric resistance
C = 1/k = compliance	C = capacitance
$\omega_0 = \sqrt{\dfrac{k}{m}} = \sqrt{\dfrac{1}{mC}}$	$\omega_0 = \sqrt{\dfrac{1}{LC}}$
Kinetic energy = $mv^2/2$	Magnetic energy = $LI^2/2$
Potential energy = $k\xi^2/2 = \xi^2/2C$	Electric energy = $q^2/2C$
Power input = Fv	Power input = VI
Ordinary Differential Equation for a forced, damped harmonic oscillator:	
$M\dfrac{dv}{dt} + bv + k\xi = F(t)$ $M\ddot{\xi} + b\dot{\xi} + k\xi = F(t)$	$L\dfrac{dI}{dt} + RI + (1/C)q = V(t)$ $L\ddot{q} + R\dot{q} + (1/C)q = V(t)$

B - 1: Schematic of Force, Damped, and Harmonic Oscillators for Mech./Elec. Analogy
(a) Mechanical Oscillator (b) Electrical Oscillator

(a)

(b)
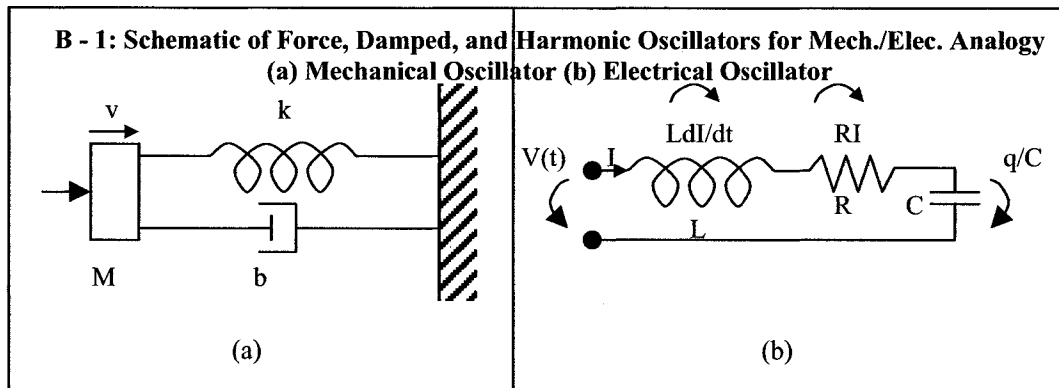
Appendix C – Details of ANSYS simulation

The code altered for this analysis is property of ANSYS and so cannot be published publicly. However, details used in the simulation are presented.

The approach to the electrostatic-structural analysis used is ESSOLV[****], which ANSYS has since replaced, making it obsolete. ESSOLV is a sequential coupled electro-static structural macro where both structural and electrostatic domains are meshed. The electrostatic field mesh morphs to accommodate the deformed cantilever beam.

Four elements are used in the simulation for the structural analysis.

1) The beam is modeled with Plane 82 - an 8-noded plane strain element. This element is used to simply represent thick elements.

2) The air gap as a null element

3) The underside of the beam as a contact surface element Conta172 – a 3-noded 2D line meshing element

4) The bottom electrode as a target surface element, Targe169.

Only one electrostatic element, Plane121 – a 2D 8-noded electrostatics element, is utilized. It is applicable to a two-dimensional, electrostatic field analysis and has one degree of freedom, voltage, at each node.

Structural boundary conditions are applied to the end of the beam and the large displacement effects option is utilized. Electrical boundary conditions include applying the input voltage to the lines around the beam and zero voltage to the bottom electrode line.

These parameters described are then assembled into a code that first uses Finite Element analysis (FEA) to calculate the electrostatic force, applies that force in a structural FEA analysis, plots the displacement result and increments the voltage. The program uses a loop function that is reversed once the threshold voltage is found. The loop then

---

[****]ANSYS: http://www.ansys.com/industries/mems/mems-feature-es-coupling.asp#essolv
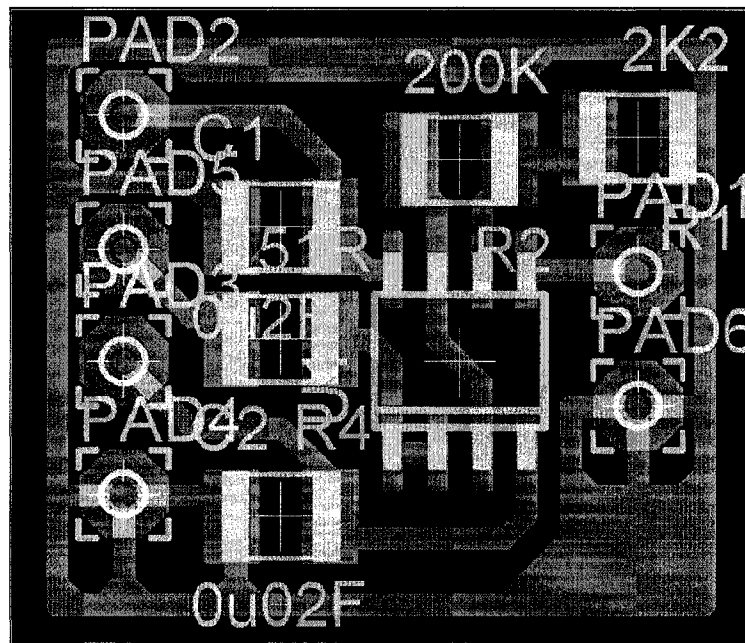
~221~

continues in the same way but decrements the voltage until the restoring force is found.

Appendix D – Dynamic Electrical Testing: Operational Amplifier Design
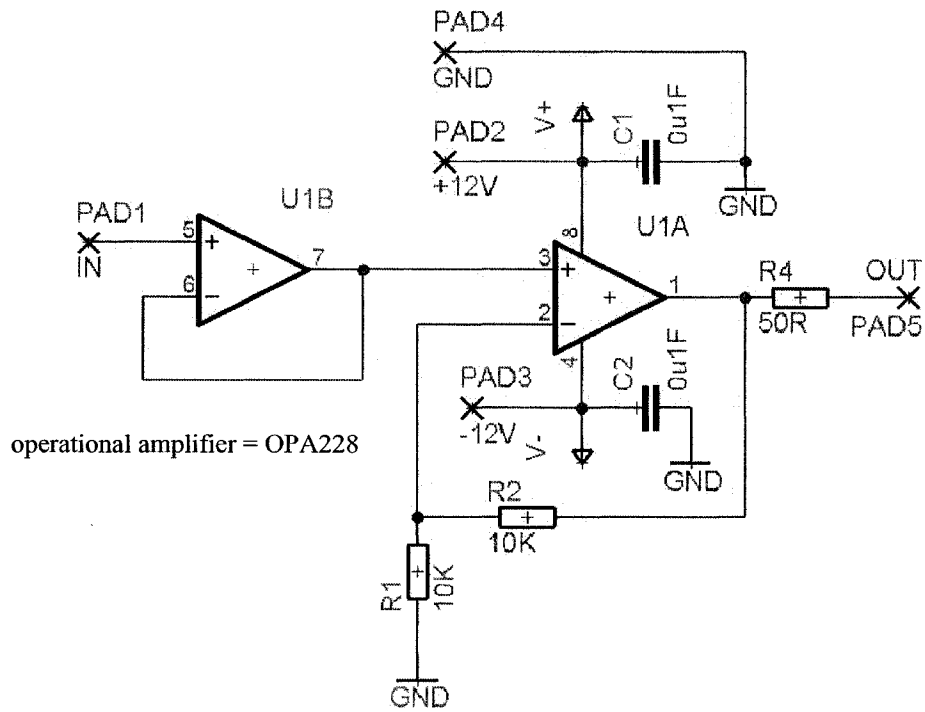
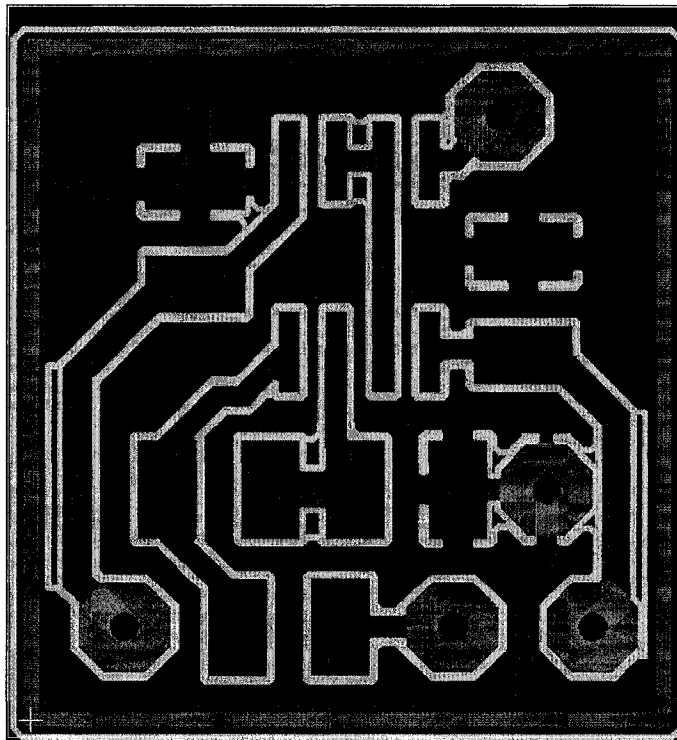## 1   Board iteration #1[††††]
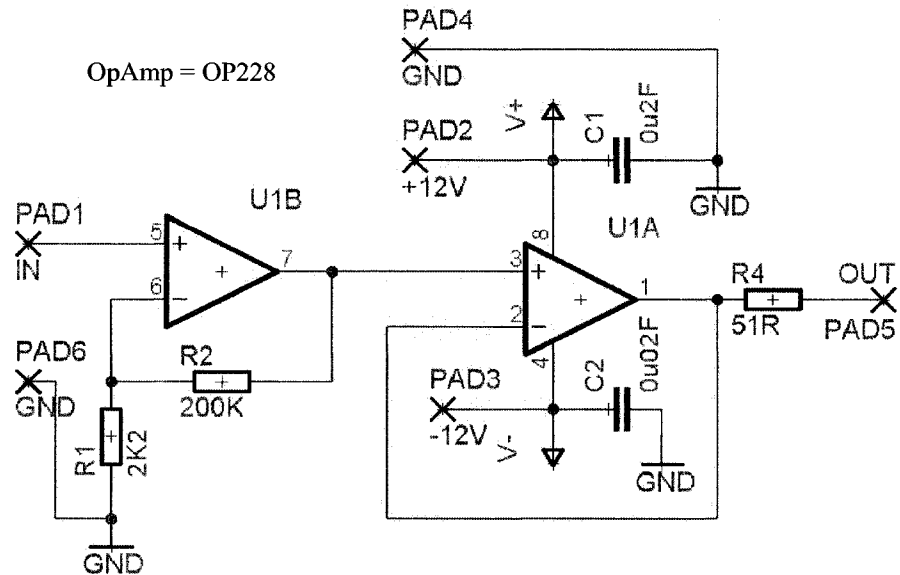
OpAmp_it1.sch

OpAmp_it1.brd

[††††] Board designed, fabricated, and assembled by Ben Bathgate, 2003.

2. Board Iteration #2[‡‡‡‡]

operational amplifier = OPA228

OpAmp_it2.sch

OpAmp_it2.brd

[‡‡‡‡] Board designed, fabricated, and assembled by Ben Bathgate, 2003.

~224~

Appendix E – Micromechanical Resonator Impedance Calculations

1 Matlab Program Used for Impedance

```
%properties
e0=8.85e-12;
A=6.25e-10; %area of electrodes 25x25um
p=2320; %density
Vp=20; %polarization Voltage
Q=4.53; %average of analytical Q
f=[45000:0.1:70000];
w=[f].*2.*pi;

%dimensions of Standard beam
lb=200e-6;
bb=25e-6;
t=2e-6;
d=2e-6;
m=lb*bb*t*p; %mass of the beam

%Electrical Equivalent Circuit Parameters
diCdx=e0*A/(d^2);
n=Vp*diCdx;
k=(53978*2*pi)^2*m; %use natural angular frequency

Rx=(sqrt(k*m))/(Q*n^2)
Lx=m/(n^2);
Cx=n^2/k;
Co=e0*A/d;


%impedance calculations
z=abs((j.*[w].*Co+(1./(j.*[w].*Lx+(1./(j.*[w].*Cx))+[Rx]))).^(-1));
z=z.';

f=[w]./2./pi;
f=f.';

zstat=abs((j.*[w].*Co).^(-1));
zstat=zstat.';

zmot=abs(j.*[w].*Lx+(1./(j.*[w].*Cx))+[Rx]);
zmot=zmot.';
```

```
resRLC=1/2/pi*((1/Lx/Cx)-(Rx/Lx)^2)^(1/2) %resonant frequency of Motional RCL
circuit

test=[[z],[zstat],[zmot]];
plot(f,test)
xlabel('Frequency (Hz)'),ylabel('Impedance of Electrical Equivalent Circuit (ohm)')
title('Impedance of Device vs. Frequency')
```

Appendix F – Parts List For Bench-Top Interferometer

Item	Manufacturer	Part Number
Breadboard		
HeNe Gas Laser	JDS Uniphase	
Optical Isolator	Optics for Research	OFR 10-5-NIR
Beamsplitters (x3)	Newport Optics	BK7
Mirrors (x3)	Thor Labs Inc.	BB1-E02
Translation stages (x4)	Standa	002009
Neutral Density Filter	Edmund Industrial Optics	46211, 0.15
Optical Fibre Light Source		
Lens (x4)	Edmund Industrial Optics	PCX elf 100: 32482 PCX elf 25: 45098 PCX elf 50: 32478 DCX elf 25: 32490
Lens holders		
Post holders		
Posts		

Fibre Interferometer

Item	Manufacturer	Part Number
1550nm DFB Laser Source	Thor Labs Inc.	S1FC1550
Polarization independent fibre optic circulator	Alcatel	OPTOA0003601
Optical Power Meter		HP8153A
Single Mode Fibres		SMF-28

~227~